Uncovering Novel Phases in Complex Magnetic Materials Using Resonant X-ray Scattering

Benjamin Zager

A thesis submitted in partial fulfillment of the requirements for the Degree of Doctor of Philosophy in the Department of Physics at Brown University

Providence, Rhode Island

October 2024

© Copyright 2024 Benjamin Zager

This dissertation by Benjamin Zager is accepted in its present form by the Department of Physics as satisfying the dissertation requirement for the degree of Doctor of Philosophy.

Date _____ _____

Kemp Plumb, Advisor

Recommended to the Graduate Council

Date _____ _____

Brad Marston, Reader

Date _____ _____

Peter Weber, Reader

Approved by the Graduate Council

Date _____ _____

Thomas A. Lewis, Dean of the Graduate School

Benjamin Zager

Education

Brown University, Providence, RI
Ph.D. Physics - May 2024
M.S. Physics - May 2021

Tufts University, Medford, MA
B.S. Engineering Physics and Applied Mathematics - May 2019

Research Experience

National Synchrotron Light Source II (NSLS-II), Brookhaven National Laboratory
Postdoctoral Research Associate June 2024 - Present
- Developing capabilities for resonant inelastic x-ray scattering (RIXS) with in situ strain control

Plumb Lab, Brown University Department of Physics
Graduate Research Assistant June 2020 - May 2024
- Studied novel electronic and magnetic phenomena in quantum materials
- Carried out crystal growth and materials characterization
- Conducted x-ray scattering and spectroscopy experiments at numerous synchrotron light sources around the world
- Mentored undergraduate and masters students

Cebe Research Group, Tufts University Department of Physics & Astronomy
Undergraduate Research Assistant September 2016 - May 2019
- Worked on thermal and structural analysis of polymer nanofibers
- Designed and built a humidity controlled electrospinning chamber
- Characterized electrospun nanofibers with x-ray diffraction, IR spectroscopy, and differential scanning calorimetry

Advanced Technology for Large Structural Systems (ATLSS), Lehigh University
Undergraduate Researcher Summer 2018
- Worked on fatigue testing of orthotropic steel bridge deck design for a New York City bridge
- Streamlined strain gage data analysis procedure with Matlab
- Carried out inspections of weld details to locate fatigue cracking
- Worked on standardizing steel specimen inventory using Autocad

Undergraduate Researcher Summer 2017
- Researched and developed computer vision software for automated detection of steel corrosion
- Distinguished corrosion using color and texture features based on HSV color frequencies and edge density statistics
- Detected corrosion in high variance images with 90% accuracy

Teaching Experience

Brown University Department of Physics
- Graduate teaching assistant for Physics 50/70 labs (introductory mechanics), Fall 2019
- Graduate teaching assistant for Physics 60/160 labs (introductory electromagnetism/waves and optics), Spring 2020

Tufts University Department of Physics and Astronomy
- Teaching assistant for Physics 11 (calculus-based introductory mechanics), Fall 2017
- Grader for Physics 1 (algebra-based introductory mechanics), Fall 2018

Publications

1. **B. Zager**, R. Fan, P. Steadman, and K. Plumb, Double-Q spin chirality stripes in the anomalous Hall antiferromagnet $CoNb_3S_6$, arXiv preprint arXiv:2307.03776 (2023).
2. A. de la Torre, **B. Zager**, F. Bahrami, M. H. Upton, J. Kim, G. Fabbris, G.-H. Lee, W. Yang, D. Haskel, F. Tafti, and K. W. Plumb Momentum-independent magnetic excitation continuum in the honeycomb iridate $H_3LiIr_2O_6$, Nature Comm. 14, 5018 (2023).
3. A. de la Torre, **B. Zager**, J. R. Chamorro, M. H. Upton, G. Fabbris, D. Haskel, D. Casa, T. M. McQueen, and K. W. Plumb Electronic ground state of two nonmagnetic pentavalent honeycomb iridates, Phys. Rev. Materials 6, 084406 (2022).

4. **B. Zager**, J. R. Chamorro, L. Ge, F. Bahrami, V. Bisogni, J. Pelliciari, J. Li, G. Fabbris, T. M. McQueen, M. Mourigal, and K. W. Plumb Electronic structure of the frustrated diamond lattice magnet $NiRh_2O_4$ Phys. Rev. B 106, 045134 (2022).
5. A. de la Torre, **B. Zager**, F. Bahrami, M. DiScala, J. R. Chamorro, M. H. Upton, G. Fabbris, D. Haskel, D. Casa, T. M. McQueen, F. Tafti, and K. W. Plumb Enhanced hybridization in the electronic ground state of the intercalated honeycomb iridate $Ag_3LiIr_2O_6$, Phys. Rev. B 104, L100416 (2021).

Presentations

1. Chiral spin texture in the anomalous Hall antiferromagnet $CoNb_3S_6$, APS March Meeting 2023
2. Chiral spin texture in the anomalous Hall antiferromagnet $CoNb_3S_6$, APS New England Section Meeting 2022
3. Electronic structure of the frustrated diamond lattice magnet $NiRh_2O_4$, APS March Meeting 2022
4. X-ray absorption studies of structural distortion in $Ag_3LiIr_2O_6$, APS March Meeting 2021

Workshops/Schools

22nd National School on Neutron and X-ray Scattering (virtual)
2021 PARADIM Summer School on Density Functional Theory for Experimentalists

Award and Honors

Award of Excellence as a Graduate Teaching Assistant (Brown University, 2020)
Amos Emerson Dolbear Scholarship (Tufts University, 2019)
Sigma Pi Sigma (Tufts University, 2018)
Tau Beta Pi (Tufts University, 2018)

Abstract of "Uncovering Novel Phases in Complex Magnetic Materials Using Resonant X-ray Scattering" by Benjamin Zager, Ph.D., Brown University, October 2024

Materials with strongly interacting electrons exhibit a wide variety of unconventional ordering phenomena that are both fundamentally rich and promising for many potential technological applications. These phases often involve coupling between spin, charge, orbital, and lattice degrees of freedom, precisely tuned by a hierarchy of energy scales. They may also involve more subtle degrees of freedom that may be elusive to many common experimental probes. In this thesis, I discuss a series of resonant elastic and inelastic x-ray scattering experiments (REXS/RIXS) on complex magnetic materials to uncover the microscopic mechanisms behind the novel magnetic phenomena observed in these materials.

$NiRh_2O_4$ is a $S = 1$ frustrated diamond lattice antiferromagnet that may be in proximity to a quantum critical point. I carried out RIXS measurements to unravel the spin-orbital-lattice entangled ground state in $NiRh_2O_4$.

$CoNb_3S_6$ is an intercalated transition metal dichalcogenide (iTMD) exhibiting a giant anomalous Hall effect (AHE) that cannot be explained by its putative collinear antiferromagnetic order. Using REXS, I discovered a long-wavelength modulation of the magnetic structure that gives rise to a novel striped pattern in the scalar spin chirality.

The properties of iTMDs are highly sensitive to the precise stoichiometry of intercalated $3d$ ions. I carried out comprehensive magnetic and structural characterization on $CoNb_3S_6$ and the related material $NiNb_3S_6$ with varying Co and Ni stoichiometry to understand the dependence of the magnetic properties on sample composition.

$NiGa_2S_4$ is a nearly ideal $S = 1$ triangular lattice magnet which shows no long

range magnetic order and exhibits a variety of unconventional magnetic properties. I carried out REXS measurements to probe the magnetic correlations within a small sample volume to disentangle structural and magnetic disorder. I find a correlation length that is longer than that found in previous measurements, as well as a temperature-induced shift in the magnetic wavevector. Using RIXS, I ruled out the previously reported negative charge transfer ground state and instead found a mixed valence state.

Acknowledgments

I would first like to thank my advisor Kemp Plumb for sparking my interest in magnetism and scattering, giving me the opportunity to work on such exciting projects, and providing strong guidance and support throughout my Ph.D. I would like to thank my lab mates Alberto de la Torre, Tsung-Han Yang, Qiaochu Wang, and Michael DiScala for all of their involvement in experiments, sample preparation, and analysis. I would also like to thank my committee members Brad Marston and Peter Weber for their insightful comments and discussion.

Throughout my Ph.D., I carried out 26 x-ray scattering experiments or "beamtimes" at 8 different synchrotron light sources. I am indebted to the many beamline scientists, staff, and post-docs at these facilities who supported me throughout my experiments, often exceeding expectations to ensure everything ran smoothly. This includes Raymond Fan, Paul Steadman, and Mark Sussmuth from Diamond I10, Stefano Agrestini from Diamond I21, Valentina Bisogni, Jonathan Pelliciari, and Jiemin Li from NSLS-II SIX, Andi Barbour, Claudio Mazzoli, and Rahul Jangid from NSLS-II CSX, Christie Nelson from NSLS-II ISR, Eugen Weschke from BESSY II UE46_PGM-1, Jacob Ruff and Suchi Sarkar from CHESS QM2, Ronny Sutarto from CLS REIXS, Di-Jing Huang, Hsiao-Yu Huang, Jun Okamoto, and Ganesh Channagoudra from TPS 41A, Sujoy Roy and Sophie Morley from ALS COSMIC, Padraic Shafer from ALS 4.0.2, Mary Upton from APS Sector 27, George Sterbinsky from APS 9-BM, and any others who I may have missed.

I would like to thank Juan Chamorro, Tyrel McQueen, Faranak Bahrami, and Fazel Tafti for providing me with samples, as well as Martin Mourigal, Luwei Ge, and Matthew Stone for

providing inelastic neutron scattering data. I am thankful for the valuable discussions with Arun Paramekanti, Pat Clancy, Hlynur Gretarsson, Cristian Batista, and Frank de Groot, whose insights enabled many breakthroughs in my work. I would like to thank Calvin Bales and other members of the Mitrovic lab for providing me with liquid nitrogen whenever I was setting up chemical vapor transport.

I would like to thank all of my professors at Tufts who inspired me to pursue a physics Ph.D., including Peggy Cebe, Tim Atherton, Bruce Boghosian, Tom Vandervelde, and any others I may have missed.

I would like to thank Hannah Weller for producing the template for this thesis.

I am grateful for Brown University ice hockey club, Providence Community Ultimate Team (PCUT), The Parlour, and Myrtle for allowing me to pursue my interests in sports and music.

Finally, I would like to thank my parents and my siblings Zach, Carly, Matt, and Eric for their endless support and encouragement.

Contents

List of Figures

List of Tables

CHAPTER 1

Introduction

This chapter provides an overview of ceoncepts from condensed matter physics that are essential to this thesis. The first section introduces the concept of strongly correlated materials using the Hubbard model. It then describes the physical processes that determine the local degrees of freedom on each ion. Next, it demonstrates how interactions occur in the simplest case and introduces the wide variety of interactions that may occur in general. The second section covers ordering phenomena, mainly magnetism, which arise from interactions, and the corresponding excitations. It then covers the more exotic ordering phenomena that appear in this thesis involving frustrated magnetism and composite degrees of freedom such as spin-orbital moments and spin chirality. The final two sections cover the specific types of materials appearing in this thesis. General background on solid state and condensed matter physics can be found in [1–4]. More background on magnetism and strongly correlated materials can be found in [5–8].

1.1 Electrons in solids

1.1.1 Strongly correlated materials

The properties of crystalline solids are governed mainly by the valence electrons, which occupy the highest energy levels. These electrons are bound by the periodic potential of the crystal lattice where individual atomic energy levels become dispersive energy bands. This is the scope of *band theory*, where the electrons are considered as effectively noninteracting particles. The key result being that materials with a partially occupied valence band are *conductors* i.e. metals, while materials with a fully occupied valence band are *insulators* [1, 2].

In some cases, particularly when valence electrons occupy d and f shells, interactions cannot be ignored. In these highly localized orbitals, Coulomb repulsion is not effectively screened and electron-electron interactions drastically alter the electronic ground state. In these *strongly correlated materials*, Coulomb repulsion produces an insulating state in a material with a partially filled valence band, known as a *Mott insulator* or more generally a *correlated insulator*. In this state, unpaired electrons are localized to the lattice sites. Their charge, spin, and orbital degrees of freedom interact to form a diverse range of ordering phenomena and other emergent behaviors [5].

The main concept driving the Mott insulator state and other strong correlation effects is the interplay between kinetic energy and Coulomb repulsion. Consider a 1D lattice with a single electronic state available on each site, which can be occupied by up to two electrons with opposite spin, as required by the Pauli exclusion principle. The electrons' kinetic energy can be described by some *hopping* parameter t, which is the tunneling amplitude between neighboring sites. Coulomb repulsion can be described by an energy cost U for electrons to occupy the same site. This gives the simplest model that can describe a correlated insulator state, known as the *Hubbard model*, given by the Hamiltonian

$$\mathcal{H}_{\text{Hub}} = -t \sum_{\langle ij \rangle \sigma} (c^{\dagger}_{i\sigma} c_{j\sigma} + \text{h.c.}) + U \sum_{i} n_{i\uparrow} n_{i\downarrow} \tag{1.1}$$

where $c^\dagger_{i\sigma}$ and $c_{i\sigma}$ are fermion creation and annihilation operators for an electron with spin $\sigma =\uparrow,\downarrow$ at site i, h.c. denotes the Hermitian conjugate of the first term, and $n_{i\sigma} = c^\dagger_{i\sigma}c_{i\sigma}$ is the number operator of for electrons with spin σ on site i. The notation $\langle ij\rangle$ denotes summing over all nearest neighbor pairs. The average number of electrons per site is known as the *filling*. We will consider the most common case of $n = 1$, known as *half-filling*.

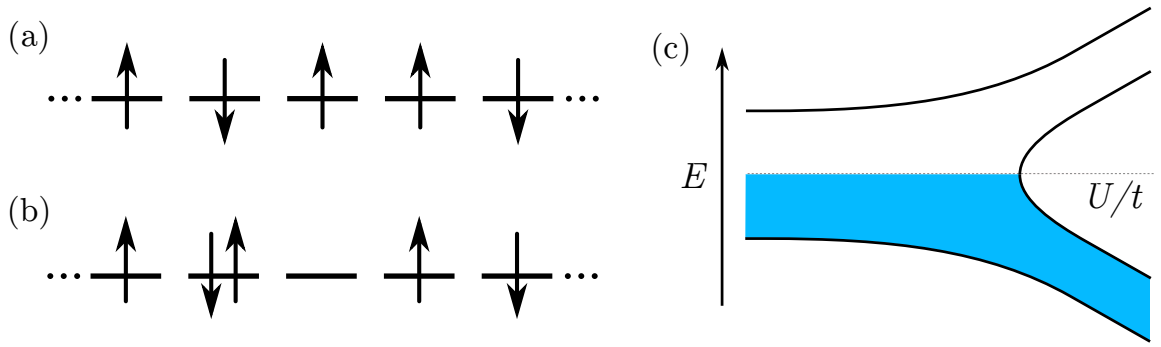

Figure 1.1: (a) 1D Hubbard model at half-filling with randomly oriented spins. (b) Electron hopping to a neighboring site, creating an excitation of energy U. (c) Schematic density of states for the Hubbard model as a function of U/t. showing the Metal-insulator transition as the partially filled valence band is split into a lower and upper Hubbard subband.

In the limit of $U/t \ll 1$, the Hubbard model reduces to a simple tight-binding model, which yields a metallic state for $n = 1$. In the limit of $U/t \gg 1$, the half-filled valence band is split into a fully occupied lower band and an empty upper band. This corresponds to an insulating state, with energy gap $E_g \sim U - W$, where $W = 2zt$ is the *bandwidth*, z is the coordination number or the number of nearest neighors for each lattice site. There is thus some critical $U = U_c \sim W$ at which the system undergoes a *metal-insulator transition*.

1.1.2 Local degrees of freedom

In the previous section, we considered a 1D lattice with a single electronic state on each site. However, real materials form 3D lattices with each site contributing a full atomic multiplet of states. This section describes degrees of freedom and corresponding the energy scales related to the local states on each site in a correlated insulator. The largest class of such materials are compounds containing $3d$ transition metal ions. In these materials, the valence electron wavefunctions are highly localized and resemble atomic orbitals. However, the spherical

symmetry of a free ion is broken by the anisotropy of the crystal lattice. The local degree of freedom in these materials is the many-body ground state of a d^n configuration, where $n \leq 10$ depends on the particular element and oxidation state. For example, $3d^8$ for Ni^{2+}, $3d^7$ for Co^{2+}, and $5d^5$ for Ir^{4+}. The interactions that determine this ground state are the *Hund's coupling* (also known as the intra-atomic exchange), *spin-orbit coupling*, and the perturbations induced by the surrounding ions in the crystalline environment, known as the *crystal field*.

In this section, we will use the single-electron description to develop a simple qualitative picture. Section 2.6 will introduce the many-body formulation used for quantitative calculations. The electronic wavefunctions can be represented in the basis of the d orbitals, given by the spherical harmonics with $l = 2$. To accomodate the anisotropy of the crystal lattice, we use the real spherical harmonics in cartesian coordinates, which are linear combinations of the complex spherical harmonics $|l, l^z\rangle = |2, l^z\rangle = |l^z\rangle$

$$\begin{aligned} e_g &\begin{cases} |x^2 - y^2\rangle = |0\rangle \\ |z^2\rangle = \frac{1}{\sqrt{2}}(|2\rangle + |-2\rangle) \end{cases} \\ t_{2g} &\begin{cases} |xy\rangle = -\frac{i}{\sqrt{2}}(|2\rangle - |-2\rangle) \\ |xz\rangle = -\frac{1}{\sqrt{2}}(|1\rangle - |-1\rangle) \\ |yz\rangle = \frac{i}{\sqrt{2}}(|1\rangle + |-1\rangle) \end{cases} \end{aligned} \tag{1.2}$$

The Hubbard U described in the previous section parameterizes the monopole component of the Coulomb interaction that localizes electrons to their respective sites. There are also higher order multipole components that act between electrons on the same site. These interactions will be discussed in more detail in section 2.6, but the dominant effect can be described by

$$\mathcal{H}_{\text{Hund}} = -J_H \sum_{i \neq j} (2\boldsymbol{S}_i \cdot \boldsymbol{S}_j + \tfrac{1}{2}) \tag{1.3}$$

where J_H called the Hund's coupling, $\boldsymbol{S}_i$ is the spin of an electron in orbital i. This interaction causes electrons to occupy parallel spin states on separate orbitals, maximizing the total spin

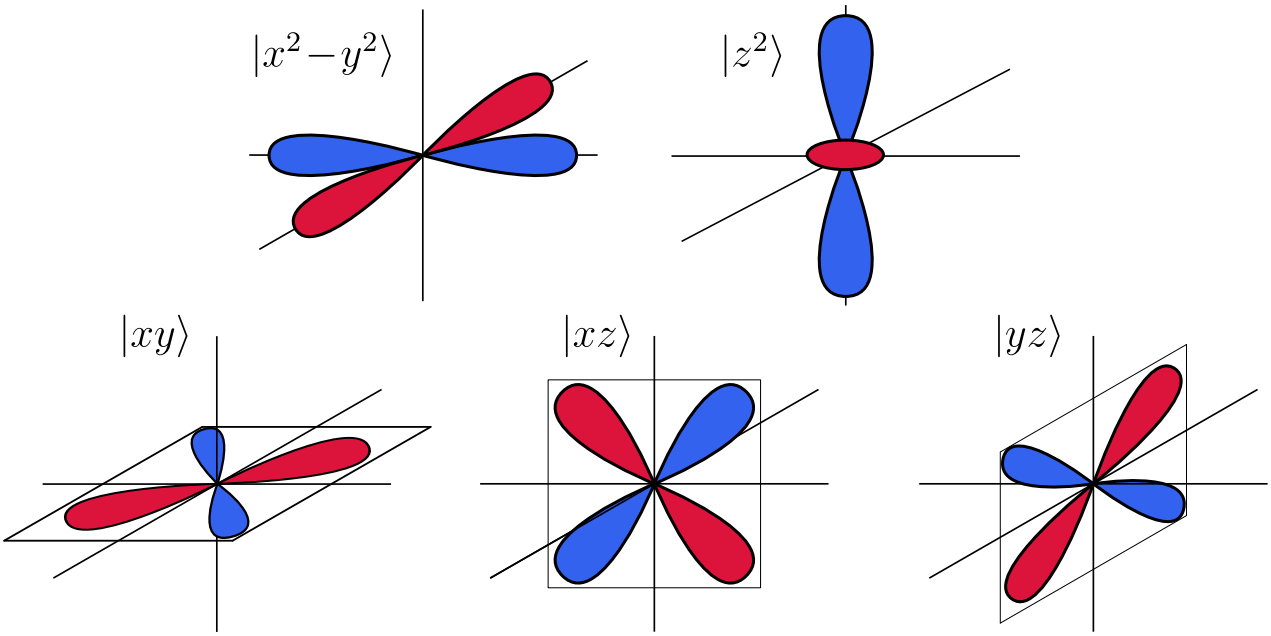

Figure 1.2: Shapes of the d orbitals in the cartesian basis. The red and blue indicate regions of the wavefunction with opposite phase.

of the atom. For an isolated ion, this is known as the first Hund's rule. Similar effects lead electrons to maximize the orbital angular momentum for a given maximal spin, known as the second Hund's rule. By minimizing the Coulomb repulsion between valence electrons, the spin and orbital angular momentum are determined, along with the corresponding orbital occupation.

Spin-orbit coupling (SOC) also plays an important role in the determining the electronic ground state. In the LS or Russel-Sanders coupling scheme relevant for (especially $3d$) transition metal ions, the SOC is given by

$$\mathcal{H}_{\mathrm{SOC}} = \lambda \boldsymbol{L}\cdot\boldsymbol{S}, \tag{1.4}$$

where λ is the spin-orbit coupling constant. $\boldsymbol{S}$ and $\boldsymbol{L}$ are the net spin and orbital angular momentum summed over all electrons. This interaction determines the total angular momentum $\boldsymbol{J} = \boldsymbol{L} + \boldsymbol{S}$ and gives the third Hund's rule: minimize J for a less than half-filled shell (normal multiplet), and maximize J for more than half-filled shell (inverted multiplet).

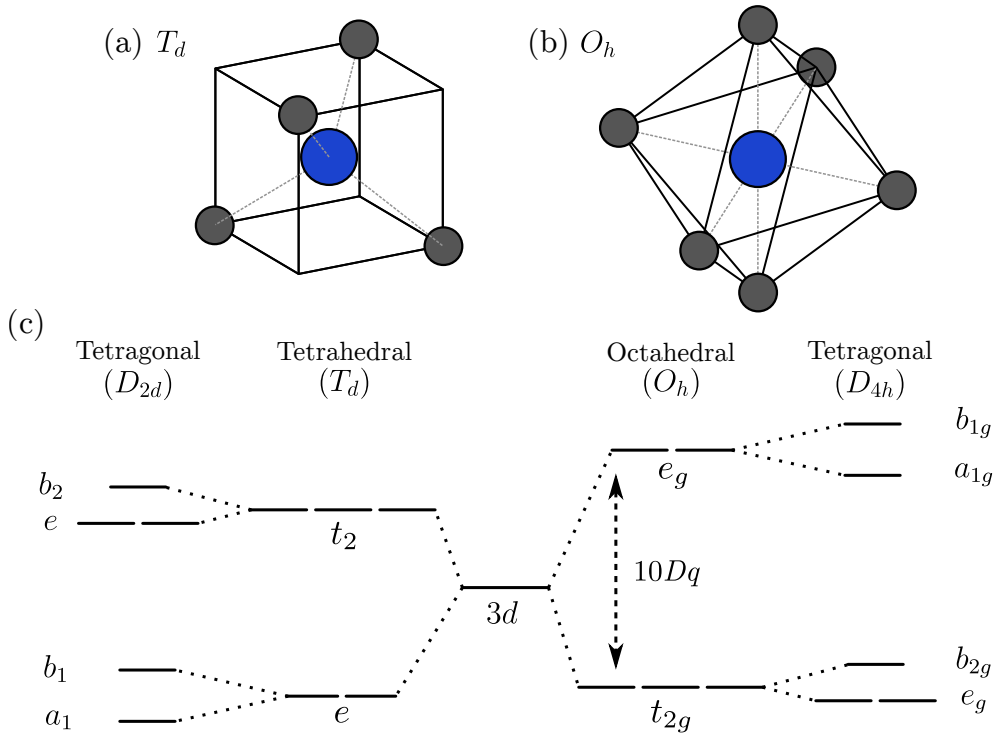

Figure 1.3: (a) Tetrahedral coordination geometry (b) Octahedral coordination geometry (c) Branching of $3d$ orbitals upon symmetry reduction by a tetrahedral or octahedral crystal field, and further reduction by a tetragonal distortion, where the sign of the splitting shown here corresponds to an elongation.

The Hund's coupling and SOC determine the electronic ground state of an isolated atom or ion according to Hund's rules. In a crystal, the spherical symmetry is lowered to some discrete symmetry determined by the local coordination geometry, classified by its *point group*. A transition metal cation in a crystal is surrounded by anions called *ligands*, which are typically chalcogens or halogens with fully occupied p shells (O^{2-}, S^{2-}, Cl^{-}, F^{-}, etc.). This anisotropic environment is known as the *crystal field* and breaks the degeneracy of the d orbitals, which can be explained by two mechanisms: electrostatic repulsion and metal-ligand hybridization.

In the ideal case of a purely ionic crystal, valence electrons are fully localized on each ion, with no overlap between neighboring sites. In this case, we can consider the ligands as negative point charges. The electrons on the metal site are repelled by these charges, which splits the degenerate d orbitals into subsets based on their shape. The orbitals with lobes pointing toward the ligands will have higher energy than those with lobes pointing in between

the ligands.

For the most common case of octahedral coordination, where the ligands are centered along the cartesian axes drawn in Fig. 1.2, the $|x^2 - y^2\rangle$ and $|z^2\rangle$ orbitals are split to higher energy while the $|xy\rangle$, $|xz\rangle$, and $|yz\rangle$ orbitals are split to lower energy. Another common geometry is tetrahedral, which has the opposite splitting to octahedral. The magnitude of the crystal field splitting is conventionally called $10Dq$.

We can classify any particular coordination geometry by its point group, which defines its symmetries. The orbitals are split into subsets corresponding to the irreducible representations or *irreps* of that point group. In Schoenflies notation, the point groups for octahedral and tetrahedral coordination are O_h and T_d respectively. The irreps for O_h, in Mulliken notation, are e_g ($|x^2 - y^2\rangle$ and $|z^2\rangle$) and t_{2g} ($|xy\rangle$, $|xz\rangle$, and $|yz\rangle$). For the T_d, the irreps are e and t_2, which contain the same orbitals, but without the g subscript indicating the lack of inversion symmetry for a tetrahedron.

In the presence of the crystal field, the orbital occupation depends on the relative magnitude of the Hund's coupling, crystal field splitting, and SOC. In $3d$ ions, $\lambda \ll 10Dq \sim J_H$, so we can typically consider the effects of SOC as a perturbation to the ground state determined by $10Dq$ and J_H. For $10Dq \ll J_H$, the maximum spin is still favored and the electrons will occupy the orbitals according to the first Hund's rule, forming a *high-spin state*. However, when $\Delta_{\mathrm{CF}} \sim J_H$, it may be favorable to fully occupy the lower energy orbitals first, forming a *low-spin state*.

In a state with partially occupied e_g levels, the orbital angular momentum will be zero for any linear combination of the two e_g orbitals. This is known as *orbital quenching*. When the orbital angular momentum is quenched, the spin-orbit coupling vanishes to first order and can usually be ignored when considering the local electronic ground state (although the second order contrbutions are important for other effects, discussed in section 1.1.3).

In a state with partially occupied t_{2g} orbitals, the orbital angular momentum will not in

general be quenched. We can take linear combintations of the t_{2g} orbitals to form a basis with effective orbital angular momentum $\tilde{l} = 1$. In this case, the SOC acts to first order but the sign is flipped ($\tilde{\lambda} \approx -\lambda$) and the order of the total angular momentum multiplets is reversed from that given by Hund's third rule: maximize (minimize) J for less (more) than half filled.

If the symmetry is lower than cubic, the orbitals are further split. If an octahedron or tetrahedron is elongated or compressed along a (100) axis, leaving the other two related axes equivalant, the symmetry is *tetragonal*, with point groups reduced to D_{4h} and D_{2d} respectively, as shown in Fig. 1.3. In this symmetry, the t_{2g} levels are split into b_{2g} and e_g, and the e_g levels are split into b_{1g} and a_{1g}.

According to the point charge model, the sign of the splittings shown Fig. 1.3 correspond to a tetragonal elongation. However, the sign of the splitting may not always correspond to that expected from the point charge model due to effects discussed below.

An other common symmetry is *trigonal*, which corresponds to a distortion along a (111) axis, reducing O_h to D_{3d}. This preserves the degeneracy of the e_g levels, but splits the t_{2g} levels into a_{1g} and e'_g, where the $'$ symbol distinguishes those levels from the undisturbed e_g levels from the parent symmetry. These deviations from cubic symmetry may be intrinsic to the crystal structure or may arise from a structural distortion.

Although the cubic crystal field breaks the fivefold degeneracy of the d orbitals, there is often some remaining degeneracy of the single-electron states. For certain fillings, this results in an overall degeneracy of orbital occupations. For example, there is a degeneracy of the e_g states for Cu^{2+} (d^9) or Mn^{3+} (d^4) in an octahedral crystal field or a degeneracy of the t_2 states for Ni^{2+} (d^8) in a tetrahedral crystal field.

This degeneracy is unstable and the system may undergo a spontaneous distortion, allowing for a lower energy orbital occupation. Although this distortion reduces the energy of the orbital occupation, it also induces a strain with a corresponding elastic energy cost. In the simplest model for singly or triply occupied e_g states with a twofold degeneracy, we consider

small distortions u of an octahedron, where the ligands along the z axis are displaced by $\pm u$ and the ligands along the x and y axes are displaced by $\pm\frac{1}{2}u$. The orbital splitting is linear in u and the elastic energy is quadratic, giving an energy $E = \pm gu + \frac{1}{2}Bu^2$, where g is the electron-phonon coupling and B is the bulk modulus. The minimum energy occurs at $u_0 = \pm\frac{g}{B}$ with $E_0 = -\frac{g^2}{2B}$. This spontaneous distortion to lower the orbital energy is known as the *Jahn-Teller effect*.

In a state with partially occupied t_{2g} orbitals, the situation in more complicated. First, a tetragonal or trigonal distortion splits the threefold degeneracy into a nondegenerate and a doubly degenerate state. Thus, the potential energy is asymmetric with respect to u. In addition, SOC is active to first order, and may induce a splitting comparable to the distortion-induced splitting. The resulting spin-orbital-lattice entangled states will depend on the precise energy scales of the interactions and may exhibit behavior that cannot be predicted by simple qualitative considerations.

Above we considered the crystal field splitting due to electrostatic repulsion between the d electrons and ligand ions. This provides a simple qualitative picture and captures the proper symmetry of the splitting. However, a significant and often dominant contribution to the crystal field splitting is due to the hybridization with the ligands. That is, the d orbitals are mixed with the ligand orbitals. In this picture, the d orbitals are more properly described as hybridized d-p molecular orbitals, where each d orbital hybridizes with a linear combination of p_x, p_y, p_z orbitals each of the surrounding ligands that shares the symmetry of the corresponding d orbital.

The d orbitals with lobes pointing toward the ligand sites form σ bonds involving the p orbitals parallel to the metal-ligand bond. The d orbitals with lobes pointing in between the ligand sites form π bonds involving the p orbitals perpendicular to metal-ligand bond. For example, in octahedral coordination, $|x^2 - y^2\rangle$ hybridizes with the p_x or p_y orbitals of the ligands within the xy plane, $|z^2\rangle$ hybridizes with the p_z orbitals of the ligands along the z axis. The resulting molecular orbitals retain the same symmetry of the d orbitals split by the

Coulomb repulsion in the point charge model, however the sign and magnitude of the splitting may differ.

A quantitative description of metal-ligand hybridization requires two parameters: the metal-ligand hopping t_{pd}, which may depend on the particular d and p orbitals involved in the hopping (i.e. $t_{pd\sigma}$ or $t_{pd\pi}$), and the charge transfer energy Δ, which is the energy cost to move an electron from the full ligand p shell to the partially occupied metal d shell. The charge transfer energy includes not only the energy offset of the d and p levels, but also the Coulomb energy cost of adding an additional electron to the metal site.

In section 1.1.1, we considered a system with direct hopping between the metal sites with hopping parameter t and energy cost U. In most correlated materials, the metal sites are separated by ligands, and the metal-metal hopping occurs as a second order process via the intermediate ligands, with the effective hopping parameter $t_{dd} = t_{pd}^2/\Delta$.

This leads to the distinction between two different types of correlated insulators. When the lowest energy charge excitation corresponds to metal-metal hopping, $d^n d^n \rightarrow d^{n+1} d^{n-1}$, with energy $E = U$, the system is called a Mott insulator (or Mott-Hubbard insulator) as described in section 1.1.1. When the lowest energy charge excitation corresponds to ligand-metal hopping, $d^n p^6 \rightarrow d^{n+1} p^5$, with energy $E = \Delta$, the system is called a *charge-transfer insulator*. We often refer to both types collectively as Mott insulators or more generally as correlated insulators, only distinguishing between the two different types when necessary.

1.1.3 Interactions

Starting from the 1D Hubbard model (eq. 1.1) at half filling in the limit of $U/t \gg 1$, we can show how interactions occur between neighboring sites. In the undoped case, there is one unpaired electron per site ($n = 1$) and the Hubbard model is said to be at *half-filling*. In the limit of strong repulsion $t/U \ll 1$, we expect electrons to be highly localized. We can thus carry out a perturbation calculation to obtain an effective spin-only Hamiltonian, starting with the repulsive term and perturbing with the hopping to second order. This calculation is

shown in A.1. The result is known as the *Heisenberg model*

$$\mathcal{H}_{\text{Heis}} = J \sum_{\langle ij \rangle} \boldsymbol{S}_i \cdot \boldsymbol{S}_j. \tag{1.5}$$

where $J = 4t^2/U$. Since $J > 0$, this interaction favors antiparallel alignment between nearest neighbor spins (compare to the Hund's interaction, eq. 1.3, which favors parallel spins on a given site). We can picture the second order perturbation as a virtual hopping to a neighboring site and back, which decreases the energy by $-2t^2/U$. However, this hopping is only allowed when the spins on each site are antiparallel, from the Pauli exclusion principle. This interaction is called *kinetic exchange* or sometimes Heisenberg exchange, illustrated in figure 1.4. The constant J is called the *exchange coupling* or exchange constant. In the limit of strong repulsion at half-filling, the spin degrees of freedom of the Hubbard model can be described by this effective Hamiltonian, which favors antiparallel alignment between neighboring spins because virtual hopping reduces kinetic energy.

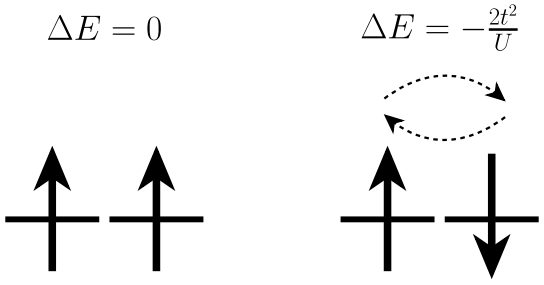

Figure 1.4: Kinetic exchange interaction arising from the virtual hopping processes in the Hubbard model.

Eq. 1.5 is the starting point for modeling magnetism in materials with localized spins. In real materials however, the magnetic interactions are far more complicated. Each site has a full set of orbitals and the hopping processes may involve the intermediate ligand orbitals. As a result, the strength and sign of the exchange interactions depend on the particular orbital occupation and the bonding geometry between neighboring sites, as described by the Goodenough-Kanamori-Anderson (GKA) rules [5].

There may also be exchange beyond nearest neighbor sites arising from higher order

hopping processes. The next-nearest neighbor exchange is denoted by J', with the sum over next-nearest neighbors indicated by $\langle\langle ij\rangle\rangle$. The next-next-nearest neighbor (or third neighbor) exchange is denoted by J'', with the sum over third nearest neighbors indicated by $\langle\langle\langle ij\rangle\rangle\rangle$. These farther neighbor interactions are often negligible compared to the nearest neighbor interactions. However, on particular lattices or for particular bonding geometries, farther neighbor exchange may be quite strong or even dominant.

The inter-site Heisenberg exchange is isotropic in spin space and is independent of the relative orientation of the spins to the crystal lattice. That is, the spins prefer to align with each other along some direction (either parallel or antiparallel depending on the sign of J), but that direction is degenerate over the surface of the unit sphere.

This degeneracy may be broken by an on-site anisotropy. In the presence of spin-orbit coupling, the orbital anisotropy induced by the crystal field will carry over to the spin. Even when the orbital moment is quenched, the second order contribution of spin-orbit coupling may be sufficient to break the degeneracy. This effect causes the spin on each site to prefer or avoid alignment with particular crystal axes and is highly dependent on orbital occupation and lattice symmetry. For example, a uniaxial anisotropy has the form $\mathcal{H}_{\text{uni}} = -KS_z^2$. When $K > 0$, the spins prefer to stay along the z axis and when $K < 0$, the spins prefer to stay within the xy plane. These two cases are known as *easy-axis* and *easy-plane* anisotropy, respectively. For strong enough easy-axis anisotropy, the Heisenberg model reduces to the *Ising model*. For strong enough easy-plane anisotropy, the Heisenberg model reduces to the *XY model*.

In addition to on-site anisotropies that act on each individual spin, there may also be anisotropic exchange interactions between sites. These can be described by the general bilinear exchange tensor $\hat{J}$ (for nearest neighbors) with $\mathcal{H}_{ij} = \boldsymbol{S}_i \cdot \hat{J} \cdot \boldsymbol{S}_j$. The diagonal components correspond to the Heisenberg exchange. The off-diagonal components can be considered separately as the symmetric and antisymmetric off-diagonal exchange. The antisymmetric

part can be written as

$$\mathcal{H}_{\mathrm{DM}} = \boldsymbol{D}_{ij} \cdot (\boldsymbol{S}_i \times \boldsymbol{S}_j) \tag{1.6}$$

where the direction of the vector $\boldsymbol{D}_{ij}$ depends on the symmetries between sites i and j, and the magnitude depends on the relative strength of spin-orbit coupling and crystal field splitting. This is called the *Dzyaloshinskii-Moriya interaction* (DMI), which can only be finite when there is no inversion center between sites i and j.

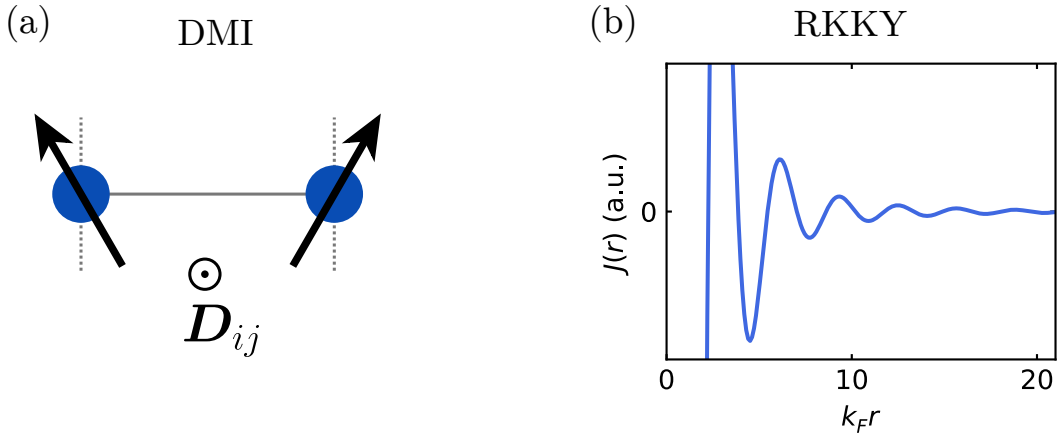

Figure 1.5: (a) Dzyaloshinskii-Moriya interaction (DMI), with DMI vector $\boldsymbol{D}_{ij}$ pointing out of the page. (b) RKKY interaction $J(r)$ between sites i and j separated by distance r. (c)

In certain systems with highly anisotropic spin-orbital moments, which are discussed in section 1.2.3, there may be a bond-dependent Ising interactions, where the spin component involved in the interaction depends on the direction of the bond. This is called a *Kitaev interaction*, with the form

$$\mathcal{H}_{ij}^{\gamma} = -K S_i^{\gamma} S_j^{\gamma} \tag{1.7}$$

for sites i and j connected by a bond associated with the spin component γ.

Another possible interaction is *biquadratic exchange* $\mathcal{H}_{\mathrm{biq}} = B(\boldsymbol{S}_i \cdot \boldsymbol{S}_j)^2$, which may arise due to magnetoelastic coupling [8–10] or higher order exchange processes for particular orbital occupations [11]. This interaction favors parallel or antiparallel spins for $B < 0$ and perpendicular spins for $B > 0$ [12–15].

All of the above interactions involve exchange processes between localized electrons on

nearby sites in insulating materials. Some materials have coexisting itinerant and localized unpaired and electrons. In this case, the itinerant electrons can mediate exchange interactions between localized electrons. This is known as the *Ruderman-Kittel-Kasuya-Yosida* (RKKY) interaction, with the form

$$J(r_{ij}) \propto \frac{\cos(2k_F r_{ij})}{r_{ij}^3} \tag{1.8}$$

between sites i and j separated by distance r_{ij}, where $\hbar k_F$ is the Fermi momentum [16]. As shown in Fig. 1.5, the RKKY interaction extends over long distances and oscillates in sign, leading to many interesting effects as we will see in chapter 4 and 5.

1.2 Ordering phenomena

Just as the atoms and molecules in ordinary matter undergo phase transitions from a disordered gas, to a short-range-correlated liquid, to a long-range-correlated solid, interacting electrons will undergo phase transitions to ordered states as temperature decreases. These transitions include magnetic order, charge order, orbital order, lattice distortions, superconductivity, metal-insulator transitions, and a wide range of other phenomena [4, 5].

1.2.1 Magnetism

Before discussing magnetic ordering, we briefly cover some basic concepts relevant to magnetism in solids. The *magnetization* $\boldsymbol{M}$ of a material, which is the magnetic moment per unit volume, responds to an applied magnetic field $\boldsymbol{H}$ according to the magnetic susceptibility tensor

$$\chi^{\alpha\beta} = \frac{\partial M^\alpha}{\partial H^\beta}. \tag{1.9}$$

For an isotropic material in the linear response regime, this simplifies to $\boldsymbol{M} = \chi \boldsymbol{H}$, where $\chi = \chi^{\alpha\beta}\delta_{\alpha\beta}$. For the layered materials in this thesis (section 1.4), we consider the in-plane and out-of-plane susceptibilities $\chi_\perp$ and $\chi_\parallel$. A response with $\chi > 0$ is known as *paramagnetism* and a response with $\chi < 0$ is known as *diamagnetism*. The diamagnetic response of electrons

in completely filled inner shells (which is the majority of the electrons in the material) is known as *Larmor diamagnetism*, caused by the field-induced orbital angular momentum. The diamagnetic response due to the orbital motion of conduction electrons is known as *Landau diamagnetism*. The paramagnetic response of localized spins in an insulator is known as *Curie paramagnetism*. The paramagnetic response of a metal due to spin splitting of the conduction band is known as *Pauli paramagnetism*.

A system of local spins on a lattice subject to the interactions described in the previous section may undergo a phase transition at some critical temperature from a disordered paramagnetic phase to a magnetically ordered phase. The specific type of magnetic ordering depends on the details of the local degree of freedom (spin/orbital moment, anisotropy), the lattice type, and the type and strength of inter-site interactions.

Ferromagnetic order is a state with all spins aligned in parallel, producing a net magnetization. *Antiferromagnetic* order is a state with spins pointing antiparallel to their neighbors, (or otherwise aligned with no net magnetization). Another similar possibility is *ferrimagnetic* order, in which spins of different sizes are oppositely aligned, producing a net magnetization.

For typical ferro- or ferrimagnetic order, the spin do not break the translational symmetry of the lattice. That is, the unit cell of the magnetic structure is identical to the unit cell of the crystal structure. For antiferromagnetic order however, the translational symmetry is often broken. That is, the spins in neighboring unit cells are oriented along opposite directions. The spins can also form modulated structures with periodicity much longer than the lattice, where adjacent spins rotate by a small angle within some plane. The spins may rotate within the plane perpendicular to the propagation direction, forming a helical structure known as *helimagnetic* order. They may also rotate within the same plane as the propagation direction, known as *cycloidal* order. A variety of other modulated magnetic structures exist [16–18].

We can describe magnetic ordering more generally in reciprocal space using a *magnetic propagation vector* or magnetic wavevector. For a lattice with multiple magnetic sites per unit

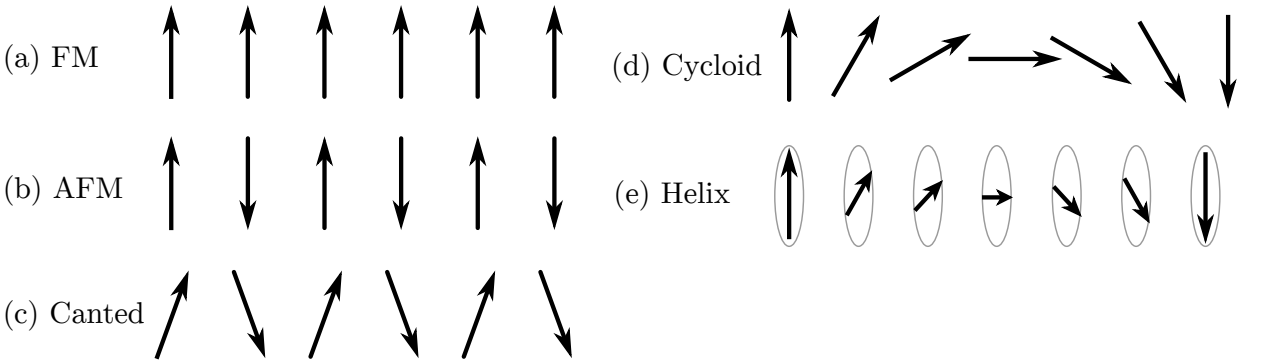

Figure 1.6: (a) Ferromagnetic order (b) Antiferromagnetic order (Néel state) (c) Canted antiferromagnetic order (d) Cycloidal order (e) Helimagnetic order

cell, the moment on site j of unit cell n at position $\boldsymbol{r}_n$ can be expressed as

$$\boldsymbol{m}_{n,j} = \sum_{\boldsymbol{k}} \boldsymbol{m}_{\boldsymbol{k},j} e^{i\boldsymbol{k}\cdot\boldsymbol{r}_n} \tag{1.10}$$

where $\boldsymbol{m}_{\boldsymbol{k},j}$ is the Fourier component for site j with wavevector $\boldsymbol{k}$, given by

$$\boldsymbol{m}_{\boldsymbol{k},j} = \sum_{n} \boldsymbol{m}_{n,j} e^{-i\boldsymbol{k}\cdot\boldsymbol{r}_n}. \tag{1.11}$$

We can also define the Fourier components using the absolute positions of each site, $\boldsymbol{r}_{n,j} = \boldsymbol{r}_n + \boldsymbol{u}_j$, where $\boldsymbol{u}_j$ is the position of site j within the unit cell. This convention simply changes the relative phase factor of the Fourier components for the sites in the unit cell. Because magnetic moments must be real quantities, the Fourier components must satisfy $\boldsymbol{m}_{\boldsymbol{k},j} = \boldsymbol{m}^*_{-\boldsymbol{k},j}$ [16, 19]. In anticipation of the next chapter, we can also define the magnetic structure factor,

$$\boldsymbol{M}(\boldsymbol{k}) = \sum_{j} \boldsymbol{m}_{\boldsymbol{k},j} e^{i\boldsymbol{k}\boldsymbol{r}_j}, \tag{1.12}$$

which is simply the sum of Fourier components for the sites in the unit cell with relative phase factors.

We can classify a magnetic structure as *commensurate* or *incommensurate*. A commensurate structure has a propagation vector that is a rational multiple of a reciprocal lattice vector, i.e.

$k = \frac{n}{m}\boldsymbol{G}$ for integers m. An incommensurate structure has a propagation vector that is an irrational multiple of a reciprocal lattice vector. A commensurate structure can be described in terms of a *magnetic unit cell*, defining the primitive unit of translational symmetry in the magnetically ordered phase. An incommensurate structure cannot be described in such a way.

If $\boldsymbol{k} = (0, 0, 0)$, the magnetic order does not lower the translational symmetry of the lattice and the magnetic unit cell is identical to the structural unit cell. This is always the case for ferro- and ferrimagnetic order. However, it may also correspond to antiferromagnetic order when there are multiple spins per unit cell. Here, the Fourier components are simply the moments within the unit cell, i.e. $\boldsymbol{m}_{n,j} = \boldsymbol{m}_{0,j}$ for all n. If $\boldsymbol{k} = \frac{1}{2}\boldsymbol{G}$ for some reciprocal lattice vector $\boldsymbol{G}$, the moments are given by $\boldsymbol{m}_{n,j} = \boldsymbol{m}_{\boldsymbol{k},j}(-1)^n$. This is a simple antiferromagnet, where the magnetic order is invariant under the operation of translation by one unit cell along $\boldsymbol{k}$ followed by time-reversal. For any commensurate or incommensurate structures with arbitrary $\boldsymbol{k}$, with real space moments are given by

$$\boldsymbol{m}_{n,j} = m_{1,j}\cos(\boldsymbol{k}\cdot\boldsymbol{r}_{n,j} + \phi_j)\hat{\boldsymbol{u}}_j + m_{2,j}\sin(\boldsymbol{k}\cdot\boldsymbol{r}_{n,j} + \phi_j)\hat{\boldsymbol{v}}_j, \tag{1.13}$$

where $\hat{\boldsymbol{u}}_j$, $\hat{\boldsymbol{v}}_j$ and $\hat{\boldsymbol{w}} = \hat{\boldsymbol{u}} \times \hat{\boldsymbol{v}}$ are unit vectors defining an orthonormal frame. Here the particular type of structure depends on the orientation of $\hat{\boldsymbol{u}}_j$ and $\hat{\boldsymbol{v}}_j$ relative to $\boldsymbol{k}$ and the relative magnitude of $m_{1,j}$ and $m_{2,j}$ [16].

Magnetic ordering lowers the symmetry of the paramagnetic phase. However, there may be a degeneracy of symmetry-broken states. Thus, the system may order into different states in distinct regions called *domains*. In a ferromagnet, different domains correspond to different moment directions. The number of such domains depends on the type of anisotropy in the system, which determines the number of degenerate orientations.

In an antiferromagnet or other complex modulated structures, there are many other types of domains [20]. *Configuration domains* (also called k-domains or Q-domains) correspond to different magnetic propagation vectors, which will typically be symmetry-related wavevectors

for the given crystal structure. We can define the *star* of a magnetic propagation vector $\boldsymbol{k}$ as the set of wavectors $\boldsymbol{k}_\alpha$ generated from $\boldsymbol{k}$ by the symmetry operations of the space group. For a magnetic structure with propagation vector $\boldsymbol{k}$, domains may form with any wavevector belonging to the star of $\boldsymbol{k}$. For example, $(\frac{1}{2}00)$, $(0\frac{1}{2}0)$, and $(00\frac{1}{2})$ domains in a cubic crystal, or $(\frac{1}{2}00)$, $(0\frac{1}{2}0)$, and $(\frac{1}{2}\frac{\bar{1}}{2}0)$ domains in a hexagonal crystal. For a given configuration domain, there may be multiple possible spin orientations. This includes different Néel vector directions for a commensurate antiferromagnet. It also includes distinct rotational senses for helical or cycloidal structures. For helical or other chiral structures, these are often called *chiral domains*. There may also be domains with the same type of ordering, but with a phase shift. In an antiferromagnet, this would occur as a 180°phase shift giving parallel neighboring spins. In a incommensurate structure, this could be an arbitrary phase shift, causing a discontinuity in the modulated structure.

A magnetic phase transition can be identified experimentally by an anomaly in the temperature dependence of a bulk material property, such as magnetic susceptibility, heat capacity, or electrical resistivity (although this anomaly may arise from other types of phase transitions). *Curie-Weiss law* for paramagnetic response of local moments

$$\chi = \frac{C}{T - \Theta_{\mathrm{CW}}} \tag{1.14}$$

where C is the Curie constant and Θ_{CW} is the Curie-Weiss temperature. [21]

Bulk measurements can provide basic information such as the transition temperature, local moment size, and anisotropy. However, the precise details of the magnetic order, including the propagation vector(s) and moment orientations can only be determined by neutron diffraction or resonant elastic x-ray scattering (REXS), as we will discuss in the next chapter.

We can model magnetic phase transitions as well as the properties of the paramagnetic and ordered phases using a spin Hamiltonian such as the Heisenberg, XY, or Ising model on a given lattice with the relevant set of interactions. However, the particular type of interactions

and the corresponding interaction strengths must be determined. Even when the precise parameters for a given model are known, exact solutions exist only in the simplest cases, even in the classical limit. Thus, a variety of analytical and numerical approximation methods must be used [3, 4, 6, 8, 13, 14, 22–32].

1.2.2 Frustrated magnetism

Although interactions generally favor long range order, it is possible for ordering to be suppressed by interactions that cannot be simultaneously satisfied. This effect is called *frustration* and can be illustrated by the two simple cases in Fig. 1.7. First consider Ising spins on the vertices of a triangle as shown in Fig. 1.7(a), where each spin i can have the state $S_{z,i} = \pm S$ with $\mathcal{H} = J(S_{z,1}S_{z,2} + S_{z,2}S_{z,3} + S_{z,3}S_{z,1})$. For ferromagnetic exchange ($J < 0$), the spins will align with either $S_{z,i} = \pm S$ for all i, with a ground state energy $3JS^2$ and a twofold Kramers degeneracy. For antiferromagnetic exchange ($J > 0$), the situation is less clear. There is no unique way for all spins to satisfy the antiferromagnetic exchange interaction, as each spin cannot be antiparallel to both of its neighbors. The ground state energy is thus $-JS^2$, as there will always be one pair of parallel spins. There is now a sixfold ground state degeneracy (three Kramers pairs). In contrast to the ferromagnetic case, each of these ground states can be connected by a spin flip with no energy cost. Thus, the system can fluctuate over a set of ground states. This inability to satisfy all interactions due to geometric constraints is known as *geometric frustration*.

Another possibility is conflicting nearest and farther neighbor interactions, as shown in Fig. 1.7(b). For Ising spins on the vertices of a square, nearest-neighbor antiferromagnetic exchange $J > 0$ is not frustrated. However, next-nearest-neighbor antiferromagnetic exchange ($J' > 0$), which acts along the diagonals, cannot be simultaneously satisfied. For large enough J', the simple Néel state is destabilized. This form of frustration due to competing between multiple interactions is known as *exchange frustration*.

These toy examples demonstrate the main concept of frustrated magnetism: conflicting

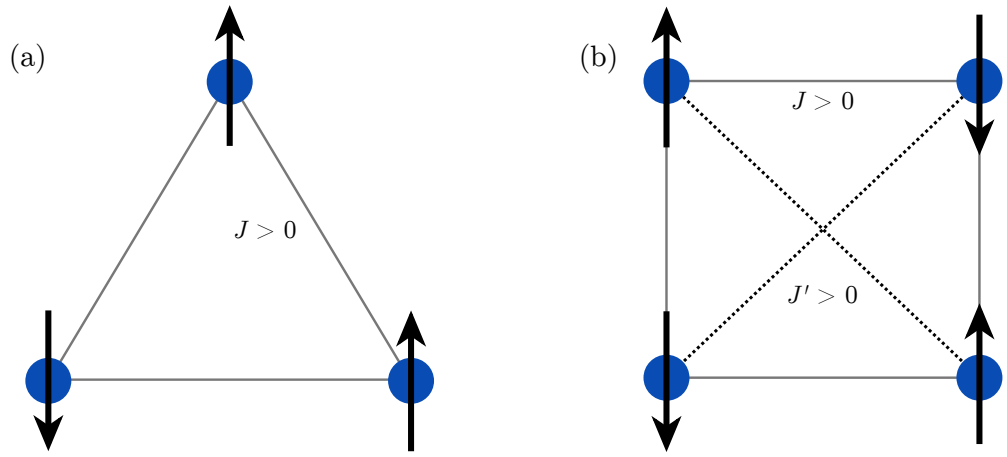

Figure 1.7: (a) Geometric frustration in an Ising model on a triangle with nearest-neighbor antiferromagnetic exchange. (b) Exchange frustration in an Ising model on a square with antiferromagnetic nearest- and next-nearest-neighbor exchange.

interactions produce a ground state degeneracy which enhances fluctuations and suppresses conventional magnetic order. However, the third law of thermodynamics requires that the system must release its residual entropy as $T \to 0$. This results in exotic magnetic phases that may occur at temperatures far below the energy scale of the exchange interactions. The degree of frustration can be quantified by the *frustration parameter* $f = |\Theta_{\mathrm{CW}}|/T_c$, where the Curie-Weiss temperature Θ_{CW} corresponds to the energy scale of the exchange interactions.

In real materials, the spins occupy sites on a periodic lattice and may possess a continuous rotational degree of freedom. On a *bipartite* lattice, the sites can be divided into two sublattices such that all nearest neighbors of a site on a given sublattice belong to the other sublattice. Examples include a 1D chain, square, simple cubic, honeycomb, or diamond lattice. These lattices support a simple Néel state for dominant nearest neighbor AFM exchange. However, a sufficiently strong next nearest neighbor AFM exchange induces exchange frustration and destabilizes the Néel state. On a diamond lattice, which is the topic of chapter 3, a next nearest neighbor exchange of $J' > \frac{1}{8}J$ will destabilize the Néel state. The theory of diamond lattice magnets is discussed in [30, 33–39].

On a lattice with triangular motifs, such as a triangular, kagome, or pyrochlore lattice, simple antiferromagnet order may be suppressed by geometric frustration, although exchange

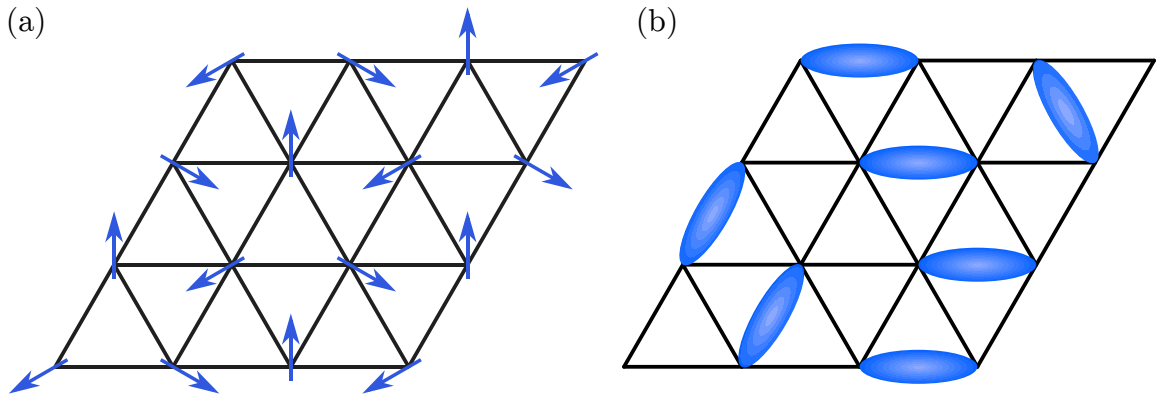

Figure 1.8: (a) 120° order on a triangular lattice Heisenberg AFM (b) Valence bond solid on a triangular lattice Heisenberg AFM

frustration may also be involved. The triangular lattice antiferromagnet, which is the topic of chapter 6, is the canonical example of a geometrically frustrated magnet [4, 5, 39–43]. For a Heisenberg model on a triangular lattice with antiferromagnetic nearest neighbor exchange, the classical ground state is a three-sublattice Néel-like state with spins on each sublattice oriented 120° relative to each other, as shown in Fig. 1.8(a).

For quantum spins, the exact ground state of the triangular lattice Heisenberg AFM has not been definitively proven. There are many alternatives to the classical ground state involving the formation of singlet states $|\psi\rangle = \frac{1}{\sqrt{2}}(|\uparrow\downarrow\rangle - |\downarrow\uparrow\rangle)$ or *valence bonds* between pairs of spins. A state with valence bonds between nearest neighbor pairs is known as a *valence bond solid* (VBS), shown in Fig. 1.8(b). The system may lower its energy further by forming a superposition of many VBS configurations, even including valence bonds between further neighbor spins. This is known as a *resonating valence bond* (RVB) state. The RVB state is particularly notable because it is a type of *quantum spin liquid* (QSL), an unconventional magnetic state that does not break any symmetries, contains highly entangled spins that may be widely separated, and exhibits excitations with fractional quantum numbers, among other exotic properties. The understanding and definitive realization of a QSL state is a major goal in the field of frustrated magnetism and condensed matter physics in general [8, 39, 44–49].

Finally, we mention a different type of frustrated magnetic state that may arise in systems with quenched disorder, known as a *spin glass*. This disorder may involve the spatial distribution

of spins, such as vacancies or nonmagnetic substitutions in a magnetic material or magnetic dopants in a nonmagnetic material. The disorder may alternatively involve randomness in the exchange interactions, perhaps due to disorder among the nonmagnetic ions mediating the exchange interactions, such as an oxygen or sulfur deficiency. Below the spin freezing temperature T_f, the spins become frozen into a randomly oriented or short-range correlated configuration characterized by slow relaxation between metastable states. Spin glasses are of particular interest because of their unique form of symmetry-breaking and non-ergodic behavior [50, 51].

1.2.3 Composite degrees of freedom

Spin-orbital moments

A growing paradigm in quantum materials and correlated electron physics is the study of novel phenomena stabilized by spin-orbit coupling (SOC), including topological insulators/semimetals, spin-orbit assisted Mott insulators, and spin-orbit entangled magnets. In f-electron systems, the local ground state is dominated by SOC. However, these systems are typically deep within the Mott insulator state with weak exchange interactions due to the highly localized nature of the f orbitals. There is thus a large separation of energy scales, with SOC much weaker than the Coulomb interaction and much stronger than the crystal field and hopping energies.

In $4d$ and $5d$ transition metal compounds, the picture is quite different. These systems have SOC comparable to the f-electron systems, but with much more spatially extended orbitals, giving weaker Coulomb repulsion and stronger crystal field splitting and intersite hopping. Thus the energy scales of the different local degrees of freedom coincide and the exchange interaction strength is large, giving rise to a rich variety of spin-orbit entangled phases [52–55]. Although the study of spin-orbital physics has mostly focused on $4d/5d$ compounds, $3d$ compounds have recently begun to attract more attention [56–62].

The two primary cases of interest for spin-orbit entangled moments with effective total

angular momentum J are $J = \frac{1}{2}$ and $J = 0$ [1]. $J = \frac{1}{2}$ moments can be realized in d^5 ions (Ir^{4+}, Ru^{3+}) in octahedral crystal fields, d^9 ions (Cu^{2+}) in tetrahedral crystal fields, or d^7 ions (Co^{2+}) in octahedral crystal fields. The most notable case is $J = \frac{1}{2}$ moments on a honeycomb lattice, which interact via the Kitaev interaction (eq. 1.7) and are predicted to host a quantum spin liquid ground state [63–65]. $J = 0$ moments can be realized in d^4 ions (Ir^{5+}, Ru^{4+}, Re^{3+}, Os^{4+}) in octahedral crystal fields, d^8 ions (Ni^{2+}) in tetrahedral crystal fields, or d^6 ions (Fe^{2+}) in tetrahedral crystal fields. In these systems, the nonmagnetic spin-orbital singlet local ground state competes with intersite exchange between $J = 1$ excited states to form a magnetically ordered condensate analogous to a Bose-Einstate condensate. This is known as *excitonic magnetism* [66].

Spin chirality

We can also consider local degrees of freedom involving multiple spins. The *scalar spin chirality* is defined as the solid angle spanned by a set of three spins on a plaquette. For spins $\boldsymbol{S}_i$, $\boldsymbol{S}_j$, and $\boldsymbol{S}_k$ on the corners of a triangular plaquette, the scalar spin chirality is given by

$$\chi_s = \boldsymbol{S}_i \cdot (\boldsymbol{S}_j \times \boldsymbol{S}_k) \tag{1.15}$$

This can only be finite for noncoplanar spins. In the adiabatic limit, a scalar spin chirality induces an effective magnetic field on conduction electrons, $\boldsymbol{b} \propto t\chi_s \hat{\boldsymbol{n}}$, where $\hat{\boldsymbol{n}}$ is the plaquette normal vector and $t = t_{ij}t_{jk}t_{ki}$ is the hopping integral around the loop $i \to j \to k \to i$. This effect can produce an anomalous Hall effect (AHE) or other time-reversal symmetry breaking phenomena in antiferromagnetic materials with noncoplanar spin structures [67]. Another quantity is the *vector spin chirality*

$$\boldsymbol{\chi}_{\mathrm{v}} = \boldsymbol{S}_i \times \boldsymbol{S}_j + \boldsymbol{S}_j \times \boldsymbol{S}_k + \boldsymbol{S}_k \times \boldsymbol{S}_i. \tag{1.16}$$

[1] Sometimes called J_{eff} to emphasize that these are not pure J states due to possible deviations from LS coupling and partial mixing by the crystal field.

This requires that the three spins be mutually noncollinear, but may be coplanar [42].

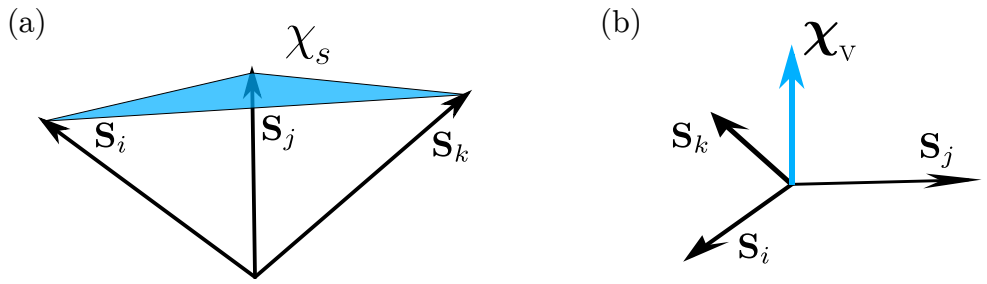

Figure 1.9: (a) Scalar spin chirality χ_s, representing the solid angle spanned by three spins on a triangular plaquette. (b) Vector spin chirality $\boldsymbol{\chi}_v$

1.3 Transition metal oxides

The largest class of strongly correlated materials is the transition metal oxides, particularly those with $3d$ transition metal ions. This includes the high temperature superconducting cuprates [68], the collosal magnetoresistance manganites [69], and many other materials exhibiting a wide range of behaviors including as metal-insulator transitions [70], and charge, spin, and orbital ordering phenomena [5].

1.3.1 Spinel structure

The spinel structure, which belongs to the cubic space group $Fd\bar{3}m$ (227), has the form AB_2X_4 where A^{2+} and B^{3+} are metal ions and X^{2-} is typically oxygen, sulfur or selenium, with eight formula units per unit cell. In this structure, the A ions form a diamond lattice of tetrahedrally coordinated sites and the B form a pyrochlore lattice of octahedrally coordinated sites, as shown in Fig. 1.10. In addition to the normal spinel structure, there is also the inverse spinel structure $B^{3+}(A^{2+}B^{3+})_2X_4$, where the half of the B^{3+} ions occupy tetrahedral sites and the A^{2+} and other half of the B^{3+} ions are distributed on octahedral sites. In addition to their diverse range of electronic and magnetic properties, spinels are especially interesting because they host both a diamond and pyrochlore lattice, canonical examples of exchange and geometric frustration respectively. There may be local spins on the A sites, the B sites,

or even both. There have thus been many complex magnetic phases identified in spinels and they remain promising for future work [71].

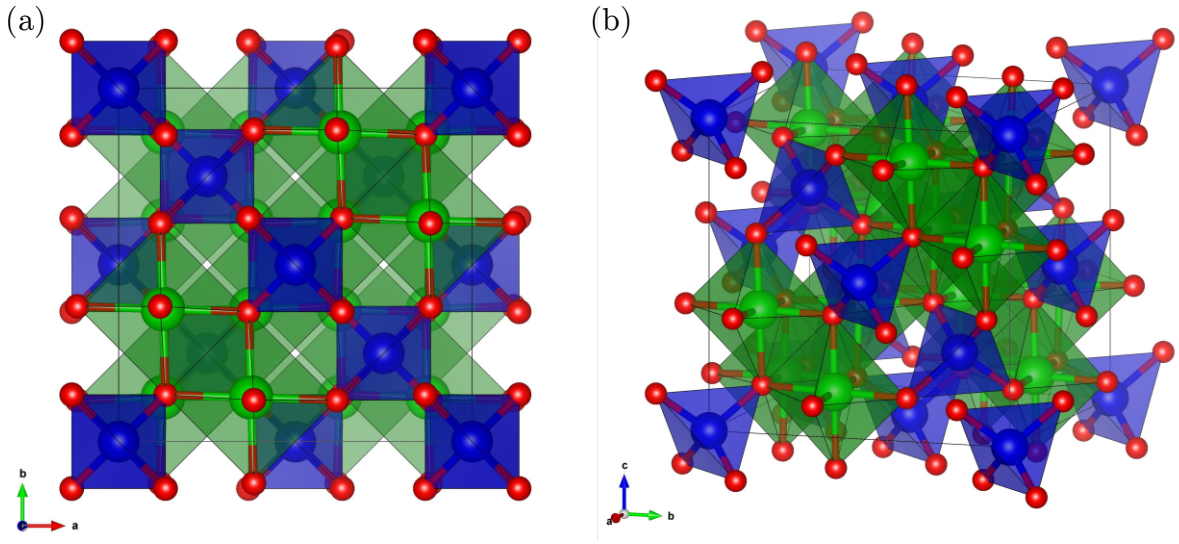

Figure 1.10: Spinel structure, with tetrahedral A sites shown in blue and octahedral B sites shown in green. (Created using VESTA [72])

1.4 van der Waals materials

van der Waals (vdW) materials consist of layers that are a single atom or unit cell thick, with the layers bonded together only by van der Waals interactions. These materials are mainly studied because they can be exfoliated to a few or even a single layer and used for devices and heterostructures. In addition, the weak interlayer coupling allows for highly two-dimensional (2D) magnetic behavior, where fluctuations are enhanced. The effect of interlayer coupling can also be tuned by varying the number of layers near the monolayer limit. vdW materials thus offer a unique platform for realizing ideal models of magnetism, with the possibility for tuning the role of fluctuations [73–76].

1.4.1 Intercalated transition metal dichalcogenides

Transition metal dichalcogenides (TMDs) MX_2, (M = transition metal ion, mainly V, Mo, Nb, Ta, and W, and X = S, Se, Te), are a class of vdW materials that are widely studied for

their nontrivial semiconducting and metallic properties, particularly in the use of devices and heterostructures. These materials exhibit weakly correlated Fermi liquid-like behavior and may exhibit phases such as superconductivity or charge density waves [77–79].

The $2H$ polytope of the transition metal dichalcognides (TMDs) can be *intercalated* with $3d$ transition metals, which occupy interstitial sites in the van der Waals gap. These intercalated transition metal dichalcogenides (iTMDs)M_xTX_2, with $M = 3d$ transition metal, $T =$ Nb, Ta, and $X =$ S, Se form a broad class of materials exhibiting a diverse range of electronic and magnetic phenomena that are both fundamentally rich and promising for device applications. These materials are highly tunable by varying the metal or chalcogen in the parent compound $2H - TX_2$, as well as the type and quantity of intercalated $3d$ ions. The $3d$ ions form a superlattice of local magnetic moments between the conducting layers of the parent compound. The parent compound is the $2H$ polytope, consisting of 2 layers per unit cell.

For $x = \frac{1}{4}$ (MT_4X_8), the $3d$ ions form a 2×2 superlattice, preserving the $P6_3/mmc$ (194) space group of the parent compound. This results in a bilayer triangular lattice of spins, with the two spins per unit cell offset purely along the c axis. For $x = \frac{1}{3}$ (MT_3X_6), the $3d$ ions form a $\sqrt{3} \times \sqrt{3}$ superlattice, with the lattice vectors rotated by 30° relative to the parent lattice (denoted by $\sqrt{3} \times \sqrt{3}R30°$), with noncentrosymmetric space group $P6_322$ (182). This results in a bilayer triangular lattice with the two spins per unit cell offset along both the c axis and within the plane [80–87]. Some iTMDs of recent interest are $CoNb_3S_6$ [88–95] (see chapters 4 and 5), $NiNb_3S_6$ [96, 97] (see chapter 5), $CrNb_3S_6$ [85, 98], $FeNb_3S_6$ [84, 99–103], $MnNb_3S_6$ [104–107], VNb_3S_6 [108–111], and $CoTa_3S_6$ [112, 113].

CHAPTER 2

Experimental Techniques

This chapter introduces the main experimental techniques used in this thesis, mostly resonant x-ray scattering. The first section covers basic x-ray diffraction from a crystal lattice. The next section introduces the theory of the electron-photon interaction for electrons in bound atomic states to derive the cross sections for x-ray absorption and resonant x-ray scattering. The remaining sections cover the specific details of x-ray absorption spectroscopy (XAS), resonant elastic x-ray scattering (REXS), and resonant inelastic x-ray scattering (RIXS). Further details on these topics can be found in [114–120].

2.1 X-ray diffraction

In a scattering experiment, a photon beam of momentum $\hbar\boldsymbol{k}$, energy $\hbar\omega$, polarization polarization $\boldsymbol{\epsilon}$, and intensity I_0 (photons per unit time) is incident upon a sample. We measure the intensity I of the scattered beam with some momentum $\hbar\boldsymbol{k}'$, energy $\hbar\omega'$, and polarization $\boldsymbol{\epsilon}'$. We define the energy transfer $\Delta E = \hbar\omega' - \hbar\omega$ and momentum transfer $\hbar\boldsymbol{Q} = \hbar\boldsymbol{k}' - \hbar\boldsymbol{k}$, where $\boldsymbol{Q}$ is known as the *scattering vector*. The angle betweem the incident and scattered wavevectors is the *scattering angle* 2θ, which can be related to the magnitude of the scattering vector by

$$Q = \frac{4\pi}{\lambda}\sin\theta \tag{2.1}$$

where $\theta = 2\theta/2$. In this section we consider x-ray diffraction, which is an elastic scattering process, so we restrict $\Delta E = 0$ and thus $|\boldsymbol{k}| = |\boldsymbol{k}'|$. We also use the *kinematic approximation*, in which we neglect multiple scattering, i.e. assume each photon is scattered no more than once.

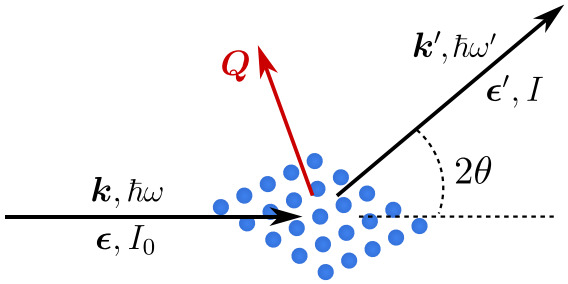

Figure 2.1: Geometry of a scattering experiment. An x-ray beam of intensity I_0 with containing photons of energy $\hbar\omega$, momentum $\hbar\boldsymbol{k}$, and polarization $\boldsymbol{\epsilon}$ scatters from a sample. The beam is scattered with some intensity I, energy $\hbar\omega'$, momentum $\hbar\boldsymbol{k}'$, and polarization $\boldsymbol{\epsilon}'$. $\boldsymbol{Q} = \boldsymbol{k}' - \boldsymbol{k}$ is the scattering vector, related to the scattering angle 2θ by $Q = \frac{4\pi}{\lambda}\sin\theta$.

The intensity I measured by a detector covering solid angle $\Delta\Omega$ is related to the *differential cross section*

$$\frac{d\sigma}{d\Omega} = \frac{I}{I_0 \Delta\Omega}. \tag{2.2}$$

Integrating this over the unit sphere gives the *total cross section*

$$\sigma = \int \frac{d\sigma}{d\Omega} d\Omega. \tag{2.3}$$

We also define the scattering amplitude M_{if}, which is the ratio of the scattered to incident electric field strength, or alternatively, the probability amplitude for a scattered photon with initial state i and final state f, related to the differential cross section by

$$\left(\frac{d\sigma}{d\Omega}\right) = |M_{if}|^2 \tag{2.4}$$

In a classical description, the electric field of an x-ray beam will oscillate an electron, causing it to radiate a spherical wave. This is known as *Thomson scattering*, which will be

described more thoroughly in the next section. Here we will just state the key results. For a single electron, the Thomson scattering amplitude is

$$M = -r_0|\boldsymbol{\epsilon}'^{*}\cdot\boldsymbol{\epsilon}| \tag{2.5}$$

where $r_0 = e^2/(4\pi\epsilon_0 mc^2)$ is the electron scattering length or the classical electron radius.

The Thomson scattering amplitude for an arbitrary charge density is given by

$$M(\boldsymbol{Q}) = -r_0|\boldsymbol{\epsilon}'^{*}\cdot\boldsymbol{\epsilon}|\int \rho(\boldsymbol{r})e^{i\boldsymbol{Q}\boldsymbol{r}}d\boldsymbol{r}. = -r_0|\boldsymbol{\epsilon}'^{*}\cdot\boldsymbol{\epsilon}|f_0(\boldsymbol{Q}) \equiv f^T(\boldsymbol{Q}). \tag{2.6}$$

where $f_0(\boldsymbol{Q})$ is the Fourier transform of the charge density. For an atom, f_0 is called *atomic form factor* (considering only the Thomson scattering contributions for now). For simplicity. we will include the scattering length and polarization factor and refer to the scattering amplitude f^T as the atomic form factor.

For an arbitrary collection of scatterers at positions $\boldsymbol{r}_m$ with form factors f_m, the total scattering amplitude is the sum over the individual scattering amplitudes with relative phase factors

$$F(\boldsymbol{Q}) = \sum_m f_m(\boldsymbol{Q})e^{i\boldsymbol{Q}\boldsymbol{r}_m}.z \tag{2.7}$$

A crystal lattice is composed of lattice sites $\boldsymbol{R}_n = n_1\boldsymbol{a}_1 + n_2\boldsymbol{a}_2 + n_3\boldsymbol{a}_3$, where the $\boldsymbol{a}_i$ are the lattice vectors and the n_i are integers. At each lattice site n there is a unit cell containing atoms j at positions $\boldsymbol{R}_n + \boldsymbol{r}_j$ with form factors $f_j(\boldsymbol{Q})$. The scattering amplitude for the crystal can thus be factored into separate sums over the unit cell and the lattice sites:

$$F(\boldsymbol{Q}) = \sum_{n,j} f_j(\boldsymbol{Q})e^{i\boldsymbol{Q}(\boldsymbol{R}_n+\boldsymbol{r}_j)} = \overbrace{\sum_j f_j(\boldsymbol{Q})e^{i\boldsymbol{Q}\boldsymbol{r}_j}}^{\text{unit cell structure factor}} \overbrace{\sum_n e^{i\boldsymbol{Q}\boldsymbol{R}_n}}^{\text{lattice sum}} = S(\boldsymbol{Q})L(\boldsymbol{Q}). \tag{2.8}$$

The lattice sum $L(\boldsymbol{Q})$ evaluates to zero unless $\boldsymbol{Q}\cdot\boldsymbol{R}_n = 2\pi m$ for some integer m. We define

the *reciprocal lattice* as the points

$$\boldsymbol{G} = h\boldsymbol{b}_1 + k\boldsymbol{b}_2 + l\boldsymbol{b}_3 \tag{2.9}$$

for integers h, k, l, called *Miller indices*, and reciprocal lattice vectors

$$\boldsymbol{b}_1 = \tfrac{2\pi}{V}\boldsymbol{a}_2 \times \boldsymbol{a}_3, \quad \boldsymbol{b}_2 = \tfrac{2\pi}{V}\boldsymbol{a}_3 \times \boldsymbol{a}_1, \quad \boldsymbol{b}_3 = \tfrac{2\pi}{V}\boldsymbol{a}_1 \times \boldsymbol{a}_2, \tag{2.10}$$

where $V = \boldsymbol{a}_1 \cdot (\boldsymbol{a}_2 \times \boldsymbol{a}_3)$ is the unit cell volume. These satisfy $\boldsymbol{a}_i \cdot \boldsymbol{b}_j = 2\pi\delta_{ij}$, where δ_{ij} is the Kronecker δ. The lattice sum will this vanish unless $\boldsymbol{Q}$ is a reciprocal lattice point. This is known as the *Laue condition*, $\boldsymbol{Q} = \boldsymbol{G}$. The intensity of x-ray diffraction from a crystal lattice can thus be described as $I(\boldsymbol{Q}) \propto |S(\boldsymbol{Q})|^2 \delta(\boldsymbol{Q} - \boldsymbol{G})$. There is only nonvanishing intensity at scattering vectors corresponding to reciprocal lattice points, with the intensity determined by the unit cell structure factor, which is the sum over the form factors with relative phase factors of the atoms in the unit cell. Using eq. 2.1 and the Laue condition, we can derive the famous *Bragg's law* (see section 5.1.5 of [114])

$$n\lambda = 2d \sin\theta, \tag{2.11}$$

for any integer n, which relates the wavelength λ and the scattering angle to the spacing d of a set of lattice planes corresponding to any reciprocal lattice point $\boldsymbol{G}$.

2.2 Theory of the electron-photon interaction

A plane wave in the quantized electromagnetic field has a vector potential

$$\boldsymbol{A}(\boldsymbol{r}, t) = \sqrt{\frac{2\pi\hbar c}{V}} \sum_{j,k} \frac{1}{\sqrt{k}} \boldsymbol{\epsilon}_j \left[\hat{a}_{k,j} e^{i(\boldsymbol{k}\cdot\boldsymbol{r} - \omega t)} + \hat{a}^\dagger_{k,j} e^{-i(\boldsymbol{k}\cdot\boldsymbol{r} - \omega t)} \right] \tag{2.12}$$

where $\hat{a}^{\dagger}_{k,j}$ and $\hat{a}_{k,j}$ are photon creation and annihilation operators for a photon with momentum $\hbar\boldsymbol{k}$ and polarization $\boldsymbol{\epsilon}_j$. The Hamiltonian for the electron-photon interaction contains four terms

$$\begin{aligned}
\mathcal{H}' &= \mathcal{H}_1 + \mathcal{H}_2 + \mathcal{H}_3 + \mathcal{H}_4 \\
\mathcal{H}_1 &= \frac{e^2}{2m}|\boldsymbol{A}|^2 \\
\mathcal{H}_2 &= -\frac{e^2}{2m^2c^2}\boldsymbol{s}\cdot\Big[\partial_t\boldsymbol{A}\times\boldsymbol{A}\Big] \\
\mathcal{H}_3 &= -\frac{e}{m}\boldsymbol{p}\cdot\boldsymbol{A} \\
\mathcal{H}_4 &= -\frac{e}{m}\boldsymbol{s}\cdot\nabla\times\boldsymbol{A},
\end{aligned} \tag{2.13}$$

where $\boldsymbol{p}$ is the electron momentum operator and $\boldsymbol{s}$ is the electron spin operator. This is derived from the low-energy limit of the Dirac equation, using the Foldy-Wouthuysen (FW) transformation, which is valid because the relevant energy scales are far below the electron rest energy (511 keV) [121]. The interaction is sufficiently weak that it can be treated as a perturbation.

$\mathcal{H}_1$ and $\mathcal{H}_2$ are both quadratic in $\boldsymbol{A}$ and thus change the photon number by 0 or ±2. $\mathcal{H}_3$ and $\mathcal{H}_4$ are linear in $\boldsymbol{A}$, and can only change the photon number by ±1. In the scattering processes that we are considering, the photon number is conserved, while in an absorption (emission) process, the photon number decreases (increases). $\mathcal{H}_1$ describes Thomson scattering, $\mathcal{H}_2$ describes nonresonant magnetic scattering, and $\mathcal{H}_3$ and $\mathcal{H}_4$ describe absorption and resonant scattering. It can be shown that in most cases $\mathcal{H}_2$ and $\mathcal{H}_4$ are much smaller than $\mathcal{H}_1$ and $\mathcal{H}_3$, so we will neglect them here [116].

Consider a x-ray photon with momentum $\hbar\boldsymbol{k}$, energy $\hbar\omega$ and polarization $\boldsymbol{\epsilon}$ scattering from a single electron in a bound state $|\alpha\rangle$, with the initial product state $|i\rangle = |\alpha\rangle|\boldsymbol{k},\boldsymbol{\epsilon}\rangle$ with energy $E_i = E_\alpha + \hbar\omega$. The final state[1] is $|f\rangle = |\beta\rangle|\boldsymbol{k}',\boldsymbol{\epsilon}'\rangle$ with energy $E_f = E_\beta + \hbar\omega'$.

Considering only elastic scattering[2], $\hbar\omega' = \hbar\omega$, $E_\beta = E_\alpha$, $|\beta\rangle = |\alpha\rangle$. To first order, the

[1]To distinguish the f labeling the final state from the form factor, it will only appear within a bra/ket or as a subscript.

[2]Although the photon transfers momentum $\hbar\boldsymbol{Q}$ to the electron, we assume that this momentum is immediately transferred to the electron's surroundings.

scattering amplitude is

$$M_{if} = \langle f|\mathcal{H}_1|i\rangle = \frac{e^2}{2m}\langle f||\boldsymbol{A}|^2|i\rangle = -r_0|\boldsymbol{\epsilon}'^{*}\cdot\boldsymbol{\epsilon}|\langle\alpha|e^{i\boldsymbol{Q}\cdot\boldsymbol{r}}|\alpha\rangle \tag{2.14}$$

where $\langle\alpha|e^{i\boldsymbol{Q}\cdot\boldsymbol{r}}|\alpha\rangle$ is the Fourier transform of the electron charge density. Summing over all electrons in an atom

$$M_{if} = -r_0|\boldsymbol{\epsilon}'^{*}\cdot\boldsymbol{\epsilon}|\sum_j \langle\alpha_j|e^{i\boldsymbol{Q}\cdot\boldsymbol{r}_j}|\alpha_j\rangle = -r_0|\boldsymbol{\epsilon}'^{*}\cdot\boldsymbol{\epsilon}|f_0(\boldsymbol{Q}) \equiv f^T(\boldsymbol{Q}), \tag{2.15}$$

where $f_0(\boldsymbol{Q})$ is the atomic form factor for Thomson scattering, as given in 2.1.

In an absorption process, the initial state is $|i\rangle = |\alpha\rangle|\boldsymbol{k},\boldsymbol{\epsilon}\rangle$ with energy $E_i = E_\alpha + \hbar\omega$ and the final state is $|f\rangle = |\beta\rangle|0\rangle$ with energy $E_f = E_\beta = E_\alpha + \hbar\omega$

$$M_{if} = -\frac{e}{m}\langle f|\boldsymbol{p}\cdot\boldsymbol{A}|i\rangle \propto \langle\beta|\boldsymbol{\epsilon}\cdot\boldsymbol{p}e^{i\boldsymbol{k}\cdot\boldsymbol{r}}|\alpha\rangle \tag{2.16}$$

Using the commutation relation for the unperturbed electron Hamiltontian $\boldsymbol{p} = \frac{im}{\hbar}[\mathcal{H}_0,\boldsymbol{r}]$,

$$M_{if} \propto \langle\beta|\boldsymbol{\epsilon}\cdot\boldsymbol{r}e^{i\boldsymbol{k}\cdot\boldsymbol{r}}|\alpha\rangle \tag{2.17}$$

Since $|\boldsymbol{k}\cdot\boldsymbol{r}|$ will be small at the relevant photon energies, we use the *dipole approximation*, $e^{i\boldsymbol{k}\cdot\boldsymbol{r}} \approx 1$ (See [121] for the treatment of higher order multipole components.). We also replace $\boldsymbol{r}$ with $\boldsymbol{R} = \sum_j \boldsymbol{r}_j$, the sum over the position operators of all electrons and generalize the states $|\alpha\rangle$ and $|\beta\rangle$ to many body states. We thus have the transition matrix element for x-ray absorption

$$M_{if} \propto \langle\beta|\boldsymbol{\epsilon}\cdot\boldsymbol{R}|\alpha\rangle. \tag{2.18}$$

Now considering a perturbation by $\mathcal{H}_3$ to second order, with initial state $|i\rangle = |\alpha\rangle|\boldsymbol{k},\boldsymbol{\epsilon}\rangle$ with

energy $E_i = E_\alpha + \hbar\omega$ and final state $|f\rangle = |\beta\rangle|\boldsymbol{k}'\boldsymbol{\epsilon}'\rangle$ with energy $E_f = E_\beta + \hbar\omega'$

$$M_{if} \propto \sum_n \frac{\langle\beta|\boldsymbol{\epsilon}'^* \cdot \boldsymbol{R}|n\rangle\langle n|\boldsymbol{\epsilon}\cdot\boldsymbol{R}|\alpha\rangle}{\hbar\omega + E_\alpha - E_n + \frac{i}{2}\Gamma} \tag{2.19}$$

where $|n\rangle$ are intermediate states of energy E_n involving an absorbed photon and Γ_n is the intermediate state lifetime. Equations 2.18 and 2.19 are the starting points for computing XAS and RXS cross sections respectively. To explicitly calculate these matrix elements, we require the wavefunctions for the initial, intermediate, and final states. These calculations will be discussed in section 2.6.

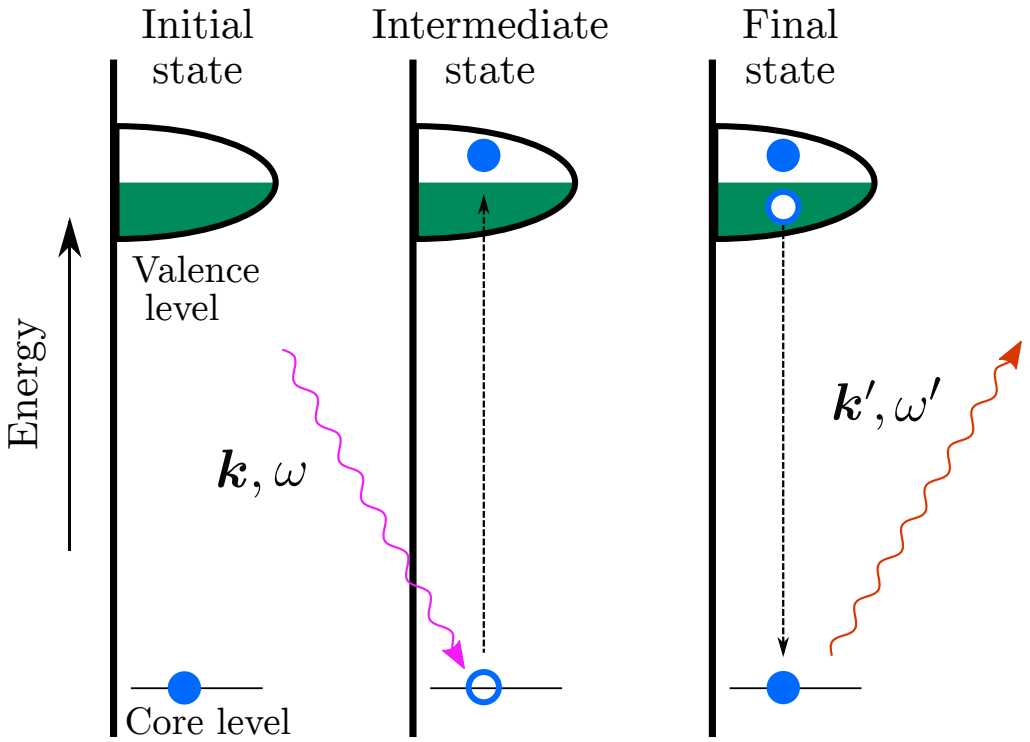

Figure 2.2: Schematic description of resonant scattering process. The initial state involes the electron system in its ground state and a photon of energy $\hbar\omega$ and momentum $\hbar\boldsymbol{k}$. In the intermediate state, the photon is absorbed to create a core hole and add an electron to an empty valence level. In the final state, the core hole is annihilated to emit a photon of energy $\hbar\omega'$ and momentum $\hbar\boldsymbol{k}'$, leaving the valence level in some state, which may be the ground state or an excited state.

2.3 X-ray absorption spectroscopy (XAS)

When an atom in a material absorbs an x-ray photon, an electron in the atom is generally excited into a continuum state (photoemission). This nonresonant absorption cross section smoothly decreases with increasing energy. If the photon energy corresponds to an energy difference between a core level electron and an empty valence level, the core electron is excited into that empty state. This is called resonant absorption and gives rise to *absorption edges* or sharp upward steps in the absorption cross section. An x-ray absorption spectroscopy (XAS) experiment measures the x-ray absorption as a function of energy across one of these edges. The absorption edges most relevant for x-ray absorption and resonant x-ray scattering on strongly correlated materials [see Fig. 2.3(b)] are as follows:

- $3d$ transition metal L-edges: 0.5-1 keV (soft x-rays)
- $3d$ transition metal K-edges: 5-9 keV (hard x-rays)
- $4d$ transition metal L-edges: tender x-ray regime: 2-4 keV (tender x-rays)
- $5d$ transition metal L-edges: hard x-ray regime: 9-12 keV (hard x-rays)
- Oxygen K-edge: 530 eV

In many cases, the x-ray absorption spectrum can be thought of as the density of empty states projected on the absorbing site, weighted by the dipole matrix elements. The presence of the core hole may also be treated as a perturbation. When the core hole wavefunction overlaps strongly with the valence states, the XAS may consist of highly mixed multiplets that do not necessarily correspond directly to the empty valence states. This is the case at the $3d$ transition metal L edges, where the $2p$ core hole has strong overlap with the $3d$ orbitals. Although this effect significantly complicates the interpretation of the spectra, it can provide a great deal of information about the valence electronic states (see section 2.6).

The transmitted intensity I of an x-ray beam with incident intensity I_0 on a sample with thickness t is

$$I(E) = I_0(E)e^{-\mu(E)t}, \tag{2.20}$$

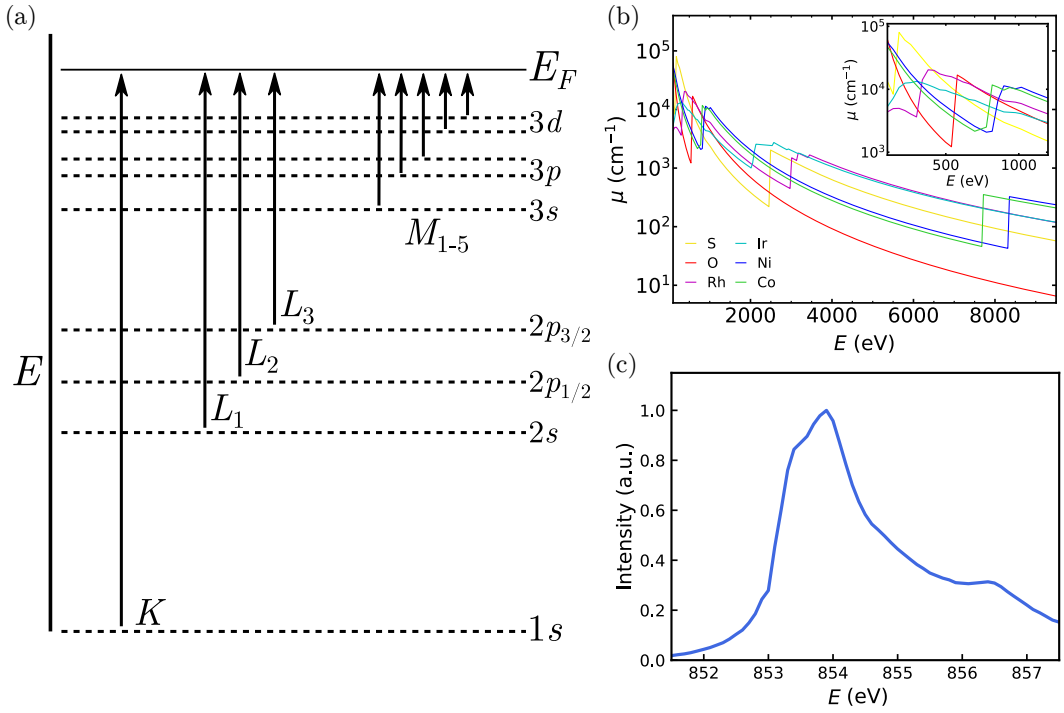

Figure 2.3: (a) Schematic of atomic absorption edges, corresponding to the binding energy of core level electrons in a given atom (b) Absorption coefficients of select elements as a function of energy. (c) X-ray absorption spectrum of $NiRh_2O_4$ at the Ni L_3 edge measured in total fluorescence yield.

where $\mu(E)$ is the energy-dependent absorption coefficient or absorption length, where we neglect other processes such as scattering, which are often much weaker than absorption. The absorption coefficient is related to the absorption cross section of an atom by $\mu = \rho\sigma_{\text{abs}}$, where ρ is the atomic number density. For a material with multiple types of atoms, this becomes $\mu = \sum_j \rho_j \sigma_{\text{abs},j}$. The XAS can be directly measured by measuring the transition as a function of energy,

$$\mu(E) = -\frac{1}{t} \log \frac{I(E)}{I_0}. \tag{2.21}$$

However, it is often not possible to directly measure XAS in transmission. For instance, soft x-rays have an attenuation length on the order of 100 nm in solids. In an XAS experiment, we are typically not concerned with the absolute absorption, but rather the spectral shape of the absorption across the edge. We can instead measure the x-rays or electrons emitted by the various core-hole decay processes as a proxy of the true x-ray absorption cross section.

The measurement of the total x-ray emission from core-hole decay processes is called *total fluorescence yield* (TFY). It is sometimes useful to measure a select energy range of emitted x-rays, known as *partial fluorescence yield* (PFY). Another method is to measure the emitted electrons, either as photoelectrons or as a drain current, known as *total electron yield* (TEY). In fluorescence yield, the spectral shape is distorted due to saturation and self-absorption effects. Electron yield does not suffer from these effects, but is more surface sensitive.

There are many different types of XAS experiments, depending on the particular absorbing element, edge, energy range around a given edge, and x-ray polarizations. *X-ray absorption near-edge structure* (XANES) measures the absorption at energies close to the edge, which correspond to transitions to empty bound states in the valence level. The XANES provides information about the local electronic structure at the absorping site, such as oxidation state and spin-orbit coupling. *Extended x-ray absorption fine structure* (EXAFS) considers the oscillations in the absorption far above the edge. These oscillations are due to backscattered photoelectrons causing energy-dependent constructive or desctructive interference at the absorbing site. This interference pattern can be Fourier transformed to obtain a real space description of the local atomic structure, with sensitivity to details that may be missed by x-ray or neutron diffraction measurements [114]. *X-ray magnetic circular dichroism* (XMCD) is the difference in absorption, or dichroism, between opposite circularly polarized x-rays, typically with a magnetic field along the direction of the beam to polarize the spins. XMCD provides information about broken time reversal symmetry states such as ferromagnetic order. It is especially useful for determining the separate spin and orbital contributions to the magnetic moment, as well as any anisotropy in the spin density. *X-ray linear dichroism* (XLD) or x-ray natural linear dichroism (XNLD) is the dichroism between x-rays with orthogonal linear polarization. This provides information about the charge anisotropy, such as the orbital occupation. *X-ray magnetic linear dichroism* (XMLD) is the XLD with the polarizations set parallel and perpendicular to the spin alignment axis, which can be set by a magnetic field. This provides information about the charge anisotropy induced by the spin alignment through

spin orbit coupling. XMLD is useful for studing antiferromagnets, which do not exhibit an XMCD signal.

2.4 Resonant elastic x-ray scattering (REXS)

In this section we consider elastic scattering with x-ray energy near an atomic absorption edge, known as resonant elastic x-ray scattering (REXS) or resonant x-ray diffraction (RXD) [119, 121–125]. The atomic form factor described above has the more general form

$$f = f^T + f^M + f' + if'' \tag{2.22}$$

where f^T corresponds to Thomson scattering, f^M corresponds to nonresonant magnetic scattering, which is usually very weak, and $f^R = f' + if''$ is the resonant form factor, also known as the dispersion correction, which only becomes relevant at particular photon energies and is the topic of this section. The resonant form factor is given by eq. 2.19 restricted to elastic scattering, i.e. the final state equals the initial state,

$$f^R \propto \sum_n \frac{\langle\alpha|\boldsymbol{\epsilon}'^*\cdot\boldsymbol{R}|n\rangle\langle n|\boldsymbol{\epsilon}\cdot\boldsymbol{R}|\alpha\rangle}{\hbar\omega - E_n + E_\alpha + \frac{i}{2}\Gamma} \tag{2.23}$$

However, it is rarely necessary to carry out quantitative calculations of the resonant scattering amplitude for REXS. By expressing $\boldsymbol{R}$ in terms of vector spherical harmonics, we can write f^R in terms of the polarization vectors and the rank-2 resonant scattering tensor [122, 123]

$$f^R \propto \boldsymbol{\epsilon}'^*\cdot\hat{f}\cdot\boldsymbol{\epsilon}. \tag{2.24}$$

The symmetry of this tensor depends on the point group at the scattering site. For studying magnetism, it is often sufficient to assume a spherically symmetric atom, reduced to cylindical symmetry by a moment of orientation $\boldsymbol{m}$, which gives

$$f^R = F^{(0)}\boldsymbol{\epsilon}'^*\cdot\boldsymbol{\epsilon} + F^{(1)}(\boldsymbol{\epsilon}'^*\times\boldsymbol{\epsilon})\cdot\boldsymbol{m} + F^{(2)}(\boldsymbol{\epsilon}'^*\cdot\boldsymbol{m})(\boldsymbol{\epsilon}\cdot\boldsymbol{m}). \tag{2.25}$$

The first term in eq. 2.25 is only sensitive to charge scattering and will give rise to structural Bragg peaks. It will also produce peaks from charge ordering or charge density waves, with much higher sensitivity than non-resonant Thomson scattering.

The second and third term in eq. 2.25 are sensitive to magnetism. Considering only the second term and using eq. 2.8, we find that a magnetic structure with propagation vector $\boldsymbol{q}$ will give rise to magnetic scattering at $\boldsymbol{Q} = \boldsymbol{G} \pm \boldsymbol{q}$, where $\boldsymbol{G}$ is a reciprocal lattice vector. The third term is quadratic in $\boldsymbol{m}$ and can produce magnetic scattering at $\boldsymbol{Q} = \boldsymbol{G}$ and $\boldsymbol{Q} = \boldsymbol{Q} \pm 2\boldsymbol{q}$, i.e. zeroth and second order satellites. This contribution is often negligible and we ignore it here. The structure factor for resonant magnetic scattering can now be calculated as

$$F(\boldsymbol{Q}) \propto (\boldsymbol{\epsilon}'^{*} \times \boldsymbol{\epsilon}) \cdot \sum_{j} \boldsymbol{m}_{\boldsymbol{q},j} e^{i\boldsymbol{Q}\boldsymbol{r}_j}, \tag{2.26}$$

with corresponding intensity $I = |F(\boldsymbol{Q})|^2$, where $\boldsymbol{m}_{\boldsymbol{q},j}$ is the Fourier component for magnetic propagation vector $\boldsymbol{q}$ of site j in the unit cell.

To utilize the REXS for determining the precise structure of ordered spins and orbitals, as well as for disentangling charge, spin, and orbital degrees of freedom, we must vary the polarizations $\boldsymbol{\epsilon}$ and $\boldsymbol{\epsilon}'$ with respect to the sample frame. This can be accomplished by two methods: (1) directly varying the polarization of the incident and/or scattered beam and (2) rotating the sample about the azimuthal angle to change the reference frame of the scattering tensor $\hat{f}$ while maintaining the same scattering condition.

We describe the x-ray polarization relative to the scattering plane. σ polarization corresponds to polarization perpendicular to the scattering plane. π polarization corresponds to polarization within the scattering plane, perpendicular to the x-ray wavevector. The polarization dependent scattering intensity $I_{\boldsymbol{\epsilon}'\boldsymbol{\epsilon}}$ can thus be considered in four distinct channels for the two incident and two outgoing polarizations: $I_{\sigma'\sigma}$, $I_{\pi'\sigma}$, $I_{\sigma'\pi}$, and $I_{\pi'\pi}$, which we denote by ϵ-ϵ' (i.e. the σ-π' channel refers to the intensity $I_{\pi'\sigma}$). In most cases, the scattered polarization is not resolved, so the measured intensity is a sum of two polarization channels corresponding

to a given incident polarization: $I_\sigma = I_{\sigma'\sigma} + I_{\pi'\sigma}$ and $I_\pi = I_{\sigma'\pi} + I_{\pi'\pi}$. For each of these four channels, we can relate the $\boldsymbol{\epsilon}'^* \times \boldsymbol{\epsilon}$ factor to the scattering geometry:

$$\begin{aligned} \boldsymbol{\sigma}' \times \boldsymbol{\sigma} &= 0 \\ \boldsymbol{\pi}' \times \boldsymbol{\sigma} &= -\hat{\boldsymbol{k}}' \\ \boldsymbol{\sigma}' \times \boldsymbol{\pi} &= \hat{\boldsymbol{k}} \\ \boldsymbol{\pi}' \times \boldsymbol{\pi} &= \hat{\boldsymbol{k}}' \times \hat{\boldsymbol{k}}, \end{aligned} \tag{2.27}$$

where $\hat{\boldsymbol{k}}$ and $\hat{\boldsymbol{k}}'$ are unit vectors parallel to the wavevectors of the incident and scattered beam. Thus, we see that the σ-σ' channel does not contribute to magnetic scattering in this approximation, as $\boldsymbol{\sigma} = \boldsymbol{\sigma}'$. The π-σ' and σ-π' channels (a.k.a. the cross-polarized channels) are sensitive to the projection of the moment along $-\boldsymbol{k}'$ and $\boldsymbol{k}$ respectively, i.e. *within* the scattering plane, while the π-π' channel is sensitive to the projection of the moment *perpendicular* to the scattering plane. In the following sections, we will cover the formalism for explicit calculations of the polarization dependent REXS intensity.

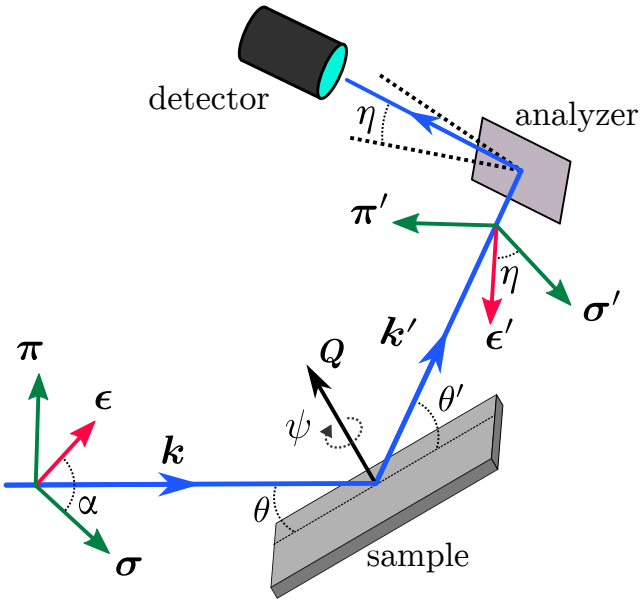

Figure 2.4: Geometry of a typical REXS experiment. scattering vector $\boldsymbol{Q}$, scattering angle $2\theta = \theta + \theta'$, incident linear polarization angle α, polarization analyzer angle η, azimuthal angle ψ,

2.4.1 Full linear polarization analysis (FLPA)

When the linear polarization of the incident beam can be varied continuously and the measured polarization of the scattered beam can be selected with a polarization analyzer, we can carry out *full linear polarization analysis* (FLPA) [126–133].

Let $\hat{\boldsymbol{Q}}$ be the unit vector along the direction of the scattering vector $\boldsymbol{Q}$ and let $\hat{\boldsymbol{Q}}_\perp$ be a direction perpendicular to $\hat{\boldsymbol{Q}}$ within the scattering plane. The directions of the incident and scattered beam are given by

$$\begin{aligned} \hat{\boldsymbol{k}} &= \hat{\boldsymbol{Q}}_\perp \cos\theta + \hat{\boldsymbol{Q}} \sin\theta \\ \hat{\boldsymbol{k}}' &= \hat{\boldsymbol{Q}}_\perp \cos\theta - \hat{\boldsymbol{Q}} \sin\theta. \end{aligned} \tag{2.28}$$

where θ is half of the Bragg angle. We can represent the polarization in the basis $\boldsymbol{\sigma}$ (perpendicular to the scattering plane) and $\boldsymbol{\pi}$ (parallel to the scattering plane), given by

$$\begin{aligned} \boldsymbol{\sigma} &= \boldsymbol{\sigma}' = (\hat{\boldsymbol{k}} \times \hat{\boldsymbol{k}}')/\sin(2\theta) \\ \boldsymbol{\pi} &= \hat{\boldsymbol{k}} \times \boldsymbol{\sigma} \\ \boldsymbol{\pi}' &= \hat{\boldsymbol{k}}' \times \boldsymbol{\sigma}. \end{aligned} \tag{2.29}$$

The arbitrary linear polarization vectors are then given by

$$\begin{aligned} \boldsymbol{\epsilon} &= \boldsymbol{\sigma} \cos\alpha + \boldsymbol{\pi} \sin\alpha \\ \boldsymbol{\epsilon}' &= \boldsymbol{\sigma}' \cos\eta + \boldsymbol{\pi}' \sin\eta. \end{aligned} \tag{2.30}$$

FLPA does not require any particular sample geometry and the sample angle and position remains stationary. The guarantees that the beam is hitting the same position on the sample with the same incident and outgoing angles, allowing for a direct comparison of intensities within a given FLPA scan. However, it requires both a continuously variable linear polarization angle and a polarization analyzer. The former is a common feature of soft x-ray beamlines, but is usually not available for hard x-ray beamlines.

2.4.2 Azimuthal rotation

Another way to vary the projection of the x-ray polarization onto the sample frame is to rotate the sample about the scattering vector $\boldsymbol{Q}$, known as *azimuthal rotation* [129, 134–138]. In the previous section, we fixed $\boldsymbol{Q}_\perp$ to be within scattering plane. Here we allow $\boldsymbol{Q}_\perp$ to rotate by an angle ψ within the plane perpendicular to $\boldsymbol{Q}$, where $\psi = 0°$ corresponds to within the scattering plane. The incident and outgoing wavevectors are

$$\begin{aligned} \hat{\boldsymbol{k}} &= [\hat{\boldsymbol{Q}}_\perp \cos\psi + (\hat{\boldsymbol{Q}}_\perp \times \hat{\boldsymbol{Q}}) \sin\psi] \cos\theta + \hat{\boldsymbol{Q}} \sin\theta \\ \hat{\boldsymbol{k}}' &= [\hat{\boldsymbol{Q}}_\perp \cos\psi + (\hat{\boldsymbol{Q}}_\perp \times \hat{\boldsymbol{Q}}) \sin\psi] \cos\theta - \hat{\boldsymbol{Q}} \sin\theta. \end{aligned} \tag{2.31}$$

The incident and scattered polarization vectors can then be calculated from eq. 2.29. Azimuthal rotation requires $\boldsymbol{Q}$ to be along a rotation axis of the instrument, and is thus limited to a single $\boldsymbol{Q}$ without remounting the sample. The beam is also not guaranteed to hit the same spot on the sample, so it is difficult to compare absolute intensity at different azimuthal angles. To avoid this issue, one can consider the azimuthal angle dependence of the intensity ratio for σ and π polarization.

2.4.3 Circular dichroism (CD)

The circular dichroism (CD) in the REXS intensity [129, 139–143] provides information about the symmetry of the underlying magnetic order. For circularly polarized x-rays $\boldsymbol{\epsilon}_\pm = \frac{1}{\sqrt{2}}(\boldsymbol{\sigma} \mp i\boldsymbol{\pi})$, the intensity $I_\pm = I_{\pm\pm} + I_{\mp\pm}$ is

$$I_\pm = \frac{1}{2}(|F_{\sigma'\sigma}|^2 + |F_{\sigma'\pi}|^2 + |F_{\pi'\sigma}|^2 + |F_{\pi'\pi}|^2) \pm \mathrm{Im}(F_{\sigma'\sigma}F^*_{\sigma'\pi} + F_{\pi'\sigma}F^*_{\pi'\pi}), \tag{2.32}$$

The circular dichroism is

$$I_+ - I_- = 2\,\mathrm{Im}(F_{\pi'\sigma}F^*_{\pi'\pi}), \tag{2.33}$$

where we let $F_{\sigma'\sigma} = 0$. Thus, a necessary, but insufficient condition for finite CD is a finite structure factor for both σ-π' and π-π'.

2.5 Resonant inelastic x-ray scattering (RIXS)

We now consider resonant inelastic x-ray scattering (RIXS) [116, 117, 120], where the final state of the resonant scattering process is no longer restricted to the ground state. RIXS is a momentum-resolved *photon-in photon-out* spectroscopy[3] that can probe a wide range of charge-neutral excitations. This includes intraatomic excitations within the multiplet determined by the crystal-field, spin-orbit coupling, and Hund's coupling, known as *dd* excitations. RIXS can also probe intersite charge excitations, such as a metal-metal Mott excitation ($d^n d^n \rightarrow d^{n-1} d^{n+1}$) or a ligand-metal charge-transfer excitation ($d^n \rightarrow d^{n-1}\underline{L}$). RIXS can also probe collective excitations such as phonons, magnons, or other more exotic excitations such as spinons or orbitons. In contrast to the local electronic excitations, these collective excitations may exhibit a dispersion, which can be measured by RIXS.

The schematic of the resonant scattering process in Fig. 2.2 describes the *direct* RIXS process, where the core to valence level transition is a dipole-allowed transition. This is the dominant mechanism for RIXS at transition metal L edges and K edges of p-shell elements. There is however an *indirect* RIXS process that occurs when the core-valence level transition is not dipole-allowed, such as transition metal K-edges. Here we only consider direct RIXS.

To understand the incident energy dependence of the RIXS spectrum, one typically measures a RIXS energy map, a series of energy-loss spectra at incident x-ray energies across the relevant absorption edge for a given momentum transfer and polarization [see Fig. 3.1(b) and Fig. 6.5(a)].

A RIXS energy map contains two general types of energy-loss features. *Raman*-like features exhibit a constant energy-loss with respect to incident energy, i.e. $\Delta E = E_{\text{in}} - E_{\text{out}}$ is constant. *Emission* (or fluorescence) features exhibit a constant final energy with respect to incident energy, i.e. $E_{\text{out}} = E_{\text{in}} - \Delta E$ is constant. In a plot of intensity with E_{in} on the x-axis and ΔE on the y-axis, Raman and emission features appear as horizontal and diagonal lines

[3] As opposed to a photon-in electron-out or electron-in photon out spectroscopy.

respectively.

Unlike REXS, which can modeled using geometric and symmetry considerations without considering the precise atomic states, RIXS often requires explicit calculation of the cross section to make sense of the data, which we discuss in the next section.

2.6 Multiplet calculations

To make sense of XAS and RIXS measurements, we can directly compute the spectrum by diagonalizing the Hamiltonian of a model system. Although it is possible to model collective excitations in RIXS [144], here we will only consider local excitations.

Starting from a set of single-electron basis states, as described in section 1.1.2, we can define a basis of many-body Fock states, where each basis state is a particular occupation of the single particle states. For p single particle states, each basis vector can be represented by $|n_1 n_2 \dots n_p\rangle$, where $n_i = 0$ or 1 is the occupation of state i. For a system with m single-electron states and n electrons, the size N of the basis is

$$N = \frac{m!}{n!(m-n)!}. \tag{2.34}$$

We separately consider the initial/final RIXS state (the initial XAS state) and the intermediate RIXS state (the final XAS state). The initial/final state corresponds to a d^n configuration with Hamiltonian $\mathcal{H}_i$. The intermediate state corresponds to a $2p^5 d^{n+1}$ configuration with Hamiltonian $\mathcal{H}_n$. After diagonalizing $\mathcal{H}_i$ and $\mathcal{H}_n$, we can compute the RIXS and XAS cross sections using the appropriate transition operators. The RIXS intensity is given by

$$I_{\text{RIXS}}(\omega, \omega', \boldsymbol{k}, \boldsymbol{k}', \boldsymbol{\epsilon}, \boldsymbol{\epsilon}') = \sum_i \frac{e^{-\frac{E_i}{k_B T}}}{Z} \sum_f \left| \sum_n \frac{\langle f|\mathcal{D}^\dagger|n\rangle\langle n|\mathcal{D}|i\rangle}{\hbar\omega - E_n + E_i + i\Gamma_n} \right|^2 \frac{\Gamma_f/\pi}{(\hbar\omega - E_f + E_i)^2 + \Gamma_f^2} \tag{2.35}$$

where $|i\rangle$ and $|f\rangle$ are eigenstates of $\mathcal{H}_i$, $|n\rangle$ are eigenstates of $\mathcal{H}_n$, $\mathcal{D}$ is a transition operator, Γ_f is the final state lifetime, Γ_n is the intermediate state lifetime. Here we only consider dipole

transitions, so $\mathcal{D}$ reduces to a dipole operator, defined in [120, 145]. We include a sum over thermally populated ground states weighted by a Boltzmann factor, with partition function Z. The XAS is given by

$$I_{\mathrm{XAS}}(\omega, \boldsymbol{\epsilon}) = \sum_i \frac{e^{-\frac{E_i}{k_B T}}}{Z} \sum_n \left| \langle n|\mathcal{D}|i\rangle \right|^2 \frac{\Gamma_n/\pi}{(\hbar\omega - E_n + E_i)^2 + \Gamma_n^2}. \tag{2.36}$$

2.6.1 Single-ion model

In the single-ion model, we consider a d^n ion with Coulomb interaction, spin-orbit coupling (SOC), and crystal field splitting,

$$\mathcal{H}_i = \mathcal{H}_U + \mathcal{H}_{\mathrm{CF}} + \mathcal{H}_{\mathrm{SOC}}, \tag{2.37}$$

where the Coulomb interaction is

$$\mathcal{H}_U = \sum_{\alpha\beta\gamma\delta\sigma\sigma'} U_{\alpha\sigma,\beta\sigma',\gamma\sigma',\delta\sigma} f^\dagger_{\alpha\sigma} f^\dagger_{\beta\sigma'} f_{\gamma\sigma'} f_{\delta\sigma}, \tag{2.38}$$

where $f^\dagger$ and f are fermion creation and annihilation operators and U is the rank-4 Coulomb tensor

$$\begin{aligned} &U^{i,j,t,u}_{m_{l_i} m_{s_i}, m_{l_j} m_{s_j}, m_{l_t} m_{s_t}, m_{l_u} m_{s_u}} \\ &= \frac{1}{2} \delta_{m_{s_i}, m_{s_t}} \delta_{m_{s_j}, m_{s_u}} \delta_{m_{l_i} + m_{l_j}, m_{l_t} + m_{l_u}} \sum_k C_{l_i, l_t}(k, m_{l_i}, m_{l_t}) C_{l_u, l_j}(k, m_{l_u}, m_{l_j}) F^k_{i,j,t,u}, \end{aligned} \tag{2.39}$$

where $C_{l_i,l_t}(k, m_{l_i}, m_{l_t})$ are the Gaunt coefficients and F^k_{ijtu} are the Slater integrals. This describes the Coulomb interaction between orbitals indexed by α, β, γ, and δ, and spin indexed by σ and σ'. Here the relevant parameters in $\mathcal{H}_U$ are the Slater integrals F^k and G^k, which are calculated from Cowan's code [146] using the Hartree-Fock method for free ions. For the Coulomb interaction between two d orbitals in the single-ion model, the only relevant

Slater integrals are F^2_{dd} and F^4_{dd}. The spin-orbit coupling is given by

$$\mathcal{H}_{\mathrm{SOC}} = \lambda \boldsymbol{L}\cdot\boldsymbol{S}, \tag{2.40}$$

where $\boldsymbol{L}$ and $\boldsymbol{S}$ are the orbital and spin angular momentum operators for the many-body state. The crystal field $\mathcal{H}_{\mathrm{CF}}$ is given by a 5×5 matrix that is diagonal in the $(d_{z^2}, d_{xz}, d_{yz}, d_{x^2-y^2}, d_{xy})$ basis. For an octahedral field with splitting $10Dq$, with a tetragonal distortion that causes splittings Δt_{2g} and Δe_g, these diagonal matrix elements are

$$E_{z^2} = 6Dq + \tfrac{2}{5}\Delta t_{2g} - \tfrac{4}{5}\Delta e_g \tag{2.41}$$

$$E_{xz} = -4Dq - \tfrac{3}{5}\Delta t_{2g} + \tfrac{1}{5}\Delta e_g \tag{2.42}$$

$$E_{yz} = -4Dq - \tfrac{3}{5}\Delta t_{2g} + \tfrac{1}{5}\Delta e_g \tag{2.43}$$

$$E_{x^2} = 6Dq + \tfrac{2}{5}\Delta t_{2g} + \tfrac{1}{5}\Delta e_g \tag{2.44}$$

$$E_{xy} = -4Dq + \tfrac{2}{5}\Delta t_{2g} + \tfrac{1}{5}\Delta e_g. \tag{2.45}$$

For a tetrahedral crystal field, the value of $10Dq$ is simply negative. For trigonal crystal field, the trigonal splitting δ appears as off-diagonal matrix elements

$$\mathcal{H}_{\mathrm{trig}} = \begin{bmatrix} 6Dq & 0 & 0 & 0 & 0 \\ 0 & -4Dq & \delta & 0 & \delta \\ 0 & \delta & -4Dq & 0 & \delta \\ 0 & 0 & 0 & 6Dq & 0 \\ 0 & \delta & \delta & 0 & -4Dq \end{bmatrix}. \tag{2.46}$$

To include the spin degree of freedom, we use a 10×10 matrix with equal crystal field splitting for each spin the same orbital. The intermediate state $(2p^5 3d^{n+1})$ Hamiltonian is given by

$$\mathcal{H}_n = \mathcal{H}_i + \mathcal{H}_p + \mathcal{H}_{pd} \tag{2.47}$$

where $\mathcal{H}_i$ has the same form as above but for a $3d^9$ configuration. $\mathcal{H}_p$ is the Hamiltonian for the $2p$ core levels which includes an on-site energy difference and spin-orbit coupling λ_{2p}. $\mathcal{H}_{pd}$ is the Coulomb interaction between the core hole and valence electrons, which is parameterized by the Slater integrals F^2_{pd}, G^1_{pd}, and G^3_{pd}.

2.6.2 Anderson impurity model

To more accurately capture the local electronic structure in materials with strong metal-ligand hybrization, we can use an Anderson impurity model (AIM), in which a partially filled d shell or *impurity* is hybridized with a fully occupied *bath* of uncorrelated ligand orbitals.

For an octahedral cluster, there are 10 metal d orbitals and 36 ligand p orbitals (6 orbitals on each of 6 ligands). However, we can reduce the basis size and drastically improve computational efficiency using *symmetry-adapted ligand orbitals*. Each d orbital will only hybridize with the set of ligand p orbitals sharing the same symmetry. We can thus consider only 10 bath states, each consisting of a linear combination of ligand orbitals possessing the same symmetry as a given d orbital. Each of these symmetry adapted orbitals will only hybridize with the d orbital of equivalent symmetry.

In this model, we have the single ion Hamiltonian for the metal site, a Hamiltonian for the uncorrelated bath states, and a hybridization or hopping matrix. The core hole in the intermediate state is treated similarly to the single ion case. Since the numer of electrons on the metal site is no longer fixed, we now include a the monopole part of the Coulomb interaction to impose an energy cost for adding an electron to the metal site, parameterized by U_{dd}. The hopping matrix V is parameterized by the hopping parameters V_{eg} and V_{t2g}, which mix the corresponding impurity and bath states. We also set the energy offset for the impurity and bath states, parameterized by the charge transfer energy Δ, as described in section 1.1.2. These energies, E_d and E_L, are set such that the configurations d^nL^{10}, $d^{n+1}L^9$, and $d^{n+2}L^8$ have total energy $E = 0$, $E = \Delta$, and $E = 2\Delta + U_{dd}$. Further details are given in [147].

CHAPTER 3

Electronic structure of the frustrated diamond-lattice magnet $NiRh_2O_4$

This chapter describes measurements of the electronic structure and lattice dynamics of $NiRh_2O_4$, a spinel compound with Ni^{2+} on the tetrahedral A-sites forming the only known realization of a $S = 1$ diamond lattice magnet. This material has a small tetragonal distortion that does not fully quench the orbital degree of freedom, leading to a spin-orbital-lattice entangled local ground state. The interplay between frustrated magnetism and competing local ground states makes $NiRh_2O_4$ an ideal candidate for realizing exciting new phenomena at the intersection of quantum spin liquid-like states and quantum critical phenonena.

I first present the results of resonant inelastic x-ray scattering (RIXS) measurements and explain the key features of the spectrum using a single-ion model. I then extend this to a two-site model to account for Ni-Rh hybridization, informed by x-ray absorption spectroscopy measurements. Next, I present inelastic neutron scattering measurements which identify the presence of electron phonon coupling. By including the effects of electron phonon coupling, I am able to provide a complete description of the RIXS spectrum. This chapter is adapted from the work published in [148]. For completeness, I note a recent work on $NiRh_2O_4$, which uses a new synthesis method and identifies a magnetic phase transition [149].

3.1 Introduction

Materials with frustrated magnetic interactions provide a platform for realizing novel phases which avoid conventional symmetry-breaking order [8]. Such phases are acutely sensitive to a hierarchy of competing energy scales involving spin, charge, orbital, and lattice degrees of freedom [5]. This enables precise tuning of the collective orders in these systems to explore new phenomena and develop new technologies [150]. Along this line, there has recently been a significant interest in novel phases driven by strong spin orbit coupling (SOC) that has motivated significant work on $4d/5d$ transition metal compounds [54]. In some cases, however, the relatively weak SOC in $3d$ compounds may still become relevant. In particular, when there is an orbital degeneracy, SOC may compete with the Jahn-Teller (JT) effect to produce a spin-orbital-lattice entangled state [151].

The spinel structure comprises an intensely studied class of materials with both fundamental significance and widespread applications. The general formula AB_2X_4 contains tetrahedrally coordinated A^{2+} ions and octahedrally coordinated B^{3+} ions which occupy diamond and pyrochlore sublattices respectively. In the case of magnetic B ions, the system forms a prototypical geometrically frustrated pyrochlore magnet. On the other hand, for magnetic A site ions, the bipartite diamond lattice may be frustrated in the presence of competing nearest and next-nearest neighbor antiferromagnetic exchange [71]. Previously studied diamond lattice magnets include the A-site spinels Co_3O_4 [152], AAl_2O_4 (A = Mn, Fe, Co) [153, 154], ASc_2S_4 (A = Mn, Fe) [155, 156], $MnSc_2Se_4$ [157], and ARh_2O_4 (A = Co, Cu, Ni) [158, 159], as well as the lanthanides $LiYbO_2$ [160] and $NaCeO_2$ [161]. These materials host a variety of magnetic phenomena, ranging from long-range ordered states to disordered spin liquid and spin glass states. In many cases, especially in the presence of an orbital degree of freedom, these materials lie near a quantum critical point, with multiple competing phases exhibiting strong sensitivity to disorder and external perturbations [61, 162–169]. It is thus essential to characterize the microscopic energy scales associated with the spin, lattice, and orbital degrees of freedom in these materials.

Another topic of recent interest is frustrated magnetism in spin-1 materials [170–172], which support more degrees of freedom than spin-$\frac{1}{2}$, while still being sensitive to quantum fluctuations. In particular, recent studies have predicted spin-1 diamond lattice antiferromagnets to host unconventional magnetic phenomena, namely topological paramagnetism [173], spiral spin liquid phases [30], quantum critical phenomena [174], and excitonic magnetism [25].

The spinel $NiRh_2O_4$ contains spin-1 Ni^{2+} ions on the A sites and nonmagnetic Rh^{3+} ions on the B sites, thus realizing the only known spin-1 on a diamond lattice. Early studies identified a cubic to tetragonal structural transition at 390 K [175] and an apparent antiferromagnetic transition at $T_N = 18$ K [176]. However, a recent study on high quality samples found no sign of magnetic order down to 0.1 K [159], implying that chemical disorder may have stabilized ordering found in the original studies. In that study, specific heat and x-ray diffraction measurements found a small entropy loss associated with the structural distortion at $T = 440$ K, indicating only a partial lifting of orbital degeneracy. This finding is consistent with the $p_{\text{eff}} = 3.3\mu_B$ paramagnetic moment that is significantly larger than the pure spin-1 value of $2.83\mu_B$, implying an orbital contribution to the magnetism. The Curie-Weiss temperature of $\Theta_{\text{CW}} = -11$ K indicates a large frustration parameter $f = \Theta_{\text{CW}}/T_N > 100$. Inelastic neutron scattering (INS) found gapped dispersive magnetic excitations suggestive of a valence bond ground state [159]. However, an incomplete knowledge of the electronic ground state has limited modeling of the INS data. Recent theoretical work predicted that spin-orbit coupling, crystal fields, and correlations generate a spin-orbital singlet ground state in $NiRh_2O_4$ [25, 177]. Such a state would explain the absence of magnetic ordering and key features of the magnetization, specific heat, and neutron data. But measurements of the high energy excitations characterizing the orbital configurations of $NiRh_2O_4$ are required to confirm this picture.

In this chapter, we use a combination of resonant inelastic x-ray (RIXS), x-ray absorption spectroscopy (XAS), and inelastic neutron scattering to provide a detailed account of the electronic structure of $NiRh_2O_4$. We observe crystal field excitations for Ni^{2+} in a distorted

tetrahedral environment that are well-described by a single-ion model including Coulomb interaction, spin-orbit coupling, crystal field splitting. We find additional electronic excitations corresponding to two-site Rh to Ni charge transfer. We also find that the orbital excitations are coupled to optical phonons giving rise to distinct phonon sidebands that dress *d*-*d* excitations. These results provide a detailed description of the local electronic structure of a novel frustrated magnet along with the key energy scales required for understanding the magnetic ground state and low-energy excitations. We have additionally shown that both covalency and lattice dynamics play essential roles in this material and should be considered in any realistic model for the magnetism. These insights provide guidance for exploring novel effects in $NiRh_2O_4$ and other magnetically frustrated spinels using pressure, magetic fields, and chemical substitution.

This chapter is organized as follows. In section 3.2, we describe the experimental details. In section 3.3, we present the RIXS, XAS, and INS results and describe our attempts to model the data. We first use a single ion model for Ni^{2+} in a distorted tetrahedral crystal field, then a minimal two-site Ni-Rh hopping model, and finally we incorporate electron phonon coupling in order to capture the lineshapes of the RIXS spectra. Our findings are summarized in section 3.4.

3.2 Experiment

Polycrystalline $NiRh_2O_4$ was synthesized following the methods described in [159]. The samples contain 4% nonmagnetic Rh_2O_3 by mass, which is not expected to contribute any observable effects to our measurements.

Resonant inelastic x-ray scattering (RIXS) measurements at the Ni L_3 edge were performed at the soft inelastic x-ray scattering (SIX) beamline 2-ID [178] at the National Synchrotron Light Source II (NSLS-II) at Brookhaven National Laboratory. Measurements were carried out at 40 K and 25 K using an incident x-ray polarization in both linear horizontal (π) and linear vertical (σ) geometries. The scattering angle was fixed at 90° to minimize the contribution

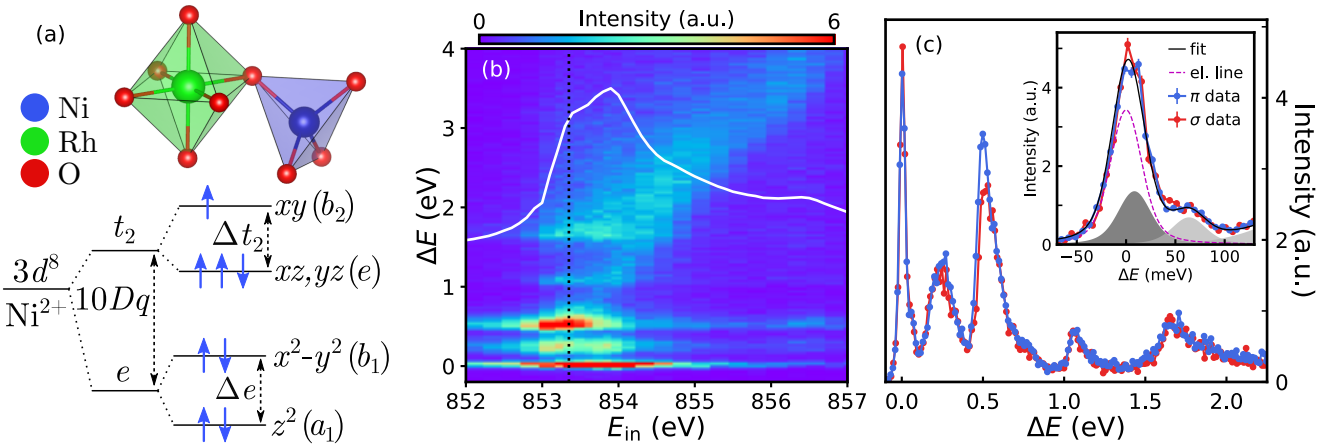

Figure 3.1: Overview of Ni L_3 edge RIXS data measured at $T = 40$ K and $2\theta = 90°$. (a) Local coordination of Ni and Rh in $NiRh_2O_4$. Rh is octahedrally coordinated while Ni^{2+} $3d$ orbitals are split by tetrahedral crystal field with tetragonal distortion $\Delta t_2 > 0$. (b) Measured RIXS intensity vs. energy loss and incident energy measured in π polarization. The XAS measured in total fluorescence yield is plotted in white. (c) RIXS spectrum in both π and σ polarization at $E_{in} = 853.4$ eV, indicated by the dashed line in (b). The inset shows the low-energy part of the spectrum and an empirical fit.

from Thomson elastic scattering and giving a momentum transfer of $Q = 0.61$ Å^{-1}. The incident x-ray energy was varied across the Ni L_3 edge (∼853 eV). The combined energy resolution was determined to be 31 meV based on the full width at half maximum (FWHM) of the elastic signal from carbon tape.

X-ray absorption spectroscopy (XAS) measurements at the O K edge were performed at NSLS-II beamline 2-ID (SIX), measured in fluorescence yield (FY). XAS measurements at the Rh L edges at Advanced Photon Source 4-ID-D, measured in total electron yield (TEY).

Inelastic neutron scattering (INS) measurements were performed on the Fine Resolution Fermi chopper spectrometer (SEQUOIA) at the Spallation Neutron Source, Oak Ridge National Laboratory. The incident neutron energy was fixed at 160 meV using the coarse resolution chopper (FC2) rotating at 600 Hz. The same 4 g sample used in [159] was loaded in an aluminum can, and held at 3.6 K for the measurement. Scattering contributions from the sample environment were removed by subtraction of an empty can data set during data reduction.

3.3 Results

Fig. 3.1(b) shows the RIXS intensity as a function of incident energy E_{in} and energy loss ΔE measured at 25 K with incident π polarization. The XAS, shown in white, contains a weak pre-edge feature at 852.9 eV, a main peak split into two features at 853.4 eV and 853.8 eV, and a satellite peak at 856.4 eV. The RIXS spectrum shows an elastic line at $\Delta E = 0$ eV, five Raman-like features at 0.065 eV, 0.25 eV, 0.5 eV, 1.1 eV, and 1.6 eV, a broad charge-transfer (CT) background between 2 and 4 eV, and a fluorescence line (FL) at constant scattered photon energy.

Fig. 3.1(c) shows RIXS scans at the main resonance of $E_{\text{in}} = 853.4$ eV, indicated by the dotted line in Fig. 3.1(b), in both π and σ incident polarization at 40 K. The inset shows the low energy region near the elastic line. The elastic intensity due to Thomson scattering is expected to be strongly suppressed in the π-polarized data for the 90° scattering angle configuration of these measurements. However, the π and σ-polarized data show similar intensity around $\Delta E = 0$, suggesting unresolved low energy excitations. The elastic line cannot be fit by a single resolution-limited Voigt function, further indicating the presence of unresolved low energy contributions. This can be explained by the ∼12 meV dispersive magnetic excitation observed in inelastic neutron scattering [159]. By including an additional resolution-limited Voigt function at 12 meV, we obtain an adequate fit to the quasi-elastic line, as shown in the inset of Fig. 3.1(c) for the π-polarized data, which also includes contributions from two overlapping higher energy peaks. A similar fit can be obtained for the σ-polarized data, with a slightly larger contribution from the elastic peak likely originating from Thomson scattering that contributes in that geometry.

3.3.1 Single-ion model

To identify the features in the measured spectra, we calculate the RIXS cross section [120] from exact diagonalization of a model Hamiltonian for a single Ni^{2+} ion including Coulomb interaction, spin-orbit coupling (SOC), and crystal field (CF) splitting. Calculations were

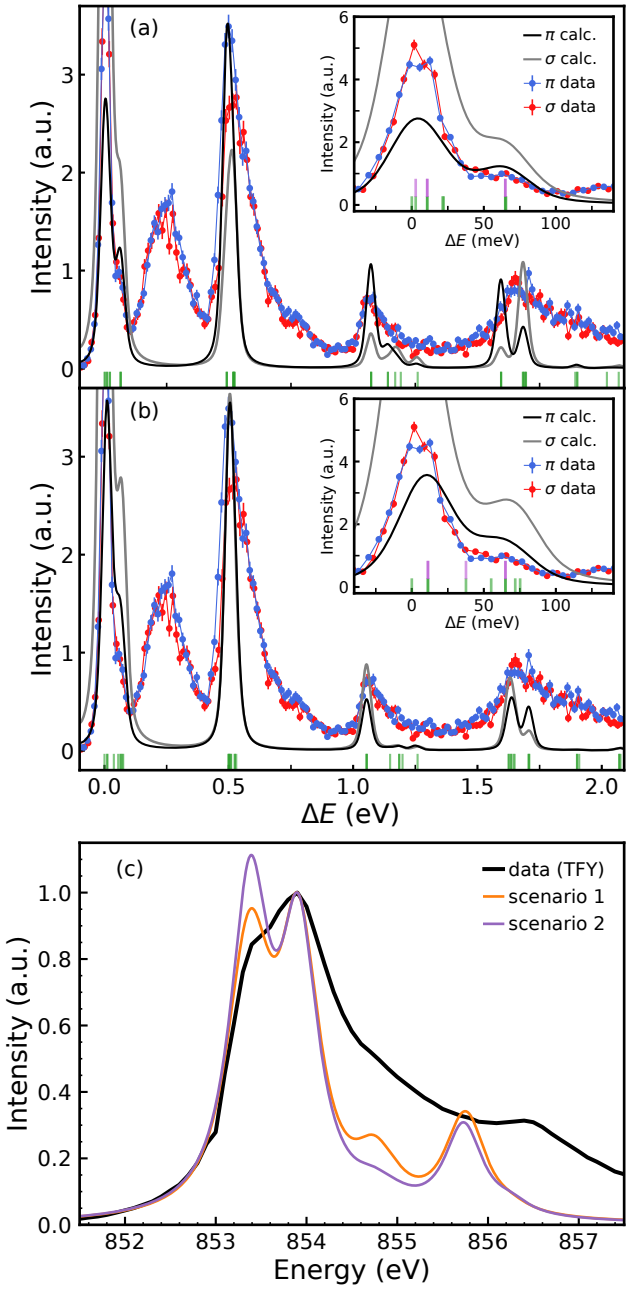

Figure 3.2: Comparison of the two crystal field schemes used for modeling the RIXS data. Scenario 1 ($\Delta t_2 > 0$) is shown in (a) and scenario 2 ($\Delta t_2 < 0$) is shown in (b). The green ticks indicate the eigenvalues. The purple ticks in the inset indicate which eigenvalues are dipole-allowed transitions from the ground state for comparison to the neutron data [159]. (c) Comparison of the two schemes for modeling the Ni L_3 XAS (TFY). The calculated XAS spectra are normalized to the intensity at the maximum of the measured spectrum.

implemented using the EDRIXS package [145], with further details described in section 2.6.

The initial/final state corresponds to a $3d^8$ configuration with 45 states. The intermediate state

corresponds to a $2p^5 3d^9$ configuration with 60 states. The Hamiltonians for the initial ($3d^8$) and intermediate ($3d^9 2p^5$) states are given by eq. **??** and 2.47 respectively. The calculated RIXS spectra are convolved with a 31 meV FWHM Gaussian to account for the experimental energy-loss resolution. The spectra are calculated for $2\theta = 90^\circ$ scattering angle corresponding to $Q = 0.61$ Å^{-1}, powder averaged over 100 random orientations of $\boldsymbol{Q}$ uniformly sampled over the surface of a sphere.

Onsite Coulomb interactions are parameterized by the Slater integrals: F^2_{dd}, and F^4_{dd} describe the direct Coulomb repulsion between d electrons, F^2_{pd} describes direct Coulomb repulsion between d electrons and the $2p$ core hole, and G^1_{pd} and G^3_{pd} describe the Coulomb exchange between d electrons and the $2p$ core hole. Initial values for the above parameters have been calculated for a free Ni^{2+} ion in $3d^8$ and $2p^5 3d^9$ configurations by the Hartree-Fock method using Cowan's code [146]. To account for the reduced intra-atomic repulsion due to covalency effects in the solid, we include empirical scale factors on F_{dd}, F_{pd}, and G_{pd} that are determined by fitting to the RIXS data.

The crystal-field is parameterized by the tetrahedral splitting $10Dq < 0$ and the splitting due to the tetragonal distortion $\Delta t_2 = E_{b_2} - E_{e'}$, $\Delta e = E_{b_1} - E_{a_1}$. The tetrahedral crystal field (T_d point group) splits the d^8 configuration into $e^4 t_2^4$. The tetragonal distortion ($T_d \rightarrow D_{2d}$) further splits the e doublet into a_1 (d_{z^2}) and b_1 ($d_{x^2-y^2}$) singlets, and the t_2 triplet into a b_2 (d_{xy}) singlet and e' (d_{xy}, d_{yz}) doublet, as shown in Fig. 3.1(a). These symmetry considerations leave the sign and magnitude of the splittings unconstrained. There have been no reported direct measurements of the crystal field splitting in $NiRh_2O_4$, and there are conflicting reports of the sign of the tetragonal splitting. This splitting cannot be constrained only from knowledge of the crystal structure because expectations from electrostatic considerations are often inaccurate due to additional effects from covalency and spin-orbit coupling [5]. As we will show below, both effects are significant in $NiRh_2O_4$.

The low temperature structure reported in [159] is tetragonal with elongated NiO_4 tetrahedra and compressed RhO_6 octahedra. This led the authors to propose a crystal field scheme

with the t_2 levels split into a lower b_2 state and upper e' states ($\Delta t_2 < 0$), following the model from [179], as expected from electrostatic considerations. However, the DFT calculation in [177] suggests that the t_2 levels are split into lower e' states and an upper b_2 state ($\Delta t_2 > 0$). We find that although a single ion model fails to reproduce the 0.25 eV peak, the asymmetric lineshapes of the high energy peaks, and the polarization dependence of the quasielastic peak, it enables us to distinguish the two crystal field scenarios and place useful constraints on the magnitudes of tetragonal splitting and spin orbit coupling.

We constrain our model to maintain consistency with material trends for insulating Ni compounds and with other spectroscopic measurements on $NiRh_2O_4$ [179, 180]. The peaks around 0.5 eV and 1 eV fix the value of $10Dq \approx 0.55$ eV, as they correspond to $e^4t_2^4 \rightarrow e^3t_2^5$ and $e^4t_2^4 \rightarrow e^2t_2^6$ transitions. This $10Dq$ value is consistent with DFT [177] and the values for tetrahedrally coordinated Ni^{2+} in other compounds [179]. We can also constrain the value of atomic spin-orbit coupling λ by the requirement of a dipole-allowed level near 11 meV to agree with the neutron scattering data [159]. Finally, the peak at 1600 meV corresponds to an excitation within the Hund's multiplet and fixes the value of F_{dd}. To match the energy of the highest energy peak, F_{dd} must be set to 0.5, giving a Hund's coupling of $J_H = \frac{1}{14}(F_{dd}^2 + F_{dd}^4) = 0.71$ eV. This parameter also sets the energy of intra-t_2 spin-flip excitations ($S = 1 \rightarrow S = 0$) between 1.1 and 1.3 eV. These excitations have minimal intensity in the computed RIXS cross section and we do not expect to observe them above the signal-to-noise of our data, see Fig. 3.2 (a) and (b). The 50% reduction in the intra-atomic Coulomb interaction F_{dd}, compared with the atomic values, suggests strong Ni-O covalency [181] and already indicates the inadequacy of a single ion model for $NiRh_2O_4$, we address this later in section 3.3.2. The Slater integrals F_{pd} and G_{pd} determine the intermediate state energies and do not affect the RIXS peak energies. However, they do influence the RIXS intensities and energy splitting of the main XAS peak. We have tested models for tetrahedral compression and elongation and find that they both capture many features of the data; table 3.1 shows the best parameters for the two scenarios (1) $\Delta t_2 > 0$ and (2) $\Delta t_2 < 0$, plotted in Fig. 3.2. Δe

Table 3.1: Parameters for the single-ion model using $\Delta t_2 > 0$ and $\Delta t_2 < 0$. $10Dq$, Δt_2, Δe, and λ are in meV. F_{dd}, F_{pd}, and G_{pd} are dimensionless.

	$10Dq$	Δt_2	Δe	λ	F_{dd}	F_{pd}	G_{pd}
$\Delta t_2 > 0$	-580	70	56	13	0.5	0.7	0.75
$\Delta t_2 < 0$	-530	-50	-40	27	0.5	0.7	0.75

is underdetermined by our data and mainly contributes to the splitting of the peaks above 500 meV. Here, we assume that Δe has the same sign as Δt_2. We also expect $|\Delta e| < |\Delta t_2|$, due to the reduced Ni-O hybridization of the e states compared to the t_2 states in tetrahedral symmetry. We find that the constraint $\Delta e = 0.8\Delta t_2$ provides an adequate agreement with the data as shown in Fig. 3.2. Both models reproduce the observed peaks at 65 meV, 0.5 eV, 1 eV and 1.6 eV and while scenario 1 better reproduces the small dichroism of the 0.5 eV feature, scenario 2 more faithfully reproduces the negligible dichroism of the 1 eV and 1.6 eV peaks. The high energy excitations, $\Delta E > 500$ meV, are far above the insulating gap in $NiRh_2O_4$ and are thus coupled to delocalized states. This effect is not captured in the single-ion model and may explain the Fano-like lineshape. However, we found that a more careful examination of the low energy excitations for $E < 100$ meV enables a distinction between crystal field models.

The low energy part of the spectrum is shown in the insets of Fig. 3.2 (a) and (b), with the purple markers indicating energy levels with nonvanishing neutron cross section. Since photons emitted with energies close to the absorption edge are more likely to be reabsorbed, we expect strong self absorption effects near the elastic line and our model should predict a larger quasi-elastic intensity than what is observed. The observed intensities are also likely modified by intersite magnetic exchange interactions [177] that are not included in our single site model. Nevertheless, a careful comparison of the observed linear dichroism at low energy transfers reveals that scenario 1, $\Delta t_2 > 0$, is more consistent with our data. The low energy subspace of scenario 1 is equivalent to the model from [177], and yields excited states at 3^*, $11(2)^*$, 22(2), and $65(3)^*$ meV. The low energy subspace of scenario 2 is equivalent to the model from [179], yielding excited states at $11(2)^*$, 38^*, 55, $65(2)^*$, 72, and 75 meV. Asterisks indicate those states with nonvanishing neutron intensity and parentheses indicate the state

degeneracy, disregarding any splitting of less than 1 meV. The calculation for scenario 1 shows that the dominant contribution to the quasi-elastic RIXS intensity comes from the ground state and a 3 meV excitation for both polarizations [Fig. 3.2 (a)]. This is consistent with the nearly equivalent quasielastic lines we measured for each polarization. However, for scenario 2, the dominant contribution comes from the ground state for σ polarization and from the 11 meV excitation for π polarization [Fig. 3.2 (b)]. Although the energies of these excitations fall within our experimental resolution, scenario 2 should result in a more pronounced difference in the quasielastic lineshape between σ and π polarizations and that is not consistent with our data.

To provide an additional check for our single ion model, we compare with the measured x-ray absorption spectrum (XAS) at the Ni L_3 edge measured in total fluorescence yield (TFY) shown in Fig. 3.2(c). The main XAS peak is split into lower and upper peaks at 853.4 and 853.8 eV, corresponding to the states $2p^5e^4t_2^5$ and $2p^5e^3t_2^6$. In the single-ion model, this splitting depends on $10Dq$, F_{pd}, and G_{pd}. Although the XAS lineshape is known to be distorted by TFY measurements, the calculated spectrum shows better qualitative agreement with our data for scenario 1. In particular, a model with $\Delta t_2 > 0$ more faithfully reproduces the relative intensities of the 853.4 and 853.8 eV peaks, and captures additional observed intensity at 854.7 eV that is not predicted by a model with $\Delta t_2 < 0$ [Fig 3.2 (c)]. However, we find that for either scenario, the single-ion model cannot capture the large, ~ 3 eV, splitting between the main peak and satellite peak at 856.4 eV.

Based on the above considerations, we conclude that scenario 1, splitting the t_2 levels into lower energy d_{xz}, d_{yz} orbitals and a higher energy d_{xy} orbital, is the correct crystal field scheme in $NiRh_2O_4$. However, there are many notable discrepancies between the single ion model and our data. First, a single-ion model completely fails to reproduce the intense 250 meV RIXS peaks for any reasonable set of parameters (see 3.5) and second, it does not accurately capture the broad asymmetric lineshape of the 0.5 eV peak. Both of these features in the RIXS spectra arise because of two distinct effects that cannot be accounted for in a single-ion description.

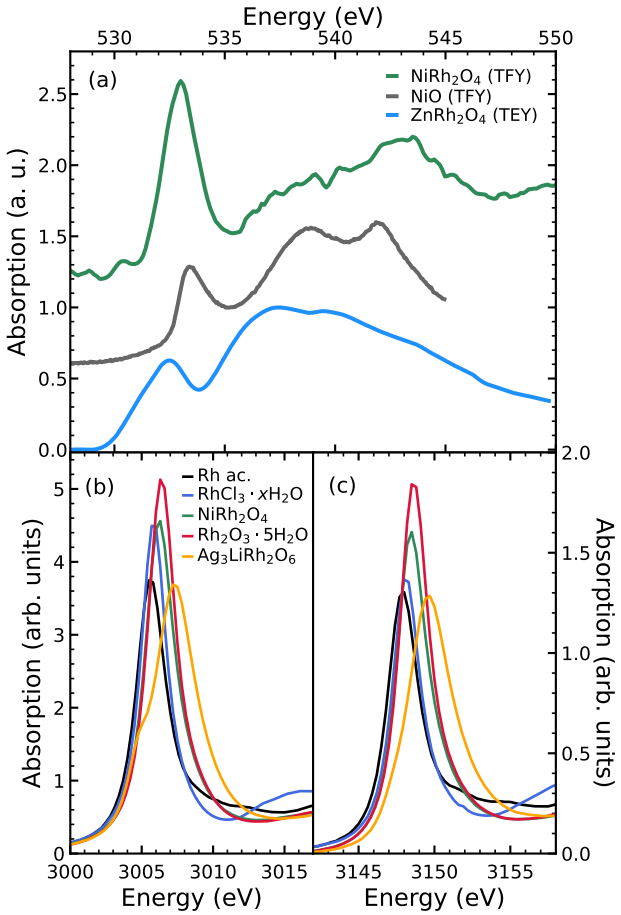

Figure 3.3: (a) XAS at the O K edge for $NiRh_2O_4$ (TFY), with NiO (TFY) and $ZnRh_2O_4$ (TEY) for comparison (NiO data from [182] and $ZnRh_2O_4$ data from [183]) (b) XAS measured at the Rh L_3 edge and (c) the Rh L_2 edge.

First, there is strong Ni-Rh hybridization, and second, there is strong electron-phonon coupling. The evidence for each of these effects and a detailed discussion of their respective influence on the RIXS spectra and magnetism in $NiRh_2O_4$ is discussed below in sections 3.3.2 and 3.3.3.

3.3.2 Ni-Rh hybridization

We now extend our model to include the influence of electronic hybridization between Ni and Rh sites. Such metal-metal hybridization is supported both by experiment and ab-initio calculations. Density functional theory calculations [177] have found strong Ni-Rh hybridization is mediated by the intermediate oxygens. Furthermore, the calculation found an insulating gap of 250 meV, with the highest occupied and lowest unoccupied states having

mostly Rh and Ni character respectively. This suggests that the lowest interband transition consists of Rh→Ni excitations.

We have carried out x-ray absorption (XAS) measurements at the O K and Rh L edges in order to characterize the electronic states at the Rh and O sites in $NiRh_2O_4$. Fig. 3.3(a) shows the O K edge XAS for $NiRh_2O_4$ measured in total fluorescence yield (TFY), with the spectra for NiO (TFY) and $ZnRh_2O_4$ (TEY) shown for comparison. NiO provides a comparison to bonding in an NiO_6 octahedron while $ZnRh_2O_4$, being isostructural to the cubic phase of $NiRh_2O_4$, provides a comparison to bonding in a RhO_6 octahedron in the absence of an unfilled neighboring $3d$ shell.

The pre-edge region contains a small peak at 530.5 eV and a large peak at 533 eV, corresponding to O $2p$ states hybridized with empty metal d states. The region above 535 eV corresponds to Ni $4sp$ and Rh $5sp$ states. By comparing to the projected density of states from DFT calculations [177], we can assign the small pre-edge peak at 530.5 eV to the unfilled Ni t_2 states and the large peak at 533 eV to the unfilled Rh e_g states. The pre-edge peak intensity is determined by both the number of empty metal states and the degree of hybridization [184]. In NiO and $ZnRh_2O_4$, where the metal sites provide two empty states per O site, the pre-edge peak intensities are comparable. In $NiRh_2O_4$, there are 2 empty Rh states and 0.5 empty Ni states per O site. This small increase in the number of available states alone cannot explain the significant enhancement of pre-edge peak intensity. The intensity can thus be explained by an increased hybridization due to the cooperative influence of the Ni and Rh. This can be expected based on the large inductive effect of Rh^{3+} [185]. It may also be enhanced due to the long range exchange interactions. In the five-site exchange pathway A-O-B-O-A via a nonmagnetic B cation, the dominant contribution is thought to involve the empty states at the B sites [186–188].

Fig. 3.3(b) and Fig. 3.3(c) show the XAS at the Rh L_3 and L_2 edges respectively, for $NiRh_2O_4$ and reference samples with known valence: Rh acetate (2+), $RhCl_3 \cdot xH_2O$ (3+), $Rh_2O_3 \cdot 5H_2O$ (3+), $Ag_3LiRh_2O_6$ (4+) [189]. The sharp white line peaks correspond to

Table 3.2: Table of peak positions and widths in eV extracted from the Rh L edge XAS by fitting a Lorentzian + arctangent lineshape.

	E_{L3}	E_{L2}	Γ_{L3}	Γ_{L2}
Rh acetate	3005.5(1)	3147.7(1)	2.0(1)	1.8(2)
$RhCl_3 \cdot xH_2O$	3005.7(1)	3148.0(1)	1.8(1)	1.6(2)
$NiRh_2O_4$	3006.1(1)	3148.3(1)	2.0(1)	1.7(2)
$Rh_2O_3 \cdot 5H_2O$	3006.3(1)	3148.5(1)	1.9(1)	1.7(2)
$Ag_3LiRh_2O_6$	3007.0(1)	3149.4(1)	3.0(2)	2.4(3)

transitions from $2p$ core levels to empty $4d$ states. The Rh^{2+} and Rh^{3+} spectra contain a single peak at each edge, while the Rh^{4+} spectrum contains a shoulder on the low energy side, corresponding to the empty t_{2g} state. As expected, this shoulder is suppressed at the L_2 edge [190]. To quantify the Rh valence, we obtain the white line peak position for each compound from a fit to a Lorentzian plus arctangent lineshape [191, 192]. The results of this fit are summarized in table 3.2. The reference compounds for Rh^{3+} show a 0.6 eV (0.5 eV) difference in peak position at the L_3 (L_2) edge. The higher peak position of Rh_2O_3 compared to $RhCl_3$ can be attributed to the larger covalency of the Rh-O bond compared to the Rh-Cl bond, giving a more delocalized charge density around the Rh site in Rh_2O_3 [193]. We find that the peak position for $NiRh_2O_4$ lies between these two compounds with no significant differences between lineshapes and peak widths. This confirms that despite the strong hybridization, Rh maintains the charge distribution of the 3+ oxidation state with no signs of charge disproportionation, which often occurs in mixed 3d/4d compounds [194–196].

Having confirmed the strong Ni-Rh hybridization and Rh oxidation state in $NiRh_2O_4$, we assign the RIXS peak at 250 meV to a two-site orbital excitation from Rh t_{2g} to Ni t_2, corresponding to the transition Ni $3d^8$ + Rh $4d^6$ $\rightarrow$ Ni $3d^9$ + Rh $4d^5$. This assignment is corroborated by our effective two site model discussed below. Although such metal-metal charge transfer (MMCT) is well known from optical studies of spinel ferrites [197, 198], there are few reports of these features seen in RIXS [199–201].

A full microscopic description of MMCT in $NiRh_2O_4$ is considerably complicated by the 12-fold nearest neighbor Ni-Rh coordination with intermediate Ni-O-Rh bond angles that

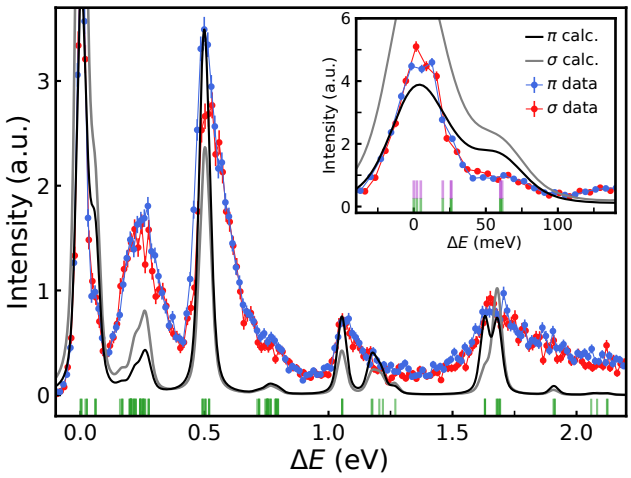

Figure 3.4: Calculated RIXS spectrum from the two-site model with $t = 30$ meV, $\Delta = -600$ meV compared with measured data. The green ticks indicate the eigenvalues. The purple ticks in the inset indicate which eigenvalues are dipole-allowed transitions from the ground state for comparison to the neutron data [159].

prohibit any strict orthogonality constraints on hopping pathways. In order to capture the essential features of Ni-Rh hybridization present in the RIXS spectra, we construct a minimal model by adding a single set of filled Rh t_{2g} states to the single-ion model from the previous section. To reduce the size of the Hilbert space, we neglect the empty Rh e_g orbitals which are separated by the large octahedral crystal field splitting of ~ 2 eV on the Rh site [177]. In this two-site model, the Ni^{2+} and Rh^{3+} sites are each subject to Coulomb, crystal field, and spin-orbit interactions, with on-site energy difference Δ and hopping t. Since multiple sites are involved, we now include the monopole part of the Coulomb interaction at each site $U_{\mathrm{Ni}} = 6$ eV and $U_{\mathrm{Rh}} = 3$ eV. We assume an equal hopping from each Ni t_2 to each Rh t_{2g} and neglect any hopping from the Ni e levels.

The initial/final state in this model is a mixture of the configurations $3d^8t_{2g}^6$, $3d^9t_{2g}^5$, and $3d^{10}t_{2g}^4$, with 120 total states. The intermediate state is a mixture of the configurations $2p^53d^9t_{2g}^6$ and $2p^53d^{10}t_{2g}^5$, with 96 total states. We ignore any interactions between the core hole and the Rh site. The initial/final state Hamiltonian is given by

$$\mathcal{H}_i = \mathcal{H}_{\mathrm{Ni}} + \mathcal{H}_{\mathrm{Rh}} + V \tag{3.1}$$

where $\mathcal{H}_{\mathrm{Ni}}$ and $\mathcal{H}_{\mathrm{Rh}}$ are the Hamiltonians for the Ni and Rh sites, and V is the hybridization term which mixes the single-ion states, given by

$$V = \begin{pmatrix} 0 & T^\dagger \\ T & 0 \end{pmatrix}, \qquad T = \begin{pmatrix} 0 & t & t & 0 & t \\ 0 & t & t & 0 & t \\ 0 & t & t & 0 & t \end{pmatrix}. \tag{3.2}$$

This equally mixes each of the 5 Ni d orbitals with each of the 3 Rh t_{2g} orbitals. Since this model considers multiple sites, we now include the monopole term in the Coulomb interaction on each site, $F^0 = U + \frac{2}{63}(F^2 + F^4)$, where $U_{\mathrm{Ni}} = 6$ eV, $U_{\mathrm{Rh}} = 3$ eV. The intermediate state Hamiltonian $\mathcal{H}_n$ is equivalent to that of the single-ion model, since we neglect any explicit interaction between the core-hole and the Rh site. The effective charge transfer energy Δ gives the energy of the Ni $3d^9$ Rh $4d^5$ configuration relative to Ni $3d^8$ Rh $4d^6$ before any splitting. We use this to determine the on-site energies E_{Ni} and E_{Rh} for the initial state by solving the linear system of equations

$$n_{\mathrm{Ni}}E_{\mathrm{Ni}} + n_{\mathrm{Rh}}E_{\mathrm{Rh}} + \tfrac{1}{2}n_{\mathrm{Ni}}(n_{\mathrm{Ni}} - 1)U_{\mathrm{Ni}} + \tfrac{1}{2}n_{\mathrm{Rh}}(n_{\mathrm{Rh}} - 1)U_{\mathrm{Rh}} = 0 \tag{3.3}$$

$$(n_{\mathrm{Ni}} + 1)E_{\mathrm{Ni}} + (n_{\mathrm{Rh}} - 1)E_{\mathrm{Rh}} + \tfrac{1}{2}n_{\mathrm{Ni}}(n_{\mathrm{Ni}} + 1)U_{\mathrm{Ni}} + \tfrac{1}{2}(n_{\mathrm{Rh}} - 1)(n_{\mathrm{Rh}} - 2)U_{\mathrm{Rh}} = \Delta. \tag{3.4}$$

In the intermediate state, we obtain the on-site energies of the Ni and Rh d orbitals E'_{Ni} and E'_{Rh}, as well as the Ni $2p$ orbitals E_p, from the system of equations

$$6E_p + n_{\mathrm{Ni}}E'_{\mathrm{Ni}} + n_{\mathrm{Rh}}E'_{\mathrm{Rh}} + \tfrac{1}{2}n_{\mathrm{Ni}}(n_{\mathrm{Ni}} - 1)U_{\mathrm{Ni}} + \tfrac{1}{2}n_{\mathrm{Rh}}(n_{\mathrm{Rh}} - 1)U_{\mathrm{Rh}} + 6n_{\mathrm{Ni}}U_{pd} = 0 \tag{3.5}$$

$$6E_p + (n_{\mathrm{Ni}} + 1)E'_{\mathrm{Ni}} + (n_{\mathrm{Rh}} - 1)E'_{\mathrm{Rh}} + \tfrac{1}{2}(n_{\mathrm{Ni}} + 1)n_{\mathrm{Ni}}U_{\mathrm{Ni}} + \tfrac{1}{2}(n_{\mathrm{Rh}} - 1)(n_{\mathrm{Rh}} - 2)U_{\mathrm{Rh}} + 6(n_{\mathrm{Ni}} + 1)U_{pd} = \Delta \tag{3.6}$$

$$5E_p + (n_{\mathrm{Ni}} + 1)E'_{\mathrm{Ni}} + n_{\mathrm{Rh}}E'_{\mathrm{Rh}} + \tfrac{1}{2}(n_{\mathrm{Ni}} + 1)n_{\mathrm{Ni}}U_{\mathrm{Ni}} + \tfrac{1}{2}n_{\mathrm{Rh}}(n_{\mathrm{Rh}} - 1)U_{\mathrm{Rh}} + 5(n_{\mathrm{Ni}} + 1)U_{pd} = 0. \tag{3.7}$$

The effective crystal field parameters obtained from a single-ion model must also be adjusted in the presence of hopping. As shown in Fig. 3.4, we find good agreement between data and model for the parameters $\Delta = -600$ meV, $t = 30$ meV, $10Dq = -550$ meV, $\lambda = 13$ meV, and $\Delta t_2 = 40$ meV, with the same constraint $\Delta e = 0.8\Delta t_2$. We also set the Rh tetragonal splitting $\Delta t_{2g} = 0$ meV, but the results are mostly unchanged for nonzero Δt_{2g}. This corresponds to scenario 1 discussed above, but similar results are obtained for scenario 2 (see 3.5). We emphasize that the two-site model does not preserve the symmetry of the Ni site, making it ineffective for comparing the two scenarios. This is evident from the inset of Fig. 3.4, where all low-energy levels have non-negligible dipole character.

Despite the simplicity, the minimal model provides a robust qualitative description of the data, reproducing the energy of all observed RIXS excitations over a 2 eV range of energy transfers with effective parameters describing the approximate energy scales of the Ni-Rh hybridization. A more detailed approach should incorporate the empty Rh e_g levels, which may be essential to the long range exchange interaction, and might consider a double cluster model [202, 203], or symmetry-adapted Rh orbitals [147]. In addition, through comparison of high energy inelastic neutron scattering data that is sensitive to optical phonons, with the RIXS spectra, we find that lattice vibrations enter as an essential energy scale coupled to the electronic states in $NiRh_2O_4$. A consideration of electron phonon coupling and vibronic excitations is thus necessary to capture the broad asymmetric lineshape of the RIXS spectra, as discussed in the following section.

3.3.3 Electron-phonon coupling

In orbitally degenerate systems, there is a tendency for strong electron-lattice coupling. In many cases, the degeneracy may be lifted by a static lattice distortion via the Jahn-Teller (JT) mechanism [180, 204]. Another possibility is the formation of vibronic modes via the dynamical JT effect, where orbital degeneracy is broken by coupling to lattice vibrations [60]. When the JT distortion energy is comparable to the spin-orbit coupling, the system may host

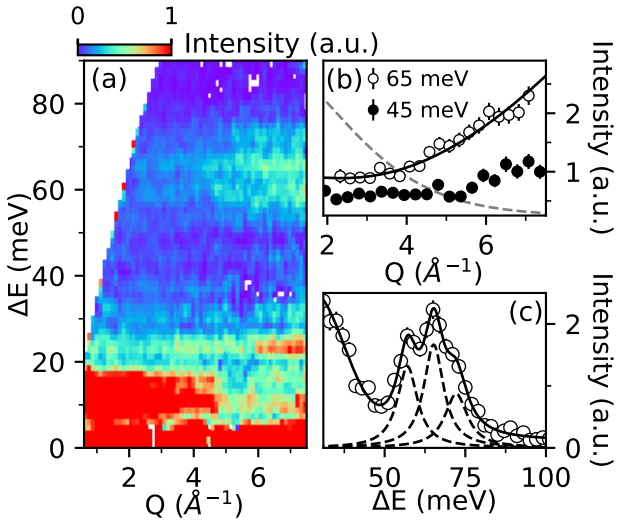

Figure 3.5: (a) Inelastic neutron scattering spectra $I(Q, E)$ of $NiRh_2O_4$ at $T = 3.6$ K. Collective spin-orbit excitations are visible around 10 meV, and the highest energy optical phonons appear between 60 and 70 meV. (b) Constant energy cuts through $I(Q, E)$ integrated over $E \pm 5$ meV, dashed line shows the momentum dependence of the Ni^{2+} form-factor $|f(Q)|^2$, solid line is a fit to $C|f(Q)|^2 + AQ^2 + B$ as described in the text. (c) Constant momentum-transfer cut integrated over $Q = 6 \pm 1$ Å^{-1}, solid line is a fit to three Lorentzians as described in the text.

a set of spin-orbital-lattice entangled states [151]. In $NiRh_2O_4$, the tetragonal distortion does not fully lift the orbital degeneracy [159]. The weak tetrahedral crystal field splitting (in comparison to octahedral) enables the JT energy to be comparable to SOC. Based on these considerations, we expect lattice dynamics to play a key role in the low-lying spin-orbital excitations.

Here we consider the effects of electron-phonon coupling on the RIXS spectrum of $NiRh_2O_4$. Although the RIXS spectra may contain contributions from optical phonons, their precise energies are obscured by the relatively coarse energy resolution on the scale of the phonon energies, and the coincidence of optical phonons with low energy electronic excitations. In order to more precisely quantify optical phonon energies in $NiRh_2O_4$, we have re-examined the inelastic neutron scattering data for energies up to 100 meV, covering the full phonon bandwidth. The high energy inelastic neutron scattering data is shown in Fig. 3.5(a). Below 20 meV, the previously reported collective spin-orbit excitation is visible. As discussed above,

this feature was not directly resolved in the RIXS spectra, but accounts for the broadening of the elastic line (inset of Fig. 3.1(c) and is captured by the single-ion model. At higher energies, we observe optical phonons, centered around 65 meV, coincident with the intra-t_2 excitation in the RIXS spectrum. The quadratically increasing intensity with increasing momentum transfer as shown in Fig. 3.5(b) indicates that this signal originates primarily from scattering by phonons, but we also find a component attributable to magnetic scattering. By fitting this cut to $I(Q) = C|f(Q)|^2 + AQ^2 + B$, where $f(Q)$ is the Ni^{2+} magnetic form-factor, A, B, and C are constants, we obtain a good description of the data with the parameters $A = 0.04$, $B = 0.2$, $C = 0.78$. Optical phonon energies were extracted directly from the constant momentum transfer cut in Fig. 3.5(c). We found that including three Lorentzian functions centered at 57.2(6), 65.3(5), and 72(1) meV and with energy linewidths of Γ = 7.6(1.7), 7.5(2.5), and 8.5(2.0) meV respectively was necessary to adequately describe the data. The phonon linewidths are significantly broadened over the instrumental resolution of $\sim$ 4.3-meV Gaussian FWHM at 65 meV. These high energy phonons originate from vibrations of Ni coordinating O tetrahedra, and we expect six distinct modes in this energy range for a cubic cell that are further split in the tetragonal phase [180, 205, 206]. Although the broad phonon lineshapes we observed may be accounted for by unresolved phonon mode splittings, it may also indicate phonon damping caused by coupling to other electronic excitations. Indeed, the coinciding energy of these phonons and the intra-t_2 crystal field excitation measured by RIXS suggests the possibility of a hybridized vibrational-electronic or "vibronic" excitation in $NiRh_2O_4$.

Such electron phonon coupling occurs because the charge distribution of the excited state on Ni repels the surrounding oxygen ions. For the intra t_2 excitation at 65 meV, the extra electron in the d_{xy} orbital is partially screened by the resulting d_{xz}/d_{yz} hole. However, the $e \rightarrow t_2$ excitation at 500 meV similarly leaves an extra charge in the t_2 levels, with a hole in the e levels. In this case, we expect the screening to be less effective, and thus the $e \rightarrow t_2$ excitation should couple even more strongly to phonons. We can use these considerations to model the lineshape of the 500 meV RIXS peak as a vibronic excitation. Although the

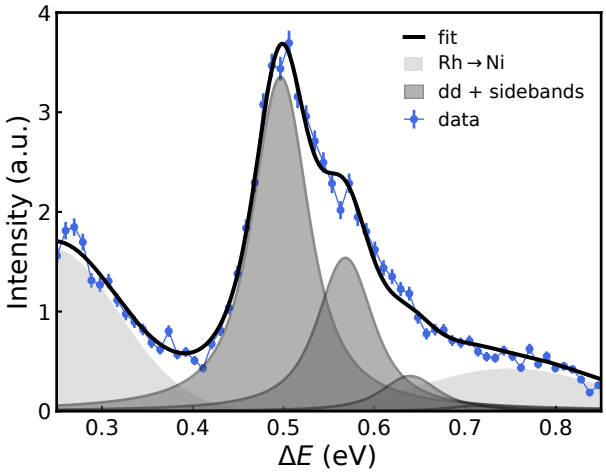

Figure 3.6: Poisson model for phonon sidebands fit to the 500 meV RIXS peak, including Gaussian fits to the overlapping neighboring peaks. The phonon sideband cross-section was modeled using equation 3.8 and Huang-Rhys parameter $g = 0.46(3)$, $\omega_0 = 71(2)$ meV, $E_0 = 497(2)$ meV, and $\Gamma = 60(2)$ meV.

single-ion model indicates at least two states comprise this peak and the neutron data shows at least three phonon modes may be involved in the coupling, we will consider a tractable model that includes only a single electronic excitation coupled to a single phonon as such a model is sufficient to capture the essential features of our data. Within this simplified model, we treat the main peak at energy $E_0 = 496$ meV as a bare d-d excitation, or zero-phonon line. This bare dd-excitation is dressed by additional phonon sidebands corresponding to a d-d excitation plus n phonons of energy E_{ph}. We assume a Lorentzian lineshape of FWHM width Γ for each peak separated by energy E_{ph} with relative intensities given by a Poisson distribution [207]

$$I_n = e^{-g}\frac{g^n}{n!}, \tag{3.8}$$

where g is the dimensionless electron-phonon coupling, which can be interpreted as the mean number of phonons emitted by the excitation. Fig. 3.6 shows a fit of this minimal model to the 500 meV RIXS peak for $E_0 = 497(2)$ meV, $E_{\text{ph}} = 71(2)$ meV, $\Gamma = 60(2)$ meV, and $g = 0.46(3)$ providing an excellent description of the data. The large value of Γ compared to the phonon energies suggests that there are many overlapping excitations within each phonon sideband. This is consistent with the single-ion model for scenario 1 that gives two crystal field

excitations, at 492 and 517 meV. Both of these may couple to optical phonons with energies between 57 and 72 meV. A more complete model for electron phonon coupling in $NiRh_2O_4$ would consider the separate *d*-*d* excitations and their coupling to multiple phonons, but the resolution of our measurement is not sufficient to constrain such a model.

3.4 Discussion and Conclusion

We have characterized the site-specific local electronic structure of $NiRh_2O_4$ using resonant inelastic x-ray scattering and x-ray absorption spectroscopy. We have compared two possible scenarios for the tetragonal splitting within a single ion model and showed that $\Delta t_2 > 0$ is more likely than $\Delta t_2 < 0$, and estimated that $\Delta t_2 = 70$ meV and $\lambda = 13$ meV. These parameters are the most relevant to modeling the magnetism in $NiRh_2O_4$ [25, 177]. The crystal field splittings are in agreement with DFT calculations that determined $\Delta t_2 = 100$ meV and $\lambda = 10$ meV from NMTO downfolding. The single ion model also required a 50% reduction of the F_{dd} Slater parameters, suggesting a significant degree of covalency in $NiRh_2O_4$.

The O K edge XAS data suggests a significant degree of hybridization between O p states and empty metal d states, which can only be explained by a metal-metal charge transfer between adjacent Ni and Rh sites. The Rh L edge XAS confirmed that the Rh ions maintain the nominal 3+ oxidation state, despite the strong hybridization and tendency toward charge disproportionation in related systems. By extending the RIXS model to include metal-metal charge transfer between Ni and Rh sites as parameterized by an effective hopping $t = 30$ meV, we captured Rh-Ni two-site excitations observed at 250 and 750 meV in the RIXS spectrum. Such an explicit demonstration of the failure of a single ion model and requirement for metal-metal charge transfer in $NiRh_2O_4$ highlights the importance of metal-metal hybridization in mixed 3d-4d/5d compounds in general. This hybridization can affect both the magnetic degrees of freedom and exchange interactions so it should be an essential consideration in the design of novel magnetic states in materials such as spinels, double perovskites [208, 209], or $A_2Mo_3O_8$ compounds [172, 210].

A detailed analysis of the RIXS lineshape also revealed that lattice vibrations influence the magnetism in $NiRh_2O_4$ through strong electron-phonon coupling. Inelastic neutron scattering reveals multiple optical phonons overlapping in energy with the intra-t_2 excitation, suggesting a hybridized orbital-lattice excitation between 60 and 70 meV. This effect was observed in the RIXS spectra as a phonon-dressed crystal field excitation at higher energy. Our results provide quantitative constraints on the key parameters for modeling the single-ion ground state and low-lying excitations, as well the long-range superexchange mechanism in $NiRh_2O_4$. We also demonstrate the importance of additional degrees of freedom, namely covalency and phonons, which can alter magnetic ground states [211]. Our results also demonstrate the use of RIXS for probing spin-orbit entangled states in $3d$ transition metal compounds [57] and for probing hybridized states in mixed 3d-4d/5d compounds [212].

In addition to the predicted phenomena associated with spin-1 frustrated diamond lattice antiferromagnets, we propose that $NiRh_2O_4$ may host a variety of novel magneto-elastic and magneto-optical effects due to its rich spectrum of low-energy spin-orbital-lattice excitations [180, 204, 213, 214]. Future studies on $NiRh_2O_4$ could use pressure, magnetic fields or chemical substitution to explore the predicted phase diagram and observe quantum critical phenomena [25, 30, 174]. These studies would greatly benefit from the synthesis of single crystals or thin films. Should such crystals become available, another potentially fruitful route would be ultrafast optics to study the spin-orbital and crystal field excitations with the lattice out-of-equilibrium [215–217]. By resonantly exciting the lattice, it may be possible to stabilize an excitonic condensate of $J = 1$ moments [25].

3.5 Additional figures for RIXS calculations

In this section, we show the dependence of the calculated RIXS spectra on the model parameters, as well as calculated RIXS energy maps showing the incident energy dependence. Fig. 3.7 and Fig. 3.8 show the calculated spectra from the single-ion model for scenarios 1 and 2 respectively, demonstrating the dependence on the parameters F_{dd}, $10Dq$, Δt_2, Δe, and

λ. In each plot, the given parameter is varied with all other parameters fixed to the optimal values reported in the main text. Fig. 3.9 shows the dependence of the two-site model on the parameters Δ, t, Δt_2, Δe, λ, and Rh Δt_{2g}. Fig. 3.10 and 3.11 show the incident energy dependence of the RIXS spectra for the single-ion and two-site models respectively. The energy loss extends up to 4 eV to allow a direct comparison to the measured RIXS map shown in the main text.

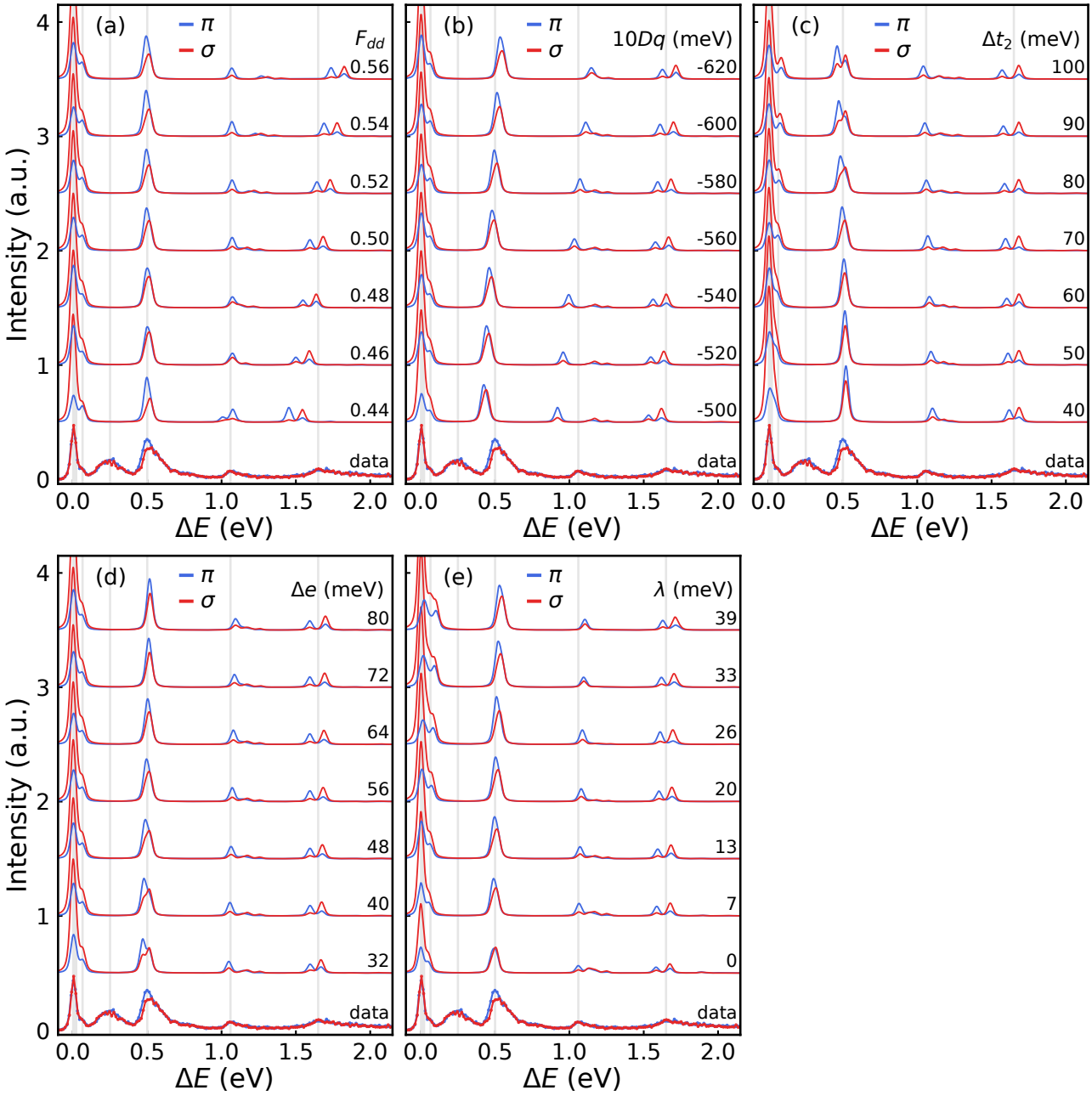

Figure 3.7: Calculated RIXS spectra for scenario 1, varying each parameter with all other parameters fixed to the optimal values. Vertical gray lines mark the energies of the measured peaks. (a) F_{dd} (b) $10Dq$ (c) Δt_2 (d) Δe (e) λ

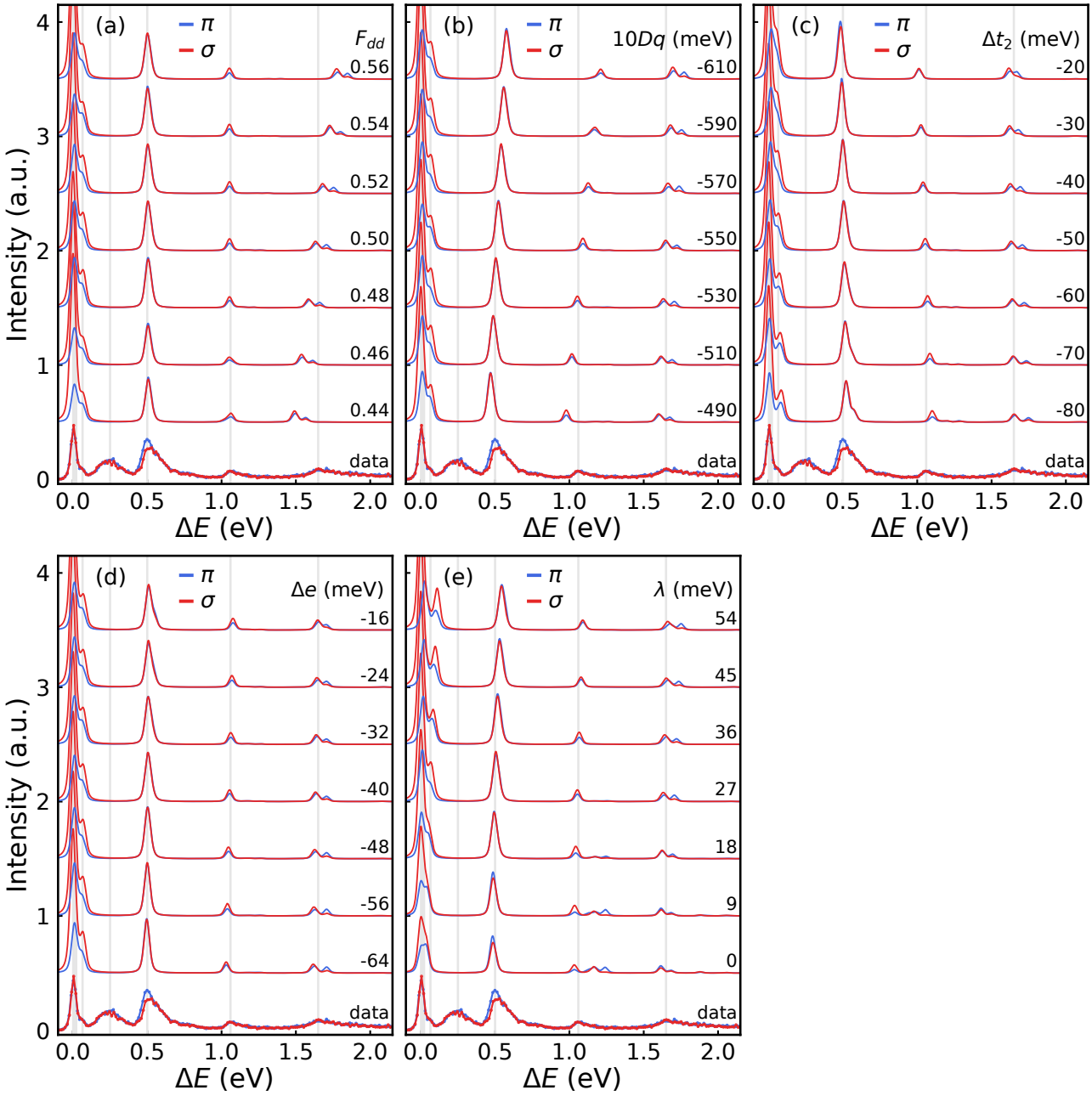

Figure 3.8: Calculated RIXS spectra for scenario 2, varying each parameter with all other parameters fixed to the optimal values. Vertical gray lines mark the energies of the measured peaks. (a) F_{dd} (b) 10Dq (c) Δt_2 (d) Δe (e) λ

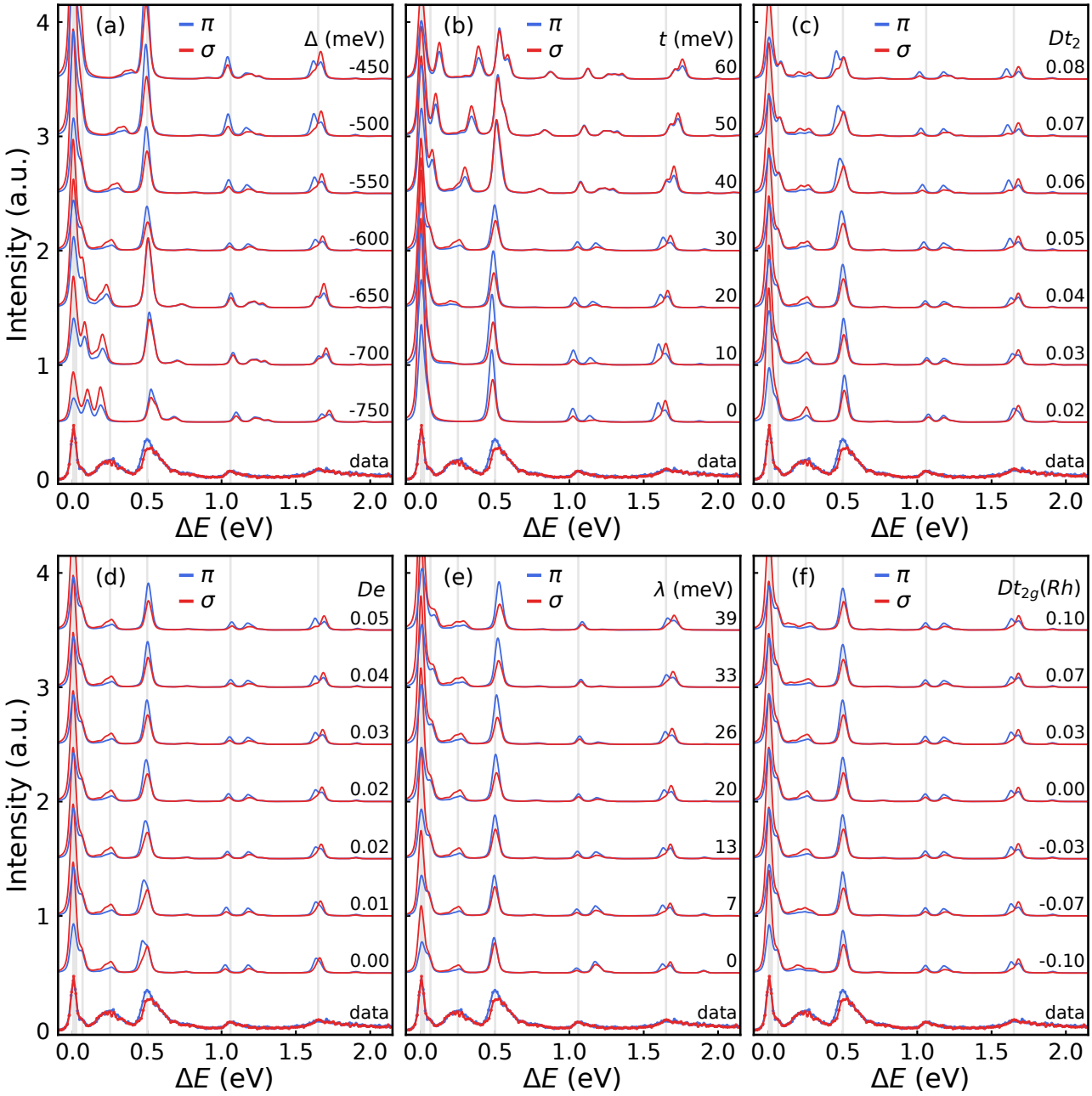

Figure 3.9: Calculated RIXS spectra for scenario 1 using the two-site model, varying each parameter with all other parameters fixed to optimal values. (a) Δ (b) t (c) Δt_2 (d) Δe (e) λ (f) Rh Δt_{2g}

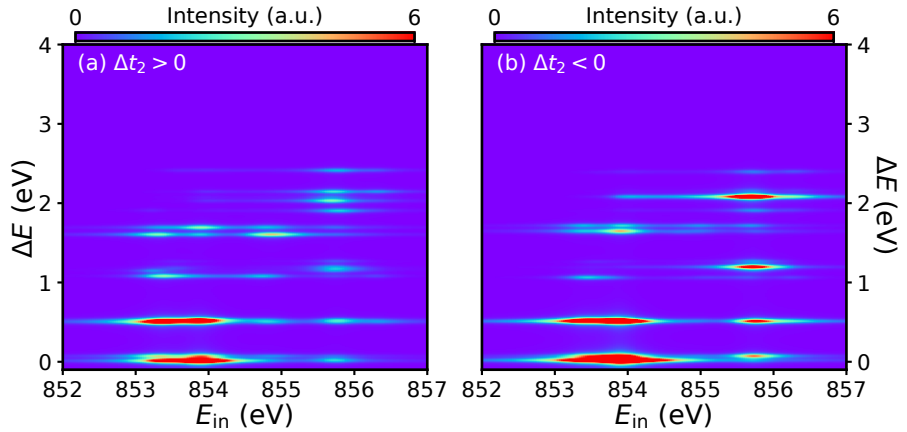

Figure 3.10: Calculated RIXS maps for π-polarization using the single-ion model. (a) scenario 1 (b) scenario 2

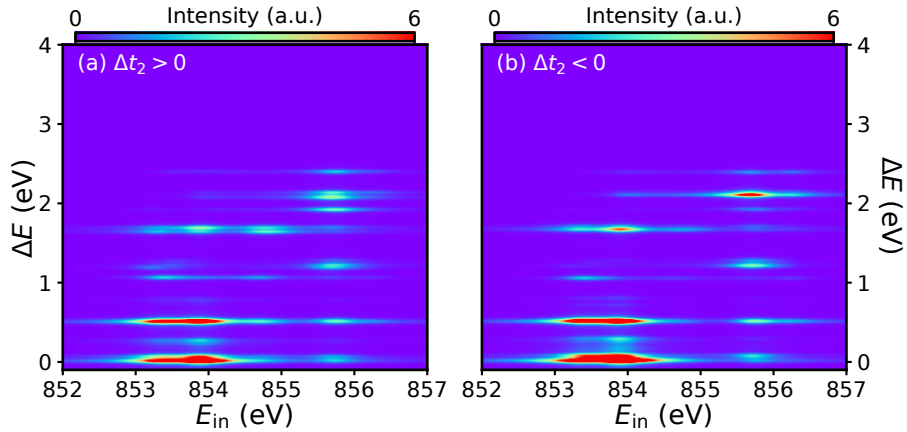

Figure 3.11: Calculated RIXS maps for π-polarization using the two-site model. (a) Scenario 1 (b) Scenario 2

CHAPTER 4

Double-Q spin chirality stripes in the anomalous Hall antiferromagnet $CoNb_3S_6$

$CoNb_3S_6$ is an intercalated transition metal dichalconide exhibiting a giant anomalous Hall effect (AHE) that cannot be explained by the previously determined collinear antiferromagnetic order. This chapter presents resonant elastic x-ray scattering (REXS) measurements that reexamine the magnetic structure $CoNb_3S_6$. Utilizing the high momentum resolution of soft x-ray REXS and the polarization dependence of the magnetic scattering, I uncovered a $2Q$ magnetic structure that forms a striped pattern in the scalar spin chirality. These results may provide an explanation of the AHE and enable the realization of other novel phenomena in $CoNb_3S_6$. This chapter is adapted from work for an upcoming publication, currently available as a preprint [218].

4.1 Introduction

Materials with complex magnetic phases beyond collinear ferro- and antiferromagnetism exhibit a diverse range of phenomena that are fundamentally rich and promising for many potential applications as next-generation electronic and spintronic devices. These phases include non-coplanar, chiral, and topological spin textures [219, 220], altermagnetism [221, 222],

multiferroics [223], and multipolar magnetism [224]. A commonality of all of these phases is that the magnetic symmetries allow for the coupling between charge, magnetism, and the lattice from which effective composite degrees of freedom emerge and give rise to novel macroscopic responses.

Such complex magnetic phases are stabilized in transition metal dichalcogenides (TMDs) intercalated with $3d$ transition metal ions through an interplay between localized spins on the $3d$ sites and itinerant electrons in the host layers [81, 84]. Diverse phenomena are possible depending on the host compound, intercalation species, and intercalation ratio. $CoNb_3S_6$ is of particular interest because it exhibits a giant anomalous Hall effect (AHE) with a nearly vanishing uniform magnetization, implicating a non-trivial magnetic structure [88, 89, 225]. A series of neutron diffraction measurements have found the symmetry-related magnetic propagation vectors $(\frac{1}{2}00)$, $(0\frac{1}{2}0)$, and $(\frac{1}{2}\overline{\frac{1}{2}}0)$, but disagree on the orientation of the moments and the presence of single-Q domains or multi-Q order [89, 95, 112, 225–227]. Elucidating the precise details of the magnetic structure is an essential step towards understanding the origin of the giant AHE in this antiferromagnet, and potentially tuning the properties to realize new functionalities.

In this chapter, we reexamine the magnetic structure of $CoNb_3S_6$ using Co L_3 edge resonant elastic x-ray scattering (REXS). The exceptional momentum resolution of our measurements reveal an exotic double-Q ($2Q$) magnetic order with a non-collinear commensurate $\boldsymbol{Q}_0 = (\frac{1}{2}00)$ component and incommensurate $\boldsymbol{Q}_0 \pm \boldsymbol{q}$ helical modulation. The helical modulation varies between samples with identical bulk characterization, and even between Q-domains of a single sample, implicating an underlying magnetic frustration that is relieved through minute lattice strain or correlated defects. In all cases the $2Q$ magnetic order gives rise to a staggered scalar spin chirality ordering with a modulated stripe or checkerboard pattern. Such a staggered spin chirality provides strong evidence for magnetic frustration generated by biquadratic magnetic interactions [27, 228, 229] and opens the possibility of nonlinear or nonreciprocal transport phenomena [230] in a class of frustrated magnets.

4.2 Experiment

Single crystals were grown using chemical vapor transport [88] with the nominal stoichiometry Co:Nb:S=1:3:6. Six different samples from the same growth were measured. All samples undergo magnetic transitions at 28.6 K, and exhibit sharp (100) Bragg peaks, indicating a well-ordered triangular lattice of intercalated Co ions. REXS experiments were performed at the I10 beamline at Diamond Light Source using the RASOR endstation [231] with the experimental geometry shown in Fig. 4.3(b). Samples were mounted in the $(HK0)$ scattering plane to access $(\frac{1}{2}00)$ and $(0\frac{1}{2}0)$ magnetic wavevectors at $2\theta = 106.2^{\circ}$ at the Co L_3 edge (778.5 eV). In this geometry the x-ray beam scatters from a natural facet on the crystal side probing an effective area of 20×200 μm, and with a penetration depth of 0.3 μm. Thus, our measurements probe a macroscopic sample volume containing many basal plane layers. Full reciprocal space maps were collected for four different samples using an area detector. Full linear polarization analysis (FLPA) was carried out on a fifth sample using a point detector and multilayer polarization analyzer optimized for the Co L_3 edge [128]. Measurements were performed for zero-field-cooling (ZFC) and field-cooling (FC) under the application of a 0.1 T permanent magnet along the c-axis.

Heat capacity, magnetic susceptibility, and electrical transport measurements were carried out using a Quantum Design Physical Property Measurement System (PPMS). Susceptibility was measured using the vibrating sample mount (VSM) with the magnetic field along the sample c-axis. Electrical transport was measured with the van der Paux method using a 2 mA excitation current. 50 μm Au wires were attached the samples using silver paint.

Images of the single crystals used for our measurement are shown in figure 4.1. The samples are naturally mirror faceted; however, we note the roughness of the scattering surface of S4 seen in 4.1(b) and (c), which will be discussed below. Samples were pre-aligned on copper bars and subsequently mounted on the copper sample holder using GE varnish. The temperature sensor was located on the coldfinger, at the base of the sample holder closest to S4. To fit the four samples on the sample holder, they were mounted in different geometries, with differing

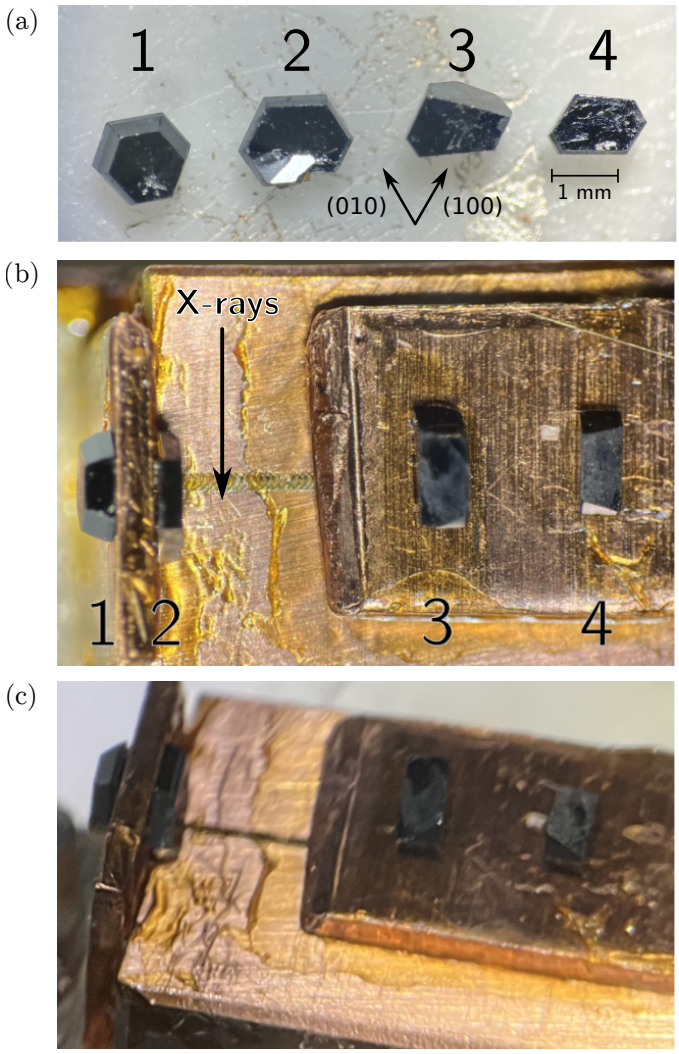

Figure 4.1: (a) Microscope image of samples 1-4 (S1-S4). (b) Image of samples 1-4 mounted for the RASOR endstation Diamond I10, showing the beam direction at $\theta = 0°$. (c) Same as (b) from a different angle.

areas in contact with the holder. Thus, each sample experiences a different cooling efficiency.

4.3 Results

4.3.1 Sample characterization

Fig. 4.2(a) shows the heat capacity of S1-S4. All samples display a clear second-order transition at $T_N = 28.6$ K. The entropy loss at the transition is slightly greater for S3 and S4, indicating possible intrinsic differences between samples. Fig. 4.2(b) shows the magnetic

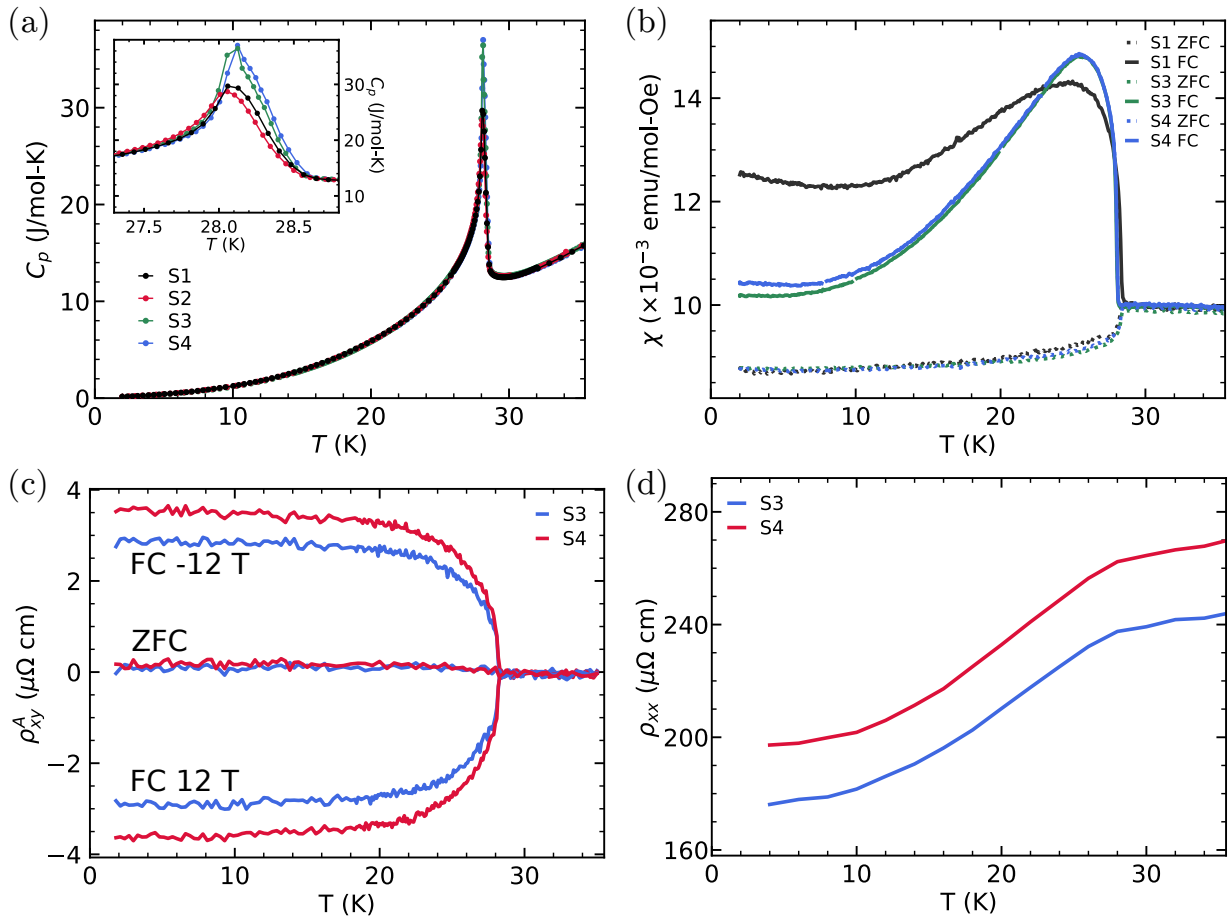

Figure 4.2: (a) Heat capacity vs. temperature for samples 1-4. (b) Magnetic susceptibility vs. temperature measured with a 0.1 T field with both zero-field-cooling and field-cooling for samples 1,3, and 4. (c) Anomalous Hall resistivity ρ_{xy} vs. T for samples 3 and 4. (d) Longitudinal resistivity ρ_{xx} vs. T for samples 3 and 4.

susceptibility vs. temperature for S1, S3, and S4. S2 was too small to produce a sufficient signal. A constant background χ_0 was subtracted from each sample, with $\chi_0 = -2$, 13, and 2.3 $\times 10^{-3}$ emu/mol-Oe for S1, S3, and S4 respectively. All samples show a transition at $T_N = 28.6$ K with a large splitting between field (FC) and zero field cooling (ZFC), consistent with previous reports [88, 91, 226, 227, 232]. Fig. 4.2(c) shows the anomalous Hall conductivity $\sigma^A_{xy} = \rho^A_{xy}/[\rho^2_{xx} + (\rho^A_{xy})^2]$ vs. temperature for S3 and S4, measured for zero-field cooling and ± 12 T field-cooling. Fig. 4.2(d) shows the longitudinal resistivity for S3 and S4.

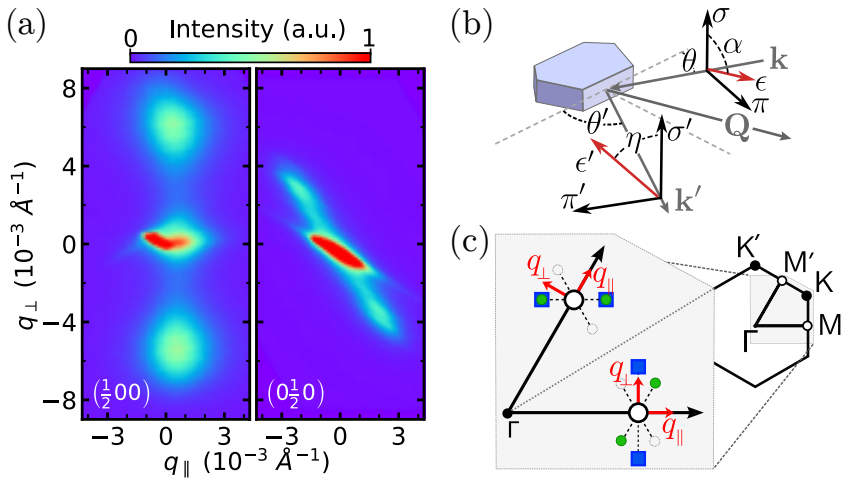

Figure 4.3: (a) Magnetic REXS intensity in S3 at 16 K. (b) Experimental geometry, incident (outgoing) polarization channels σ (σ') and π (π') correspond to α (η) of 0° and 90° respectively. (c) Summary of observed magnetic peaks in the triangular lattice Brillouin zone. White circles are $\boldsymbol{Q}_0 = (\frac{1}{2}00)$ and $(0\frac{1}{2}0)$, green circles show the magnetic reflections observed in S1, S2, S4, S5 and blue squares show those found in S3 as in (a). Dashed lines with empty markers show positions of symmetry allowed peaks that were not observed.

4.3.2 Reciprocal space map

Representative reciprocal space maps of the magnetic scattering are shown in Fig. 4.3(a). Primary magnetic reflections at $\boldsymbol{Q}_0 = (\frac{1}{2}00)$ and $(0\frac{1}{2}0)$ were observed in all samples, consistent with previous reports [89, 112, 225–227]. Our fine resolution measurements also revealed satellite magnetic reflections at $\boldsymbol{Q}_0 \pm \boldsymbol{q}$ [Fig. 4.3]. These satellites represent a long-wavelength incommensurate modulation of the magnetism that was not previously observed because of the relatively coarse momentum resolution used in the reported neutron experiments [89, 112, 225–227].

Since magnetic order in the intercalated TMDs is known to exhibit subtle sample dependence [103, 233], we have measured the magnetic reflections from five well characterized samples (S1-S5) to provide a comprehensive picture of the magnetism. We observed two different satellite wavevectors across these samples as summarized in Fig. 4.3(b). In S1, S2, S4 and S5, satellites appear at $(\frac{1}{2}, \pm\delta, 0)$ and $(\pm\delta, \frac{1}{2}, 0)$. In S3, one set of satellites appears at $(\pm\delta, \frac{1}{2}, 0)$ while the other set appears at $(\frac{1}{2} \mp \delta, \pm 2\delta, 0)$, i.e. purely transverse to the main peak (see 4.12). We find $\delta = 3.0(3) \times 10^{-3}$ r.l.u. $= 3.7(3) \times 10^{-3}$ Å^{-1} at $T = 14$ K, corresponding to a modulation

with 170(15) nm wavelength, or 97(10) nm for S3 ($\frac{1}{2}00$). These observations were consistent across multiple zero-field-cooled (ZFC) and field-cooled (FC) cycles on all samples. No spatial variation was observable when scanning the beam across a given sample surface.

The different satellite wavevectors appearing between ($\frac{1}{2}00$) and ($0\frac{1}{2}0$) reflections in S3 [Fig. 4.3(a)] break both C_6 rotational and mirror symmetry about (110) of the $P6_322$ space group, while the satellite reflections observed in S1, S2, S4, and S5 possess mirror symmetry but break the C_6 rotational symmetry. Such symmetry reductions indicate that ($\frac{1}{2}00$) and ($0\frac{1}{2}0$) belong to distinct Q-domains as will be further confirmed by the FLPA presented below. The observed sample and domain dependence indicates that the particular long wavelength magnetic modulation in each domain of a given sample is selected by a symmetry-breaking field such as small lattice strains that are quenched in during crystal synthesis, or local correlated defects and stoichiometric variations [90, 91, 233, 234].

Fig. 4.4 shows the temperature-dependent integrated intensities at $\boldsymbol{Q}_0 = (\frac{1}{2}00)$ and $\boldsymbol{Q}_0 + (\overline{\delta}\, 2\delta\, 0)$ from S3. The magnetic reflections have a critical temperature of $T_N = 28.5$ K corresponding the the onset of the Hall response [Fig. 4.4 (b)]. We also observed a smooth decrease in the magnitude of the satellite wave vector towards $\boldsymbol{Q}_0$ as temperature is decreased [Fig. 4.4], characteristic of a helical magnetic modulation [17]. Energy scans across the 778.5 eV resonance are typical for Co^{2+} [131, 235] and confirm the magnetic origin of all observed peaks [inset of Fig. 4.4, and Fig. 4.5 (b)].

4.3.3 Circular dichroism

Further details of the magnetic structure are revealed through polarization-dependent REXS. All magnetic reflections exhibit finite circular dichroism (CD) (see section 2.4.3), as shown in Fig. 4.5, arising at $\boldsymbol{Q}_0$ from non-collinearity of the commensurate component, and at $\boldsymbol{Q}_0 \pm \boldsymbol{q}$ from a helical modulation. Variation of the CD along the transverse directions suggests the presence of opposite chirality domains on a length scale comparable to the 200 μm beam size. We also find that the CD varies between subsequent ZFC and 0.1 T FC measurements,

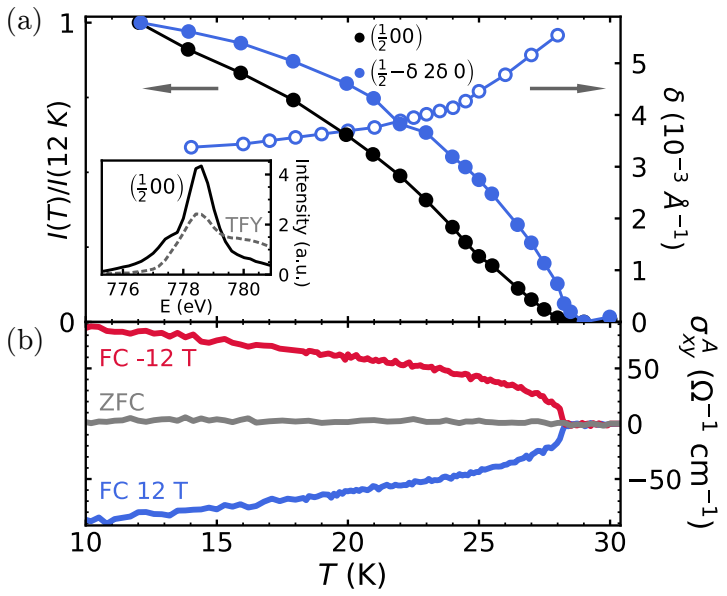

Figure 4.4: (a) Normalized temperature dependence of main and satellite peak, and δ in satellite wavevector $(\delta, -2\delta, 0)$ for S3 measured on the point detector with π polarized x-rays. The inset shows a fixed-Q energy scan of the main peak, with the dashed line showing total fluorescence yield (TFY). (b) Anomalous Hall conductivity σ^A_{xy} of S3 determined from the Hall and longitudinal resistivities measured in zero field after $\pm$12 T field cooling.

especially for the $(\frac{1}{2}00)$ peaks, consistent with a redistribution of these chiral domains under field cooling, as recently observed by optical circular dichroism [232].

A necessary condition for finite CD is a finite structure factor for both σ-π' and π-π. This requires both an in- and out-of-plane spin component, which indicates that the modulation is helical and confirms the FLPA results that the commensurate component must be noncollinear (see section 4.3.4). Fig. 4.6 shows the calculated CD as a function of canting angle ν at $\mu = 109°$.

The magnetic structure determined from FLPA is consistent with the CD-REXS results. The condition for CD at $\boldsymbol{Q}_0$ is finite intensity in both σ-π and π-π, which arises from the noncollinear moments with both in- and out-of-plane components. The CD at $\boldsymbol{Q}_0 \pm \boldsymbol{q}$ requires a helical structure or a more complex chiral modulation. We note that there is a contribution to the CD from the structural peaks on second harmonic, which is forbidden for Thomson scattering. This is due to the imperfect circular polarization of the second harmonic, giving unequal combinations of σ and π polarization between $C+$ and $C-$ [128].

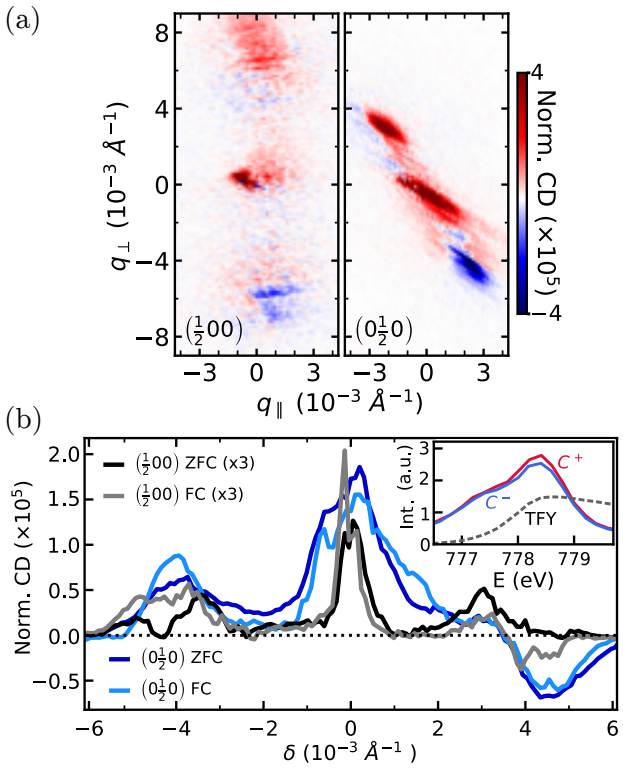

Figure 4.5: (a) Field-cooled (FC) CD. (b) FC vs ZFC cuts along $(\delta, -2\delta, 0)$ at $(\frac{1}{2}00)$ and along $(\delta 00)$ at $(0\frac{1}{2}0)$, averaged over 0.0025 Å^{-1} along the transverse direction. The normalized CD is defined as $(C^+ - C^-)/\int(C^+ + C^-)$. Inset shows energy scans at fixed $\boldsymbol{Q} = (\frac{1}{2} - \delta, 2\delta, 0)$.

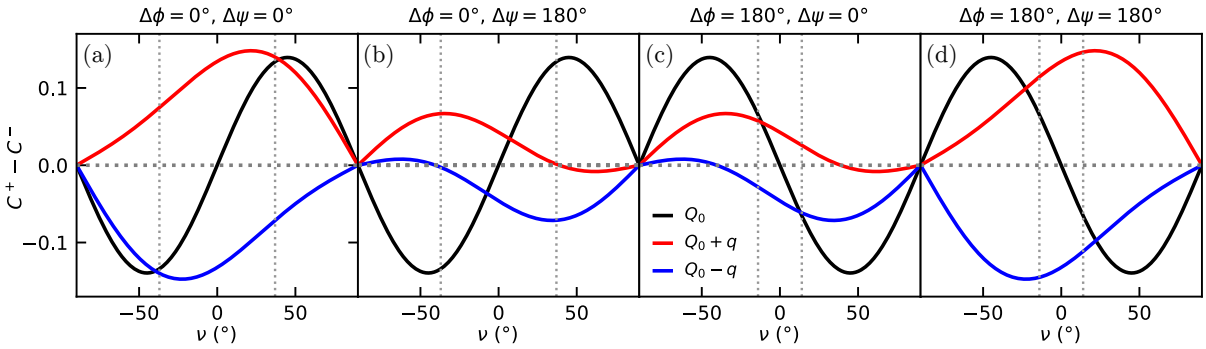

Figure 4.6: Dependence of the CD on the canting angle ν at $\boldsymbol{Q}_0 = (\frac{1}{2}00)$ and $\boldsymbol{Q}_0 \pm (0\delta 0)$ for each of the four phase combinations with $\mu = 109°$. The vertical dashed lines show the value of ν determined from FLPA for each choice of phases.

4.3.4 Full linear polarization analysis (FLPA)

Orientations of the magnetic Fourier components $\boldsymbol{m}_{\boldsymbol{Q}_0,n}$ were determined from full linear polarization analysis (FLPA) (see section 2.4.1)[128–133] by measuring the intensity at $\boldsymbol{Q}_0$ as a function of incident polarization angle α and analyzer angle η [Fig. 4.3(b)]. As expected for

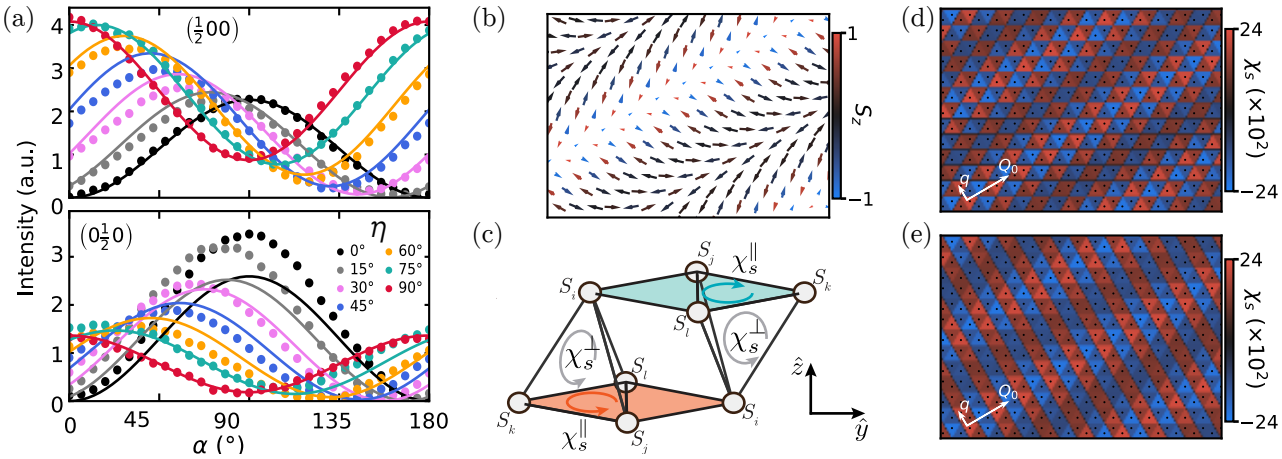

Figure 4.7: (a) FLPA data and model at $(\frac{1}{2}00)$ and $(0\frac{1}{2}0)$. (b) Real space depiction of magnetic structure on a single sublattice for $\boldsymbol{Q}_0=(\frac{1}{2}00)$ and $\boldsymbol{q}=(-\delta,2\delta,0)$ with $\delta=0.053$ r.l.u., $\phi=45°$, $\mu=110°$, $\nu=30°$. (c) Co^{2+} triangular plaquettes used to define the intra- and inter-sublattice scalar spin chirality contributions $\chi_s^{\parallel}$ and $\chi_s^{\perp}$. (d) Scalar spin chirality contribution from the inter-sublattice plaquettes $\chi_s^{\perp}$ for the spin configuration in (c) with $\Delta\phi=0$, $\Delta\psi=180°$. The color of each triangle represents χ_s projected onto the z component of the plaquette and summed over the three plaquettes sharing a vertex plotted as black dots. (e) Same as (d) but with $\Delta\phi=180°$, $\Delta\psi=180°$.

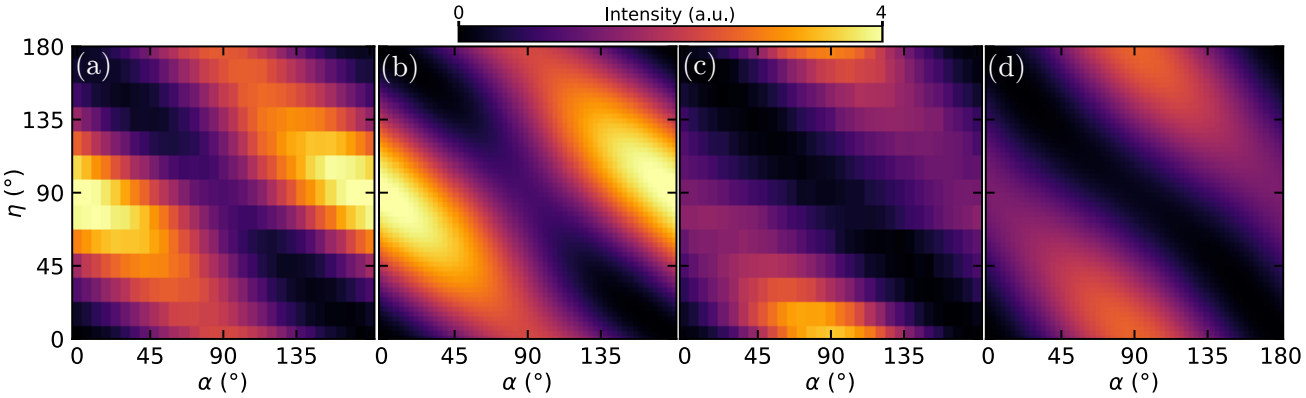

Figure 4.8: Additional data from FLPA measurements. (a) FLPA data at $(\frac{1}{2}00)$. (b) FLPA calculation at $(\frac{1}{2}00)$ using the parameters from Table 4.1. (c) FLPA data at $(0\frac{1}{2}0)$. (d) FLPA calculation at $(0\frac{1}{2}0)$ using the parameters from Table 4.1.

the $E1$-$E1$ contribution to magnetic scattering, the σ-σ' intensity is always zero. The σ-π' and π-σ' intensity originates from the component of the moment in the crystallographic a-b (basal) plane and the π-π' intensity arises from the out-of-plane component. Fig. 4.8 shows the complete FLPA dataset as a colormap along with the model calculations. We note that the analyzer reduces the intensity by two orders of magnitude, so the signal at the satellites was too weak to carry out FLPA.

We considered the following $2Q$ magnetic structure [27] with propagation vectors $\boldsymbol{Q}_0$ and $\boldsymbol{Q}_0 \pm \boldsymbol{q}$

$$\begin{aligned}\boldsymbol{m}_n(\boldsymbol{r}_j) = &\cos(\boldsymbol{q}\cdot\boldsymbol{r}_j + \psi_n)\cos(\boldsymbol{Q}_0\cdot\boldsymbol{r}_j + \phi_n)\hat{\boldsymbol{u}}_n \\ &+ \sin(\boldsymbol{Q}_0\cdot\boldsymbol{r}_j + \phi_n)\hat{\boldsymbol{v}}_n, \\ &+ \cos(\boldsymbol{q}\cdot\boldsymbol{r}_j + \psi_n + \tfrac{\pi}{2}\chi)\cos(\boldsymbol{Q}_0\cdot\boldsymbol{r}_j + \phi_n)\hat{\boldsymbol{w}}_n.\end{aligned} \tag{4.1}$$

Where $n=1,2$ labels the sublattices at 2 Co sites in the unit cell, $\chi=\pm1$ is the helix chirality, ϕ_n and ψ_n are the phases on sublattice n for $\boldsymbol{Q}_0$ and $\boldsymbol{Q}_0\pm\boldsymbol{q}$ respectively, and $\hat{\boldsymbol{u}}_n$, $\hat{\boldsymbol{v}}_n$, and $\hat{\boldsymbol{w}}_n$ are unit vectors, assumed to be orthogonal to maintain a constant moment size. The Fourier components of this structure are

$$\begin{aligned}\boldsymbol{m}_{\boldsymbol{Q}_0,n} &= \boldsymbol{m}^*_{-\boldsymbol{Q}_0,n} = -\tfrac{i}{2}e^{i\phi_n}\hat{\boldsymbol{v}}_n \\ \boldsymbol{m}_{\boldsymbol{Q}_0\pm\boldsymbol{q},n} &= \boldsymbol{m}^*_{-\boldsymbol{Q}_0\mp\boldsymbol{q},n} = \tfrac{1}{4}e^{i\phi_n\pm i\psi_n}(\hat{\boldsymbol{u}}_n \pm i\hat{\boldsymbol{w}}_n).\end{aligned} \tag{4.2}$$

We parameterize the magnetic structure with the angle μ_n between $\hat{\boldsymbol{u}}_n$ and the lattice vector $\boldsymbol{a}_1 = a\hat{\boldsymbol{x}}$ in the a-b plane, out-of-plane canting angle ν_n of $\boldsymbol{v}_n$, and phases ϕ_n, ψ_n. We fit the commensurate component $\boldsymbol{m}_{\boldsymbol{Q}_0,n}$ to the measured FLPA shown in Fig. 4.7(a). $\nu_1=\nu_2$ is ruled out as this always leads to zero π-π' intensity, inconsistent with the observed FLPA and CD. For our analysis, we have fixed $\mu_1=\mu_2=\mu$ and $\nu_1=-\nu_2=\nu$. We find no improvements by relaxing these constraints.

While ϕ_n and ψ_n cannot be uniquely determined from our measurements, symmetry constrains $\Delta\phi=\phi_2-\phi_1$ to either 0° or 180° [103]. We separately consider $\Delta\phi=0°$ or $\Delta\phi=180°$ and find $\mu=109(1)°$ at $(\frac{1}{2}00)$ and $\mu=12(1)°$ at $(0\frac{1}{2}0)$ for each case, or nearly $\pm80°$ from $\boldsymbol{Q}_0$. The in-plane angle relative to $\boldsymbol{Q}_0$ is opposite in each domain, with the same broken symmetry as the modulation wavevectors in S1 and S2. For $\Delta\phi = 0°$ we find $\nu = 37(2)°$ at $(\frac{1}{2}00)$ and $\nu=24(2)°$ at $(0\frac{1}{2}0)$. While for $\Delta\phi=180°$, we find $\nu=14(2)°$ at $(\frac{1}{2}00)$ and $\nu=9(2)°$ at $(0\frac{1}{2}0)$. Both cases adequately describe the data at $(\frac{1}{2}00)$ while neither fully matches the intensity at π-σ for $(0\frac{1}{2}0)$. We attribute this discrepancy to a slight analyzer misalignment. Furthermore, we cannot rule out contributions from domains with different moment orientations. The results

Table 4.1: Parameters obtained from FLPA describing the commensurate Fourier component, for the two possible choices of $\Delta\phi$.

	$\Delta\phi = 0°$		$\Delta\phi = 180°$	
Peak	μ	ν	μ	ν
$(\frac{1}{2}00)$	109(1)°	37(2)°	109(1)°	14(2)°
$(0\frac{1}{2}0)$	12(1)°	24(2)°	12(1)°	9(2)°

of our fit are summarized in Table 4.1 and Fig. 4.7(b) shows a real-space representation of the non-coplanar magnetic structure found in S3.

4.3.5 Description of the Magnetic structure

Our data reveal that the magnetic structure of $CoNb_3S_6$ is comprised of two propagation vectors $\boldsymbol{Q}_0$ and $\boldsymbol{q}$. There are two possible magnetic structures that may be consistent with this observation. In the previous section, we considered the case with magnetic propagation vectors $\pm\boldsymbol{Q}_0$ and $\pm(\boldsymbol{Q}_0 \pm \boldsymbol{q})$. The second possible scenario is a structure with propagation vectors $\boldsymbol{Q}_0$ and $\boldsymbol{q}$, giving rise to higher harmonic peaks at $\boldsymbol{Q}_0 \pm \boldsymbol{q}$. We cannot directly rule out low-angle peaks at $\boldsymbol{q}$ that were inaccessible in our scattering geometry. However, we did not observe any $\boldsymbol{Q}_0 \pm n\boldsymbol{q}$ for $n > 1$ higher harmonics, which would be expected in this scenario. Furthermore, neutron experiments have not reported any evidence for $\boldsymbol{q} \approx 0$ magnetic scattering [225, 226]. We thus rule out the second scenario and consider the structure with magnetic propagation vectors $\pm\boldsymbol{Q}_0$ and $\pm(\boldsymbol{Q}_0 \pm \boldsymbol{q})$ given by eq. 4.1. The magnetic moment on site j can be expressed as

$$\boldsymbol{m}(\boldsymbol{r}_j) = \sum_{\boldsymbol{Q}} \boldsymbol{m}_{\boldsymbol{Q}} e^{i\boldsymbol{Q}\boldsymbol{r}_j} \tag{4.3}$$

where $\boldsymbol{m}_{\boldsymbol{Q}}$ are the Fourier components of the magnetic moments, which, for this structure are given by eq. 4.2.

The precise value of ϕ_n affects the real-space spin structure, ruling out $\phi_n = \frac{\pi}{2}n$ ($n = 0, 1, 2, \ldots$) for which either the commensurate or incommensurate components of the magnetic

structure vanish. The precise value of ψ_n does not affect the real-space structure, since $\boldsymbol{q}$ is incommensurate with the lattice. However, the relative phases $\Delta\phi = \phi_2 - \phi_1$ and $\Delta\psi = \psi_2 - \psi_1$ do affect the real-space structure. The unit vectors defining the moment orientations are

$$\begin{aligned} \hat{\boldsymbol{u}}_n &= \hat{\boldsymbol{x}}\cos\mu + \hat{\boldsymbol{y}}\sin\mu \\ \hat{\boldsymbol{v}}_n &= -\hat{\boldsymbol{x}}\sin\mu\cos\nu_n + \hat{\boldsymbol{y}}\cos\mu\cos\nu_n + \hat{\boldsymbol{z}}\sin\nu_n \\ \hat{\boldsymbol{w}}_n &= \hat{\boldsymbol{x}}\sin\mu\sin\nu_n - \hat{\boldsymbol{y}}\sin\nu_n\cos\mu + \hat{\boldsymbol{z}}\cos\nu_n \end{aligned} \tag{4.4}$$

for $n = 1, 2$, where $\hat{\boldsymbol{x}}, \hat{\boldsymbol{y}}, \hat{\boldsymbol{z}}$ are Cartesian coordinates with $\hat{\boldsymbol{x}}$ along a and $\hat{\boldsymbol{y}}$ in the a-b plane of the crystallographic cell. μ defines the in-plane angle relative to the x-axis, ν_n defines the out-of-plane canting angle where we assume $\nu = \nu_1 = -\nu_2$. The definitions of coordinate frame $\hat{\boldsymbol{u}}, \hat{\boldsymbol{v}}, \hat{\boldsymbol{w}}$, and angles μ and ν are illustrated in Fig. 4.9.

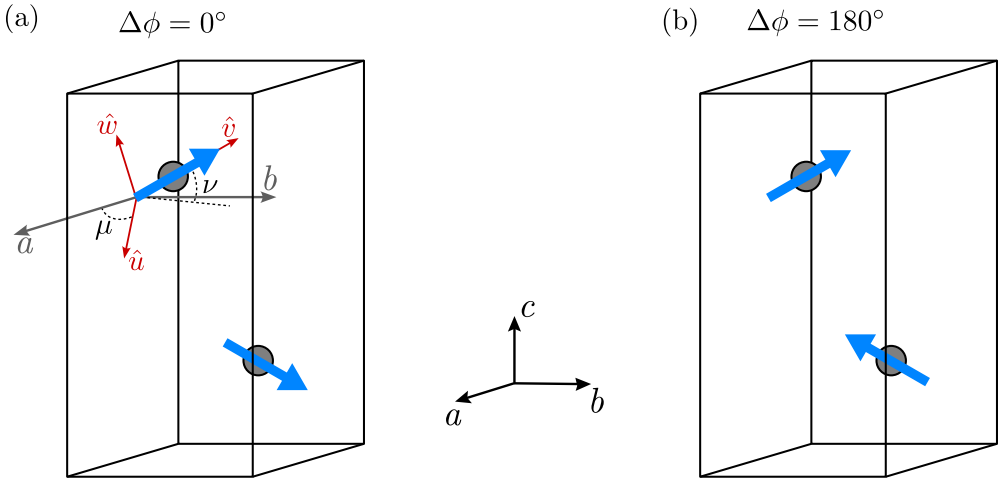

Figure 4.9: Fourier component $\boldsymbol{m}_{\boldsymbol{Q}_0}$ of the commensurate part of the magnetic structure, showing the in-plane angle μ and canting angle ν for the phase (a) $\Delta\phi = 0°$. (b) $\Delta\phi = 180°$.

4.3.6 Scalar spin chirality

The scalar spin chirality on a triangular plaquette of sites $\boldsymbol{r}_i$, $\boldsymbol{r}_j$, and $\boldsymbol{r}_k$ with moments $\boldsymbol{m}_i$, $\boldsymbol{m}_j$, and $\boldsymbol{m}_k$ is defined as $\chi_s = \boldsymbol{m}_i \cdot (\boldsymbol{m}_j \times \boldsymbol{m}_k)$. The effective magnetic field felt by a conduction electron passing over this plaquette is $\boldsymbol{b} \propto t\chi_s\hat{\boldsymbol{n}}$, where $\hat{\boldsymbol{n}}$ is the plaquette normal vector and $t = t_{ij}t_{jk}t_{ki}$ is the hopping integral around the loop $i \to j \to k \to i$. The lattice of magnetic

Co sites in $CoNb_3S_6$ consists of two triangular sublattices. Thus, there are intra-sublattice plaquettes formed by three sites in the same basal plane, as well as inter-sublattice plaquettes formed by two sites from a given sublattice and one site from the opposite one. We denote the intra- and inter-sublattices contributions as $\chi_s^{\parallel}$ and $\chi_s^{\perp}$ respectively. For intra-sublattice plaquettes,

$$\chi_s^{\parallel}(\boldsymbol{r}) = \sin(\tfrac{\pi\chi}{2}) \sin\Phi_{\boldsymbol{r}} \cos^2\Phi_{\boldsymbol{r}} [\sin(\alpha+\beta) - \sin\alpha - \sin\beta], \tag{4.5}$$

where $\boldsymbol{q} = (\alpha\beta 0)/2\pi$ is the modulation wavevector, $\Phi_{\boldsymbol{r}} = \boldsymbol{Q}_0 \cdot \boldsymbol{r} + \phi_n$, and χ is the helix chirality. This vanishes everywhere if either $\alpha = 0$ or $\beta = 0$ and is independent of ψ, μ, and ν. We can see that $\chi_s^{\parallel}$ has a fixed magnitude at all positions but oscillates in sign along the direction of $\boldsymbol{Q}_0$. The sum of $\chi_s^{\parallel}$ for the two sublattices is shown in Fig. 4.10. Since the sites on each sublattice are offset along the direction of $\boldsymbol{Q}_0$, there is a phase difference in the contribution from each sublattice. This causes some interference, seen as the black regions of vanishing χ_s.

$\chi_s^{\perp}$ does not vanish for any particular direction of $\boldsymbol{q}$, but vanishes as $q \to 0$. Similarly to $\chi_s^{\parallel}$, $\chi_s^{\perp}$ oscillates in sign along $\boldsymbol{Q}_0$, but also oscillates along $\boldsymbol{q}$. The amplitude of these oscillations depends on ν, with no oscillations for $\nu = 0$. The precise pattern of $\chi_s^{\perp}$ depends on the choice of phase differences $\Delta\phi$ and $\Delta\psi$, plotted in Fig. 4.11. Here we show the value of $\chi_s^{\perp}$ projected onto the z-component of the plaquette normal and summed over each group of three edge-sharing inter-sublattice plaquettes.

The pattern along $\boldsymbol{Q}_0$ depends on the sum $\Delta\phi+\Delta\psi$ and the pattern along $\boldsymbol{q}$ depends only on $\Delta\psi$. For $\Delta\phi+\Delta\psi=0°$ or 360°, $\chi_s^{\perp}$ forms a stripe pattern. For $\Delta\phi+\Delta\psi=180°$ $\chi_s^{\perp}$ forms a checkerboard pattern. For $\Delta\psi=0°$, $\chi_s^{\perp}$ oscillates about zero along $\boldsymbol{q}$. For $\Delta\psi=180°$, χ_s oscillates in magnitude along $\boldsymbol{q}$ without passing through zero with an amplitude that increases with increasing ν.

Although the magnitude of $\chi_s^{\perp}$ is much greater than that of $\chi_s^{\parallel}$, the relative magnitude of the effective field $\boldsymbol{b}$ is more relevant. We have already projected $\chi_s^{\perp}$ onto the z-component of the plaquette normal vectors, so we only need to consider the relative hopping integrals

around each type of plaquette, $t_{\parallel} = t^3$ and $t_{\perp} = t'^2 t$, where t and t' are the in- and out-of-plane hopping integrals along a single bond. Since the ratio of bond lengths $a'/a \approx 1.2$ Å, we expect $t' < t$. Thus, the relative contribution of $\chi_s^{\perp}$ will be reduced by a factor of t'^2/t^2. However, the qualitative behavior of $\boldsymbol{b}$ remains unaffected.

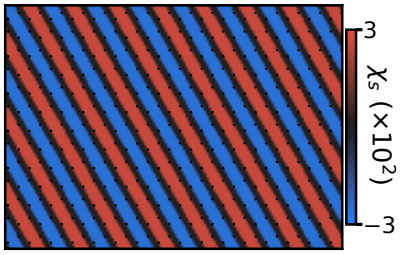

Figure 4.10: Scalar spin chirality $\chi_s^{\parallel}$ from the intra-sublattice plaquettes, summed over both sublattices for the structure $\boldsymbol{Q}_0 = (\frac{1}{2}00)$ and $\boldsymbol{q} = (-\delta, 2\delta, 0)$, $\delta = 0.053$ r.l.u., $\phi = 45°$.

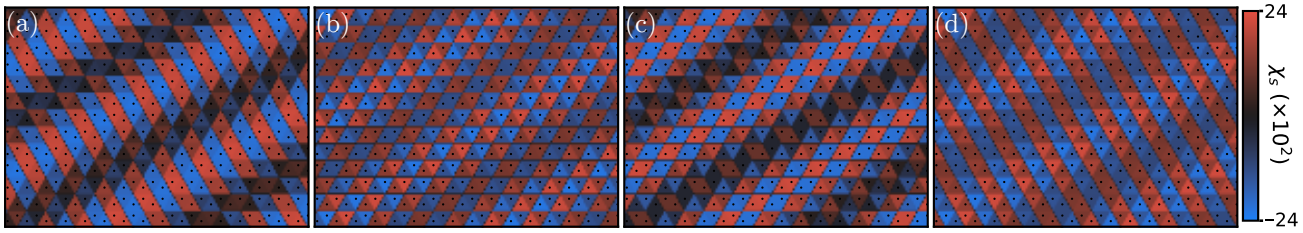

Figure 4.11: Scalar spin chirality $\chi_s^{\perp}$ from the inter-sublattice plaquettes projected on the z-component of the plaquette normal vectors for the structure with $\boldsymbol{Q}_0 = (\frac{1}{2}00)$ and $\boldsymbol{q} = (-\delta, 2\delta, 0)$, $\delta = 0.053$ r.l.u. (larger than the observed value of $\delta = 0.003$ r.l.u. to simplify visualization), $\phi = 45°$, $\mu = 110°$, $\nu = 30°$ (a) $\Delta\phi = 0°$, $\Delta\psi = 0°$. (b) $\Delta\phi = 0°$, $\Delta\psi = 180°$. (c) $\Delta\phi = 180°$, $\Delta\psi = 0°$. (d) $\Delta\phi = 180°$, $\Delta\psi = 180°$.

$\chi_s^{\parallel}$ forms stripes with propagation vector $\boldsymbol{Q}_0$ and no variation along $\boldsymbol{q}$. The stripes on each sublattice are $\pm 90°$ out of phase for $\Delta\phi = 0°$ or $180°$. $\chi_s^{\perp}$ depends on ν and forms complex structures that depend on the choice of the phase variables. We apply the constraint $\Delta\psi = 0°$ or $180°$ to consider four different combinations of phases that result in stripe or checkerboard like patterns of chirality. In all cases, the magnitudes of $\chi_s^{\parallel}$ and $\chi_s^{\perp}$ vanish as $q \to 0$. Thus, the incommensurate modulation is essential for providing a finite local scalar spin chirality in $CoNb_3S_6$.

Due to the opposite canting between sublattices, $\chi_s^{\perp}$ is much larger than $\chi_s^{\parallel}$ for the values of ν we have found. Although the relative magnitude of the intra- and inter-sublattice hopping

integrals are unknown, the effective field produced by $\chi_s^{\perp}$ will dominate for all feasible values and the qualitative behavior is unchanged by $\chi_s^{\parallel}$. In order to visualize χ_s, we project $\chi_s^{\perp}$ onto the z component of the plaquette normal vectors, shown in Fig. 4.7(d) and (e) for two different possibilities of the relative phases. In all four cases, the scalar chirality develops an intricate pattern, modulated along both $\boldsymbol{Q}_0$ and $\boldsymbol{q}$.

Such staggered chirality cannot directly account for the AHE. However, the staggered chirality in the presence of finite spin-orbit coupling may generate a net Berry curvature that can account for the AHE [236]. Furthermore, the magnetic structure we observed may generate a net chirality if the moment size is nonuniform, which can be described by relaxing the orthonormality constraint on the vectors $\hat{\boldsymbol{u}}$, $\hat{\boldsymbol{v}}$, and $\hat{\boldsymbol{w}}$. Even in the absence of a net scalar chirality, a finite local chirality should also give rise to nonlinear or nonreciprocal transport [230], which has been recently observed [237].

4.3.7 Calculation of the resonant magnetic x-ray scattering intensity

$CoNb_3S_6$ crystallizes in the chiral $P6_322$ space group (182) with lattice parameters $a = 5.75$ Å and $c = 11.89$ Å. In the fully ordered structure, the Co^{2+} ions exclusively occupy either the $2b$, $2c$, or $2d$ site [90]. Here we consider consider the $2c$ sites to be occupied, but this choice does not affect the results. We use the lattice vectors $\boldsymbol{a}_1 = (a, 0, 0)$, $\boldsymbol{a}_2 = \frac{a}{2}(-1, \sqrt{3}, 0)$, and $\boldsymbol{a}_3 = (0, 0, c)$, which give reciprocal lattice vectors $\boldsymbol{b}_1 = \frac{2\pi}{a}(1, \frac{1}{\sqrt{3}}, 0)$, $\boldsymbol{b}_2 = \frac{2\pi}{a}(0, \frac{2}{\sqrt{3}}, 0)$, and $\boldsymbol{b}_3 = \frac{2\pi}{c}(0, 0, 1)$. The REXS intensity is $I_{\boldsymbol{\epsilon}'\boldsymbol{\epsilon}}(\boldsymbol{Q}) \propto |S_{\boldsymbol{\epsilon}'\boldsymbol{\epsilon}}(\boldsymbol{Q})|^2$, as described in section 2.4. We observed no intensity in the σ-σ channel, so we let $F^{(0)} = 0$. We observed no second-order satellite reflections, so we let $F^{(2)} = 0$. We thus have

$$S_{\boldsymbol{\epsilon}'\boldsymbol{\epsilon}}(\boldsymbol{Q}) \propto (\boldsymbol{\epsilon}'^{*} \times \boldsymbol{\epsilon}) \cdot \boldsymbol{M}(\boldsymbol{Q}) \tag{4.6}$$

where $\boldsymbol{M}(\boldsymbol{Q})$ is the magnetic structure factor. For the main magnetic reflection at $\boldsymbol{Q}_0 = (\frac{1}{2}00)$,

$$\boldsymbol{M}(\boldsymbol{Q}_0) = -\tfrac{i}{2} e^{i(\frac{2}{3}\pi + \phi_1)} \hat{\boldsymbol{v}}_1 - \tfrac{i}{2} e^{i(\frac{1}{3}\pi + \phi_2)} \hat{\boldsymbol{v}}_2 \tag{4.7}$$

For the $\boldsymbol{q} = (0\delta 0)$ satellites,

$$\boldsymbol{M}(\boldsymbol{Q}_0 \pm \boldsymbol{q}) = \frac{1}{4}\left[ie^{i(\pm\frac{4\pi}{3}\delta+\phi_1)}\hat{\boldsymbol{u}}_1 \mp \chi e^{i(\pm\frac{4\pi}{3}\delta+\phi_1)}\hat{\boldsymbol{w}}_1 + ie^{i(\pm\frac{2\pi}{3}\delta+\phi_2)}\hat{\boldsymbol{u}}_2 \mp \chi e^{i(\pm\frac{2\pi}{3}\delta+\phi_2)}\hat{\boldsymbol{w}}_2\right] \quad (4.8)$$

For the $\boldsymbol{q} = (\delta, -2\delta, 0)$ satellites,

$$\boldsymbol{M}(\boldsymbol{Q}_0 \pm \boldsymbol{q}) = \frac{1}{4}\left[ie^{i(\phi_1\mp 2\pi\delta)}\hat{\boldsymbol{u}}_1 \mp \chi e^{i(\phi_1\mp 2\pi\delta)}\hat{\boldsymbol{w}}_1 + ie^{i\phi_2}\hat{\boldsymbol{u}}_2 \mp \chi e^{i\phi_2}\hat{\boldsymbol{w}}_2\right] \quad (4.9)$$

4.3.8 Reciprocal space maps for samples 1-4

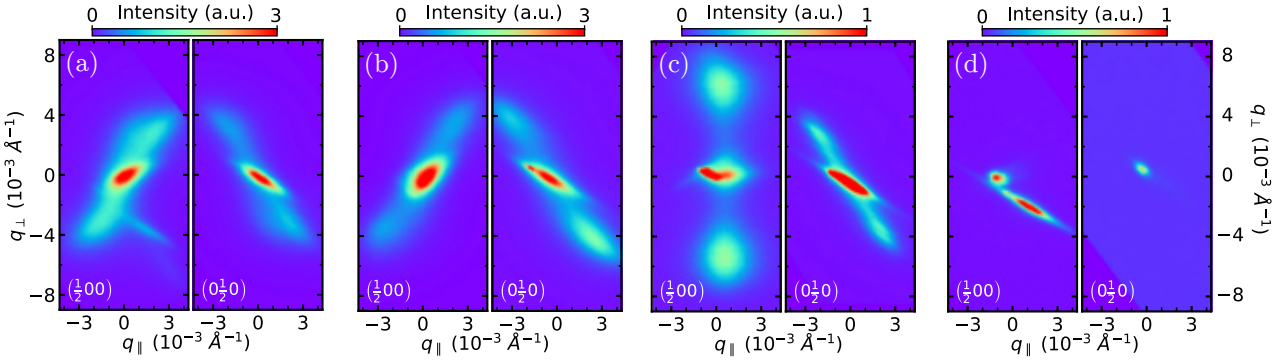

Figure 4.12: Reciprocal space maps of the magnetic scattering at $(\frac{1}{2}00)$ and $(0\frac{1}{2}0)$ in the $(HK0)$ plane integrated over 0.003 r.l.u. along the L direction for (a) Sample 1, (b) Sample 2, (c) Sample 3, and (d) Sample 4.

We measured reciprocal space maps of the magnetic scattering around the $(\frac{1}{2}00)$ and $(0\frac{1}{2}0)$ wavevectors in four samples (S1-S4), as shown in Fig. 4.12.4.12(a) and 4.12(b) show the maps for S1 and S2 respectively, which show the same structure. The modulations in the two Q_0-domains are symmetry-related, but each is missing the other symmetry-allowed q modulation. Fig. 4.12(c) shows the map for S3, as in Fig. 4.3(a). In this sample, the modulations in the two Q_0-domains are not symmetry-related. Fig. 4.12(d) shows the map for S4 from an optically rough facet, visible in figure 4.1. Reflections from S4 on this facet only shows the commensurate peaks with no satellites. The multiple peaks in the left panel are different crystal grains.

Additional measurements on S4 revealed $(\frac{1}{2}, \pm\delta, 0)$ and $(\pm\delta, \frac{1}{2}, 0)$ satellites on the opposite

facet of S4 that exhibited a mirror like surface. Thus, we attribute the absence of satellite reflections on one surface of S4 to the surface roughness evident in Fig. 4.1. This roughness likely disrupts the incommensurate order via internal strain or structural disorder, consistent with previous reports on itinerant magnets [238, 239].

4.3.9 Correlation lengths

Fig. 4.13 shows line cuts along the L direction for each main and satellite peak in all samples. We fit a Lorentzian function to obtain an out-of-plane correlation length ξ_c. Fig. 4.14 shows in-plane transverse line cuts across each peak, which we fit to obtain an in-plane correlation length ξ_{ab}. For the satellites, the transverse direction is taken with respect to $\boldsymbol{q}$, rather than $\boldsymbol{Q}_0 \pm \boldsymbol{q}$. Fig. 4.15 and Fig. 4.16 show cuts through the structural peaks measured on the second harmonic (1557 eV) at 30 K along the L direction and in-plane transverse directions respectively. The structural and magnetic correlation lengths extracted from these fits are summarized in tables 4.2 and 4.3 below. These (100)-type structural Bragg peaks arise from the superlattice of intercalated Co ions within the NbS_2 host layers and the large correlation lengths indicate a well-ordered triangular lattice of Co ions [240] in all samples studied.

The magnetic correlation lengths for the incommensurate structure are on the order of 100 nm, taken from transverse cuts along the satellite peaks. These peaks are nearly isotropic, showing similar width in any direction. This confirms that the magnetic structure we observed is intrinsic to the bulk. If the incommensurate structure was confined to the surface, these peaks would show a truncation rod-like elongation along the direction of the surface normal [241, 242]. In addition, we find that $\boldsymbol{q}$ is always along a high-symmetry direction, independent of the surface orientation.

Table 4.2: Measured correlation lengths for S1, S2, and S4.

Peak	(100)	(010)	$(\frac{1}{2}00)$	$(\frac{1}{2}\delta 0)$	$(\frac{1}{2}\bar{\delta}0)$	$(0\frac{1}{2}0)$	$(\delta\frac{1}{2}0)$	$(\bar{\delta}\frac{1}{2}0)$
Sample 1								
ξab (nm)	563(8)	570(9)	151(14)	93(3)	85(2)	247(7)	107(1)	102(2)
ξ_c (nm)	571(5)	563(5)	212(1)	135(1)	133(1)	265(2)	143(1)	172(1)
Sample 2								
ξ_{ab} (nm)	274(14)	216(12)	136(2)	197(5)	90(2)	99(2)	107(2)	122(2)
ξ_c (nm)	-	182(6)	159(2)	139(2)	112(2)	98(2)	110(2)	97(1)
Sample 4								
ξ_{ab} (nm)	394(8)	474(11)	469(40)	-	-	352(37)	-	-
ξ_c (nm)	195(2)	199(2)	146(3)	-	-	151(4)	-	-

Table 4.3: Measured correlation lengths for S3.

Peak	(100)	(010)	$(\frac{1}{2}00)$	$(\frac{1}{2}+\delta,-2\delta,0)$	$(\frac{1}{2}-\delta,2\delta,0)$	$(0\frac{1}{2}0)$	$(\delta\frac{1}{2}0)$	$(\bar{\delta}\frac{1}{2}0)$
ξ_{ab} (nm)	274(14)	216(12)	136(2)	197(5)	90(2)	99(2)	107(2)	122(2)
ξ_c (nm)	268(1)	321(2)	120(1)	111(1)	112(2)	224(3)	231(3)	153(2)

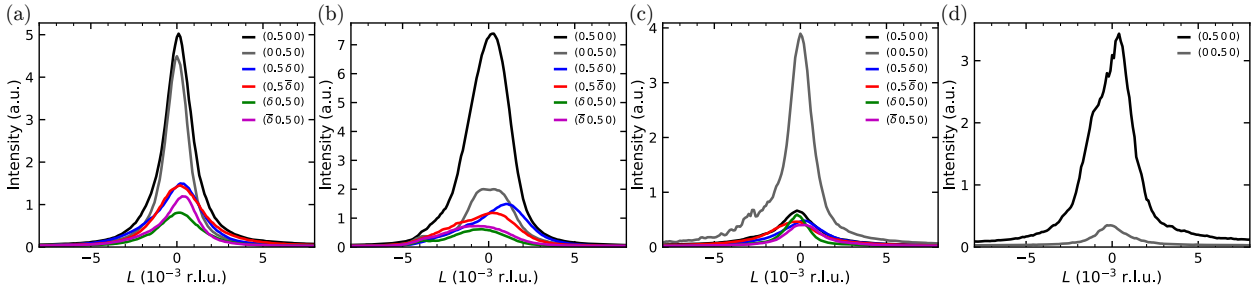

Figure 4.13: Line cuts through the magnetic peaks along the L direction integrated over 0.005 r.l.u. along the H and K directions in (a) sample 1, (b) sample 2, (c) sample 3, and (d) sample 4.

4.3.10 Temperature dependence of magnetic scattering

Fig. 4.17 shows the temperature dependence of the magnetic scattering for samples 1-4 measured from rocking scans on the point detector in π polarization. Above the transition, only the (100) or (010) structural peaks from the second harmonic of the beam remain. The insets show the integrated intensity vs. temperature with the structural peak intensity subtracted.

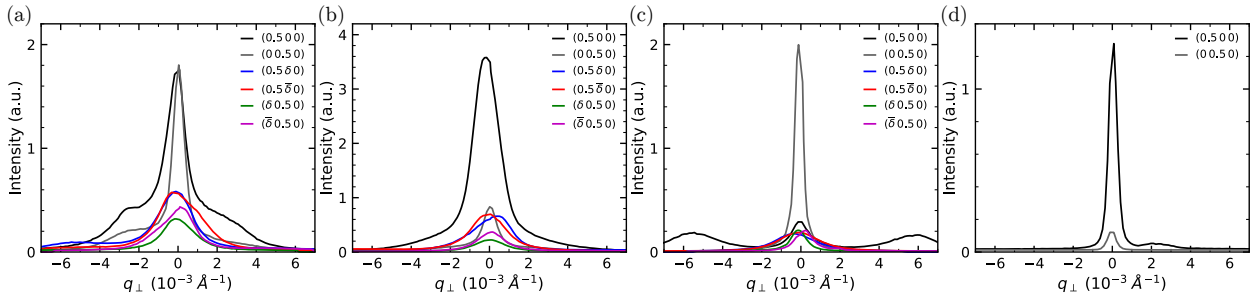

Figure 4.14: Line cuts through the magnetic peaks along the transverse in-plane direction, integrated over 0.003 r.l.u. along the L direction and 0.005 r.l.u. along the in-plane longitudinal direction, in (a) sample 1, (b) sample 2, (c) sample 3, and (d) sample 4.

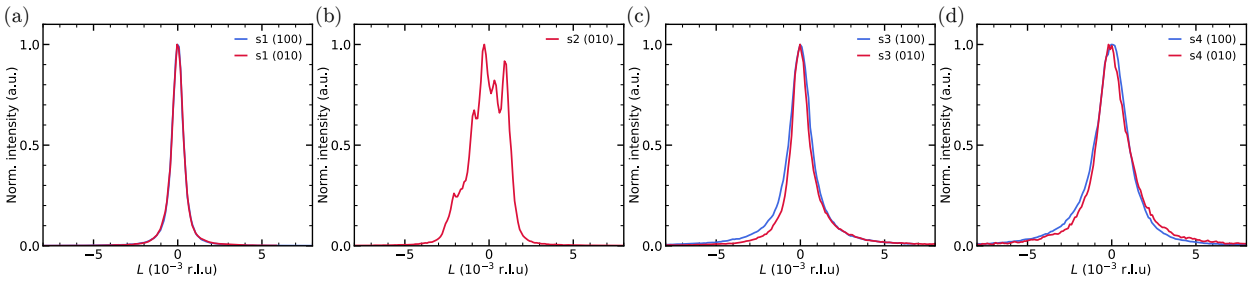

Figure 4.15: Line cuts through the structural peaks along the L direction, integrated over 0.005 r.l.u along the H and K directions, with maximum intensity normalized to 1 in (a) sample 1, (b) sample 2, (c) sample 3, and (d) sample 4, measured on the second harmonic (1557 eV) at 30 K.

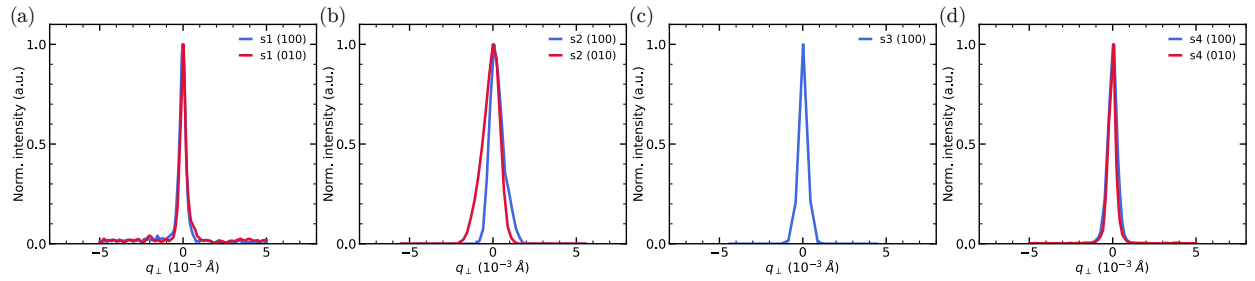

Figure 4.16: Line cuts through the structural peaks along the in-plane transverse direction, integrated over 0.003 r.l.u. along the L direction and 0.005 r.l.u. along the in-plane longitudinal direction, in (a) sample 1, (b) sample 2, (c) sample 3, and (d) sample 4, measured on the second harmonic (1557 eV) at 30 K.

Although T_N as measured through susceptibility and heat capacity is consistent across all samples, the apparent T_N in the REXS data varies between samples. This variation arises from a combination of beam heating and variable cooling efficiency for samples mounted on different locations on the sample holder as shown in Fig. 4.1.

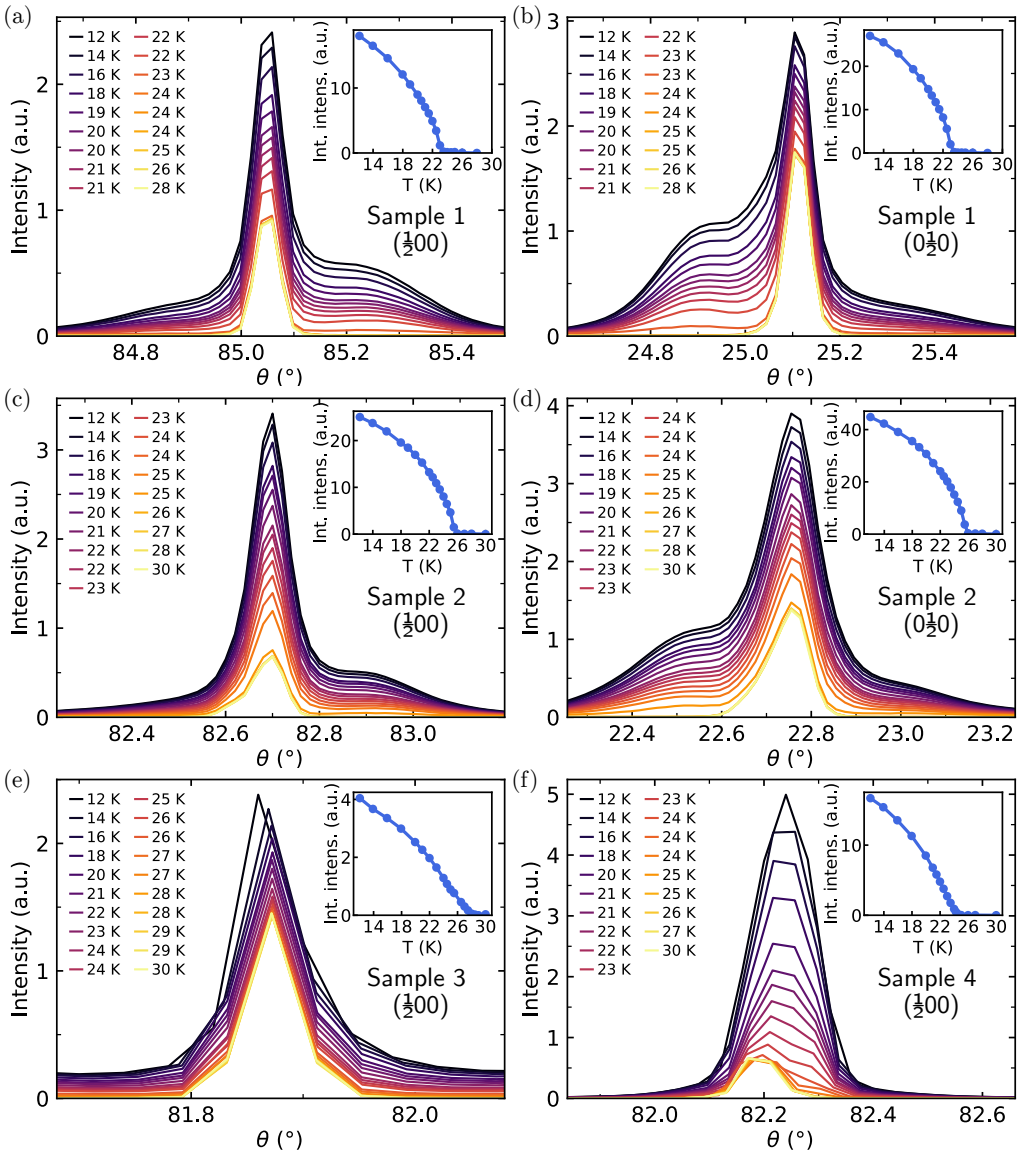

Figure 4.17: Temperature dependence of magnetic scattering measured from rocking scans around $\boldsymbol{Q}_0$ in π polarization on the point detector for (a) sample 1 ($\frac{1}{2}00$), (b) sample 1 ($0\frac{1}{2}0$), (c) sample 2 ($\frac{1}{2}00$), (d) sample 2 ($0\frac{1}{2}0$), (e) sample 3 ($\frac{1}{2}00$), (f) sample 4 ($\frac{1}{2}00$).

4.3.11 Sample dependence and broken symmetry

A striking feature of our results is the broken symmetry of the magnetic domain structure. We refer to the three possible commensurate wavevectors as Q_0-domains. For a given Q_0-domain, the symmetry-allowed directions of $\boldsymbol{q}$ form q-domains. For a given $\boldsymbol{Q}_0$, $\boldsymbol{q}$ pair, the helix chirality $\chi = \pm 1$ and canting direction $\pm\nu$ give four types of χ-domains. In all samples, we only observed a single q-domain for a given Q_0, breaking the expected symmetry between

each Q_0. The q-domains in S3 [blue squares in Fig. 4.3(c)] break both C_6 rotational and mirror symmetry about (110). The q-domains in S1 and S2, [green circles in Fig. 4.3(c)] break C_6 rotational symmetry, while retaining mirror symmetry about the (110). This same symmetry-breaking is exhibited by the in-plane orientation of the commensurate component measured from FLPA. Although we did not obtain reciprocal space maps on that sample, raw detector images show (δ00)-type peaks. It is thus likely that the in-plane orientation of the commensurate component and the helical modulation wavevector are pinned.

In helimagnets where competing and anisotropic exchange interactions control the modulation, helical wavevectors often align with the strain direction [243–247]. Similarly, small strains can modify the Fermi surface and break degeneracies between nesting vectors in itinerant magnets [248, 249]. The domain selection in S1, S2 and S4 can thus naturally be explained by a residual strain along the (110) surface normal that favors $\boldsymbol{q}$ more closely aligned with (110) [250–252]. While more significant surface roughness-induced strain or defects results in the decoherence of long range q modulations on one surface of S4.

However, in S3, the modulations at ($\frac{1}{2}$00) and (0$\frac{1}{2}$0) are not along symmetry-equivalent directions and these two peaks cannot be described as separate domains of the same structure. This suggests that the magnetic domains may be pinned to structural domains, with a different modulation type in the different structural domains [94, 233, 234, 253, 254].

4.4 Discussion

In the absence of a uniform magnetization, non-coplanar antiferromagnets support a Hall response through the scalar spin chirality $\chi_s = \boldsymbol{m}(\boldsymbol{r}_i) \cdot [\boldsymbol{m}(\boldsymbol{r}_j) \times \boldsymbol{m}(\boldsymbol{r}_k)]$ with sites i, j, k on a triangular plaquette. Conduction electrons traversing closed loops around regions of uniform χ_s accumulate a net Berry phase [67], while a Berry phase can accumulate for a non-uniform χ_s when spin-orbit coupling is present [236]. To check these possibilities in $CoNb_3S_6$, we compute χ_s for the $2Q$ magnetic structure. Since there are two triangular lattice layers per unit cell in

$CoNb_3S_6$, there may be contributions to the total spin chirality from both intra-sublattice plaquettes within the triangular lattice basal plane $\chi_s^{\parallel}$, and inter-sublattice plaquettes $\chi_s^{\perp}$ that involve two sites from one sublattice and one site from the opposite one. We compute the total scalar spin chirality using the real space spin structures found above by considering separate contributions $\chi_s^{\parallel}$ and $\chi_s^{\perp}$ [Fig. 4.7(c)]. We find that a finite incommensurate modulation $q \neq 0$ gives rise to a staggered scalar chirality in $CoNb_3S_6$, with a precise pattern that depends on the choice relative phase and canting direction ν for the magnetic structure.

The present findings clarify the microscopic origins of the giant Hall signal in $CoNb_3S_6$. For all physical choices of ν and relative phase parameters $CoNb_3S_6$ develops a striped or checkerboard pattern of scalar spin chirality modulated along both $\boldsymbol{Q}_0$ and $\boldsymbol{q}$ as shown in Fig. 4.7(d) and (e).

Thus, the large anomalous Hall signal in the presence of a staggered, not uniform, scalar chirality implicates the importance of spin-orbit coupling in $CoNb_3S_6$ [236]. Furthermore, a local, non-uniform, magnetic scalar chirality is expected to influence electronic transport in other ways. For instance a finite local chirality can generate nonlinear or nonreciprocal transport [230] as may have been recently observed [237].

We find that $CoNb_3S_6$ exhibits a unique $2Q$ magnetic structure with staggered scalar spin chirality that is distinct from the reported $3Q$ structure [112]. While our findings are fully consistent with polarized neutron diffraction [112], a more than order-of-magnitude improved momentum space resolution reveals long-wavelength helical modulations that were not accessible to the neutron experiments. Furthermore, the efficiency of REXS enabled measurements across many samples to reveal a subtle sample and domain dependence of the helical magnetic wavevector. Such differences between samples with similar thermodynamic characterization and well-ordered Co triangular lattices (see section 4.3.1) is striking, but not unexpected. Magnetic ordering in intercalated TMDs is known to be highly sensitive to minute disorder and local structural defects [103, 104, 107, 255] that may not be apparent in bulk measurements. Given that magnetic structures in a given sample were constant

across many heating and cooling cycle, the sample dependent magnetic wavevectors are likely fixed by quenched in structural domains and defects that pin magnetic domains or impart symmetry-breaking strains [94, 233, 234, 253, 256]. Such a sample dependence is revealing as it implicates a near degeneracy of helical wavevectors and likely competing, or frustrated, magnetic interactions in $CoNb_3S_6$.

While competing real-space exchange interactions may stabilize $2Q$ magnetism [27, 257], an itinerant Kondo model is more likely in $CoNb_3S_6$ given the 5.75 Å separation between nearest neighbor Co sites hosting local moments. In this case, the $2Q$ structure arises from Fermi surface nesting instabilities that generate effective biquadratic (four-spin) RKKY exchange terms. For a $\frac{3}{4}$-filled Fermi-surface on the triangular lattice, these instabilities support the $3Q$ ordering in $CoTa_3S_6$ [113, 228, 254, 258–260], but away from $\frac{3}{4}$ filling can give rise to $2Q$ ordering and stripes of scalar chirality similar to our observations [229, 254, 259]. The itinerant picture is further supported by the sample dependence that indicates very small energy differences between different incommensurate wavevectors, $\boldsymbol{q}$. Such near degeneracy can naturally arise in Fermi surface instability/momentum space description of the magnetism. A biquadratic RKKY mechanism likely also underlies $3Q$ uniform scalar chiral ordering in $CoTa_3S_6$ [112, 113]. The tunability of the magnetic structure demonstrated by pressure dependence [95] and sample dependent magnetism in $CoNb_3S_6$ and $CoTa_3S_6$ [261] together with the similarities of electronic structure between these two materials with different magnetic structures hints at the exciting possibility of controlling the magnetism in the intercalated TMDs to tune between different multi-Q orderings with a suitably chosen perturbation.

In summary, we have discovered a $2Q$ non-coplanar magnetic structure in $CoNb_3S_6$ exhibiting a staggered scalar spin chirality χ_s. Such a magnetic structure provides strong evidence for biquadratic interactions on the triangular lattice, and the apparent tunability of this order revealed through a subtle sample dependence opens up possibilities for realizing and controlling nontrivial transport phenomena in itinerant antiferromagnets. Future work is needed to understand the mechanisms underlying this magnetic structure and its impact on

transport properties, while experimental studies may attempt to control the magnetic domain pattern to affect anisotropic couplings between magnetic order and electronic transport in itinerant antiferromagnets.

CHAPTER 5

Tuning the structural and magnetic properties of Co_xNbS_2 and Ni_xNbS_2

The electronic and magnetic properties of intercalated transition metal dichalcogenides are highly sensitive to sample composition, particularly the intercalant concentration. In this chapter, we consider the evolution of the structural and magnetic properties of Co_xNbS_2 and Ni_xNbS_2 with varying composition around the ideal $x = \frac{1}{3}$. The chapter is split into two separate sections covering each material.

Using x-ray diffraction, heat capacity, magnetic susceptibility, and electrical transport measurements on Co_xNbS_2, we find find long-range antiferromagnetic order that continuously evolves into a short-range correlated glassy state as x decreases from $\frac{1}{3}$ to 0.30. Using x-ray diffraction, magnetic susceptibility, and resonant elastic x-ray scattering (REXS) on Ni_xNbS_2, we find two distinct structural phases, each hosting a different magnetic order. For nominal $x = 0.30$, we find a 2×2 superlattice corresponding to the ideal structure for $x = \frac{1}{4}$ exhibiting canted antiferromagnetic (CAF) order. For nominal $x = 0.35$, we find a $\sqrt{3} \times \sqrt{3}\,R30^\circ$ superlattice corresponding to the ideal structure for $x = \frac{1}{3}$, exhibiting an incommensurate (IC) helical order along the c-axis with a weak commensurate component, consistent with a conical or fan structure. For nominal $x = 0.33$, we find a similar strucure, with a decreased IC

component and increased C component.

5.1 Introduction

As described in chapter 4, $CoNb_3S_6$ exhibits a novel magnetic ground state that likely plays a role in the observed large anomalous Hall effect (AHE) and may enable a variety of other novel effects such as nonlinear or nonreciprocal transport and optical responses [230, 237, 262, 263]. Recently, the related material $NiNb_3S_6$ was shown to possess a helical magnetic order with propagation vector along the c axis [96]. Although this phase is not a fundamentally unique, it may enable other novel effects through the interplay of local moments and itinerant electrons [97].

However, the properties of the whole class of intercalated TMDCs are highly sensitive to the precise chemical composition and structural order, particularly of the intercalated $3d$ ions [90, 101–103, 227, 261, 264–267]. In these materials, significant variation in the electronic and magnetic properties has been reported for only slight deviations from the ideal $x = \frac{1}{3}$. There are several consequences of these deviations. First, it introduces defects in the bilayer triangular magnetic lattice, breaking the long-range periodicity and introducing random strain fields which suppresses magnetic ordering and may induce a glassy state [50, 51, 268]. In addition, it alters the Fermi level, which is set by the filling of the NbS_2 conduction band doped by the two electrons transferred from each Co^{2+} ion. This affects the strength and periodicity of the RKKY interaction or other itinerant exchange mechanisms, as well as the nesting vector of the Fermi surface [91–93, 95, 269–271]. Finally, may be effects involving defect correlations and structural domains. As defects form in the superlattice, the site occupied by each intercalant within the unit cell becomes less constrained. This allows for site disorder, with possible spatial correlations in site occupancy. Structural domains may correspond to coexisting $\sqrt{3} \times \sqrt{3}$ and 2×2 superlattice structures, or chirality domains of the $\sqrt{3} \times \sqrt{3}$ superlattice [94, 233, 234, 253, 255, 256, 267].

The sample composition dependence of Co_xNbS_2 has been previously studied in [90, 91, 227]. In [90], an AHE is observed for $x \leq \frac{1}{3}$ but not for $x > 0.35$. For $x \approx \frac{1}{3}$, the AHE shows a sign reversal below the transition and a rapid suppression at lower temperatures. As x decreases, no sign reversal is observed and the AHE persists at lower temperatures. These samples also exhibit an exchange bias. However, the systematic trend between x, transport properties, and structural properties remains inconclusive. In [227], the authors find that the AHE vanishes in underintercalated samples which also show no ferromagnetic component. However, neutron diffraction measurements find that these samples have the same $\boldsymbol{Q} = (\frac{1}{2}00)$ collinear magnetic structure. In [91], the authors found that the weak ferromagnetic moment, along with the AHE, vanish in sufur deficient samples.

A recent study considered the composition dependence of Co_xTaS_2, in which they found a continuous variation in the electronic and magnetic properties for $0.30 < x < \frac{1}{3}$, with the same underlying ground state. For $x \geq \frac{1}{3}$, they found an abrupt change in magnetic ground state with no sign of an AHE or weak ferromagnetic moment [261]. Several works have considered the electronic and magnetic properties of Fe_xNbS_2 for $0.31 \geq x \leq 0.35$, finding multiple distinct magnetic phases, as well as a charge ordered phase, that give rise to novel spintronic properties [101–103, 266].

In this chapter, we study the evolution of the structural, magnetic, and transport properties in Co_xNbS_2 and the related compound Ni_xNbS_2 over the range $0.30 < x < 0.35$. Using magnetic susceptibility, heat capacity, electrical transport, and x-ray diffraction on Co_xNbS_2, we find a continuous evolution of the structural and magnetic properties with varying x. The intercalated Co ions form a $\sqrt{3} \times \sqrt{3}\,R30°$ superlattice for all x considered. As x decreases from $\frac{1}{3}$ to 0.30, T_N is suppressed and the long-range ordered state collapses into a glassy state. The transition also splits into two stages as x decreases. The antiferromagnetic order appears with no ferromagnetic component at higher temperature. As temperature decreases, the ferromagnetic component appears and continues to increase as temperature decreases. All samples exhibit an anomalous Hall effect, but the magnitude rapidly decreases for $x \leq 0.31$.

Using magnetic susceptibility, x-ray diffraction, and resonant elastic x-ray scattering (REXS) on Ni_xNbS_2, we find two distinct structural and magnetic phases. For nominal $x = 0.30$, the Ni ions form a 2×2 superlattice with a canted antiferromagnetic (CAF) order. For nominal $x = 0.35$, the Ni ions form a $\sqrt{3} \times \sqrt{3}\,R30°$ superlattice with an incommensurate (IC) helical order along the c-axis magnetic order, as previously observed [96]. We also find a weak commensurate (C) component, indicating a slight conical tilting. For $x = 0.33$, we find a $\sqrt{3} \times \sqrt{3}\,R30°$ superlattice with a partially suppressed IC component and an increased C component.

5.2 Experiment

Magnetic susceptibility measurements were carried out a Quantum Design Physical Property Measurement System (PPMS) using the vibrating sample mount (VSM) option. Heat capacity measurements were carried out on a PPMS. Electrical transport measurements were carried out on a PPMS using the van der Paux-Hall option. Single crystal x-ray diffraction measurements were carried out on a four-circle diffractometer with a Ag K_α source and at the QM-2 beamline at the Cornell High Energy Synchrotron Source (CHESS) [272]. Resonant elastic x-ray scattering (REXS) measurements were carried out on the RSXS endstation of the REIXS beamline at the Canadian Light Source (CLS) [273].

Single crystals of Co_xNbS_2 and Ni_xNbS_2 were grown in two steps. Polycrystalline precursor was prepared using a mixture of Co/Ni, Nb, and S with molar ratios $x : 1 : 2$ for $x = 0.30$-0.35, sealed in quartz tubes and heated at 900° C for 5 days, following the procedure described in section **??**. Single crystals were grown from the polycrystalline precursor using chemical vapor transport with iodine as the transport agent, as described in section **??** and [88].

Table 5.1: Co_xNbS_2 measured properties for various x. c is in units of Å, ΔS is in units of J/mol K, A is in units of mJ/mol K^2, T_N is in K, and σ^A_{xy} is in units of $\Omega^{-1}cm^{-1}$.

Nominal x	c	ΔS	A	T_N (χ)	T_N (ρ_{xy})	σ^A_{xy}
0.30 (s1)	11.8415(9)	-	-	-	-	-
0.31 (s1)	11.8463(17)	3.66	77	19.6/25.0	17.9	1.2(2)
0.31 (s2)	11.8452(3)	3.50	74	-	-	-
0.31 (s4)	11.8381(8)	3.22	90	14.0/20.4	14.0	1.5(2)
0.31 (s5)	11.8468(10)	3.67	65	23.3/27.2	22.8	16.1(4)
0.32 (s1)	11.8588(9)	4.20	58	27.2/28.4	27.0	125(3)
0.33 (s1)	-	4.50	33	28.4	-	-
0.33 (s3)	11.8669(16)	4.65	27	28.4	28.3	92(4)
0.33 (s4)	11.8708(21)	-	-	28.4	28.3	92(4)
0.33 (s6)	11.8708(17)	-	-	-	-	-
0.34 (s2)	11.8632(9)	-	-	-	-	-
0.34 (s3)	11.8652(18)	4.43	40	28.3	28.2	124(3)
0.35 (s1)	11.8532(9)	4.27	59	27.8	-	-

5.3 Co_xNbS_2

Here we present the results of x-ray diffraction, heat capacity, magnetic susceptibility, and electrical transport measurements on Co_xNbS_2 samples grown with $0.30 < x < 0.35$. Instead of explicitly determining the value of x from energy-dispersive x-ray spectroscopy (EDX) or structural refinement, we classify the samples according to the consistent empirical trends in our measurements. We continue to label each sample by nominal value of x used for the crystal growth. For a given x, we label samples by number, i.e. s1, s2, ... sn. Table 5.1 summarizes the main results on Co_xNbS_2.

Before discussing the results in detail, we describe the trend between the nominal x and actual x. We expect the lattice parameter to increase monotonically for increasing x [103, 261, 264, 274]. However, c is maximized for $x = \frac{1}{3}$ and decreases as the nominal x increases above $\frac{1}{3}$, as shown in Fig. 5.2(b). These samples with nominal $x > \frac{1}{3}$ fit the trends in magnetic properties according to their lattice parameter, as discussed below. They also contain a CoS_2 impurity phase, indicated by the ferromagnetic transition at 124 K in the susceptibility. Furthermore, the CoS_2 content increases with increasing x. We conclude that a nominal $x > \frac{1}{3}$ promotes the formation of a CoS_2 phase and results in an actual $x < \frac{1}{3}$

[275, 276].

5.3.1 X-ray diffraction

Co_xNbS_2 crystallizes in the $\sqrt{3} \times \sqrt{3}$ superlattice for all x in the range considered here, indicated by x-ray diffraction. Fig. 5.1(a) and (b) show reciprocal space maps in the $(HK0)$ plane for $x = 0.31$ and $x = 0.33$. The intense peaks correspond to the hexagonal lattice of the NbS_2 parent compound with $a_0 = 3.32$ Å. The weaker peaks correspond to the superlattice of intercalated Co ions, appearing at $(\frac{1}{3}\frac{1}{3}0)$ positions of the host lattice, indicating a superlattice with $a = \sqrt{3}a_0 = 5.75$ Å with hexagonal lattice vectors rotated by 30° relative to the host lattice (denoted by $\sqrt{3} \times \sqrt{3}R30°$). Fig. 5.1(c) and (d) show the $(HK1)$ plane, furthing confirming the highly ordered superlattice. Fig. 5.1(e) and (f) show the $(H0L)$ plane. The presence of weak forbidden $(00L)$ peaks with odd L is likely due to stacking faults [277]. Fig. 5.2(b) shows the measured c-axis lattice parameters vs. the nominal x, as described above. The maximum and minimum of $c \approx 11.87$ Å and $c \approx 11.84$ Å are consistent with previously reported values for $x = 0.33$ and $x = 0.30$ respectively [90].

5.3.2 Heat capacity

The heat capacity exhibits a strong dependence on sample composition, as shown in Fig. 5.2(a). Each sample shows one or more peaks indicating the possibility of multiple transitions in some samples. As x decreases, T_N is suppressed, and the size of the peak decreases. To determine the magnetic contribution to the heat capacity, we subtract the nonmagnetic contribution from the lattice and conduction electrons using a Debye-Einstein model [109]

$$C_p = \gamma T + n(1-\alpha)C_{\mathrm{D}} + n\alpha C_{\mathrm{E}} \tag{5.1}$$

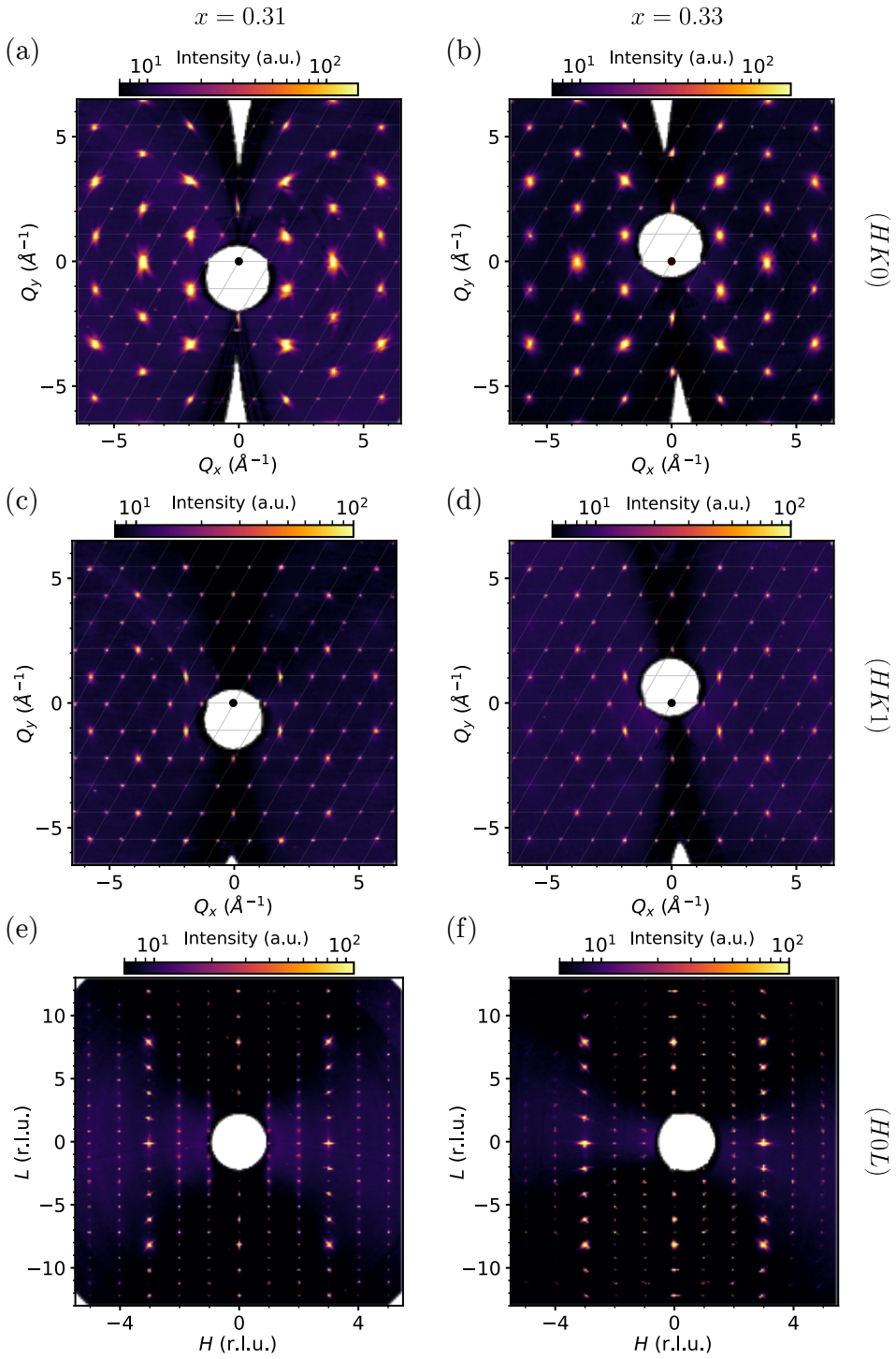

Figure 5.1: X-ray diffraction reciprocal space maps of Co_xNbS_2, (a) $x = 0.31$ $(HK0)$ plane (b) $x = 0.33$ $(HK0)$ plane (c) $x = 0.31$ $(HK1)$ plane (d) $x = 0.33$ $(HK1)$ plane (e) $x = 0.31$ $(H0L)$ plane (f) $x = 0.33$ $(H0L)$ plane The data in (a)-(d) is integrated over 0.02 r.l.u. along L. The data in (e)-(f) is integrated over 0.01 r.l.u. along K. The black dot indicates the origin of the respective plane and the gridlines correspond to the reciprocal lattice of the $\sqrt{3} \times \sqrt{3}\,R30°$ superlattice.

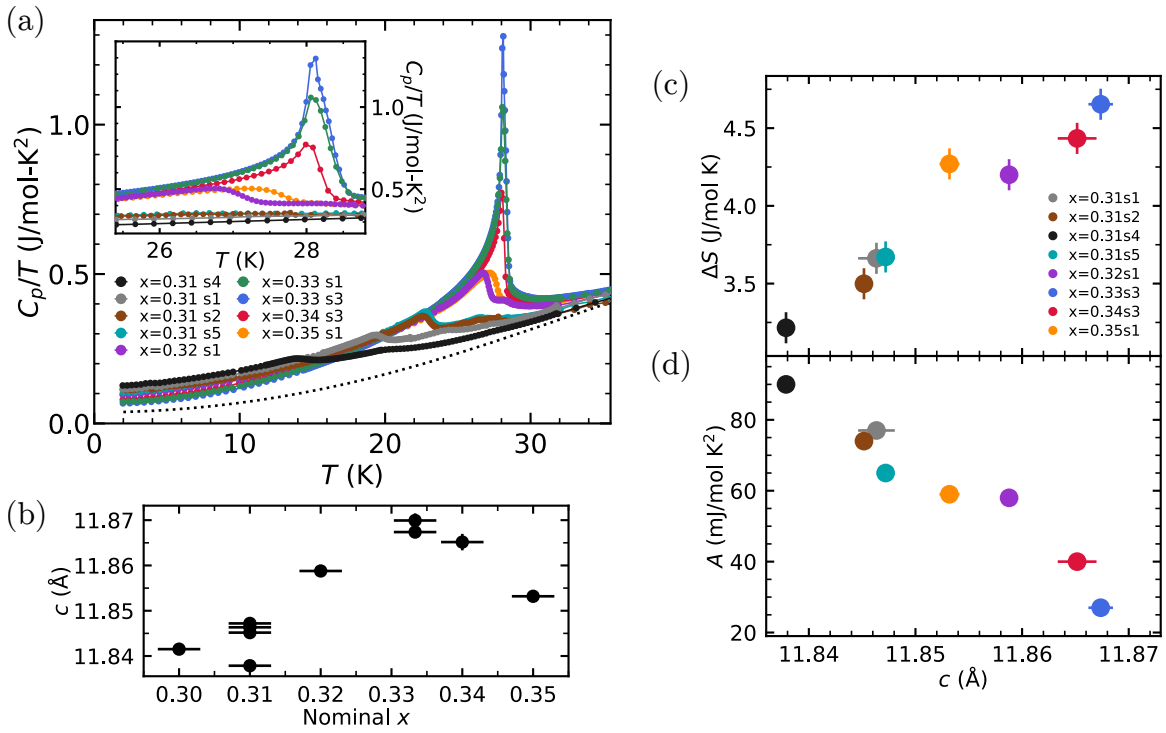

Figure 5.2: (a) Heat capacity divided by temperature vs temperature of Co_xNbS_2 for various x. The dotted line shows the estimated nonmagnetic heat capacity. (b) c-axis lattice parameter vs. nominal x. (c) Change in entropy ΔS from 2 K to 48 K vs. c-axis lattice parameter. (d) Low temperature linear component of magnetic heat capacity A vs. c.

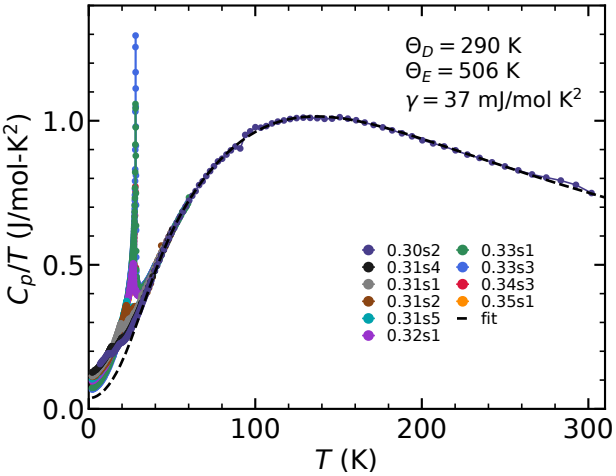

Figure 5.3: Co_xNbS_2 heat capacity up to 300 K

where $n = 10$ is the number of atoms per formula unit,[1] α is the mixing parameter,

$$C_{\mathrm{D}}(T) = 9R\left(\frac{T}{\Theta_{\mathrm{D}}}\right)^2 \int_0^{\Theta_{\mathrm{D}}/T} \frac{x^4 e^x}{(e^x - 1)^2} dx \tag{5.2}$$

is the Debye heat capacity with Debye temperature Θ_{D},

$$C_{\mathrm{E}} = 3R\left(\frac{\Theta_{\mathrm{E}}}{T}\right)^2 \frac{e^{\Theta_{\mathrm{E}}/T}}{(e^{\Theta_{\mathrm{E}}/T} - 1)^2} \tag{5.3}$$

is the Einstein heat capacity with Einstein temperature Θ_{E}, and γ is the Sommerfeld coefficient for the linear electronic contribution. The four metal atoms are better described by the Debye model and the six sulfur atoms are better described by the Einstein model, which suggests the constraint $\alpha = 0.4$ [109]. A fit to eq. 5.1 gives $\Theta_{\mathrm{D}} = 290$ K, $\Theta_{\mathrm{E}} = 506$ K, and $\gamma = 37$ mJ/mol K^2, shown in Fig. 5.3. We have assumed that γ is equal for all samples. However, this is not necessarily true because γ depends on the Fermi level, which varies with x.

Subtracting the nonmagnetic contribution to the heat capacity and computing the magnetic entropy ΔS gives the values shown in Table 5.1 and Fig. 5.2(c). After subtracting the

[1]We neglect differences in n for different x, as the maximum deviation of $x = 0.30$ gives $n = 9.9$. The resulting 1% error is less than the uncertainty in the sample mass.

nonmagnetic contribution to the heat capacity, we fit the low temperature region with $C_p = AT + BT^3$, from 2-10 K. The linear coefficient A is plotted vs. c in Fig. 5.2(d) [278].

For fully ordered $S = \frac{3}{2}$ moments, the expected entropy released by the transition is $\Delta S = R\log(2S+1) = R\ln 4 = 11.52$ J/mol K, where $R = 8.315$ J/mol K is the gas constant. Susceptibility measurements have found a paramagnetic moment of 3.0-3.15μ_B [88, 226], corresponding to an effective spin $S \sim 1.1$, likely due to strong hybridization between the local Co states and the conducting NbS_2 states [92, 93, 95, 225, 270, 279]. This would give an entropy of $\Delta S = 9.7$ J/mol K. However, neutron diffraction measurements finds an ordered moment of only 1.64-1.96μ_B[226, 227] (or 1.52μ_B for $x = 0.306$), corresponding to an effective spin of $S \approx 0.8$-1, with an entropy of $\Delta S = 8$-9 J/mol K. Thus we find at most 50-60% of the expected entropy released by the transition.

This discrepancy may be due to an overestimate of the nonmagnetic contribution and thus underestimating the magnetic entropy. Indeed, a Curie-Weiss temperature of -150 K suggests that magnetic correlations may exist far above T_N. Another possibilities is that the ordered moment determined from neutron diffraction is incorrect, due to an incorrect model for the magnetic structure, as suggested by the results of chapter 4.

In addition to the large residual entropy in the most well-ordered sample, the residual entropy continues to increase with decreasing x. This decrease can be partially explained by the decrease in the number of Co sites, which was not accounted for in the calculation of the molar heat capacity, since we do not have a quantitative measure of x. Although this has a negligible effect on the calculation of the total heat capacity, it would give up to a 10% difference in the magnetic contribution between $x = \frac{1}{3}$ and $x = 0.30$. However, the change in ΔS is far larger than this discrepancy. In addition to the residual entropy, the low temperature linear contribution to the magnetic heat capacity increases with decreasing x. Both of these trends are consistent with a the emergence of a glassy state coexisting with antiferromagnetic order [50, 51], similar to the behavior seen in Fe_xNbS_2 [101, 102, 280, 281].

Based on these results, we divide the samples into two main classes to simplify further discussion: (1) the slightly underintercalated or nearly stoichiometric samples which have nominal $x \geq 0.32$, and (2) the highly underintercalated samples, which have nominal $x \leq 0.31$. The slightly underintercalated samples correspond to the four markers on the right side of Fig. 5.2(c) and (d), each showing a distinct heat capacity peak in the inset of Fig. 5.2 and have $c > 11.85$ Å.

5.3.3 Magnetic susceptibility

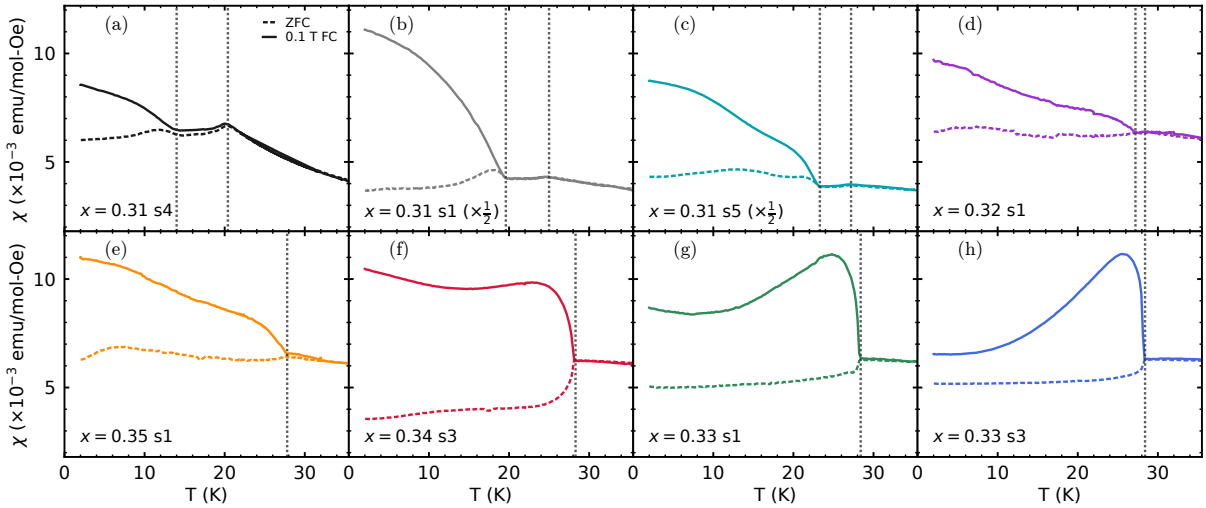

Figure 5.4: Out-of-plane magnetic susceptibility of Co_xNbS_2 for various x. Solid lines are 0.1 T field cooled, dashed lines are zero-field-cooled. Vertical dotted lines indicate transition temperatures. (a) $x = 0.31$ s4 (b) $x = 0.31$ s1 (c) $x = 0.31$ s5 (d) $x = 0.32$ s1 (e) $x = 0.33$ s1 (f) $x = 0.33$ s3 (g) $x = 0.34$ s3 (h) $x = 0.35$ s1.

The sample composition also has a significant effect on the magnetic susceptibility. Fig. 5.4 shows the out-of-plane magnetic susceptibility vs. temperature for several Co_xNbS_2 samples. All samples show an antiferromagnetic (AFM) transition with a small out-of-plane ferromagnetic (FM) moment after field-cooling, which either appears at T_N, or at a second transition below T_N.

For $x = 0.33$, the FM moment appears at the same temperature as the AFM transition. As x decreases, the FM moment appears as a separate transition at lower temperature. These separate transitions are consistent with the peaks in the heat capacity. The transition

temperatures are shown as dotted lines in Fig. 5.4. For $x = 0.33$, the FM moment is maximized just below T_N and rapidly decreases upon further cooling. As x decreases, the FM moment arises more gradually below T_N, and continues to increase upon further cooling.

The susceptibility for $x = 0.33$s3 is consistent with previous reports for Co_xNbS_2 with $x = \frac{1}{3}$ [88, 91, 226, 227, 232, 237]. However, there are some suble discrepancies. In Fig. 5.4(h), the ZFC χ decreases monotonically below $T_N = 28.4$ K. The FC χ rapidly increases below T_N, reaching a maximum at 25.6 K (2.8 K below T_N) before decresing, but remaining larger than χ above T_N.

In [88], the ZFC χ is equivalent to that in Fig. 5.4(h). However, the FC χ decreases more rapidly after reaching its maximum at 2.5 K below T_N, falling below the ZFC χ at 12 K. Similar FC behavior is seen in [226, 227, 237]. Another discrepancy is an upturn in the ZFC χ, which occurs just after reaching a minimum at the same temperature where the FC χ is maximized [226, 227].

Based on the trend of the FC χ in our data, we conclude that the decrease in the FM moment with decreasing T occurs more rapidly as x approaches the ideal $\frac{1}{3}$. Thus, the behavior described above for the FC χ falling below the ZFC χ likely corresponds to x closer to $\frac{1}{3}$ than any of our samples.

5.3.4 Electrical transport

Fig. 5.5(a) shows the temperature dependence of the anomalous Hall conductivity σ^A_{xy} of Co_xNbS_2

$$\sigma^A_{xy} = \frac{\rho^A_{xy}}{(\rho^A_{xy})^2 + (\rho_{xx})^2}. \tag{5.4}$$

These measurements were performed by field cooling under ± 12 T, then measuring ρ_{xy} and ρ_{xx} vs. temperature from 1.8-35 K under zero field. All samples exhibit an anomalous Hall effect, with the maximum σ^A_{xy} reached by each sample shown in Table 5.1 (calculated as the average magnitude of ± 12 T FC). In the samples with multiple transitions, the AHE appears

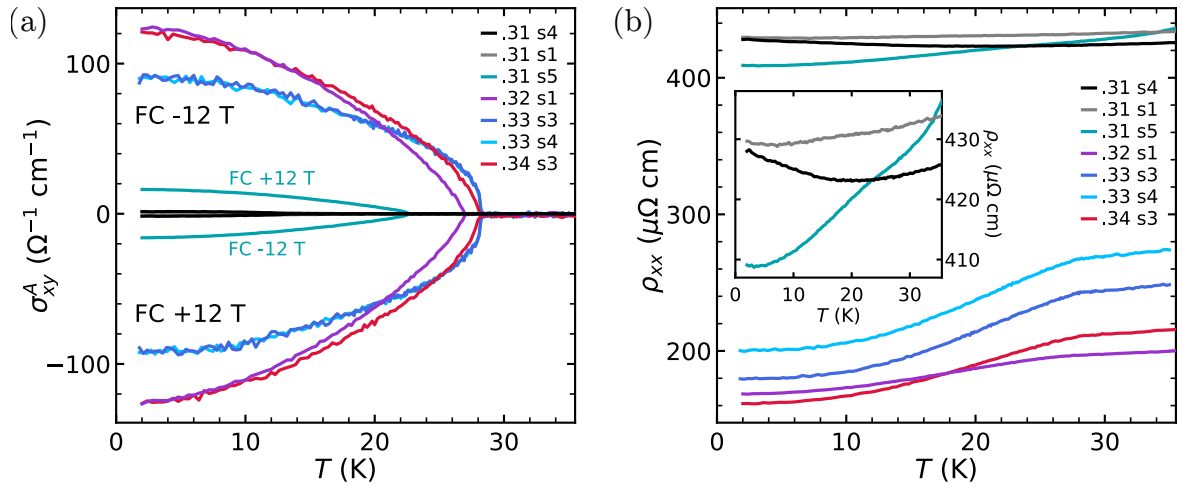

Figure 5.5: (a) Hall conductivity σ_{xy} vs. temperature for ±12 T field-cooling. (b) Longitudinal resistivity ρ_{xx} vs. temperature.

at the lower transition where the FM moment appears. Switching the field direction switches the sign of ρ^A_{xy}. All samples show $\rho^A_{xy} < 0$ for +12 T and $\rho^A_{xy} > 0$ for -12 T, with the exception of $x = 0.31$s5, which shows the opposite behavior, consistent with the previously reported reversal behavior [90]. The magnitude of σ^A_{xy} is maximized around $x = 0.32$, consistent with [90], by comparison of lattice parameters.

Fig. 5.5(b) shows the temperature dependence of the longitudinal resistivity ρ_{xx} for ZFC. No obvious differences were observed for ±12 FC. The slightly underintercalated samples show show a kink at T_N followed by a sharp decrease in ρ_{xx}. The highly underintercalated samples show a significanly larger overall ρ_{xx}, with no sharp decrease at T_N. Instead, there is a broad hump, followed by a upturn, suggesting possible Kondo-like behavior.

The sharp kink in the slightly underintercalated samples is due to the reduced in scattering of conduction electrons by disordered spins [88, 95, 282]. In the highly underintercalated samples, the overall resistivity is increased due to impurity scattering [89]. The lack of a sharp kink is due to the reduction of long-range spin correlations. The resistivity minima indicate possible Kondo-like behavior or other competing phases [283–285].

5.3.5 Discussion

We have tracked the structural, magnetic, and transport properties of Co_xNbS_2 as a function of x over the range $0.30 \leq x \leq \frac{1}{3}$. For decreasing x, find that the long-range AFM order at $x = \frac{1}{3}$ develops into a coexisting AFM and glassy state with short-range correlations. As x decreases below $\frac{1}{3}$, the increase in Co vacancies and site disorder leads to frustrated random exchange and smearing of the Fermi surface due to broken lattice translation symmetry.

The suppression of long-range AFM order and emergence of a glassy state is apparent from several trends in the data. As x decreases, we observe a decrease in T_N with the emergence of a two stage transition. The heat capacity shows an increase in residual entropy and low temperature linear component. Electrical transport measurements show a suppression in the anomalous Hall conducitivity and a lack of a sharp decrease in longitudinal resistivity at T_N. These observations are consistent with the suppression of long range order into a phase with short-range correlations and competing metastable states.

This coexisting AFM and spin glass state has been seen in the related compound Fe_xNbS_2 for $x < \frac{1}{3}$ [101, 102]. This material shows a similar trend in the heat capacity, as well as exchange bias behavior, which has been reported for underintercalated Co_xNbS_2 [90]. Our observations are also similar to previous reports of coexisting AFM and spin glass states in insulating three-dimensional frustrated magnets [286, 287]. AC susceptibility measurements [50, 51, 288], thermoremanent magnetization [101], and magnetic field-dependent heat capacity [100, 104, 289, 290] are required to further characterize the spin glass state.

As mentioned above, the resistivity minimum indicates Kondo-like behavior or other competing phases [283–285]. Pressure-dependent neutron diffraction and transport measurements on Co_xNbS_2 ($x \approx \frac{1}{3}$) find a reduction in the magnetic order parameter with increasing pressure, vanishing completely around 1.7 GPa [95, 282]. The in-plane longitudinal resistivity broadens and develops a minumum near T_N as pressure increases. Above 1.7 GPa, the minimum disappears and the resisitivity shows no sign of magnetic order. This suggests that pressure

and underintercalation may play a similar role in suppressing magnetic order by decreasing the c-axis lattice parameter, which would modify the hybridization of Co moments with the conduction band [95].

Finally, we note the discontinuous trend in the transport measurements between the slightly and highly underintercalated samples. This crossover regime and the corresponding reversal behavior warrants further study.

5.4 Ni_xNbS_2

5.4.1 X-ray diffraction

Fig. 5.6(a) and (b) show reciprocal space maps in the $(HK0)$ plane for $x = 0.30$ and $x = 0.33$. The intense peaks correspond to the hexagonal lattice of the NbS_2 parent compound with $a_0 = 3.32$ Å. The weaker peaks correspond to the superlattice of intercalated Ni ions. Unlike Co_xNbS_2, Ni_xNbS_2 crystallizes in either the 2×2 or the $\sqrt{3} \times \sqrt{3}\, R30°$ superlattice, depending on the starting x. For the $x = 0.33$ sample, the superlattice peaks appear at $(\frac{1}{3}\frac{1}{3}0)$ positions of the host lattice, indicating a superlattice with $a = \sqrt{3}a_0 = 5.75$ Å with hexagonal lattice vectors rotated by 30° relative to the host lattice (denoted by $\sqrt{3} \times \sqrt{3}\, R30°$). Weak spurious peaks with no clear index may arise from a separate misaligned grain. For $x = 0.30$, the superlattice peaks appear at $(\frac{1}{2}00)$ positions of the parent lattice, indicating a 2×2 superlattice, with the same orientation as the host lattice. The gridlines correspond to the $\sqrt{3} \times \sqrt{3}\, R30°$ reciprocal lattice. Fig. 5.6(c) and (d) show the $(HK1)$ plane, further confirming the presence of these two distinct superlattice structures. Fig. 5.6(e) and (f) show the $(H0L)$ plane. Similarly to Co_xNbS_2, the presence of forbidden peaks at $(00L)$ for odd L indicates the presence of stacking faults.

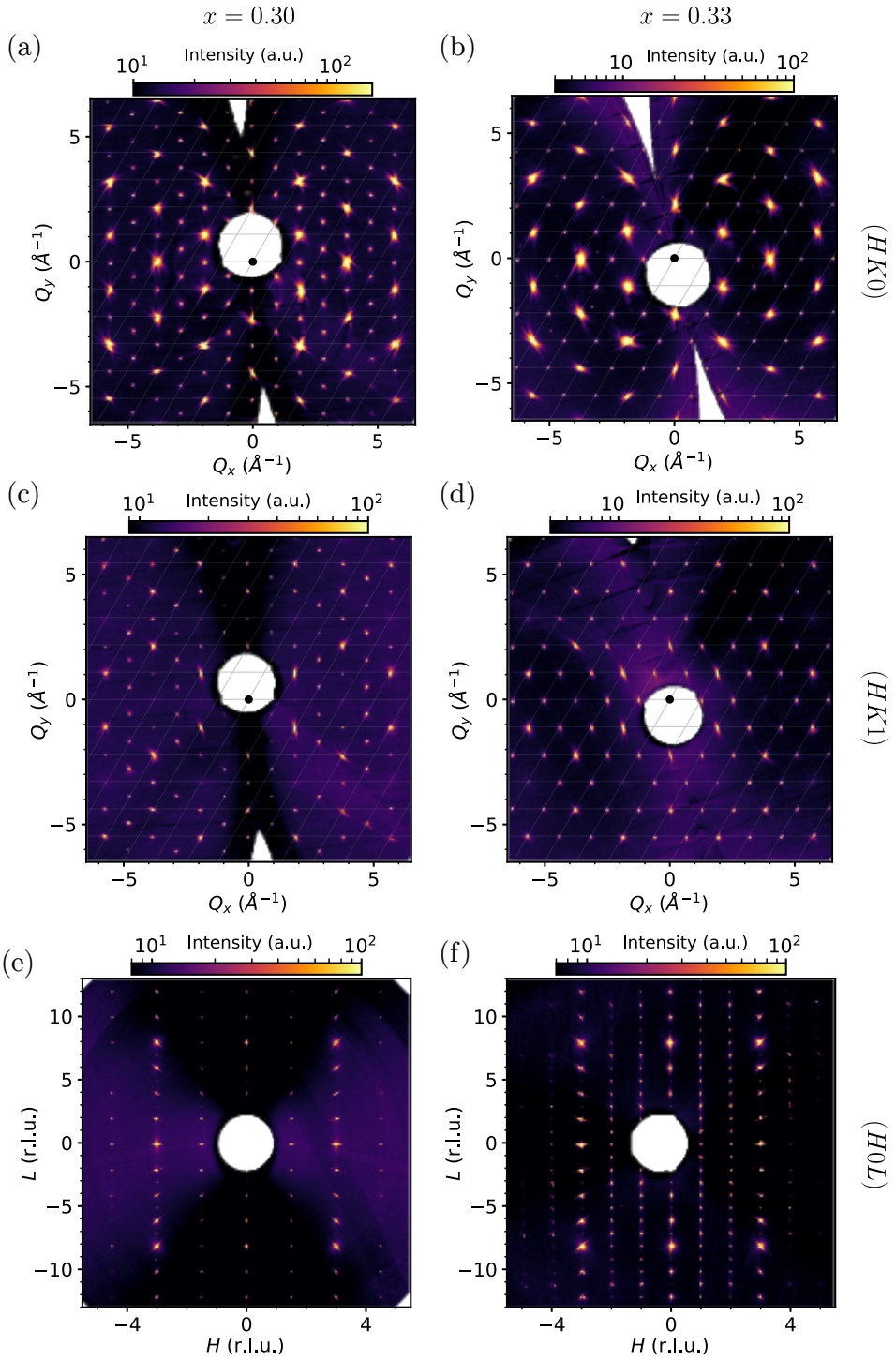

Figure 5.6: X-ray diffraction reciprocal space maps of Ni_xNbS_2, (a) $x = 0.30$ $(HK0)$, (b) $x = 0.33$s1 $(HK0)$, (c) $x = 0.30$ $(HK1)$, (d) $x = 0.33$s1 $(HK1)$, (e) $x = 0.30$ $(H0L)$, (f) $x = 0.33$s1 $(H0L)$. The data in (a)-(d) is integrated over 0.02 r.l.u. along L. The data in (e)-(f) is integrated over 0.01 r.l.u. along K. The black dot indicates the origin of the respective plane and the gridlines correspond to the reciprocal lattice of the $\sqrt{3} \times \sqrt{3}\,R30°$ superlattice.

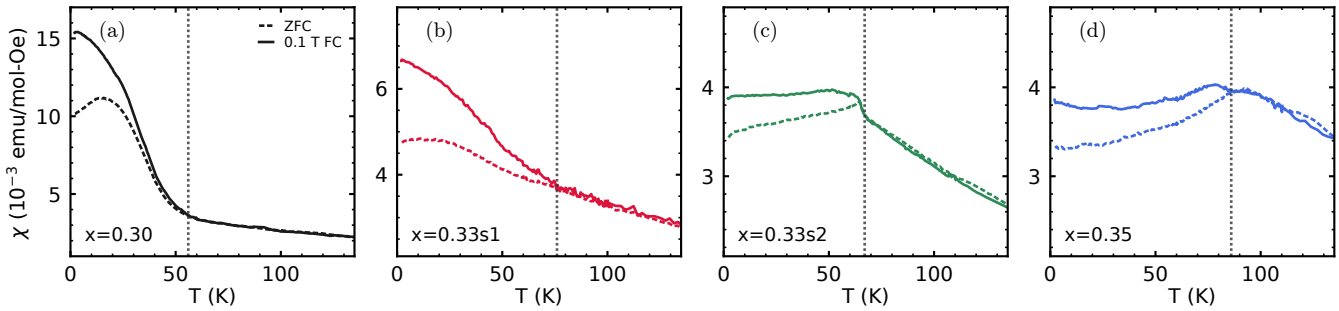

Figure 5.7: χ vs. T for Ni_xNbS_2 with various x, measured with 0.1 T along the (110) direction for field cooling and zero field cooling. Note the different y-axis ranges.

5.4.2 Magnetic susceptibility

Fig. 5.7 shows the magnetic susceptibiliy vs. temperature for different Ni_xNbS_2 samples, measured with a 0.1 T field along the (110) direction for both field cooling and zero field cooling. For $x = 0.30$ [Fig. 5.7(a)], we observe a broad transition to a weak ferromagnetic or canted antiferromagnetic (CAF) state at $T_N = 56$ K. For $x = 0.35$ [Fig. 5.7(b)], we observe an antiferromagnetic (AFM) transition at $T_N = 86$ K, consistent with the results of [96]. For $x = 0.33$, we observe a variety of behaviors, with two representative cases shown in Fig. 5.7(b) and (c). The first sample, $x = 0.33$s1, shows no sharp anomaly, but resembles a broad CAF transition at $T_N = 76$ K, similarly to $x = 0.30$. The second sample, $x = 0.33$s2, shows an AFM transition at $T_N = 67$ K similarly to $x = 0.35$.

5.4.3 Resonant elastic x-ray scattering (REXS)

To characterize the magnetic structures in Ni_xNbS_2, we carried out REXS at the Ni L_3 edge. The samples were mounted in the (HHL) scattering plane of the $\sqrt{3} \times \sqrt{3}\,R30°$ superlattice. which corresponds to the $(H0L)$ scattering plane for the 2×2 superlattice. In every sample, we find magnetic peaks around the (001) structurally forbidden Bragg peak at $2\theta = 75.6°$ at $E_i = 851.5$ eV. All measurements were performed in π polarization, which maximized magnetic intensity and minimized contamination from the (002) structural Bragg peak arising from the second harmonic content of the beam.

Temperature dependent scans along $(00L)$ for the four samples discussed above are shown

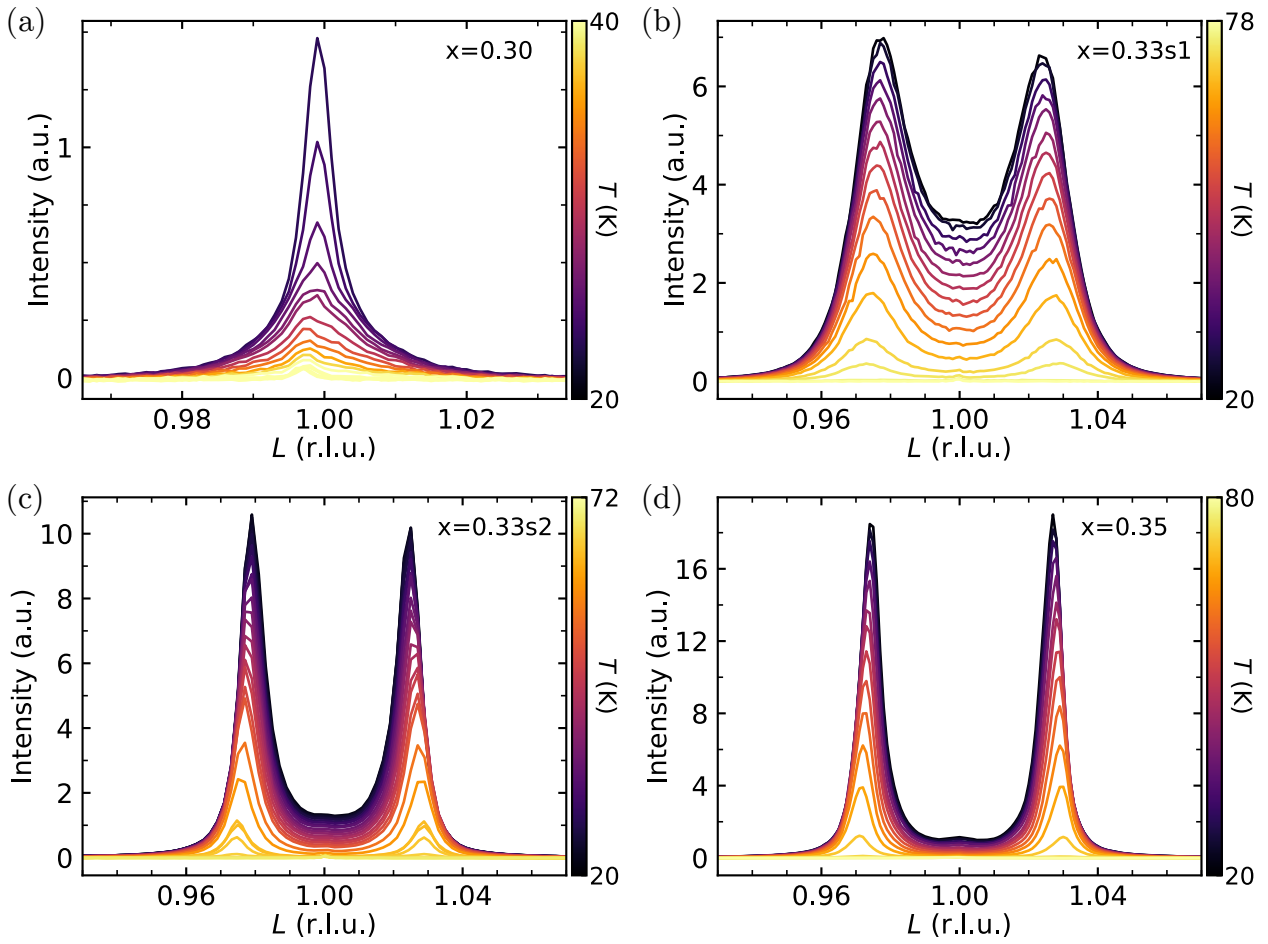

Figure 5.8: Temperature dependent REXS scans along $(00L)$ for (a) $x = 0.30$, (b) $x = 0.33$s1, (c) $x = 0.33$s2, and (d) $x = 0.35$. Note the different range along L for $x = 0.30$ and the different intensity scales for each sample.

in Fig. 5.8. For $x = 0.30$, we find a sharp commensurate (C) peak at $L = 1$. For each of the other samples, we find a broad C peak at (001) and sharp incommensurate (IC) satellites at $L = 1 \pm \delta$, with $\delta = 0.022$ - 0.030 r.l.u. dependending on temperature and sample. We fit each peak with a pseudo-Voigt function, using one for $x = 0.30$ and three for each of the other samples, with the satellites constrained to have equal width. The temperature dependence of the fit parameters is shown in Fig. 5.9.

The intensity vs. temperature for the C and IC peaks is shown in Fig. 5.9(a), with the IC intensity corresponding to the average of the two satellites. For $x = 0.35$, the intensity is dominated by the IC component. For $x = 0.33$s2, the relative intensity of the C component increases, but remains far less than the IC component. For $x = 0.33$s1, the C component is

more intense than the IC component. In this sample the C component and IC component turn on at the same temperature, while in $x = 0.35$ and $x = 0.30$, the C component appears to turn on at a slightly lower temperature than the IC component. However, this may be due to the difficulty in fitting such a broad component to the low intensity peak just below the transition. This exact or near coincidence of the onset temperature for both components confirms that the C component does not originate from impurity phase of the 2×2 superlattice. In all cases, the C and IC peak show a different characteristic temperature dependence.

The full width at half maximum (FWHM) for all peaks is nearly constant, except for $x = 0.30$, as shown in Fig. 5.9(c). This sample may be better described by a sharp peak over a diffuse background, with the diffuse component persisting at higher temperatures. This diffuse component resembles critical magnetic scattering from a fluctuating partially ordered state near the transition [291–293]. This partially ordered state is apparent in the susceptibility [Fig. 5.7(a)], which shows a signicantly broadened transition, likely due to structural disorder. This is also consistent with the lack of FC/ZFC splitting until far below the transition where the sharper peak arises.

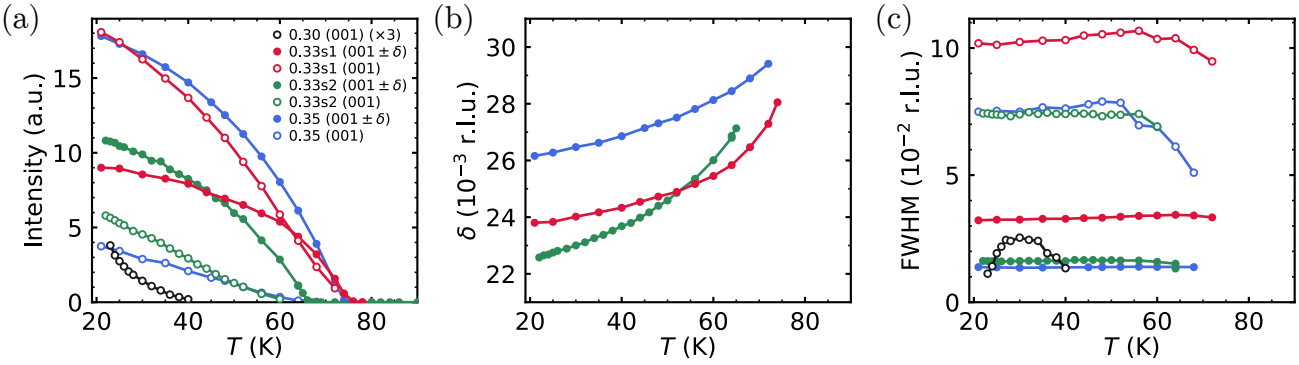

Figure 5.9: Temperature dependence of (a) integrated intensity, (b) magnitude of incommensurate wavector δ, and (c) full width at half maximum (FWHM). The filled and empty markers correspond to the incommensurate and commensurate peaks respectively.

5.4.4 Discussion

We have studied the structural and magnetic properties of Ni_xNbS_2 for samples with nominally $0.30 \leq x \leq 0.35$. For $x = 0.30$, the Ni ions form a 2×2 superlattice and order into

a canted antiferromagnetic state with a broad transition at $T_N = 56$ K. For $x \geq 0.33$, the Ni ions form a $\sqrt{3} \times \sqrt{3}\,R30°$ superlattice and order magnetically into a structure with C and IC components, indicating a conical- or fan-like structure.

Powder neutron diffraction measurements found a similar IC structure, determinining that the moments lie within the plane, with antiparallel alignment between the two spins per unit cell [96]. The appearance of a commensurate component in addition to the incommensurate satellites is consistent with an out-of-plane canting. This out-of-plane component may be parallel or antiparallel for the two spins per unit cell. The susceptibility is consistent with parallel alignment, giving a weak FM moment.

The most intringuing result is the difference between the two samples with $x = 0.33$. By decreasing x from 0.35, we observe two distinct behaviors. In $x = 0.33$s1, we observe a reduction in T_N, δ, and the correlation length, the transition is broadened, and the C component is larger than the IC component. In $x = 0.33$s2 however, we observe an even greater reduction in T_N and δ, but the correlation length is unchanged, the transition remains sharp, and the C component remains smaller than the IC component.

Thus, we cannot identify a conclusive trend in the magnetic properties with decreasing x. One possible explanation is the distinct role of vacancies and site disorder. By decreasing x, the Fermi level is decreased by hole doping, which modifies the itinerant exchange. However, with more vacancies, the site occupied by the Ni intercalants within each unit cell becomes less constrained. Thus, for a given x, the magnetic properties can be affected by the degree of site disorder. These effects are further complicated by defect correlations and structural domains [94, 233, 234, 253]. Future work should consider these effects by varying the crystal growth conditions and thus tuning the degree of quenched disorder for a given sample composition.

CHAPTER 6

Magnetic correlations and electronic structure of $NiGa_2S_4$

This chapter describes resonant x-ray scattering experiments on the $S = 1$ triangular lattice antiferromagnet $NiGa_2S_4$. Using resonant elastic x-ray scattering (REXS), we find a longer spin correlation length than previously found from neutron diffraction, as well as a previously unknown temperature-induced shift in the magnetic propagation vector. We also confirm the results of recent polarized neutron scattering measurements of the temperature dependent spin state anisotropy. Using resonant inelastic x-ray scattering (RIXS), we rule out the negative charge transfer ground state, instead finding a mixed valence state consisting of predominantly Ni^{2+} sites in a positive charge transfer ground state with Ni^{1+} impurities occupying low symmetry sites induced by sulfur vacancies.

6.1 Introduction

The triangular lattice antiferromagnet is the archetype of geometric frustration [8, 41, 42] (see section 1.2.2). For nearest neighbor Heisenberg exchange, this lattice has a 120° ordered magnetic structure. However, higher order exchange, further neighbor interactions, or anisotropy can suppress ordering and stabilize a quantum spin liquid state. These interactions

can stabilize more exotic states involving magnetic quadrupoles (nematic order), vector spin chirality, or emergent topological degrees of freedom [294].

$NiGa_2S_4$ is a nearly ideal realization of a $S = 1$ triangular lattice compound. This material consists of weakly coupled van der Waals layers, with each layer containing a triangular lattice of edge-sharing NiS_6 octahedra between 2 layers of GaS_4 tetrahedra, as shown in 6.1(a). Despite a large Curie-Weiss temperature of 80 K, long-range magnetic order has not been detected down to $T = 50$ mK. Magnetic susceptibility, heat capacity, NMR, NQR, μSR, and ESR experiments report phenomenology common to frustrated magnets including a two-step entropy release and critical slowing down of magnetic fluctuations at $T^* = 8.5$ K [295–300]. Neutron scattering experiments find short range incommensurate spin correlations starting below 20 K at a wavevector of $Q^* = (0.155, 0.155, 0)$, as shown in Fig. 6.1(b), but even at 1 K, a significant fraction of the moment remains fluctuating [300–302]. The low temperature magnetic heat capacity is proportional to T^2, indicating the presence of gapless linearly dispersive modes associated with long range ordering. This suggests the ordering of some elusive higher-order degree of freedom. A variety of explanations for this puzzling behavior have been proposed, including a vortex binding-unbinding transition of the vector spin chirality [303–306], quadrupolar or spin-nematic order [9, 10, 13–15], and C_3-symmetry-breaking bond order [10, 307].

The wavevector of the short-range incommensurate spiral correlations observed by neutron diffraction can only be explained by a dominant third-nearest-neighbor antiferromagnetic exchange and a weak nearest neighbor ferromagnetic exchange. X-ray photoelectron spectroscopy (XPS) measurements are consistent with a negative charge-transfer ground state, in which the electronic ground state is dominated by a $3d^9\underline{L}$ configuration, where $\underline{L}$ is a S $3p$ hole. It is this strong ligand hole character that allows for the large third-nearest-neighbor exchange interactions driving the incommensurate spiral correlations [308, 309]. A polarized neutron diffraction experiment found evidence for the vortex binding-unbinding transition indicated by reversal at T^* of the ratio of in-plane to out-of-plane spin component [306]. The quadrupolar

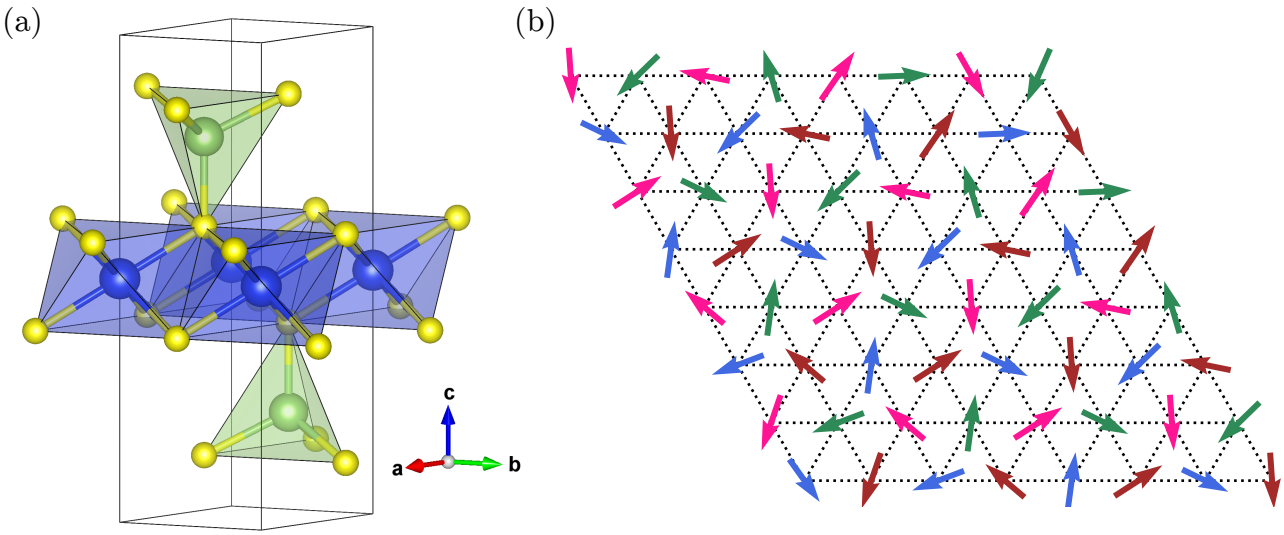

Figure 6.1: (a) Crystal structure of $NiGa_2S_4$, with Ni^{2+}, Ga^{3+}, and S^{2-} shown in blue, green, and yellow respectively. (b) Approximate spin structure of $NiGa_2S_4$, showing $(\frac{1}{6}\frac{1}{6}0)$ order composed of 120° order on four 2×2 sublattices, each shown as a different color. The true structure is incommensurate with $(0.155, 0.155, 0)$

or spin-nematic order would require the presence of biquadratic exchange interactions (see 1.1.3). A recent Raman scattering study identified a phonon mode that would provide the magnetoelastic coupling mechanism for this biquadratic exchange [9].

The magnetic properties of $NiGa_2S_4$ are known to be highly sensitive to disorder, including substitution of Ni ions with nonmagnetic or other magnetic ions [310–312], as well as sulfur off-stoichiometry [10, 313, 314]. Several experiments have found indirect signatures of structural disorder, such as a weak temperature-indepedent ESR resonance [296, 297], an extra Ga NQR peak [295, 313], and mixing of Raman and IR active phonon modes [9].

The exotic magnetic behavior of $NiGa_2S_4$ is tied to the negative charge-transfer ground state with a small energy gap, which enhances spin and charge fluctuations. This unique electronic structure suggests the possibiliy of a wide range of other effects involving strong correlations and quantum critical phenomena [294]. A recent high-pressure transport and Raman scattering study [315], found a series of pressure-induced structural transitions, one of which coincides with a metal-insulator transition in $NiGa_2S_4$. This motivates further work to understand the nontrivial electronic properties of this material and suggests routes for

realizing additional electronic and magnetic phenomena.

Here we carry out resonant x-ray scattering on $NiGa_2S_4$ to gain insight into the intriguing electronic and magnetic properties of this material. We use resonant elastic x-ray scattering (REXS) to probe the intrinsic magnetic correlations in $NiGa_2S_4$ within a small sample volume to minimize the effect of stacking faults and other structural disorder that may cut off magnetic correlations and complicate experimental interpretation. We use x-ray absorption spectroscopy (XAS) and resonant inelastic x-ray scattering (RIXS) to examine the local electronic structure of $NiGa_2S_4$. In addition, the polarization dependence of the REXS cross section allows for the determination of the spin orientations, which was left underconstrained in previous neutron experiments.

From the REXS data, we find a correlation length for the short range correlated incommensurate spiral structure that is twice as large as what was previously observed with neutron scattering. The polarization dependence is consistent with polarized neutron diffraction measurements [306]. The XAS and RIXS data cannot be explained by the negative charge transfer state proposed from previous XPS measurements. Instead, the spectrum is best described by a Ni^{2+}/Ni^{1+} mixed valence, with Ni^{1+} ions occupying low symmetry sites resulting from sulfur vacancies.

6.2 Experiment

Single crystals were grown using chemical vapor transport (CVT) as described in [313], using a starting composition of 1:2:4.04. Magnetic susceptibility was measured on a Quantum Design Physical Property Measurement System (PPMS) using the vibrating sample mount (VSM) option. Resonant elastic x-ray scattering (REXS) measurements at the Ni L_3 edge were carried out on the XUV diffractometer at the UE46 PGM-1 beamline at BESSY II [119, 316]. Resonant inelastic x-ray scattering (RIXS) measurements at the Ni L_3 edge were carried out at the I21 beamline at Diamond Light Source [317], with 39 meV FWHM energy-loss resolution

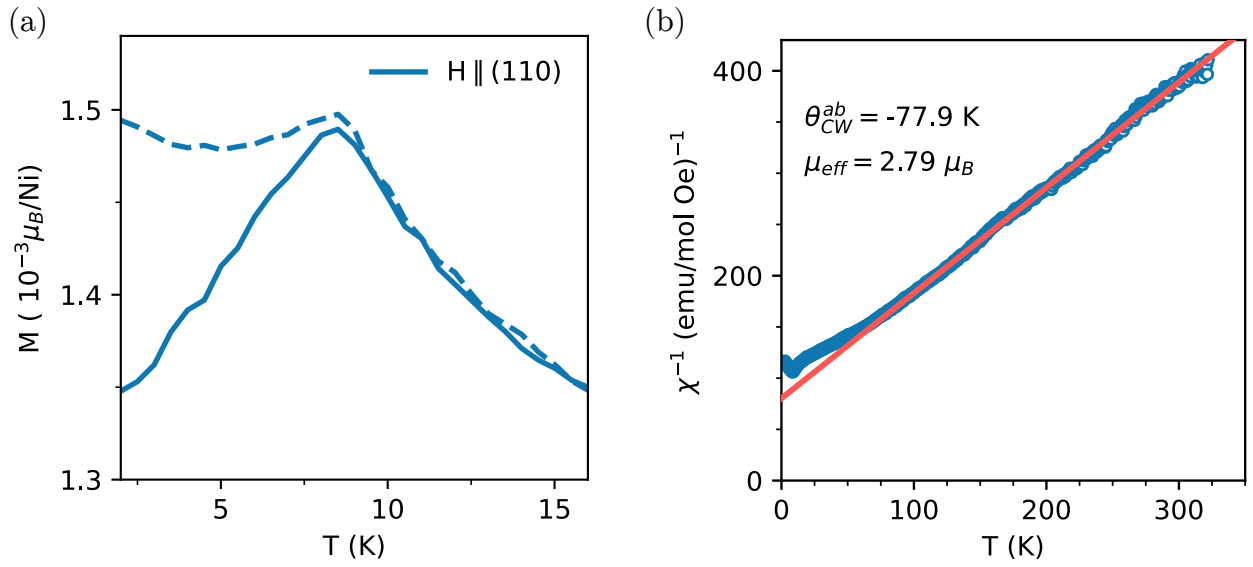

Figure 6.2: Magnetic susceptibility vs. temperature, measured with a 0.01 T field along the (110) direction for both field-cooling (FC) and zero-field-cooling (ZFC).

and at the 41A beamline at the Taiwan Photon Source [318], with 60 meV FWHM energy-loss resolution. Samples for both REXS and RIXS were cleaved immediately before loading into the scattering chamber.

6.3 Results

6.3.1 Sample characterization

Fig. 6.2(a) shows the magnetic susceptibility vs. temperature for a typical $NiGa_2S_4$ sample. The spin freezing transition appears as a kink with FC/ZFC splitting at $T^* = 8.2$ K. This value of T_f, along with the FC/ZFC splitting ratio $(\chi_{\mathrm{FC}} - \chi_{\mathrm{ZFC}})/\chi_{\mathrm{FC}} = 0.081$ at 1.8 K, indicates high quality, stoichiometric samples [294, 313]. Fig. 6.2(b) shows the Curie-Weiss fit of χ^{-1} to the $T > 150$ K region, giving $\Theta_{\mathrm{CW}} = -79.9$ K and $\mu_{\mathrm{eff}} = 2.79\mu_B$, consistent with previous reports.

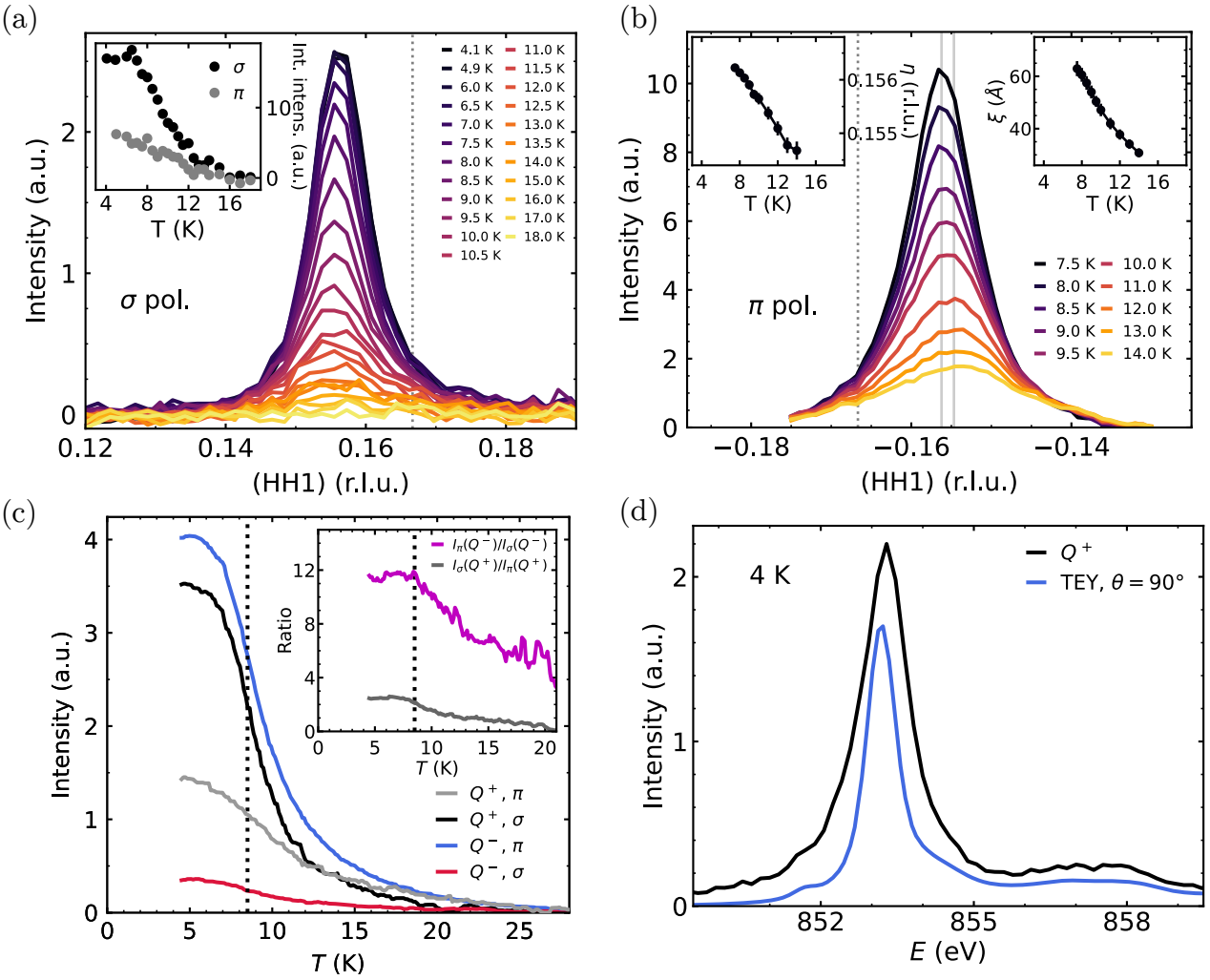

Figure 6.3: (a) REXS scans along $(HH1)$ at $\boldsymbol{Q}^+$ in σ polarization. The dotted vertical line indicates the $H = \frac{1}{6}$ commensurate position. The inset shows the integrated intensity vs. temperature for σ and π polarization. (b) REXS scans along $(HH1)$ at $\boldsymbol{Q}^-$ in π polarization. The dotted vertical line indicates the $H = -\frac{1}{6}$ commensurate position and the solid vertical lines show the shift in η between the maximum and minimum temperatures. The inset shows the value of η vs. temperature. (c) Temperature dependence of peak intensity for σ and π polarization at $\boldsymbol{Q}^\pm$. Intensities are absorption corrected. The inset shows the intensity ratios $I_\pi(\boldsymbol{Q}^-)/I_\sigma(\boldsymbol{Q}^-)$ and $I_\sigma(\boldsymbol{Q}^+)/I_\pi(\boldsymbol{Q}^+)$, with the latter being scaled by a factor of 4. The dotted vertical lines indicate $T^* = 8.5$ K. (d) Fixed-Q energy scan at $\boldsymbol{Q}^+$ and x-ray absorption measured in TEY, at 4 K.

6.3.2 Resonant elastic x-ray scattering (REXS)

We carried out REXS measurements at the Ni L_3 edge on $NiGa_2S_4$. The crystals were mounted in the (HHL) plane to access the incommensurate magnetic peaks in reflection geometry at $\boldsymbol{Q}^\pm = (001) \pm \boldsymbol{Q}^*$, $\boldsymbol{Q}^* = (\eta, \eta, 0)$, where $\eta \approx 0.156$ r.l.u., at a scattering angle

$2\theta = 120.5°$. From the x-ray absorption spectrum and fixed-Q energy scan at the magnetic peak, shown in Fig. 6.3(d), we set the incident energy to 853.25 eV for all measurements. We observe a small pre-edge peak, unusual for the Ni^{2+} L_3 edge, which will be discussed in section 6.3.3.

We measured the temperature and polarization dependence of the magnetic peaks along the $(HH1)$ direction, as shown in Fig. 6.3(a) for $\boldsymbol{Q}^+$ with σ polarization and Fig. 6.3(b) for $\boldsymbol{Q}^-$ with π polarization. Scans at 30 K, where no magnetic intensity is observed, are subtracted as background. The inset of Fig. 6.3(a) shows the integrated intensities vs. temperature for both σ and π polarizations at $\boldsymbol{Q}^+$. We observe an increase in η with decreasing temperature. The inset on the left side of Fig. 6.3(b) shows the value of η vs. temperature obtained from a Lorentzian fit. We find that η varies from 0.1562(1) r.l.u. at 4 K to 0.1547(2) r.l.u. at 14 K.

The correlation length was determined by fitting the data with a Lorentzian lineshape

$$I(\boldsymbol{Q}) = \frac{A}{1 + \xi^2(\boldsymbol{Q} - \boldsymbol{Q}^{\pm})^2}, \tag{6.1}$$

This gives a correlation length of $\xi = 63$ Å at base temperature, which is a factor of 2.5 larger than the correlation length of 25 Å determined from neutron diffraction [300–302]. This indicates that the intrinsic magnetic correlations may be longer-range than previously thought. The temperature dependent correlation length is shown in the inset on the right side of Fig. 6.3(b).

To more closely examine the temperature dependence of the magnetic scattering, we scanned temperature at fixed $\boldsymbol{Q}$. Fig. 6.3(c) shows temperature scans of the peak magnetic intensity at $\boldsymbol{Q}^{\pm}$ for both σ and π polarization. The intensity of each scan at 30 K is subtracted as background. The inset shows the intensity ratios $I_\sigma(\boldsymbol{Q}^+)/I_\pi(\boldsymbol{Q}^+)$ and $I_\pi(\boldsymbol{Q}^-)/I_\sigma(\boldsymbol{Q}^-)$. The dotted vertical line indicates $T^* = 8.5$ K. The $\boldsymbol{Q}$ position was fixed at the base temperature peak intensity during these scans. However, the shift in η does not produces a negligible error. In order to directly compare the intensities at different $\boldsymbol{Q}$, the data has been corrected by the

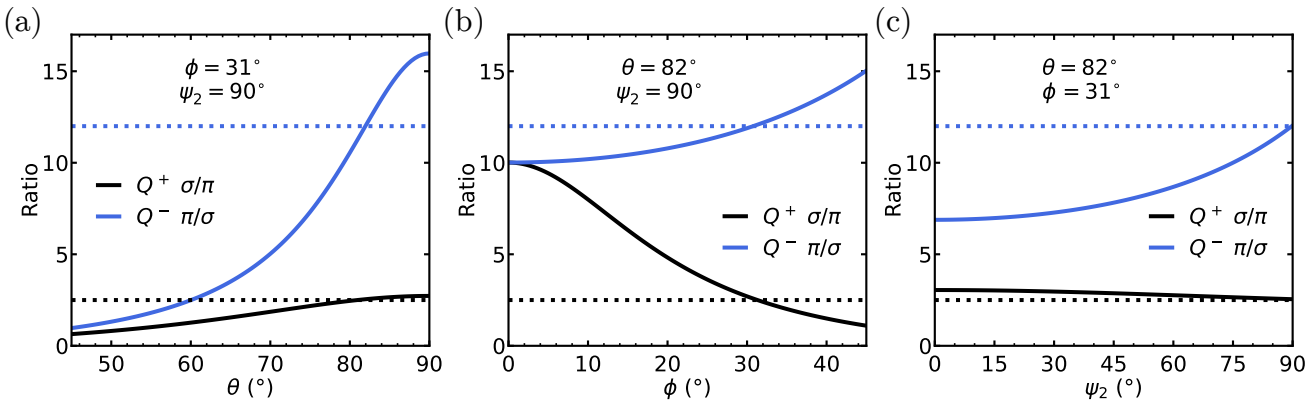

Figure 6.4: Calculated intensity ratios $I_\sigma(\boldsymbol{Q}^+)/I_\pi(\boldsymbol{Q}^+)$ (black) and $I_\pi(\boldsymbol{Q}^-)/I_\sigma(\boldsymbol{Q}^-)$ (blue) from eq. 6.2 and 6.3 as a function of (a) θ for $\phi = 31^\circ$ and $\psi_2 = 90^\circ$, (b) ϕ for $\theta = 82^\circ$ and $\psi_2 = 90^\circ$, (c) ψ_2 for $\theta = 82^\circ$ and $\phi = 31^\circ$. The horitontal dotted lines show the maximum measured values of each ratio, as shown in the inset of Fig. 6.3.

geometric factor $A = 1 + \frac{\sin\theta}{\sin\theta'}$, where we have assumed an isotropic absorption coefficienct [319].

To model the polarization dependence, we compute the REXS intensity for an incommensurate spiral with Fourier component

$$\boldsymbol{m_Q} = \sin\theta\cos\phi\hat{\boldsymbol{x}} + e^{i\psi_1}\sin\theta\sin\phi\hat{\boldsymbol{y}} + e^{i\psi_2}\cos\theta\hat{\boldsymbol{z}}, \tag{6.2}$$

where $\hat{\boldsymbol{x}}$ is parallel to $\boldsymbol{Q}^*$, $\hat{\boldsymbol{z}}$ is parallel to the c axis, and $\hat{\boldsymbol{y}} = \hat{\boldsymbol{z}} \times \hat{\boldsymbol{x}}$. The spin at position $\boldsymbol{r}_n$ is given by $\boldsymbol{m}(\boldsymbol{r}_n) = \boldsymbol{m_Q}e^{i\boldsymbol{Q}\boldsymbol{r}_n} + \boldsymbol{m_{-Q}}e^{-i\boldsymbol{Q}\boldsymbol{r}_n}$, where $\boldsymbol{m_{-Q}} = \boldsymbol{m}_{\boldsymbol{Q}}^*$. Previous neutron diffraction measurements are consistent with either and in-plane spiral with $\theta = 90^\circ$ and $\phi = 41^\circ$ or an out-of-plane spiral with $\theta = 57^\circ$ and $\phi = 0^\circ$ [302].

Since we do not resolve the polarization of the scattered beam, the intensity for incident σ and π polarization are given by $I_\sigma = I_{\sigma\sigma} + I_{\pi\sigma} = I_{\pi\sigma}$ and $I_\pi = I_{\sigma\pi} + I_{\pi\pi}$ respectively, where $I_{\boldsymbol{\epsilon}'\boldsymbol{\epsilon}}(\boldsymbol{Q}) \propto |(\boldsymbol{\epsilon}' \times \boldsymbol{\epsilon})\cdot\boldsymbol{M}(\boldsymbol{Q})|^2$ is the magnetic scattering intensity for magnetic structure factor $\boldsymbol{M}(\boldsymbol{Q})$, incident polarization $\boldsymbol{\epsilon}$, and outgoing polarization $\boldsymbol{\epsilon}'$. There is only one moment per unit cell, so $\boldsymbol{M}(\boldsymbol{Q}) = \boldsymbol{m_Q}$. We can relate the polarization vectors to the incident and scattered

x-ray wavevectors, as described in section 2.4,

$$\begin{aligned} I_\sigma &\propto |\hat{\boldsymbol{k}}' \cdot \boldsymbol{m_Q}|^2 \\ I_\pi &\propto |\hat{\boldsymbol{k}} \cdot \boldsymbol{m_Q}|^2 + |(\hat{\boldsymbol{k}}' \times \hat{\boldsymbol{k}}) \cdot \boldsymbol{m_Q}|^2. \end{aligned} \tag{6.3}$$

$\boldsymbol{Q}^+$ and $\boldsymbol{Q}^-$ are both found at $2\theta = 120.5°$, with $\theta_\mathrm{i} = 106°$ and $\theta_\mathrm{i} = 14.5°$ respectively, where $\boldsymbol{k} \parallel (110)$ at $\theta = 0°$. Thus, in the frame of eq. 6.2, $I_\sigma(\boldsymbol{Q}^+)$ is most sensitive to moment along $\hat{\boldsymbol{x}}$, $I_\pi(\boldsymbol{Q}^+)$ is most sensitive to moment along $\hat{\boldsymbol{z}}$ and $\hat{\boldsymbol{y}}$, $I_\sigma(\boldsymbol{Q}^-)$ is most sensitive to moment along $\hat{\boldsymbol{z}}$, and $I_\pi(\boldsymbol{Q}^-)$ is most sensitive to moment along $\hat{\boldsymbol{x}}$ and $\hat{\boldsymbol{y}}$.

To compare to the data, we compute the intensity ratios $I_\sigma(\boldsymbol{Q}^+)/I_\pi(\boldsymbol{Q}^+)$ and $I_\pi(\boldsymbol{Q}^-)/I_\sigma(\boldsymbol{Q}^-)$, which roughly correspond to the ratio of in-plane to out-of-plane component of $\boldsymbol{m_Q}$. The measured values of these ratios are maximized near base temperature with 2.5 and 12 for $\boldsymbol{Q}^+$ and $\boldsymbol{Q}^-$ respectively. This can be reproduced by eq. 6.2 with $\theta = 82(1)°$, $\phi = 31(1)°$, and $\psi_2 = 90(1)°$, as shown in Fig. 6.4. As temperature increases, the ratios both decrease toward zero. At 15 K, the data is consistent with $\theta = 71(1)°$, $\phi = 42(1)°$, and $\psi_2 = 90(1)°$. Thus, the spiral becomes increasingly confined within the plane as temperature decreases.

These results are consistent with recent polarized neutron scattering, which considered the temperature dependence of the ratio m_{xy}/m_z extracted from spin-flip and non-spin-flip scattering channels [306]. They found a maximum of $m_{xy}/m_z = 8$ at $T^* = 8.5$ K, which decreased to $m_{xy}/m_z = 3$ at 15 K. This ratio is related to our model by $m_{xy}/m_z = \tan\theta$, which gives $\theta = 83°$ at 8.5 K and $\theta = 72°$ at 15 K, in close agreement with out results.

6.3.3 Resonant inelastic x-ray scattering (RIXS)

We carried out RIXS measurements at the Ni L_3 edge on $NiGa_2S_4$. The sample was mounted in the (HHL) plane and we measured RIXS spectra for variable incident energy E_in, scattering angle 2θ, sample angle θ, incident polarization, and temperature. Fig. 6.5(a) shows the RIXS energy map of $NiGa_2S_4$, measured at $2\theta = 90°$, $\theta = 38°$, π polarization, and

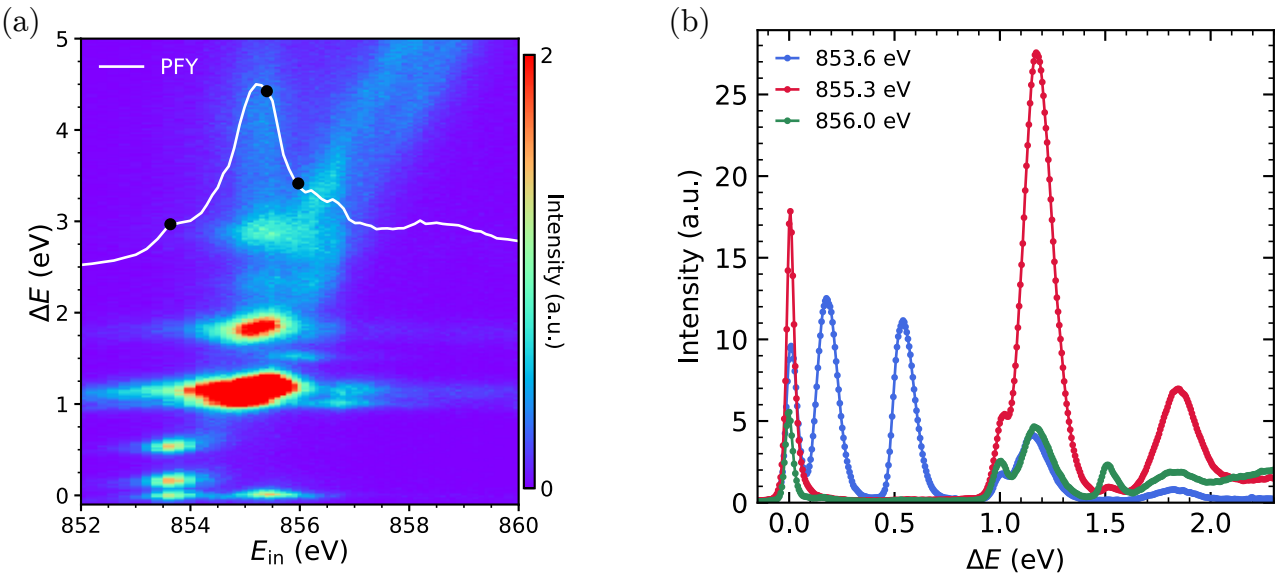

Figure 6.5: (a) RIXS energy map at $2\theta = 90°$, $\theta = 38°$, π polarization, 23 K (b) RIXS spectra at $2\theta = 90°$, $\theta = 30°$, π polarization, 62 K at the incident energy energies corresponding to the black markers in (a).

23 K. The partial fluorescence yield (PFY), shown as a white line, is obtained by integrating the RIXS intensity over energy loss at each incident energy. The black markers indicate the incident energies of the RIXS spectra shown in Fig. 6.5(b). The data in Fig. 6.5(a) was obtained at TPS 41A and all other RIXS data shown in this chapter was obtained at Diamond I21. To correct for the difference in beamline energy calibration, we shift the incident energies in the RIXS map by 2 eV.

The RIXS spectrum shows several energy-loss features that resonate at various incident energies. Here we consider the three incident energies shown as black markers in Fig. 6.5(a), with the individual spectra shown in Fig. 6.5(b). These correspond to a pre-edge at 853.6 eV, main resonance at 855.3 eV, and a post-edge shoulder at 856.0 eV. The main resonance is typical for octahedral Ni^{2+}, with peaks at 1.01 eV, 1.16 eV, 1.83 eV, 2.34 eV, 2.87 eV, 4.1 eV. The post-edge shoulder is also typical for octahedral Ni^{2+}, giving rise to the 1.51 eV "exciton" [320–325]. However, the pre-edge, with peaks at 170 meV and 530 meV, is highly unusual. No such peak has been reported for Ni^{2+} compounds.

To gain further insight into the origin of this pre-edge peak, we examine the polarization

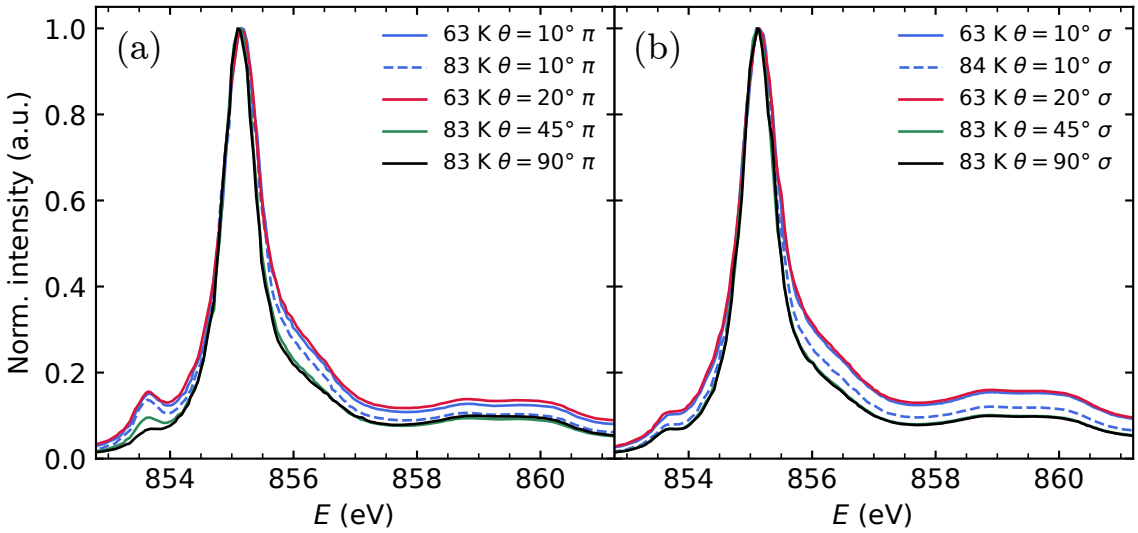

Figure 6.6: Angle dependence of Ni L_3-edge XAS (TEY) for (a) π and (b) σ polarization.

and angle dependence of the XAS. Fig. 6.6(a) and (b) show the angle-dependence of the XAS measured in TEY for π and σ polarization respectively. For σ polarization, the polarization is parallel to the sample rotation axis, so varying θ does not affect the intrinsic absorption cross section. It does however vary the effective footprint of the beam onto the sample. To account for this geometric effect, we normalize each spectrum by peak intensity. After normalization, the σ polarized absorption is angle-independent, as expected. The variation after normalization is due to temperature differences, as TEY is highly dependent on resistivity. The lack of angle dependence in the relative intensity of the pre-edge confirms that it is not a surface effect.

For π polarization, the projection of the polarization onto the sample depends on θ. At $\theta = 0°$ (grazing incidence), the polarization is along the c-axis. At $\theta = 90°$ (normal incidence), the polarization is along the (110) direction. We find that the pre-edge intensity increases with decreasing θ, i.e. it increases with increasing projection of the polarization along the c-axis.

We observe no sign of dispersion for any excitations. The incident angle dependence shows only intensity changes due to geometric effects, as shown in Fig. 6.7(a-c). The RIXS spectrum at $2\theta = 150°$, shown in Fig. 6.7(d), shows no change other than the expected increase in elastic intensity. We observe minimal temperature dependence in the RIXS spectrum, as shown in 6.8 for the main resonance and pre-edge. The inelastic peaks show slight thermal broadening at

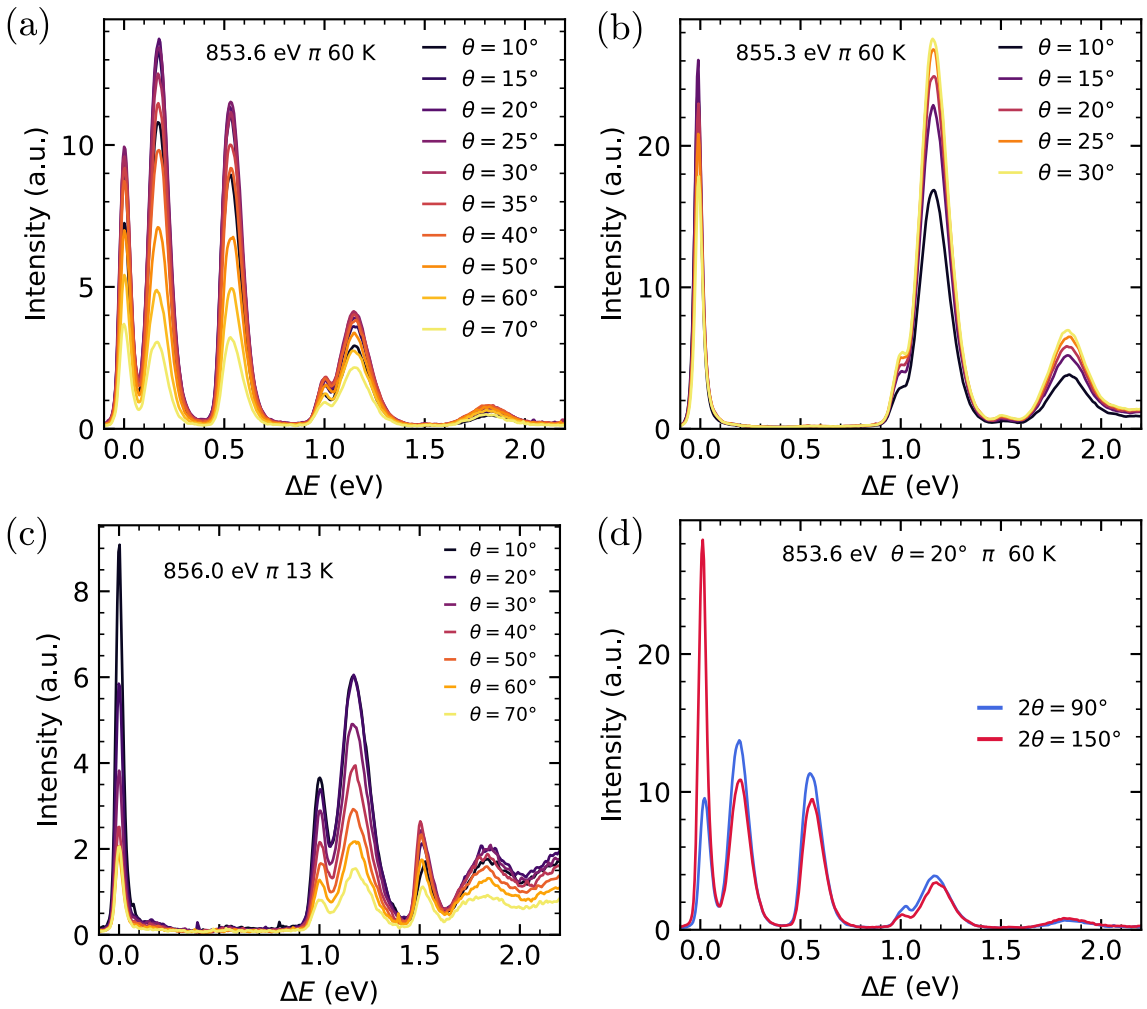

Figure 6.7: RIXS angle dependence, π polarization, (a) θ dependence, $2\theta = 90°$ at main resonance, 60 K (b) θ dependence, $2\theta = 90°$ at pre-edge, 60 K, (c) θ dependence, $2\theta = 90°$ at exciton, 13 K, (d) 2θ dependence, $\theta = 20°$, at pre-edge, 60 K

both incident energies. At the main resonance, the quasielastic intensity increases, most likely due to increased phonon scattering. However, the pre-edge quasielastic intensity is temperature independent. This suggests that the pre-edge does not strongly couple to phonons.

We model the XAS and RIXS spectra using an Anderson impurity model (AIM), as described in section 2.6. This model considers a Ni ion hybridized with a bath of ligand orbitals, including an on-site Coulomb repulsion U, ($U_{pd} = 1.2U$ for the intermediate state), Slater integral scale factors F_{dd}, F_{pd}, G_{pd}, charge-transfer energy Δ, hopping integrals $V_{eg} = -\sqrt{3}pd\sigma$, $V_{t2g} = 2pd\pi$, bath splitting $10Dq_{\text{bath}} = 2T_{pp}$, spin-orbit coupling $\lambda = 83$ meV ($\lambda_n = 102$ meV in the intermediate state), core hole spin-orbit coupling $\lambda_c = 11.4$ eV, cubic crystal field splitting

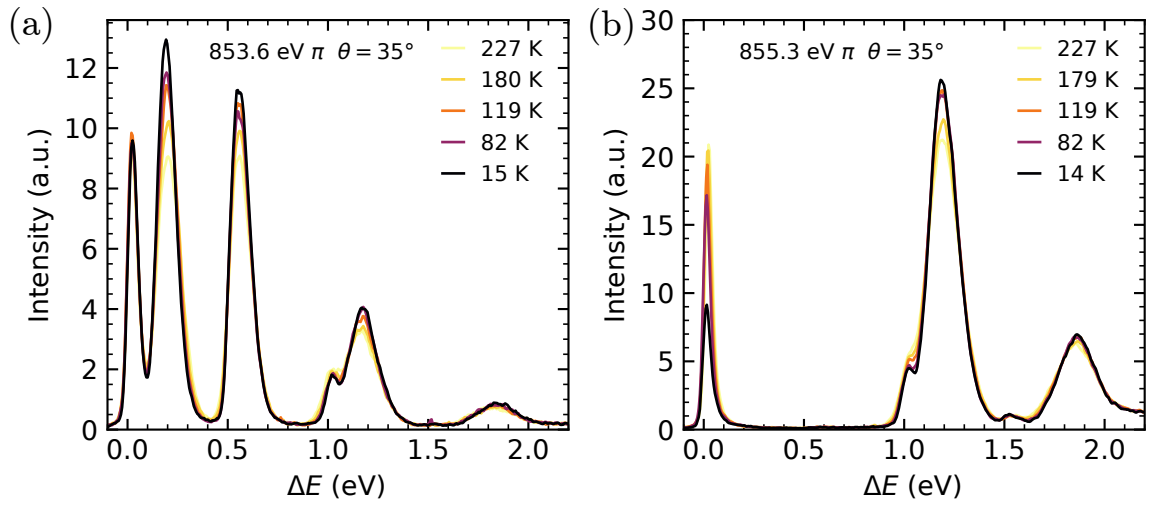

Figure 6.8: RIXS temperature dependence dependence at $2\theta = 90°$, π polarization, $\theta = 35°$ at the (a) pre-edge and (b) main resonance

$10Dq$, and trigonal splitting δ. For each of the cases considered below, we diagonalize the initial and intermediate state Hamiltonians to compute the XAS and RIXS spectra. We also compute the weight from each configuration of d orbital and ligand occupations.

We first consider the case of Ni^{2+} with negative charge transfer energy ($\Delta < 0$), with the results summarized in Fig. 6.9. This model yields a weakly split main peak at both L_3 and L_2 edges, missing the post-edge shoulder and the L_3 pre-edge. In addition, the satellite peak energies and splitting are overestimated. This model can roughly capture the energy-loss of the RIXS peaks at the main resonance, but cannot reproduce the intensities. In addition to the peaks above 1 eV, it also predicts two peaks below 1 eV, remniscent of the peaks at the pre-edge. However, the energy-loss and intensities cannot be reproduced. For the ground state $|\Psi\rangle = \alpha|d^8L^{10}\rangle + \beta|d^9L^9\rangle + \gamma|d^{10}L^8\rangle$, this model gives $\alpha^2 = 0.35$, $\beta^2 = 0.58$, and $\gamma^2 = 0.07$. This is consistent with the previous XPS results, which found $\alpha^2 = 0.25$ eV, $\beta^2 = 0.6$, and $\gamma^2 = 0.15$ using $\Delta = -1$ eV [308, 309].

To obtain more suitable description of the data, we try Ni^{2+} with $\Delta > 0$. The results are summarized in Fig. 6.10. This model accurately reproduces both the XAS and RIXS, but still cannot capture the pre-edge. This gives a ground state occupation of $\alpha^2 = 0.63$ eV, $\beta^2 = 0.35$, and $\gamma^2 = 0.02$.

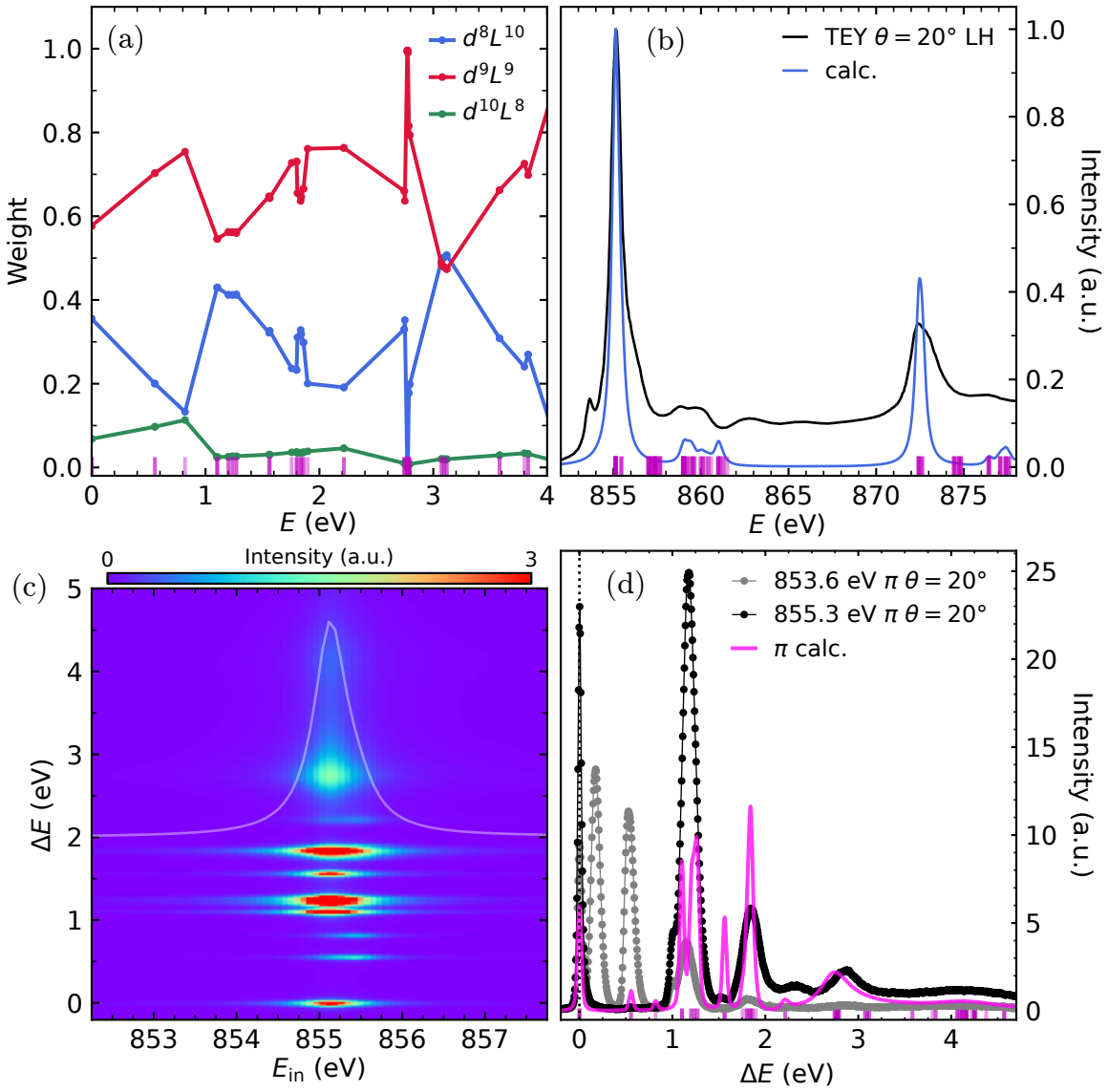

Figure 6.9: Calculation for Ni^{2+}, negative charge-transfer $U = 6.0$ eV, $U_{pd} = 7.2$ eV, $F_{dd} = 0.85$, $F_{pd} = G_{pd} = 0.8$, $\lambda = 83$ meV, $\Delta = -0.7$ eV, $10Dq = 0.4$ eV, $\delta = -0.15$ eV, $pd\sigma = -1.0$ eV, $pd\pi = 0.56$ eV, $T_{pp} = 1.0$ eV, (a) Weight of d^8L^{10}, d^9L^9, $d^{10}L^8$ configurations for calculated energy levels. (b) Calculated XAS spectrum, π polarization, $\theta = 20°$ and XAS measured from TEY. (c) Calculated RIXS energy map, π polarization, $2\theta = 90°$, $\theta = 20°$. (d) Calculated RIXS spectrum at main resonance and measured RIXS at main resonance and pre-edge.

The pre-edge cannot be reproduced by any reasonable model for Ni^{2+}. This suggests that $NiGa_2S_4$ may exhibit a mixed valence state, with either Ni^{3+} or Ni^{1+} impurities. We first consider the case of Ni^{3+}. This valence state has a much larger Hilbert space than Ni^{2+} and the parameter space cannot be as easily constrained. We thus consider a rough approximation using the same parameters as Ni^{2+}, with the results summarized in Fig. 6.11. The ground

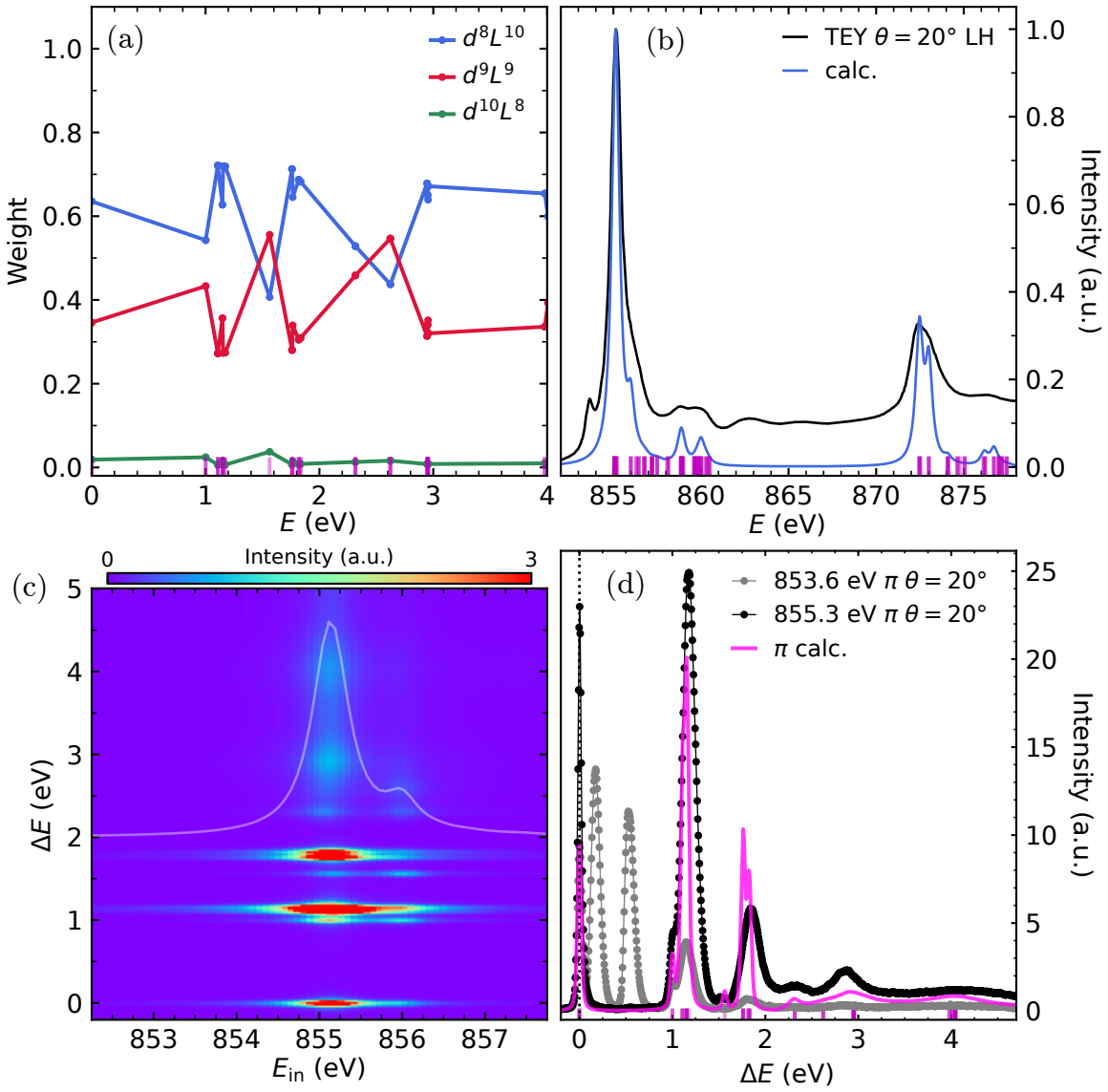

Figure 6.10: Calculation for for Ni^{2+}, positive charge-transfer. $U = 6.0$ eV, $U_{pd} = 7.2$ eV, $F_{dd} = F_{pd} = G_{pd} = 0.8$, $\lambda = 83$ meV, $\Delta = 1.8$ eV, $10Dq = 0.55$ eV, $\delta = 0$ eV, $pd\sigma = -1.04$ eV, $pd\pi = 0.58$ eV, $T_{pp} = 1.0$ eV, (a) Weight of d^8L^{10}, d^9L^9, $d^{10}L^8$ configurations for calculated energy levels. (b) Calculated XAS spectrum, π polarization, $\theta = 20°$ and XAS measured from TEY. (c) Calculated RIXS energy map, π polarization, $2\theta = 90°$, $\theta = 20°$. (d) Calculated RIXS spectrum at main resonance and measured RIXS at main resonance and pre-edge.

state is $|\Psi\rangle = \alpha|d^7L^{10}\rangle + \beta|d^8L^9\rangle + \gamma|d^9L^8\rangle + \delta|d^{10}L^7\rangle$ with $\alpha = 0.66$, $\beta = 0.32$, $\gamma = 0.018$, $\delta = 0.0002$, with a high-spin state. The XAS has a rich multiplet structure, with the lowest energy peak resembling the pre-edge. At this peak, we find RIXS peaks directly at the same energy-loss as the obvserved pre-edge RIXS peaks. However, the intensity of the higher energy peak is almost negligible. Furthermore, these low energy peaks also appear at higher incident

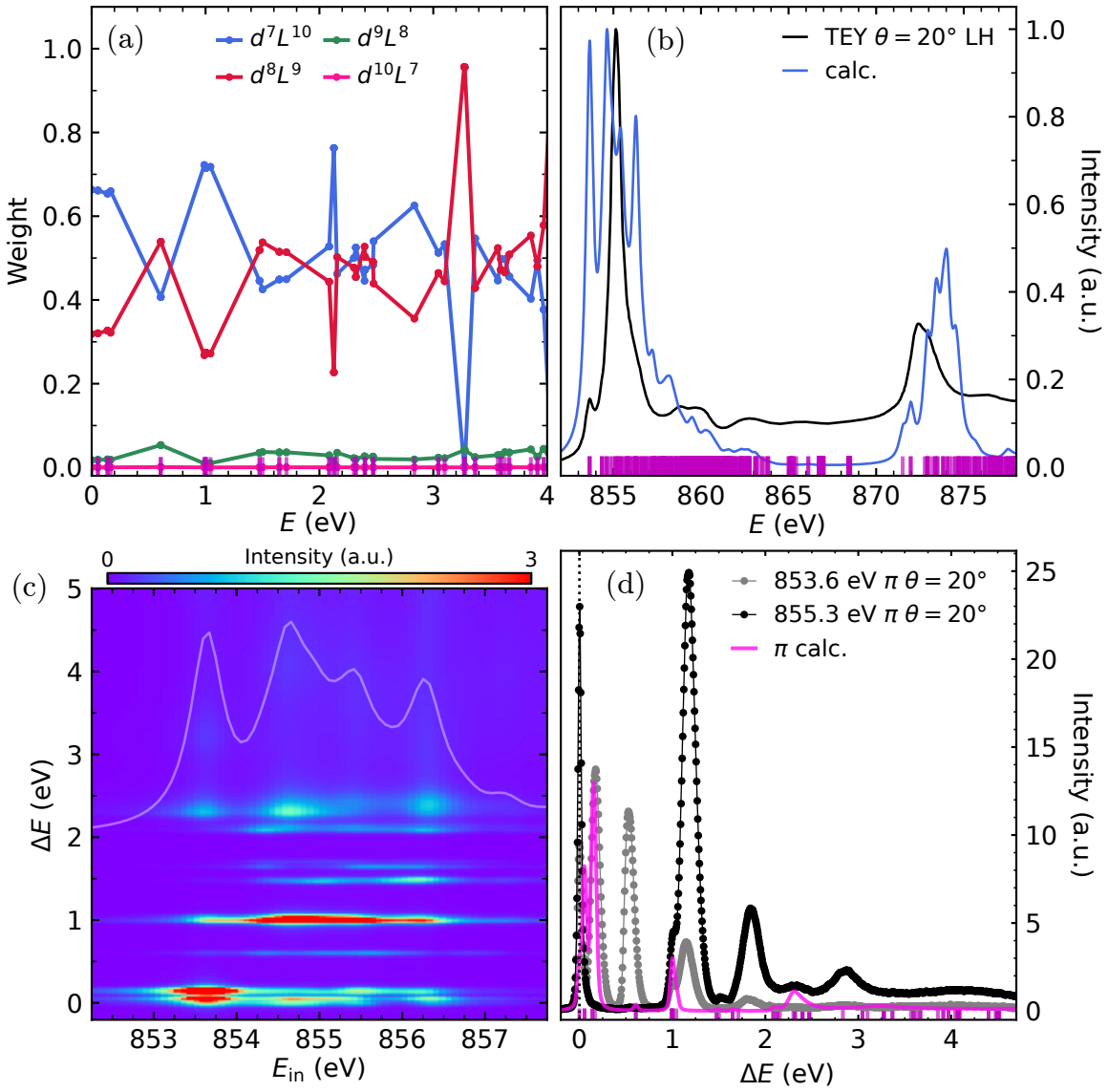

Figure 6.11: Calculation for Ni^{3+}, $\Delta > 0$ high spin state, same parameters as Ni^{2+} for $\Delta > 0$ eV. $U = 6.0$ eV, $U_{pd} = 7.2$ eV, $F_{dd} = F_{pd} = G_{pd} = 0.8$, $\lambda = 83$ meV, $\Delta = 1.8$ eV, $10Dq = 0.55$ eV, $\delta = 0$ eV, $pd\sigma = -1.04$ eV, $pd\pi = 0.58$ eV, $T_{pp} = 1.0$ eV, (a) Weight of d^7L^{10}, d^8L^9, d^9L^8, $d^{10}L^7$ configurations for calculated energy levels. (b) Calculated XAS spectrum, π polarization, $\theta = 20°$ and XAS measured from TEY. (c) Calculated RIXS energy map, π polarization, $2\theta = 90°$, $\theta = 20°$. (d) Calculated RIXS spectrum at main resonance and measured RIXS at main resonance and pre-edge.

energies, inconsistent with the data.

Next we try Ni^{1+}, with the results summarized in Fig. 6.12. The ground state is $|\Psi\rangle = \alpha|d^9L^{10}\rangle + \beta|d^{10}L^9\rangle$, with $\alpha = 0.90$ and $\beta = 0.1$. The XAS is consistent with the pre-edge. To match the low energy excitations observed at the pre-edge, this model requires $10Dq < 0$ and

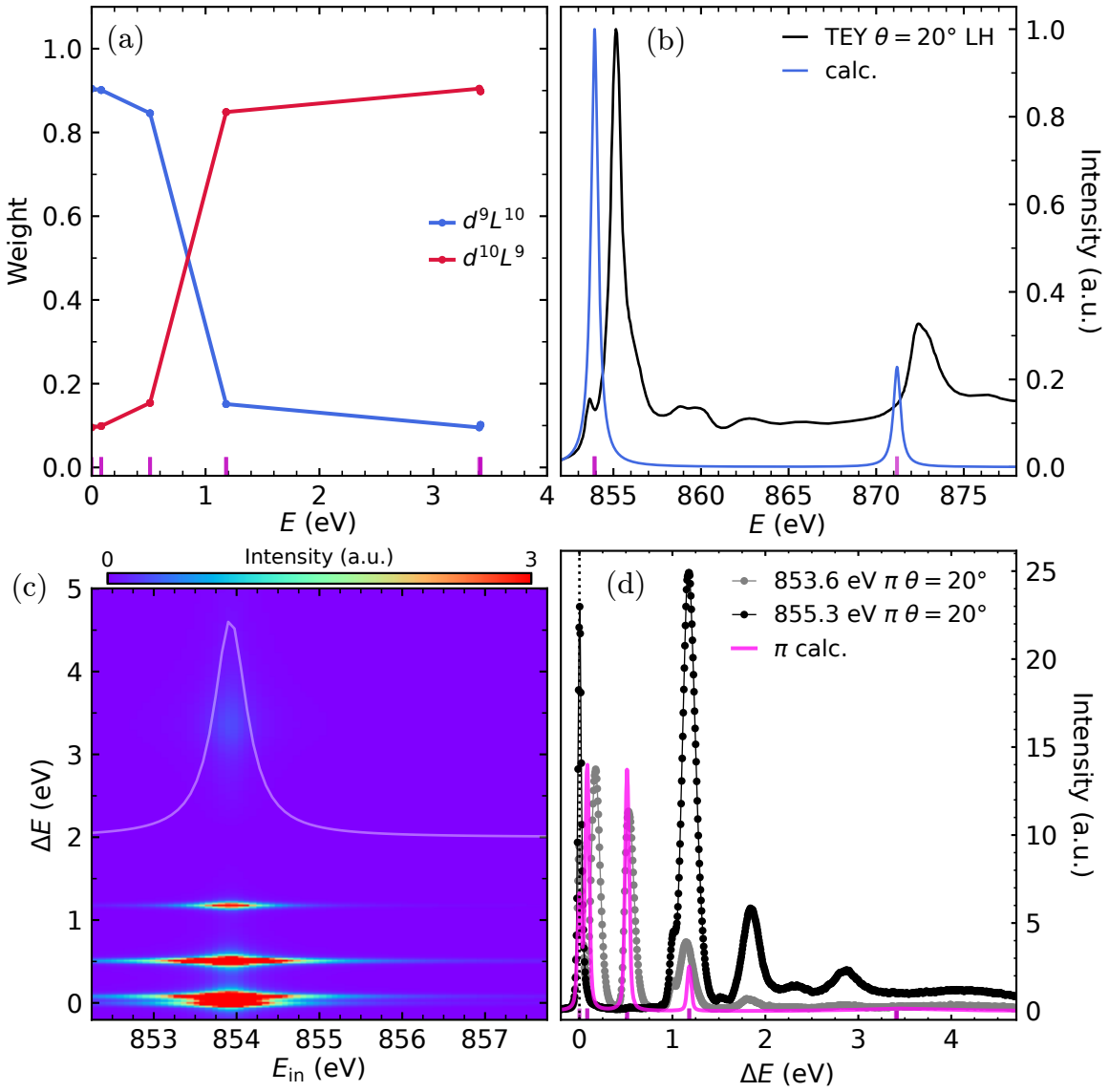

Figure 6.12: Calculation for Ni^{1+}. $U = 6.0$ eV, $U_{pd} = 7.2$ eV, $F_{dd} = F_{pd} = G_{pd} = 0.8$, $\lambda = 83$ meV, $\Delta = 1.8$ eV, $10Dq = -0.2$ eV, $\delta = 0$ eV, $pd\sigma = -0.14$ eV, $pd\pi = 0.5$ eV, $T_{pp} = 1.0$ eV, (a) Weight of d^7L^{10}, d^8L^9, d^9L^8, $d^{10}L^7$ configurations for calculated energy levels. (b) Calculated XAS spectrum, π polarization, $\theta = 20°$ and XAS measured from TEY. (c) Calculated RIXS energy map, π polarization, $2\theta = 90°$, $\theta = 20°$. (d) Calculated RIXS spectrum at main resonance and measured RIXS at main resonance and pre-edge.

$pd\pi > pd\sigma$, which corresponds to a tetrahedral crystal field. This would require the Ni^{1+} ions to occupy the tetrahedral Ga^{3+} sites. However, powder neuton diffraction has ruled out such site mixing [313]. This would also be unlikely due to the instability of Ni^{1+} on tetrahedral sites. It is well-known that tetrahedral Ni^{2+} is highly unstable [159]. Ni^{1+} has a larger ionic radius than Ni^{2+} and would thus be even less stable. Another possibility is reduced symmetry on

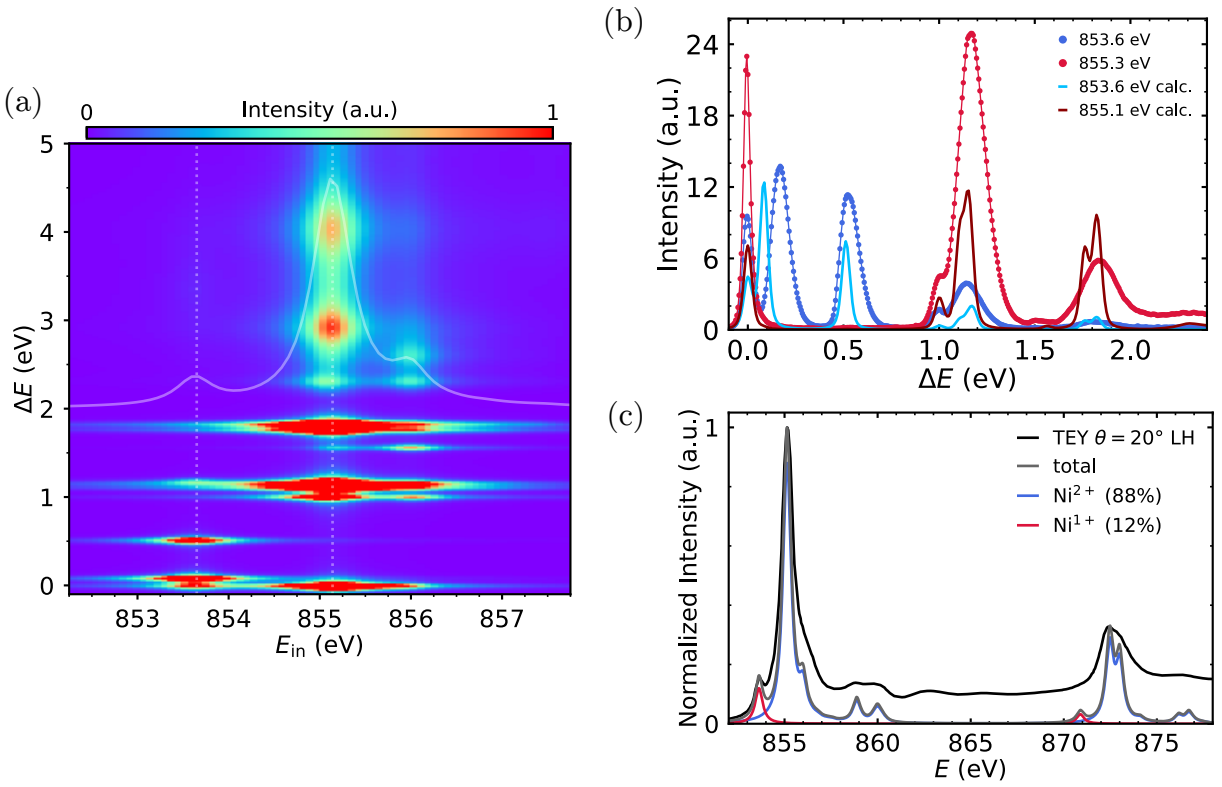

Figure 6.13: Calculations for Ni^{2+}/Ni^{1+} mixture. (a) RIXS map. (b) RIXS spectra at incident energies indicated by vertical lines in (a) plotted with measured spectra. (c) XAS spectra for each valence and total, plotted with measured spectrum.

the octahedral site by sulfur vacancies. Raman measurements have suggested local symmetry breaking at Ni sites due to sulfur vacancies, with the point group reduced to C_3 or C_{3v}.

Based on these results, the most likely scenario for the observed pre-edge is Ni^{1+} impurities on low-symmetry sites due to sulfur vacancies. To match the data, we use a 88%/12% mixture of Ni^{2+}/Ni^{1+}, as shown in Fig. 6.13. This corresponds to a 1.5% sulfur deficiency to maintain charge neutrality, i.e. $NiGa_2S_{4-x}$, with $x = 0.06$.

6.4 Discussion

From the REXS measurements, we found a correlation length of 63 Å at 4 K. This is 2.5 larger than the maximum correlation length found in previous neutron diffraction measurements [300–302]. The absorption length of $NiGa_2S_4$ for x-rays at the Ni L_3 edge is ≈500 nm, with

an effective probing depth of ≈200 nm at $\boldsymbol{Q}^{\pm}$ [326], which corresponds to approximately 170 layers in $NiGa_2S_4$. This small depth, along with the x-ray spot size of 100 μm × 50 μm, means that the effective sample volume probed by REXS is significantly less than that probed by neuton scattering, which probes the entire volume of many coaligned crystals.

The larger sample volume probed in neutron experiments makes those measurements more susceptibile to the effects of structural disorder such as stacking faults, sulfur off-stoichiometry, residual strain, or crystal mosaic. These disorder effects, which have shown signatures in a wide variety of experiments [9, 295–297, 313], may cut off magnetic correlations or produce a distribution of magnetic wavevectors, leading to an effectively shorter correlation length observed by neutron diffraction.

We observed a temperature dependence of the magnetic wavevector $\boldsymbol{Q}^* = (\eta, \eta, 0)$, with η increasing with decreasing temperature. This shift in η is nearly proportional to both the intensity (which depends on the size of the ordered moment) and the correlation length, suggesting that fluctuations play a role in setting the magnitude of the magnetic wavevector. The freezing temperature T^* is known to be sensitive to sulfur stoichiometry and magnetic or nonmagnetic impurities on the Ni site [310–313]. We expect a similar sensitivity for the onset temperature of magnetic correlations and the corresponding temperature dependent wavevector. This further suggests that inhomogeneity in larger sample volumes leads to broadening and a shorter effective correlation length. Our results call into question the intrinsic magnetic correlation length in $NiGa_2S_4$. Future work should include REXS on exfoliated flakes of $NiGa_2S_4$ to probe the magnetic correlations approaching the monolayer limit.

The RIXS spectrum of $NiGa_2S_4$ is incompatible with a negative charge transfer ground state. It can only be described by a mixed valence state consisting of predominantly positive charge transfer Ni^{2+} with Ni^{1+} impurities. The Ni^{2+} ions exhibit a typical spectrum for octahedrally coordinated Ni^{2+}, similar to that of $NiPS_3$ [320–322]. The Ni^{1+} ions occupy low-symmetry sites formed by sulfur vacancies. The data is consistent with a 88% Ni^{2+}:12%Ni^{1+} ratio, which requires a 1.5% sulfur deficiency or $NiGa_2S_{4-x}$ ($x = 0.06$) to maintain charge neutrality. These

low symmetry-sites are consistent with the anomalous signals seen in a variety of experiments, including NQR, ESR, and Raman [9, 295–297], which have been attributed to stacking faults or site mixing in addition to sulfur vacancies. Although vacancies are most likely to occur on the S1 sites not directly bonded to Ni ions, such a vacancy would lead to a local lattice distortion along the c-axis. This is consistent with the observed anisotropy of the Ni^{1+} states. These distortions may break local inversion symmetry, allowing for Dzyaloshinskii-Moriya (DM) interactions [9, 313]. We note that the reported band gap in $NiGa_2S_4$ is 0.27 eV or 0.3 eV from transport [327] and XPS [309] measurements respectively. In contrast, the band gap in $NiPS_3$ is found to be 1.6-1.8 eV [328, 329]. Thus, the defect states must be related to the intrinsic electronic properties of $NiGa_2S_4$, rather than arising from impurity phases or surface effects.

Appendix A

Appendix

A.1 Deriving the Heisenberg model from the Hubbard model

Starting from the 1D Hubbard model (eq. 1.1) at half filling in the limit of $U/t \gg 1$, we can show how interactions occur between neighboring sites. In the undoped case, there is one unpaired electron per site ($n = 1$) and the Hubbard model is said to be at *half-filling*. In the limit of strong repulsion $t/U \ll 1$, we expect electrons to be highly localized. We can thus carry out a perturbation theory to obtain an effective spin-only Hamiltonian, starting with the repulsive term and perturbing with the hopping. There are multiple ways to carry out this procedure. Here we follow the approach taken by Huang and Manousakis [330]. Split eq. 1.1 as $\mathcal{H}_{\text{Hub}} = \mathcal{H}_0 + \mathcal{H}'$ where

$$\mathcal{H}_0 = U \sum_i n_{i\uparrow} n_{i\downarrow} \tag{A.1}$$

$$\mathcal{H}' = -t \sum_{\langle ij \rangle, \sigma} (c^\dagger_{i\sigma} c_{j\sigma} + \text{h.c.}) \tag{A.2}$$

We will only consider matrix elements within the subspace of ground states, so any operator that takes a ground state out to an excited state will vanish. We initially allow arbitrary

filling before restricting to half-filling. To 2nd order,

$$\mathcal{H}_{\text{eff}} = \mathcal{H}' + \mathcal{H}' \frac{1}{E_0 - \mathcal{H}_0} \mathcal{H}' = \mathcal{H}_1 + \mathcal{H}_2 + \mathcal{H}_3 \tag{A.3}$$

$$\mathcal{H}_1 = -t \sum_{\langle ij \rangle, \sigma} [c^\dagger_{i\sigma} c_{j\sigma} + (i \leftrightarrow j)] \tag{A.4}$$

$$\mathcal{H}_2 = -\frac{2t^2}{U} \sum_{\langle ij \rangle, \sigma} (c^\dagger_{j\sigma} c_{i\sigma} n_{i\bar{\sigma}} c^\dagger_{i\sigma} c_{j\sigma} + c^\dagger_{j\bar{\sigma}} c_{i\bar{\sigma}} c^\dagger_{i\sigma} c_{j\sigma}) \tag{A.5}$$

$$\mathcal{H}_3 = -\frac{t^2}{U} \sum_{\langle ijk \rangle \sigma} [(c^\dagger_{k\sigma} c_{j\sigma} n_{j\bar{\sigma}} c^\dagger_{j\sigma} c_{i\sigma} + c^\dagger_{k\bar{\sigma}} c_{j\bar{\sigma}} c^\dagger_{j\sigma} c_{i\sigma}) + (i \leftrightarrow k)] \tag{A.6}$$

where $\bar{\sigma} = -\sigma$, $\langle ijk \rangle$ denotes sites i, j, k such that ij and jk are nearest neighbor pairs. It is clear that $\mathcal{H}_1 = \mathcal{H}'$ is a 1st order process involving a single hop between neighboring sites. At half-filling, $\mathcal{H}_1$ always takes a ground state to an excited state, so this term vanishes. $\mathcal{H}_2$ is a 2nd order process involving a virtual hop, where one electron hops to an neighboring site occupied by an opposite spin electron, followed by either of the 2 electrons hopping back to empty site. This term is allowed at half filling because the final state is a ground state. $\mathcal{H}_3$ is another 2nd order virtual process which allows hopping of an empty site. This term vanishes because there are no empty sites (holes) in the ground state at half-filling. Thus, we are left with $\mathcal{H}_2$, which can be rearranged using the fermion anticommutation relations.

$$\begin{aligned}
\mathcal{H}_2 &= -\frac{2t^2}{U} \sum_{\langle ij \rangle} \big(c^\dagger_{j\uparrow} c_{i\uparrow} n_{i\downarrow} c^\dagger_{i\uparrow} c_{j\uparrow} + c^\dagger_{j\downarrow} c_{i\downarrow} c^\dagger_{i\uparrow} c_{j\uparrow} \\
&\qquad + c^\dagger_{j\downarrow} c_{i\downarrow} n_{i\uparrow} c^\dagger_{i\downarrow} c_{j\downarrow} + c^\dagger_{j\uparrow} c_{i\uparrow} c^\dagger_{i\downarrow} c_{j\downarrow} \big) \\
&= -\frac{2t^2}{U} \sum_{\langle ij \rangle} \big(c_{i\uparrow} c^\dagger_{i\uparrow} n_{i\downarrow} n_{j\uparrow} + c_{i\downarrow} c^\dagger_{i\downarrow} n_{i\uparrow} n_{j\downarrow} \\
&\qquad - c^\dagger_{i\uparrow} c_{i\downarrow} c^\dagger_{j\downarrow} c_{j\uparrow} - c^\dagger_{i\downarrow} c_{i\uparrow} c^\dagger_{j\uparrow} c_{j\downarrow} \big) \\
&= -\frac{2t^2}{U} \sum_{\langle ij \rangle} \big[(1 - n_{i\uparrow}) n_{i\downarrow} n_{j\uparrow} + (1 - n_{i\downarrow}) n_{i\uparrow} n_{j\downarrow} \\
&\qquad - c^\dagger_{i\uparrow} c_{i\downarrow} c^\dagger_{j\downarrow} c_{j\uparrow} - c^\dagger_{i\downarrow} c_{i\uparrow} c^\dagger_{j\uparrow} c_{j\downarrow} \big]
\end{aligned} \tag{A.7}$$

At half-filling $n_{i\uparrow} + n_{i\downarrow} = 1$, so we can express the fermion operators using the following identities [4]

$$\begin{aligned} n_{i\uparrow} &= \tfrac{1}{2} + S_i^z \qquad & c_{i\uparrow}^\dagger c_{i\downarrow} &= S_i^+ \\ n_{i\downarrow} &= \tfrac{1}{2} - S_i^z \qquad & c_{i\downarrow}^\dagger c_{i\uparrow} &= S_i^- \end{aligned}$$

$$\begin{aligned} \mathcal{H}_2 &= -\frac{2t^2}{U} \sum_{\langle ij \rangle} \big[(\tfrac{1}{2} - S_i^z)^2 (\tfrac{1}{2} + S_j^z) + (\tfrac{1}{2} + S_i^z)^2 (\tfrac{1}{2} - S_j^z) \\ &\qquad - S_i^+ S_j^- - S_i^- S_j^+ \\ &= \text{const.} + \frac{4t^2}{U} \sum_{\langle ij \rangle} \big[S_i^z S_j^z + \tfrac{1}{2} (S_i^+ S_j^- + S_i^- S_j^+) \big] \end{aligned} \tag{A.8}$$

Dropping the constant and letting $J = 4t^2/U$, we obtain the *Heisenberg model*

$$\mathcal{H}_{\text{Heis}} = J \sum_{\langle ij \rangle} \boldsymbol{S}_i \cdot \boldsymbol{S}_j. \tag{A.9}$$

In the limit of strong repulsion at half-filling, the spin degrees of freedom of the Hubbard model can be described by this effective Hamiltonian, which favors antiparallel alignment between neighboring spins because virtual hopping reduces kinetic energy. This interaction is called *kinetic exchange*, illustrated in figure 1.4.

References

[1] N. W. Ashcroft and N. D. Mermin, *Solid State Physics* (Saunders, 1976).

[2] S. M. Girvin and K. Yang, *Modern Condensed Matter Physics* (Cambridge University Press, 2019).

[3] P. M. Chaikin and T. C. Lubensky, *Principles of Condensed Matter Physics* (Cambridge University Press, 1995).

[4] D. I. Khomskii, *Basic Aspects of the Quantum Theory of Solids: Order and Elementary Excitations* (Cambridge University Press, 2010).

[5] D. I. Khomskii, *Transition Metal Compounds* (Cambridge University Press, 2014).

[6] S. Blundell, *Magnetism in Condensed Matter* (Oxford University Press, 2001).

[7] P. Fazekas, *Lecture Notes on Electron Correlation and Magnetism* (World Scientific, 1999).

[8] C. Lacroix, P. Mendels, and F. Mila, *Introduction to Frustrated Magnetism: Materials, Experiments, Theory*, Vol. 164 (Springer Science & Business Media, 2011).

[9] M. E. Valentine, T. Higo, Y. Nambu, D. Chaudhuri, J. Wen, C. Broholm, S. Nakatsuji, and N. Drichko, "Impact of the lattice on magnetic properties and possible spin nematicity in the $S = 1$ triangular antiferromagnet $NiGa_2S_4$," Phys. Rev. Lett. **125**, 197201 (2020).

[10] E. M. Stoudenmire, S. Trebst, and L. Balents, "Quadrupolar correlations and spin freezing in $S = 1$ triangular lattice antiferromagnets," Phys. Rev. B **79**, 214436 (2009).

[11] F. Mila and F.-C. Zhang, "On the origin of biquadratic exchange in spin 1 chains," The European Physical Journal B-Condensed Matter and Complex Systems **16**, 7–10 (2000).

[12] M. Blume and Y. Y. Hsieh, "Biquadratic exchange and quadrupolar ordering," Journal of Applied Physics **40**, 1249–1249 (1969).

[13] S. Bhattacharjee, V. B. Shenoy, and T. Senthil, "Possible ferro-spin nematic order in $NiGa_2S_4$," Phys. Rev. B **74**, 092406 (2006).

[14] A. Läuchli, F. Mila, and K. Penc, "Quadrupolar phases of the $S = 1$ bilinear-biquadratic heisenberg model on the triangular lattice," Phys. Rev. Lett. **97**, 087205 (2006).

[15] H. Tsunetsugu and M. Arikawa, "Spin nematic phase in $S = 1$ triangular antiferromagnets," J. Phys. Soc. Jpn. **75**, 083701 (2006).

[16] J. Rodríguez-Carvajal and J. Villain, "Magnetic structures," Comptes Rendus Physique **20**, 770–802 (2019).

[17] Y. A. Izyumov, "Modulated, or long-periodic, magnetic structures of crystals," Soviet Physics Uspekhi **27**, 845–867 (1984).

[18] T. Chattopadhyay, "Modulated magnetic phases," International Journal of Modern Physics B **7**, 3225–3254 (1993).

[19] E. Ressouche, "Reminder: Magnetic structures description and determination by neutron diffraction," École thématique de la Société Française de la Neutronique **13**, 02001 (2014).

[20] S.-W. Cheong, M. Fiebig, W. Wu, L. Chapon, and V. Kiryukhin, "Seeing is believing: visualization of antiferromagnetic domains," npj Quantum Materials **5**, 3 (2020).

[21] S. Mugiraneza and A. M. Hallas, "Tutorial: a beginner's guide to interpreting magnetic susceptibility data with the curie-weiss law," Communications Physics **5**, 95 (2022).

[22] H. T. Diep *et al.*, *Frustrated spin systems* (World Scientific, 2013).

[23] D. Landau and K. Binder, *A Guide to Monte Carlo Simulations in Statistical Physics*, 5th ed. (Cambridge University Press, 2021).

[24] O. Eriksson, A. Bergman, L. Bergqvist, and J. Hellsvik, *Atomistic Spin Dynamics: Foundations and Applications* (Oxford University Press, 2017).

[25] F.-Y. Li and G. Chen, "Spin-orbital entanglement in d^8 Mott insulators: Possible excitonic magnetism in diamond lattice antiferromagnets," Phys. Rev. B **100**, 045103 (2019).

[26] T. Nomura, Y. Yamamoto, and K. Yoshii, "Weak-coupling mean-field theory of magnetic properties of $NiGa_2S_4$," Journal of the Physical Society of Japan **89**, 024704 (2020).

[27] O. Heinonen, R. A. Heinonen, and H. Park, "Magnetic ground states of a model for $M Nb_3S_6$ ($M = Co, Fe, Ni$)," Phys. Rev. Materials **6**, 024405 (2022).

[28] Z. Kai-Cheng, L. Yong-Feng, L. Yong, and C. Feng, "Monte Carlo study of the magnetic properties of spin liquid compound $NiGa_2S_4$," Chin. Phys. B **23**, 057501 (2014).

[29] A. Völl and S. Wessel, "Spin dynamics of the bilinear-biquadratic $S = 1$ heisenberg model on the triangular lattice: A quantum monte carlo study," Phys. Rev. B **91**, 165128 (2015).

[30] F. L. Buessen, M. Hering, J. Reuther, and S. Trebst, "Quantum spin liquids in frustrated spin-1 diamond antiferromagnets," Phys. Rev. Lett. **120**, 057201 (2018).

[31] I. Niesen and P. Corboz, "Ground-state study of the spin-1 bilinear-biquadratic heisenberg model on the triangular lattice using tensor networks," Phys. Rev. B **97**, 245146 (2018).

[32] A. Szasz, C. Wang, and Y.-C. He, "Phase diagram of a bilinear-biquadratic spin-1 model on the triangular lattice from density matrix renormalization group simulations," Phys. Rev. B **106**, 115103 (2022).

[33] D. Bergman, J. Alicea, E. Gull, S. Trebst, and L. Balents, "Order-by-disorder and spiral spin-liquid in frustrated diamond-lattice antiferromagnets," Nature Physics **3**, 487–491 (2007).

[34] S. Lee and L. Balents, "Theory of the ordered phase in a-site antiferromagnetic spinels," Phys. Rev. B **78**, 144417 (2008).

[35] J.-S. Bernier, M. J. Lawler, and Y. B. Kim, "Quantum order by disorder in frustrated diamond lattice antiferromagnets," Phys. Rev. Lett. **101**, 047201 (2008).

[36] J. Oitmaa, "Diamond lattice heisenberg antiferromagnet," Journal of Physics: Condensed Matter **30**, 155801 (2018).

[37] J. Oitmaa, "Frustrated diamond lattice antiferromagnet," Phys. Rev. B **99**, 134407 (2019).

[38] X.-P. Yao, J. Q. Liu, C.-J. Huang, X. Wang, and G. Chen, "Generic spiral spin liquids," Frontiers of Physics **16**, 1–13 (2021).

[39] J. R. Chamorro, T. M. McQueen, and T. T. Tran, "Chemistry of quantum spin liquids," Chemical Reviews **121**, 2898–2934 (2021).

[40] G. H. Wannier, "Antiferromagnetism. the triangular ising net," Phys. Rev. **79**, 357–364 (1950).

[41] M. F. Collins and O. A. Petrenko, "Review/synthèse: Triangular antiferromagnets," Canadian Journal of Physics **75**, 605–655 (1997).

[42] H. Kawamura, "Universality of phase transitions of frustrated antiferromagnets," Journal of Physics: Condensed Matter **10**, 4707 (1998).

[43] Y. Li, P. Gegenwart, and A. A. Tsirlin, "Spin liquids in geometrically perfect triangular antiferromagnets," Journal of Physics: Condensed Matter **32**, 224004 (2020).

[44] L. Balents, "Spin liquids in frustrated magnets," Nature **464**, 199–208 (2010).

[45] F. Mila, "Quantum spin liquids," European Journal of Physics **21**, 499 (2000).

[46] J. Knolle and R. Moessner, "A field guide to spin liquids," Annual Review of Condensed Matter Physics **10**, 451–472 (2019).

[47] L. Savary and L. Balents, "Quantum spin liquids: a review," Reports on Progress in Physics **80**, 016502 (2016).

[48] Y. Zhou, K. Kanoda, and T.-K. Ng, "Quantum spin liquid states," Rev. Mod. Phys. **89**, 025003 (2017).

[49] C. Broholm, R. J. Cava, S. A. Kivelson, D. G. Nocera, M. R. Norman, and T. Senthil, "Quantum spin liquids," Science **367**, eaay0668 (2020).

[50] K. Binder and A. P. Young, "Spin glasses: Experimental facts, theoretical concepts, and open questions," Rev. Mod. Phys. **58**, 801–976 (1986).

[51] J. A. Mydosh, "Spin glasses: redux: an updated experimental/materials survey," Reports on Progress in Physics **78**, 052501 (2015).

[52] W. Witczak-Krempa, G. Chen, Y. B. Kim, and L. Balents, "Correlated quantum phenomena in the strong spin-orbit regime," Annual Review of Condensed Matter Physics **5**, 57–82 (2014).

[53] J. G. Rau, E. K.-H. Lee, and H.-Y. Kee, "Spin-orbit physics giving rise to novel phases in correlated systems: Iridates and related materials," Annual Review of Condensed Matter Physics **7**, 195–221 (2016).

[54] T. Takayama, J. Chaloupka, A. Smerald, G. Khaliullin, and H. Takagi, "Spin–orbit-entangled electronic phases in $4d$ and $5d$ transition-metal compounds," Journal of the Physical Society of Japan **90**, 062001 (2021).

[55] I. Rousochatzakis, N. B. Perkins, Q. Luo, and H.-Y. Kee, "Beyond Kitaev physics in strong spin-orbit coupled magnets," Reports on Progress in Physics **87**, 026502 (2024).

[56] C. Kim, H.-S. Kim, and J.-G. Park, "Spin-orbital entangled state and realization of Kitaev physics in 3d cobalt compounds: a progress report," Journal of Physics: Condensed Matter **34**, 023001 (2021).

[57] H. Huang, A. Singh, C. Wu, J. Xie, J. Okamoto, A. Belik, E. Kurmaev, A. Fujimori, C. Chen, S. Streltsov, *et al.*, "Resonant inelastic x-ray scattering as a probe of $J_{\text{eff}} = 1/2$ state in $3d$ transition-metal oxide," npj Quantum Materials **7**, 1–6 (2022).

[58] P. M. Sarte, M. Songvilay, E. Pachoud, R. A. Ewings, C. D. Frost, D. Prabhakaran, K. H. Hong, A. J. Browne, Z. Yamani, J. P. Attfield, E. E. Rodriguez, S. D. Wilson, and C. Stock, "Spin-orbit excitons in CoO," Phys. Rev. B **100**, 075143 (2019).

[59] B. Yuan, M. B. Stone, G.-J. Shu, F. C. Chou, X. Rao, J. P. Clancy, and Y.-J. Kim, "Spin-orbit exciton in a honeycomb lattice magnet $CoTiO_3$: Revealing a link between magnetism in d- and f-electron systems," Phys. Rev. B **102**, 134404 (2020).

[60] A. Krimmel, M. Mücksch, V. Tsurkan, M. M. Koza, H. Mutka, and A. Loidl, "Vibronic and magnetic excitations in the spin-orbital liquid state of $FeSc_2S_4$," Phys. Rev. Lett. **94**, 237402 (2005).

[61] K. W. Plumb, J. R. Morey, J. A. Rodriguez-Rivera, H. Wu, A. A. Podlesnyak, T. M. McQueen, and C. L. Broholm, "Antiferromagnetic and orbital ordering on a diamond lattice near quantum criticality," Phys. Rev. X **6**, 041055 (2016).

[62] Y. Nii, H. Sagayama, H. Umetsu, N. Abe, K. Taniguchi, and T. Arima, "Interplay among spin, orbital, and lattice degrees of freedom in a frustrated spinel Mn_3O_4," Phys. Rev. B **87**, 195115 (2013).

[63] S. M. Winter, A. A. Tsirlin, M. Daghofer, J. van den Brink, Y. Singh, P. Gegenwart, and R. Valentí, "Models and materials for generalized Kitaev magnetism," Journal of Physics: Condensed Matter **29**, 493002 (2017).

[64] H. Takagi, T. Takayama, G. Jackeli, G. Khaliullin, and S. E. Nagler, "Concept and realization of Kitaev quantum spin liquids," Nature Reviews Physics **1**, 264–280 (2019).

[65] S. Trebst and C. Hickey, "Kitaev materials," Physics Reports **950**, 1–37 (2022), kitaev materials.

[66] S. Bhowal and I. Dasgupta, "Spin–orbit effects in pentavalent iridates: models and materials," Journal of Physics: Condensed Matter **33**, 453001 (2021).

[67] N. Nagaosa, J. Sinova, S. Onoda, A. H. MacDonald, and N. P. Ong, "Anomalous hall effect," Rev. Mod. Phys. **82**, 1539–1592 (2010).

[68] B. Keimer, S. A. Kivelson, M. R. Norman, S. Uchida, and J. Zaanen, "From quantum matter to high-temperature superconductivity in copper oxides," Nature **518**, 179–186 (2015).

[69] A. P. Ramirez, "Colossal magnetoresistance," Journal of Physics: Condensed Matter **9**, 8171 (1997).

[70] M. Imada, A. Fujimori, and Y. Tokura, "Metal-insulator transitions," Rev. Mod. Phys. **70**, 1039–1263 (1998).

[71] V. Tsurkan, H.-A. Krug von Nidda, J. Deisenhofer, P. Lunkenheimer, and A. Loidl, "On the complexity of spinels: Magnetic, electronic, and polar ground states," Physics Reports **926**, 1–86 (2021).

[72] K. Momma and F. Izumi, "*VESTA3* for three-dimensional visualization of crystal, volumetric and morphology data," Journal of Applied Crystallography **44**, 1272–1276 (2011).

[73] K. S. Burch, D. Mandrus, and J.-G. Park, "Magnetism in two-dimensional van der waals materials," Nature **563**, 47–52 (2018).

[74] M. Gibertini, M. Koperski, A. F. Morpurgo, and K. S. Novoselov, "Magnetic 2d materials and heterostructures," Nature nanotechnology **14**, 408–419 (2019).

[75] Q. H. Wang, A. Bedoya-Pinto, M. Blei, A. H. Dismukes, A. Hamo, S. Jenkins, M. Koperski, Y. Liu, Q.-C. Sun, E. J. Telford, H. H. Kim, M. Augustin, U. Vool, J.-X. Yin, L. H. Li, A. Falin, C. R. Dean, F. Casanova, R. F. L. Evans, M. Chshiev, A. Mishchenko, C. Petrovic, R. He, L. Zhao, A. W. Tsen, B. D. Gerardot, M. Brotons-Gisbert, Z. Guguchia,

X. Roy, S. Tongay, Z. Wang, M. Z. Hasan, J. Wrachtrup, A. Yacoby, A. Fert, S. Parkin, K. S. Novoselov, P. Dai, L. Balicas, and E. J. G. Santos, "The magnetic genome of two-dimensional van der waals materials," ACS Nano **16**, 6960–7079 (2022).

[76] M. Hossain, B. Qin, B. Li, and X. Duan, "Synthesis, characterization, properties and applications of two-dimensional magnetic materials," Nano Today **42**, 101338 (2022).

[77] A. V. Kolobov and J. Tominaga, *Two-dimensional transition-metal dichalcogenides*, Vol. 239 (Springer, 2016).

[78] S. Manzeli, D. Ovchinnikov, D. Pasquier, O. V. Yazyev, and A. Kis, "2D transition metal dichalcogenides," Nature Reviews Materials **2**, 1–15 (2017).

[79] G. H. Han, D. L. Duong, D. H. Keum, S. J. Yun, and Y. H. Lee, "van der Waals metallic transition metal dichalcogenides," Chemical reviews **118**, 6297–6336 (2018).

[80] E. A. Marseglia, "Transition metal dichalcogenides and their intercalates," International Reviews in Physical Chemistry **3**, 177–216 (1983).

[81] S. S. P. Parkin and R. H. Friend, "3d transition-metal intercalates of the niobium and tantalum dichalcogenides. i. magnetic properties," Philosophical Magazine B **41**, 65–93 (1980).

[82] S. S. P. Parkin and R. H. Friend, "3d transition-metal intercalates of the niobium and tantalum dichalcogenides. ii. transport properties," Philosophical Magazine B **41**, 95–112 (1980).

[83] S. S. P. Parkin and A. R. Beal, "3d transition metal intercalates of the niobium and tantalum dichalcogenides," Philosophical Magazine B **42**, 627–642 (1980).

[84] L. S. Xie, S. Husremović, O. Gonzalez, I. M. Craig, and D. K. Bediako, "Structure and magnetism of iron- and chromium-intercalated niobium and tantalum disulfides," Journal of the American Chemical Society **144**, 9525–9542 (2022).

[85] Y. Cao, Z. Huang, Y. Yin, H. Xie, B. Liu, W. Wang, C. Zhu, D. Mandrus, L. Wang, and W. Huang, "Overview and advances in a layered chiral helimagnet $Cr_{1/3}NbS_2$," Materials Today Advances **7**, 100080 (2020).

[86] Z. Wang, R. Li, C. Su, and K. P. Loh, "Intercalated phases of transition metal dichalcogenides," SmartMat **1**, e1013 (2020).

[87] M. Rajapakse, B. Karki, U. O. Abu, S. Pishgar, M. R. K. Musa, S. S. Riyadh, M. Yu, G. Sumanasekera, and J. B. Jasinski, "Intercalation as a versatile tool for fabrication, property tuning, and phase transitions in 2D materials," npj 2D Materials and Applications **5**, 30 (2021).

[88] N. J. Ghimire, A. Botana, J. Jiang, J. Zhang, Y.-S. Chen, and J. Mitchell, "Large anomalous hall effect in the chiral-lattice antiferromagnet $CoNb_3S_6$," Nature Communications **9**, 1–6 (2018).

[89] G. Tenasini, E. Martino, N. Ubrig, N. J. Ghimire, H. Berger, O. Zaharko, F. Wu, J. F. Mitchell, I. Martin, L. Forró, and A. F. Morpurgo, "Giant anomalous hall effect in quasi-two-dimensional layered antiferromagnet $Co_{1/3}NbS_2$," Phys. Rev. Research **2**, 023051 (2020).

[90] S. Mangelsen, P. Zimmer, C. Näther, S. Mankovsky, S. Polesya, H. Ebert, and W. Bensch, "Interplay of sample composition and anomalous hall effect in Co_xNbS_2," Phys. Rev. B **103**, 184408 (2021).

[91] H. Tanaka, S. Okazaki, K. Kuroda, R. Noguchi, Y. Arai, S. Minami, S. Ideta, K. Tanaka, D. Lu, M. Hashimoto, V. Kandyba, M. Cattelan, A. Barinov, T. Muro, T. Sasagawa, and T. Kondo, "Large anomalous hall effect induced by weak ferromagnetism in the noncentrosymmetric antiferromagnet $CoNb_3S_6$," Phys. Rev. B **105**, L121102 (2022).

[92] X. P. Yang, H. LaBollita, Z.-J. Cheng, H. Bhandari, T. A. Cochran, J.-X. Yin, M. S. Hossain, I. Belopolski, Q. Zhang, Y. Jiang, N. Shumiya, D. Multer, M. Liskevich, D. A.

Usanov, Y. Dang, V. N. Strocov, A. V. Davydov, N. J. Ghimire, A. S. Botana, and M. Z. Hasan, "Visualizing the out-of-plane electronic dispersions in an intercalated transition metal dichalcogenide," Phys. Rev. B **105**, L121107 (2022).

[93] P. Popčević, Y. Utsumi, I. Biało, W. Tabis, M. A. Gala, M. Rosmus, J. J. Kolodziej, N. Tomaszewska, M. Garb, H. Berger, I. Batistić, N. Barišić, L. Forró, and E. Tutiš, "Role of intercalated cobalt in the electronic structure of $Co_{1/3}NbS_2$," Phys. Rev. B **105**, 155114 (2022).

[94] S. Lim, S. Singh, F.-T. Huang, S. Pan, K. Wang, J. Kim, J. Kim, D. Vanderbilt, and S.-W. Cheong, "Magnetochiral tunneling in paramagnetic $Co_{1/3}NbS_2$," Proceedings of the National Academy of Sciences **121**, e2318443121 (2024).

[95] P. Popčević, I. Batistić, A. Smontara, K. Velebit, J. Jaćimović, I. Živković, N. Tsyrulin, J. Piatek, H. Berger, A. Sidorenko, H. Rønnow, L. Forró, N. Barišić, and E. Tutiš, "Electronic transport and magnetism in the alternating stack of metallic and highly frustrated magnetic layers in $Co_{1/3}NbS_2$," Phys. Rev. B **107**, 235149 (2023).

[96] Y. An, P. Park, C. Kim, K. Zhang, H. Kim, M. Avdeev, J. Kim, M.-J. Han, H.-J. Noh, S. Seong, J.-S. Kang, H.-D. Kim, and J.-G. Park, "Bulk properties of the chiral metallic triangular antiferromagnets $Ni_{1/3}NbS_2$ and $Ni_{1/3}TaS_2$," Phys. Rev. B **108**, 054418 (2023).

[97] Y. U. Boucher, I. Biało, M. A. Gala, W. Tabiś, M. Rosmus, N. Olszowska, J. J. Kolodziej, B. Gudac, M. Novak, N. K. C. Muniraju, I. Batistić, N. Barišić, P. Popčević, and E. Tutiš, "Intercalation-induced states at the fermi level and the coupling of intercalated magnetic ions to conducting layers in $Ni_{1/3}NbS_2$," Phys. Rev. B **109**, 085135 (2024).

[98] Y. Togawa, T. Koyama, K. Takayanagi, S. Mori, Y. Kousaka, J. Akimitsu, S. Nishihara, K. Inoue, A. S. Ovchinnikov, and J. Kishine, "Chiral magnetic soliton lattice on a chiral helimagnet," Phys. Rev. Lett. **108**, 107202 (2012).

[99] A. Little, C. Lee, C. John, S. Doyle, E. Maniv, N. L. Nair, W. Chen, D. Rees, J. W.

Venderbos, R. M. Fernandes, *et al.*, "Three-state nematicity in the triangular lattice antiferromagnet $Fe_{1/3}NbS_2$," Nature materials **19**, 1062–1067 (2020).

[100] S. C. Haley, S. F. Weber, T. Cookmeyer, D. E. Parker, E. Maniv, N. Maksimovic, C. John, S. Doyle, A. Maniv, S. K. Ramakrishna, A. P. Reyes, J. Singleton, J. E. Moore, J. B. Neaton, and J. G. Analytis, "Half-magnetization plateau and the origin of threefold symmetry breaking in an electrically switchable triangular antiferromagnet," Phys. Rev. Research **2**, 043020 (2020).

[101] E. Maniv, R. A. Murphy, S. C. Haley, S. Doyle, C. John, A. Maniv, S. K. Ramakrishna, Y.-L. Tang, P. Ercius, R. Ramesh, *et al.*, "Exchange bias due to coupling between coexisting antiferromagnetic and spin-glass orders," Nature Physics **17**, 525–530 (2021).

[102] E. Maniv, N. L. Nair, S. C. Haley, S. Doyle, C. John, S. Cabrini, A. Maniv, S. K. Ramakrishna, Y.-L. Tang, P. Ercius, R. Ramesh, Y. Tserkovnyak, A. P. Reyes, and J. G. Analytis, "Antiferromagnetic switching driven by the collective dynamics of a coexisting spin glass," Science Advances **7**, eabd8452 (2021).

[103] S. Wu, Z. Xu, S. C. Haley, S. F. Weber, A. Acharya, E. Maniv, Y. Qiu, A. A. Aczel, N. S. Settineri, J. B. Neaton, J. G. Analytis, and R. J. Birgeneau, "Highly tunable magnetic phases in transition-metal dichalcogenide $Fe_{1/3+\delta}NbS_2$," Phys. Rev. X **12**, 021003 (2022).

[104] S. K. Karna, F. N. Womack, R. Chapai, D. P. Young, M. Marshall, W. Xie, D. Graf, Y. Wu, H. Cao, L. DeBeer-Schmitt, P. W. Adams, R. Jin, and J. F. DiTusa, "Consequences of magnetic ordering in chiral $Mn_{1/3}NbS_2$," Phys. Rev. B **100**, 184413 (2019).

[105] Y. Dai, W. Liu, Y. Wang, J. Fan, L. Pi, L. Zhang, and Y. Zhang, "Critical phenomenon and phase diagram of mn-intercalated layered $MnNb_3S_6$," Journal of Physics: Condensed Matter **31**, 195803 (2019).

[106] M. Ohkuma, M. Mito, H. Deguchi, Y. Kousaka, J. Ohe, J. Akimitsu, J. Kishine,

and K. Inoue, "Nonequilibrium chiral soliton lattice in the monoaxial chiral magnet $MnNb_3S_6$," Phys. Rev. B **106**, 104410 (2022).

[107] A. E. Hall, J. C. Loudon, P. A. Midgley, A. C. Twitchett-Harrison, S. J. R. Holt, D. A. Mayoh, J. P. Tidey, Y. Han, M. R. Lees, and G. Balakrishnan, "Comparative study of the structural and magnetic properties of $Mn_{1/3}NbS_2$ and $Cr_{1/3}NbS_2$," Phys. Rev. Mater. **6**, 024407 (2022).

[108] K. Lu, D. Sapkota, L. DeBeer-Schmitt, Y. Wu, H. B. Cao, N. Mannella, D. Mandrus, A. A. Aczel, and G. J. MacDougall, "Canted antiferromagnetic order in the monoaxial chiral magnets $V_{1/3}TaS_2$ and $V_{1/3}NbS_2$," Phys. Rev. Materials **4**, 054416 (2020).

[109] A. E. Hall, D. D. Khalyavin, P. Manuel, D. A. Mayoh, F. Orlandi, O. A. Petrenko, M. R. Lees, and G. Balakrishnan, "Magnetic structure investigation of the intercalated transition metal dichalcogenide $V_{1/3}NbS_2$," Phys. Rev. B **103**, 174431 (2021).

[110] H. Wang, X.-P. Ma, X.-Y. Zeng, J. Gong, J.-F. Lin, X.-Y. Wang, Z.-Y. Dai, K. Han, Y.-T. Wang, and T.-L. Xia, "Anomalous hall effect and topological hall effect in the noncollinear antiferromagnet $V_{0.3}NbS_2$," Phys. Rev. B **107**, 134436 (2023).

[111] B. Edwards, O. Dowinton, A. Hall, P. Murgatroyd, S. Buchberger, T. Antonelli, G.-R. Siemann, A. Rajan, E. A. Morales, A. Zivanovic, *et al.*, "Giant valley-zeeman coupling in the surface layer of an intercalated transition metal dichalcogenide," Nature Materials **22**, 459–465 (2023).

[112] H. Takagi, R. Takagi, S. Minami, T. Nomoto, K. Ohishi, M.-T. Suzuki, Y. Yanagi, M. Hirayama, N. Khanh, K. Karube, *et al.*, "Spontaneous topological hall effect induced by non-coplanar antiferromagnetic order in intercalated van der waals materials," Nature Physics **19**, 961–968 (2023).

[113] P. Park, W. Cho, C. Kim, Y. An, Y.-G. Kang, M. Avdeev, R. Sibille, K. Iida, R. Kajimoto, K. H. Lee, *et al.*, "Tetrahedral triple-q ordering in the metallic triangular lattice

antiferromagnet $Co_{1/3}TaS_2$," Nature Communications **14** (2023), 10.1038/s41467-023-43853-4.

[114] J. Als-Nielsen and D. McMorrow, *Elements of Modern X-ray Physics* (John Wiley & Sons, 2011).

[115] F. De Groot and A. Kotani, *Core Level Spectroscopy of Solids* (CRC press, 2008).

[116] J. Stöhr, *The Nature of X-Rays and Their Interactions with Matter* (Springer Nature, 2023).

[117] M. Van Veenendaal, *Theory of Inelastic Scattering and Absorption of X-rays* (Cambridge University Press, 2015).

[118] M. Altarelli, "Resonant x-ray scattering: A theoretical introduction," in *Magnetism: A Synchrotron Radiation Approach*, edited by E. Beaurepaire, H. Bulou, F. Scheurer, and J.-P. Kappler (Springer Berlin Heidelberg, Berlin, Heidelberg, 2006) pp. 201–242.

[119] J. Fink, E. Schierle, E. Weschke, and J. Geck, "Resonant elastic soft x-ray scattering," Reports on Progress in Physics **76**, 056502 (2013).

[120] L. J. P. Ament, M. van Veenendaal, T. P. Devereaux, J. P. Hill, and J. van den Brink, "Resonant inelastic x-ray scattering studies of elementary excitations," Rev. Mod. Phys. **83**, 705–767 (2011).

[121] S. Di Matteo, "Resonant x-ray diffraction: multipole interpretation," Journal of Physics D: Applied Physics **45**, 163001 (2012).

[122] J. P. Hannon, G. T. Trammell, M. Blume, and D. Gibbs, "X-ray resonance exchange scattering," Phys. Rev. Lett. **61**, 1245–1248 (1988).

[123] J. Hill and D. McMorrow, "Resonant exchange scattering: polarization dependence and correlation function," Acta Crystallographica Section A: Foundations of Crystallography **52**, 236–244 (1996).

[124] L. Paolasini, "Resonant and magnetic x-ray diffraction by polarized synchrotron radiation," JDN **13**, 03002 (2014).

[125] M. W. Haverkort, N. Hollmann, I. P. Krug, and A. Tanaka, "Symmetry analysis of magneto-optical effects: The case of x-ray diffraction and x-ray absorption at the transition metal $L_{2,3}$ edge," Phys. Rev. B **82**, 094403 (2010).

[126] C. Mazzoli, S. B. Wilkins, S. Di Matteo, B. Detlefs, C. Detlefs, V. Scagnoli, L. Paolasini, and P. Ghigna, "Disentangling multipole resonances through a full x-ray polarization analysis," Phys. Rev. B **76**, 195118 (2007).

[127] R. D. Johnson, S. R. Bland, C. Mazzoli, T. A. W. Beale, C.-H. Du, C. Detlefs, S. B. Wilkins, and P. D. Hatton, "Determination of magnetic order of the rare-earth ions in multiferroic $TbMn_2O_5$," Phys. Rev. B **78**, 104407 (2008).

[128] H. Wang, P. Bencok, P. Steadman, E. Longhi, J. Zhu, and Z. Wang, "Complete polarization analysis of an apple ii undulator using a soft x-ray polarimeter," Journal of Synchrotron Radiation **19**, 944–948 (2012).

[129] T. Frawley, R. Schoonmaker, S. H. Lee, C.-H. Du, P. Steadman, J. Strempfer, K. A. Ziq, S. J. Clark, T. Lancaster, and P. D. Hatton, "Elucidation of the helical spin structure of FeAs," Phys. Rev. B **95**, 064424 (2017).

[130] J. Herrero-Martín, A. N. Dobrynin, C. Mazzoli, P. Steadman, P. Bencok, R. Fan, A. A. Mukhin, V. Skumryev, and J. L. García-Muñoz, "Direct observation of noncollinear order of Co and Mn moments in multiferroic $Mn_{0.85}Co_{0.15}Wo_4$," Phys. Rev. B **91**, 220403 (2015).

[131] G. Subías, J. Blasco, J. Herrero-Martín, J. A. Rodríguez-Velamazán, M. Valvidares, R. Fan, P. Steadman, and J. García, "Magnetic ordering in $La_{1.5}Ca_{0.5}CoO_4$ revealed by resonant magnetic x-ray scattering and neutron diffraction," Phys. Rev. B **103**, 184422 (2021).

[132] M. C. Rahn, J.-R. Soh, S. Francoual, L. S. I. Veiga, J. Strempfer, J. Mardegan, D. Y. Yan, Y. F. Guo, Y. G. Shi, and A. T. Boothroyd, "Coupling of magnetic order and charge transport in the candidate dirac semimetal $EuCd_2As_2$," Phys. Rev. B **97**, 214422 (2018).

[133] W. Simeth, A. Bauer, C. Franz, A. Aqeel, P. J. Bereciartua, J. A. Sears, S. Francoual, C. H. Back, and C. Pfleiderer, "Resonant elastic x-ray scattering of antiferromagnetic superstructures in $EuPtSi_3$," Phys. Rev. Lett. **130**, 266701 (2023).

[134] V. Scagnoli, S. W. Huang, M. Garganourakis, R. A. de Souza, U. Staub, V. Simonet, P. Lejay, and R. Ballou, "Dzyaloshinskii-Moriya driven helical-butterfly structure in $Ba_3NbFe_3Si_2O_{14}$," Phys. Rev. B **88**, 104417 (2013).

[135] M. Ramakrishnan, Y. Joly, Y. W. Windsor, L. Rettig, A. Alberca, E. M. Bothschafter, P. Lejay, R. Ballou, V. Simonet, V. Scagnoli, and U. Staub, "Crystal symmetry lowering in chiral multiferroic $Ba_3TaFe_3Si_2O_{14}$ observed by x-ray magnetic scattering," Phys. Rev. B **95**, 205145 (2017).

[136] A. Biffin, R. D. Johnson, I. Kimchi, R. Morris, A. Bombardi, J. G. Analytis, A. Vishwanath, and R. Coldea, "Noncoplanar and counterrotating incommensurate magnetic order stabilized by kitaev interactions in $\gamma-Li_2IrO_3$," Phys. Rev. Lett. **113**, 197201 (2014).

[137] A. Biffin, R. D. Johnson, S. Choi, F. Freund, S. Manni, A. Bombardi, P. Manuel, P. Gegenwart, and R. Coldea, "Unconventional magnetic order on the hyperhoneycomb kitaev lattice in $\beta-Li_2IrO_3$: Full solution via magnetic resonant x-ray diffraction," Phys. Rev. B **90**, 205116 (2014).

[138] S. C. Williams, R. D. Johnson, F. Freund, S. Choi, A. Jesche, I. Kimchi, S. Manni, A. Bombardi, P. Manuel, P. Gegenwart, and R. Coldea, "Incommensurate counterrotating magnetic order stabilized by kitaev interactions in the layered honeycomb $\alpha-Li_2IrO_3$," Phys. Rev. B **93**, 195158 (2016).

[139] A. M. Mulders, S. M. Lawrence, A. J. Princep, U. Staub, Y. Bodenthin, M. García-Fernández, M. Garganourakis, J. Hester, R. Macquart, and C. D. Ling, "Circularly polarized soft x-ray diffraction study of helical magnetism in hexaferrite," Phys. Rev. B **81**, 092405 (2010).

[140] Y. Hiraoka, Y. Tanaka, T. Kojima, Y. Takata, M. Oura, Y. Senba, H. Ohashi, Y. Wakabayashi, S. Shin, and T. Kimura, "Spin-chiral domains in $Ba_{0.5}Sr_{1.5}Zn_2Fe_{12}O_{22}$ observed by scanning resonant x-ray microdiffraction," Phys. Rev. B **84**, 064418 (2011).

[141] S. L. Zhang, G. van der Laan, and T. Hesjedal, "Direct experimental determination of spiral spin structures via the dichroism extinction effect in resonant elastic soft x-ray scattering," Phys. Rev. B **96**, 094401 (2017).

[142] R. Misawa, H. Ueda, K. Kimura, Y. Tanaka, and T. Kimura, "Chirality and magnetic quadrupole order in $Pb(TiO)Cu_4(PO_4)_4$ probed by interference scattering in resonant x-ray diffraction," Phys. Rev. B **103**, 174409 (2021).

[143] K. T. Kim, J. Y. Kee, M. R. McCarter, G. van der Laan, V. A. Stoica, J. W. Freeland, R. Ramesh, S. Y. Park, and D. R. Lee, "Origin of circular dichroism in resonant elastic x-ray scattering from magnetic and polar chiral structures," Phys. Rev. B **106**, 035116 (2022).

[144] M. W. Haverkort, "Theory of resonant inelastic x-ray scattering by collective magnetic excitations," Phys. Rev. Lett. **105**, 167404 (2010).

[145] Y. Wang, G. Fabbris, M. Dean, and G. Kotliar, "EDRIXS: An open source toolkit for simulating spectra of resonant inelastic x-ray scattering," Computer Physics Communications **243**, 151–165 (2019).

[146] R. D. Cowan, *The Theory of Atomic Structure and Spectra* (Univ of California Press, Berkeley, CA, 1981).

[147] M. W. Haverkort, M. Zwierzycki, and O. K. Andersen, "Multiplet ligand-field theory using Wannier orbitals," Phys. Rev. B **85**, 165113 (2012).

[148] B. Zager, J. R. Chamorro, L. Ge, F. Bahrami, V. Bisogni, J. Pelliciari, J. Li, G. Fabbris, T. M. McQueen, M. Mourigal, and K. W. Plumb, "Electronic structure of the frustrated diamond lattice magnet $NiRh_2O_4$," Phys. Rev. B **106**, 045134 (2022).

[149] Y. Haraguchi, D. Nishio-Hamane, and H. A. Katori, "Magnetic ordering in the $J_{\mathrm{eff}} = 0$ nickelate $nirh_2o_4$ prepared via a solid-state metathesis," Phys. Rev. Mater. **7**, 084413 (2023).

[150] D. Basov, R. Averitt, and D. Hsieh, "Towards properties on demand in quantum materials," Nature materials **16**, 1077–1088 (2017).

[151] S. V. Streltsov and D. I. Khomskii, "Jahn-Teller effect and spin-orbit coupling: Friends or foes?" Phys. Rev. X **10**, 031043 (2020).

[152] W. Roth, "The magnetic structure of Co_3O_4," Journal of Physics and Chemistry of Solids **25**, 1–10 (1964).

[153] N. Tristan, J. Hemberger, A. Krimmel, H.-A. Krug von Nidda, V. Tsurkan, and A. Loidl, "Geometric frustration in the cubic spinels $M Al_2O_4$ (M = Co, Fe, and Mn)," Phys. Rev. B **72**, 174404 (2005).

[154] A. Krimmel, H. Mutka, M. M. Koza, V. Tsurkan, and A. Loidl, "Spin excitations in frustrated A-site spinels investigated with inelastic neutron scattering," Phys. Rev. B **79**, 134406 (2009).

[155] V. Fritsch, J. Hemberger, N. Büttgen, E.-W. Scheidt, H.-A. Krug von Nidda, A. Loidl, and V. Tsurkan, "Spin and orbital frustration in $MnSc_2S_4$ and $FeSc_2S_4$," Phys. Rev. Lett. **92**, 116401 (2004).

[156] S. Gao, O. Zaharko, V. Tsurkan, Y. Su, J. S. White, G. S. Tucker, B. Roessli, F. Bourdarot, R. Sibille, D. Chernyshov, *et al.*, "Spiral spin-liquid and the emergence of a vortex-like state in $MnSc_2S_4$," Nature physics **13**, 157–161 (2017).

[157] K. Guratinder, V. Tsurkan, L. Prodan, L. Keller, J. P. Embs, F. Juranyi, M. Medarde, C. Rüegg, and O. Zaharko, "Magnetic order and exchange coupling in the frustrated diamond-lattice antiferromagnet $MnSc_2Se_4$," Phys. Rev. B **105**, 174423 (2022).

[158] L. Ge, J. Flynn, J. A. M. Paddison, M. B. Stone, S. Calder, M. A. Subramanian, A. P. Ramirez, and M. Mourigal, "Spin order and dynamics in the diamond-lattice heisenberg antiferromagnets $CuRh_2O_4$ and $CoRh_2O_4$," Phys. Rev. B **96**, 064413 (2017).

[159] J. R. Chamorro, L. Ge, J. Flynn, M. A. Subramanian, M. Mourigal, and T. M. McQueen, "Frustrated spin one on a diamond lattice in $NiRh_2O_4$," Phys. Rev. Materials **2**, 034404 (2018).

[160] M. M. Bordelon, C. Liu, L. Posthuma, E. Kenney, M. J. Graf, N. P. Butch, A. Banerjee, S. Calder, L. Balents, and S. D. Wilson, "Frustrated heisenberg J_1-J_2 model within the stretched diamond lattice of $LiYbO_2$," Phys. Rev. B **103**, 014420 (2021).

[161] M. M. Bordelon, J. D. Bocarsly, L. Posthuma, A. Banerjee, Q. Zhang, and S. D. Wilson, "Antiferromagnetism and crystalline electric field excitations in tetragonal $NaCeO_2$," Phys. Rev. B **103**, 024430 (2021).

[162] G. Chen, L. Balents, and A. P. Schnyder, "Spin-orbital singlet and quantum critical point on the diamond lattice: $FeSc_2S_4$," Phys. Rev. Lett. **102**, 096406 (2009).

[163] L. Savary, E. Gull, S. Trebst, J. Alicea, D. Bergman, and L. Balents, "Impurity effects in highly frustrated diamond-lattice antiferromagnets," Phys. Rev. B **84**, 064438 (2011).

[164] H. S. Nair, Z. Fu, J. Voigt, Y. Su, and T. Brückel, "Approaching the true ground state of frustrated *A*-site spinels: A combined magnetization and polarized neutron scattering study," Phys. Rev. B **89**, 174431 (2014).

[165] G. J. MacDougall, A. A. Aczel, Y. Su, W. Schweika, E. Faulhaber, A. Schneidewind, A. D. Christianson, J. L. Zarestky, H. D. Zhou, D. Mandrus, and S. E. Nagler, "Revisiting the ground state of $CoAl_2O_4$: Comparison to the conventional antiferromagnet $MnAl_2O_4$," Phys. Rev. B **94**, 184422 (2016).

[166] A. Biffin, C. Rüegg, J. Embs, T. Guidi, D. Cheptiakov, A. Loidl, V. Tsurkan, and R. Coldea, "Magnetic field dependence of excitations near spin-orbital quantum criticality," Phys. Rev. Lett. **118**, 067205 (2017).

[167] V. Tsurkan, L. Prodan, V. Felea, I. Filippova, V. Kravtsov, A. Günther, S. Widmann, H.-A. Krug von Nidda, J. Deisenhofer, and A. Loidl, "Structure, magnetic susceptibility, and specific heat of the spin-orbital-liquid candidate $FeSc_2S_4$: Influence of Fe off-stoichiometry," Phys. Rev. B **96**, 054417 (2017).

[168] T. Naka, J. Valenta, J. Kaštil, M. Míšek, J. Prchal, V. Sechovský, H. Abe, T. Nakane, M. Nakayama, and T. Uchikoshi, "Chemical and physical pressure effects in the A-site spinel antiferromagnets CoM_2O_4 (M = Al, Co, and Rh)," Materials Research Express **7**, 056105 (2020).

[169] H. Cho, C. H. Kim, Y. Lee, K. Komatsu, B.-G. Cho, D.-Y. Cho, T. Kim, C. Kim, Y. Kim, T. Y. Koo, Y. Noda, H. Kagi, D. I. Khomskii, D. Seoung, and J.-G. Park, "Pressure-induced transition from $J_{\text{eff}} = \frac{1}{2}$ to $S = \frac{1}{2}$ states in $CuAl_2O_4$," Phys. Rev. B **103**, L081101 (2021).

[170] F.-Y. Li and G. Chen, "Competing phases and topological excitations of spin-1 pyrochlore antiferromagnets," Phys. Rev. B **98**, 045109 (2018).

[171] J. Q. Liu, F.-Y. Li, G. Chen, and Z. Wang, "Featureless quantum paramagnet with frustrated criticality and competing spiral magnetism on spin-1 honeycomb lattice magnet," Phys. Rev. Research **2**, 033260 (2020).

[172] J. R. Morey, A. Scheie, J. P. Sheckelton, C. M. Brown, and T. M. McQueen, "$Ni_2Mo_3O_8$:

Complex antiferromagnetic order on a honeycomb lattice," Phys. Rev. Materials **3**, 014410 (2019).

[173] C. Wang, A. Nahum, and T. Senthil, "Topological paramagnetism in frustrated spin-1 Mott insulators," Phys. Rev. B **91**, 195131 (2015).

[174] G. Chen, "Quantum paramagnet and frustrated quantum criticality in a spin-one diamond lattice antiferromagnet," Phys. Rev. B **96**, 020412(R) (2017).

[175] S. Horiuti and S. Miyahara, "Tetragonal distortion of $NiRh_2O_4$," Journal of the Physical Society of Japan **19**, 423–424 (1964).

[176] G. Blasse and D. Schipper, "Antiferromagnetism of $CoRh_2O_4$ and $NiRh_2O_4$," Physics Letters **5**, 300 (1963).

[177] S. Das, D. Nafday, T. Saha-Dasgupta, and A. Paramekanti, "$NiRh_2O_4$: A spin-orbit entangled diamond-lattice paramagnet," Phys. Rev. B **100**, 140408(R) (2019).

[178] J. Dvorak, I. Jarrige, V. Bisogni, S. Coburn, and W. Leonhardt, "Towards 10 mev resolution: The design of an ultrahigh resolution soft x-ray rixs spectrometer," Review of Scientific Instruments **87**, 115109 (2016).

[179] P. Gütlich, K. M. Hasselbach, H. Rummel, and H. Spiering, "^{61}Ni Mössbauer spectroscopy of magnetic hyperfine interaction in nickel spinels," The Journal of Chemical Physics **81**, 1396–1405 (1984).

[180] V. Kocsis, S. Bordács, D. Varjas, K. Penc, A. Abouelsayed, C. A. Kuntscher, K. Ohgushi, Y. Tokura, and I. Kézsmárki, "Magnetoelasticity in ACr_2O_4 spinel oxides (A = mn, fe, co, ni, and cu)," Phys. Rev. B **87**, 064416 (2013).

[181] F. de Groot, "X-ray absorption and dichroism of transition metals and their compounds," Journal of Electron Spectroscopy and Related Phenomena **67**, 529–622 (1994).

[182] E. Z. Kurmaev, R. G. Wilks, A. Moewes, L. D. Finkelstein, S. N. Shamin, and J. Kuneš, "Oxygen x-ray emission and absorption spectra as a probe of the electronic structure of strongly correlated oxides," Phys. Rev. B **77**, 165127 (2008).

[183] M. J. Wahila, Z. W. Lebens-Higgins, A. J. Jackson, D. O. Scanlon, T.-L. Lee, J. Zhang, K. H. L. Zhang, and L. F. J. Piper, "Band edge evolution of transparent $ZnM_2^{III}O_4$ (M^{III} = Co, Rh, Ir) spinels," Phys. Rev. B **100**, 085126 (2019).

[184] F. Frati, M. O. Hunault, and F. M. de Groot, "Oxygen K-edge x-ray absorption spectra," Chemical reviews **120**, 4056–4110 (2020).

[185] M. Lenglet, "Ligand field spectroscopy and chemical bonding in Cr^{3+}-, Fe^{3+}-, Co^{2+}- and Ni^{2+}-containing oxidic solids: Influence of the inductive effect of the competing bonds and magnetic interactions on the degree of covalency of the 3d M–O bonds," Materials Research Bulletin **35**, 531–543 (2000).

[186] I. Mayer and S. Angelov, "The mechanism of participation of non-magnetic B-site cations in the superexchange in spinels," physica status solidi (b) **106**, 467–471 (1981).

[187] M. Zhu, D. Do, C. R. Dela Cruz, Z. Dun, J.-G. Cheng, H. Goto, Y. Uwatoko, T. Zou, H. D. Zhou, S. D. Mahanti, and X. Ke, "Ferromagnetic superexchange in insulating Cr_2MoO_6 by controlling orbital hybridization," Phys. Rev. B **92**, 094419 (2015).

[188] V. M. Katukuri, P. Babkevich, O. Mustonen, H. C. Walker, B. Fåk, S. Vasala, M. Karppinen, H. M. Rønnow, and O. V. Yazyev, "Exchange interactions mediated by nonmagnetic cations in double perovskites," Phys. Rev. Lett. **124**, 077202 (2020).

[189] F. Bahrami, X. Hu, Y. Du, O. I. Lebedev, C. Wang, H. Luetkens, G. Fabbris, M. J. Graf, D. Haskel, Y. Ran, and F. Tafti, "First demonstration of tuning between the Kitaev and Ising limits in a honeycomb lattice," Science Advances **8**, eabl5671 (2022).

[190] T. Burnus, Z. Hu, H. Wu, J. C. Cezar, S. Niitaka, H. Takagi, C. F. Chang, N. B. Brookes, H.-J. Lin, L. Y. Jang, A. Tanaka, K. S. Liang, C. T. Chen, and L. H. Tjeng, "X-ray

absorption and x-ray magnetic dichroism study on Ca_3CoRhO_6 and Ca_3FeRhO_6," Phys. Rev. B **77**, 205111 (2008).

[191] J. P. Clancy, A. Lupascu, H. Gretarsson, Z. Islam, Y. F. Hu, D. Casa, C. S. Nelson, S. C. LaMarra, G. Cao, and Y.-J. Kim, "Dilute magnetism and spin-orbital percolation effects in $Sr_2Ir_{1-x}Rh_xO_4$," Phys. Rev. B **89**, 054409 (2014).

[192] S. Chikara, G. Fabbris, J. Terzic, G. Cao, D. Khomskii, and D. Haskel, "Charge partitioning and anomalous hole doping in Rh-doped Sr_2IrO_4," Phys. Rev. B **95**, 060407(R) (2017).

[193] Y. Wu and D. E. Ellis, "X-ray absorption near-edge spectra and electronic structure of rhodium compounds," Journal of Physics: Condensed Matter **7**, 3973–3989 (1995).

[194] D. Meyers, S. Middey, J.-G. Cheng, S. Mukherjee, B. Gray, Y. Cao, J.-S. Zhou, J. Goodenough, Y. Choi, D. Haskel, *et al.*, "Competition between heavy fermion and kondo interaction in isoelectronic A-site-ordered perovskites," Nature communications **5**, 1–6 (2014).

[195] M. Kobayashi, M. Seki, M. Suzuki, R. Okano, M. Kitamura, K. Horiba, H. Kumigashira, A. Fujimori, M. Tanaka, and H. Tabata, "Intervalence charge transfer and charge transport in the spinel ferrite ferromagnetic semiconductor Ru-doped $CoFe_2O_4$," Phys. Rev. B **105**, 205103 (2022).

[196] K. Takubo, S. Hirata, J.-Y. Son, J. W. Quilty, T. Mizokawa, N. Matsumoto, and S. Nagata, "X-ray photoemission study of $CuIr_2S_4$: Ir^{3+}-Ir^{4+} charge ordering and the effect of light illumination," Phys. Rev. Lett. **95**, 246401 (2005).

[197] W. F. J. Fontijn, P. J. van der Zaag, L. F. Feiner, R. Metselaar, and M. A. C. Devillers, "A consistent interpretation of the magneto-optical spectra of spinel type ferrites (invited)," Journal of Applied Physics **85**, 5100–5105 (1999).

[198] K. J. Kim, H. S. Lee, M. H. Lee, and S. H. Lee, "Comparative magneto-optical investigation of $d-d$ charge–transfer transitions in Fe_3O_4, $CoFe_2O_4$, and $NiFe_2O_4$," Journal of Applied Physics **91**, 9974–9977 (2002).

[199] A. Agui, T. Uozumi, M. Mizumaki, and T. Kääambre, "Intermetallic charge transfer in $FeTiO_3$ probed by resonant inelastic soft x-ray scattering," Phys. Rev. B **79**, 092402 (2009).

[200] S. G. Chiuzbăian, S. Brignolo, C. F. Hague, R. Delaunay, M. Guarise, A. Nicolaou, Z. Yang, H. Zhou, and J.-M. Mariot, "Spectroscopic evidence for superexchange in the ferrimagnetic spinel $FeCr_2S_4$," The Journal of Physical Chemistry C **121**, 22369–22376 (2017).

[201] B. Liu, E. N. Glass, R.-P. Wang, Y.-T. Cui, Y. Harada, D.-J. Huang, S. Schuppler, C. L. Hill, and F. M. F. de Groot, "Cobalt-to-vanadium charge transfer in polyoxometalate water oxidation catalysts revealed by $2p3d$ resonant inelastic x-ray scattering," Phys. Chem. Chem. Phys. **20**, 4554–4562 (2018).

[202] R. J. Green, M. W. Haverkort, and G. A. Sawatzky, "Bond disproportionation and dynamical charge fluctuations in the perovskite rare-earth nickelates," Phys. Rev. B **94**, 195127 (2016).

[203] E. B. Guedes, F. Abud, H. P. Martins, M. Abbate, R. F. Jardim, and R. J. O. Mossanek, "Role of Ti-Ru interaction in $SrTi_{0.5}Ru_{0.5}O_3$: Physical properties, x-ray spectroscopy, and cluster model calculations," Phys. Rev. B **100**, 075132 (2019).

[204] V. Kocsis, S. Bordács, J. Deisenhofer, L. F. Kiss, K. Ohgushi, Y. Kaneko, Y. Tokura, and I. Kézsmárki, "Strong magneto-optical effects in ACr_2O_4 (A = Fe, Co) spinel oxides generated by tetrahedrally coordinated transition metal ions," Phys. Rev. B **97**, 125140 (2018).

[205] M. Ptak, M. Maczka, A. Gągor, A. Pikul, L. Macalik, and J. Hanuza, "Temperature-dependent XRD, IR, magnetic, SEM and TEM studies of Jahn–Teller distorted $NiCr_2O_4$ powders," Journal of Solid State Chemistry **201**, 270–279 (2013).

[206] Z. Wang, S. Saxena, P. Lazor, and H. O'Neill, "An in situ raman spectroscopic study of pressure induced dissociation of spinel $NiCr_2O_4$," Journal of Physics and Chemistry of Solids **64**, 425–431 (2003).

[207] A. Geondzhian, A. Sambri, G. M. De Luca, R. Di Capua, E. Di Gennaro, D. Betto, M. Rossi, Y. Y. Peng, R. Fumagalli, N. B. Brookes, L. Braicovich, K. Gilmore, G. Ghiringhelli, and M. Salluzzo, "Large polarons as key quasiparticles in $SrTiO_3$ and $SrTiO_3$-based heterostructures," Phys. Rev. Lett. **125**, 126401 (2020).

[208] T. Saha-Dasgupta, "Double perovskites with $3d$ and $4d/5d$ transition metals: compounds with promises," Materials Research Express **7**, 014003 (2020).

[209] M.-C. Lee, S. Lee, C. J. Won, K. D. Lee, N. Hur, J.-L. Chen, D.-Y. Cho, and T. W. Noh, "Hybridized orbital states in spin-orbit coupled $3d$-$5d$ double perovskites studied by x-ray absorption spectroscopy," Phys. Rev. B **97**, 125123 (2018).

[210] K. Park, G. L. Pascut, G. Khanal, M. O. Yokosuk, X. Xu, B. Gao, M. J. Gutmann, A. P. Litvinchuk, V. Kiryukhin, S. W. Cheong, D. Vanderbilt, K. Haule, and J. L. Musfeldt, "Band-mott mixing hybridizes the gap in $Fe_2Mo_3O_8$," Phys. Rev. B **104**, 195143 (2021).

[211] L. Xu, N. A. Bogdanov, A. Princep, P. Fulde, J. Van Den Brink, and L. Hozoi, "Covalency and vibronic couplings make a nonmagnetic $j = 3/2$ ion magnetic," npj Quantum Materials **1**, 1–6 (2016).

[212] W. Jin, S. H. Chun, J. Kim, D. Casa, J. P. C. Ruff, C. J. Won, K. D. Lee, N. Hur, and Y.-J. Kim, "Magnetic excitations in the double-perovskite iridates La_2MIrO_6 (M = Co, Ni, and Zn) mediated by $3d$-$5d$ hybridization," Phys. Rev. B **105**, 054419 (2022).

[213] A. Smerald and G. Jackeli, "Giant magnetoelastic-coupling driven spin-lattice liquid state in molybdate pyrochlores," Phys. Rev. Lett. **122**, 227202 (2019).

[214] K. Amelin, Y. Alexanian, U. Nagel, T. Rõõm, J. Robert, J. Debray, V. Simonet, C. Decorse, Z. Wang, R. Ballou, E. Constable, and S. de Brion, "Terahertz magneto-optical investigation of quadrupolar spin-lattice effects in magnetically frustrated $Tb_2Ti_2O_7$," Phys. Rev. B **102**, 134428 (2020).

[215] A. Marciniak, S. Marcantoni, F. Giusti, F. Glerean, G. Sparapassi, T. Nova, A. Cartella, S. Latini, F. Valiera, A. Rubio, *et al.*, "Vibrational coherent control of localized *dd* electronic excitation," Nature Physics **17**, 368–373 (2021).

[216] D. Afanasiev, J. Hortensius, B. Ivanov, A. Sasani, E. Bousquet, Y. Blanter, R. Mikhaylovskiy, A. Kimel, and A. Caviglia, "Ultrafast control of magnetic interactions via light-driven phonons," Nature materials **20**, 607–611 (2021).

[217] E. Ergeçen, B. Ilyas, D. Mao, H. C. Po, M. B. Yilmaz, J. Kim, J.-G. Park, T. Senthil, and N. Gedik, "Magnetically brightened dark electron-phonon bound states in a van der waals antiferromagnet," Nature Communications **13**, 1–7 (2022).

[218] B. Zager, R. Fan, P. Steadman, and K. Plumb, "Double-Q spin chirality stripes in the anomalous hall antiferromagnet $CoNb_3S_6$," arXiv preprint arXiv:2307.03776 (2023), 10.48550/arXiv.2307.03776.

[219] C. Sang-Wook and X. Xianghan, "Magnetic chirality," NPJ Quantum Materials **7** (2022), 10.1038/s41535-022-00447-5.

[220] S. Nakatsuji and R. Arita, "Topological magnets: Functions based on berry phase and multipoles," Annual Review of Condensed Matter Physics **13**, 119–142 (2022).

[221] L. Šmejkal, J. Sinova, and T. Jungwirth, "Beyond conventional ferromagnetism and antiferromagnetism: A phase with nonrelativistic spin and crystal rotation symmetry," Phys. Rev. X **12**, 031042 (2022).

[222] L. Šmejkal, J. Sinova, and T. Jungwirth, "Emerging research landscape of altermagnetism," Phys. Rev. X **12**, 040501 (2022).

[223] M. Fiebig, T. Lottermoser, D. Meier, and M. Trassin, "The evolution of multiferroics," Nature Reviews Materials **1**, 1–14 (2016).

[224] H. Watanabe and Y. Yanase, "Group-theoretical classification of multipole order: Emergent responses and candidate materials," Phys. Rev. B **98**, 245129 (2018).

[225] S. S. P. Parkin, E. A. Marseglia, and P. J. Brown, "Magnetic structure of $Co_{1/3}NbS_2$ and $Co_{1/3}TaS_2$," Journal of Physics C: Solid State Physics **16**, 2765–2778 (1983).

[226] K. Lu, A. Murzabekova, S. Shim, J. Park, S. Kim, L. Kish, Y. Wu, L. DeBeer-Schmitt, A. A. Aczel, A. Schleife, N. Mason, F. Mahmood, and G. J. MacDougall, "Understanding the anomalous hall effect in $Co_{1/3}NbS_2$ from crystal and magnetic structures," arXiv (2022), 10.48550/arxiv.2212.14762.

[227] A. Zhang, K. Deng, J. Sheng, P. Liu, S. Kumar, K. Shimada, Z. Jiang, Z. Liu, D. Shen, J. Li, J. Ren, L. Wang, L. Zhou, Y. Ishikawa, T. Ohhara, Q. Zhang, G. McIntyre, D. Yu, E. Liu, L. Wu, C. Chen, and Q. Liu, "Chiral dirac fermion in a collinear antiferromagnet," Chinese Physics Letters **40**, 126101 (2023).

[228] S. Hayami, R. Ozawa, and Y. Motome, "Effective bilinear-biquadratic model for noncoplanar ordering in itinerant magnets," Phys. Rev. B **95**, 224424 (2017).

[229] S. Hayami, "Multiple-Q magnetism by anisotropic bilinear-biquadratic interactions in momentum space," Journal of Magnetism and Magnetic Materials **513**, 167181 (2020).

[230] S. Hayami and M. Yatsushiro, "Nonreciprocal transport in noncoplanar magnetic systems without spin–orbit coupling, net scalar chirality, or magnetization," Journal of the Physical Society of Japan **91**, 094704 (2022).

[231] T. A. W. Beale, T. P. A. Hase, T. Iida, K. Endo, P. Steadman, A. R. Marshall, S. S. Dhesi, G. van der Laan, and P. D. Hatton, "Rasor: An advanced instrument for soft x-ray reflectivity and diffraction," Review of Scientific Instruments **81**, 073904 (2010).

[232] P. Gu, Y. Peng, S. Yang, H. Wang, S. Ye, H. Wang, Y. Li, T. Xia, J. Yang, and Y. Ye, "Probing the anomalous hall transport and magnetic reversal of chiral-lattice antiferromagnet $Co_{1/3}NbS_2$," arXiv preprint arXiv:2306.09616 (2023).

[233] B. H. Goodge, O. Gonzalez, L. S. Xie, and D. K. Bediako, "Consequences and control of multiscale order/disorder in chiral magnetic textures," ACS Nano **17**, 19865–19876 (2023).

[234] K. Du, F.-T. Huang, J. Kim, S. J. Lim, K. Gamage, J. Yang, M. Mostovoy, J. Garlow, M.-G. Han, Y. Zhu, and S.-W. Cheong, "Topological spin/structure couplings in layered chiral magnet $Cr_{1/3}TaS_2$: The discovery of spiral magnetic superstructure," Proceedings of the National Academy of Sciences **118**, e2023337118 (2021).

[235] J. Herrero-Martín, A. N. Dobrynin, C. Mazzoli, P. Steadman, P. Bencok, R. Fan, A. A. Mukhin, V. Skumryev, and J. L. García-Muñoz, "Direct observation of noncollinear order of co and mn moments in multiferroic $Mn_{0.85}Co_{0.15}Wo_4$," Phys. Rev. B **91**, 220403 (2015).

[236] S.-S. Zhang, H. Ishizuka, H. Zhang, G. B. Halász, and C. D. Batista, "Real-space berry curvature of itinerant electron systems with spin-orbit interaction," Phys. Rev. B **101**, 024420 (2020).

[237] J. Mi, J. Li, M. Li, S. Xu, S. Yu, Z. Li, X. Fan, H. Zhu, Q. Tao, L. Li, and Z. Xu, "Third order nonlinear transport properties in topological chiral antiferromagnetic semimetal $CoNb_3S_6$," arXiv preprint arXiv:2312.05824 (2023).

[238] E. Fawcett, "Spin-density-wave antiferromagnetism in chromium," Rev. Mod. Phys. **60**, 209–283 (1988).

[239] Z. Boekelheide, E. Helgren, and F. Hellman, "Spin-density wave in polycrystalline cr films from infrared reflectivity," Phys. Rev. B **76**, 224429 (2007).

[240] T. Ueno, K. Yamamoto, H. Matsukura, T. Kusawake, and K. ichi Ohshima, "X-ray structural study of the layered compounds Co_xNbS_2," Science and Technology of Advanced Materials **6**, 684–688 (2005), https://doi.org/10.1016/j.stam.2005.05.007 .

[241] G. M. Watson, D. Gibbs, G. H. Lander, B. D. Gaulin, L. E. Berman, H. Matzke, and W. Ellis, "Resonant x-ray scattering studies of the magnetic structure near the surface of an antiferromagnet," Phys. Rev. B **61**, 8966–8975 (2000).

[242] K. Ran, Y. Liu, Y. Guang, D. M. Burn, G. van der Laan, T. Hesjedal, H. Du, G. Yu, and S. Zhang, "Creation of a chiral bobber lattice in helimagnet-multilayer heterostructures," Phys. Rev. Lett. **126**, 017204 (2021).

[243] K. Shibata, J. Iwasaki, N. Kanazawa, S. Aizawa, T. Tanigaki, M. Shirai, T. Nakajima, M. Kubota, M. Kawasaki, H. Park, *et al.*, "Large anisotropic deformation of skyrmions in strained crystal," Nature nanotechnology **10**, 589–592 (2015).

[244] Y. Nii, T. Nakajima, A. Kikkawa, Y. Yamasaki, K. Ohishi, J. Suzuki, Y. Taguchi, T. Arima, Y. Tokura, and Y. Iwasa, "Uniaxial stress control of skyrmion phase," Nature communications **6**, 8539 (2015).

[245] A. Chacon, A. Bauer, T. Adams, F. Rucker, G. Brandl, R. Georgii, M. Garst, and C. Pfleiderer, "Uniaxial pressure dependence of magnetic order in MnSi," Phys. Rev. Lett. **115**, 267202 (2015).

[246] S. Lee, T. Choi, W. Ratcliff, R. Erwin, S.-W. Cheong, and V. Kiryukhin, "Single ferroelectric and chiral magnetic domain of single-crystalline $BiFeO_3$ in an electric field," Phys. Rev. B **78**, 100101 (2008).

[247] N. S. Gusev, A. V. Sadovnikov, S. A. Nikitov, M. V. Sapozhnikov, and O. G. Udalov,

"Manipulation of the Dzyaloshinskii–Moriya interaction in Co/Pt multilayers with strain," Phys. Rev. Lett. **124**, 157202 (2020).

[248] G. Simutis, J. Küspert, Q. Wang, J. Choi, D. Bucher, M. Boehm, F. Bourdarot, M. Bertelsen, C. N. Wang, T. Kurosawa, *et al.*, "Single-domain stripe order in a high-temperature superconductor," Communications Physics **5**, 296 (2022).

[249] P. Canfield, R. Movshovich, R. Robinson, J. Thompson, Z. Fisk, W. Beyermann, A. Lacerda, M. Hundley, R. Heffner, D. MacLaughlin, F. Trouw, and H. Ott, "Groundstate properties of YbBiPt," Physica B: Condensed Matter **197**, 101–108 (1994).

[250] T. Inami, N. Terada, H. Kitazawa, and O. Sakai, "Resonant magnetic x-ray diffraction study on the triangular lattice antiferromagnet $GdPd_2Al_3$," Journal of the Physical Society of Japan **78**, 084713 (2009).

[251] T. Matsumura, T. Yamamoto, H. Tanida, and M. Sera, "Temperature-dependent cycloidal magnetic structure in $GdRu_2Al_{10}$ studied by resonant x-ray diffraction," Journal of the Physical Society of Japan **86**, 094709 (2017).

[252] M. Tsukagoshi, T. Matsumura, S. Michimura, T. Inami, and S. Ohara, "Competition between helimagnetic and ferroquadrupolar ordering in a monoaxial chiral magnet $DyNi_3Ga_9$ studied by resonant x-ray diffraction," Phys. Rev. B **105**, 014428 (2022).

[253] Y. Horibe, J. Yang, Y.-H. Cho, X. Luo, S. B. Kim, Y. S. Oh, F.-T. Huang, T. Asada, M. Tanimura, D. Jeong, and S.-W. Cheong, "Color theorems, chiral domain topology, and magnetic properties of Fe_xTaS_2," Journal of the American Chemical Society **136**, 8368–8373 (2014).

[254] Y. Akagi, M. Udagawa, and Y. Motome, "Hidden multiple-spin interactions as an origin of spin scalar chiral order in frustrated kondo lattice models," Phys. Rev. Lett. **108**, 096401 (2012).

[255] V. Dyadkin, F. Mushenok, A. Bosak, D. Menzel, S. Grigoriev, P. Pattison, and D. Chernyshov, "Structural disorder versus chiral magnetism in $Cr_{1/3}NbS_2$," Phys. Rev. B **91**, 184205 (2015).

[256] Y. J. Choi, S. B. Kim, T. Asada, S. Park, W. Wu, Y. Horibe, and S.-W. Cheong, "Giant magnetic coercivity and ionic superlattice nano-domains in $Fe_{0.25}TaS_2$," Europhysics Letters **86**, 37012 (2009).

[257] G. Marmorini and T. Momoi, "Magnon condensation with finite degeneracy on the triangular lattice," Phys. Rev. B **89**, 134425 (2014).

[258] I. Martin and C. D. Batista, "Itinerant electron-driven chiral magnetic ordering and spontaneous quantum hall effect in triangular lattice models," Phys. Rev. Lett. **101**, 156402 (2008).

[259] R. Ozawa, S. Hayami, K. Barros, G.-W. Chern, Y. Motome, and C. D. Batista, "Vortex crystals with chiral stripes in itinerant magnets," Journal of the Physical Society of Japan **85**, 103703 (2016).

[260] S. Hayami and Y. Motome, "Topological spin crystals by itinerant frustration," Journal of Physics: Condensed Matter **33**, 443001 (2021).

[261] P. Park, W. Cho, C. Kim, Y. An, M. Avdeev, K. Iida, R. Kajimoto, and J.-G. Park, "Composition dependence of bulk properties in the Co-intercalated transition metal dichalcogenide $Co_{1/3}TaS_2$," Phys. Rev. B **109**, L060403 (2024).

[262] Z. Du, H.-Z. Lu, and X. Xie, "Nonlinear Hall effects," Nature Reviews Physics **3**, 744–752 (2021).

[263] Y. Tokura and N. Nagaosa, "Nonreciprocal responses from non-centrosymmetric quantum materials," Nature communications **9**, 3740 (2018).

[264] Y. Liu, Z. Hu, X. Tong, E. D. Bauer, and C. Petrovic, "Electrical and thermal transport in van der waals magnets $2H{-}M_xTaS_2(M = Mn, Co)$," Phys. Rev. Res. **4**, 013048 (2022).

[265] Y. Kousaka, T. Ogura, J. Jiang, K. Mizutani, S. Iwasaki, J. Akimitsu, and Y. Togawa, "An emergence of chiral helimagnetism or ferromagnetism governed by Cr intercalation in a dichalcogenide $CrNb_3S_6$," APL Materials **10**, 090704 (2022).

[266] S. Wu, R. Basak, W. Li, J.-W. Kim, P. J. Ryan, D. Lu, M. Hashimoto, C. Nelson, R. Acevedo-Esteves, S. C. Haley, J. G. Analytis, Y. He, A. Frano, and R. J. Birgeneau, "Discovery of charge order in the transition metal dichalcogenide Fe_xNbS_2," Phys. Rev. Lett. **131**, 186701 (2023).

[267] C.-W. Chen, S. Chikara, V. S. Zapf, and E. Morosan, "Correlations of crystallographic defects and anisotropy with magnetotransport properties in Fe_xTaS_2 single crystals ($0.23 \leq x \leq 0.35$)," Phys. Rev. B **94**, 054406 (2016).

[268] S. Syzranov, "Effect of vacancy defects on geometrically frustrated magnets," Phys. Rev. B **106**, L140202 (2022).

[269] Z. Hawkhead, T. J. Hicken, N. P. Bentley, B. M. Huddart, S. J. Clark, and T. Lancaster, "Band-filling-controlled magnetism from transition metal intercalation in $N_{1/3}NbS_2$ revealed with first-principles calculations," Phys. Rev. Mater. **7**, 114002 (2023).

[270] H. Park and I. Martin, "DFT + DMFT study of the magnetic susceptibility and the correlated electronic structure in transition-metal intercalated NbS_2," Phys. Rev. B **109**, 085110 (2024).

[271] T. Hatanaka, T. Nomoto, and R. Arita, "Magnetic interactions in intercalated transition metal dichalcogenides: A study based on *ab initio* model construction," Phys. Rev. B **107**, 184429 (2023).

[272] K. Nygren, D. Pagan, J. Ruff, E. Arenholz, and J. Brock, ""cartography"' in 7-dimensions at CHESS: Mapping of structure in real space, reciprocal space, and time using high-energy x-rays," Synchrotron Radiation News **33**, 11–16 (2020).

[273] D. G. Hawthorn, F. He, L. Venema, H. Davis, A. J. Achkar, J. Zhang, R. Sutarto, H. Wadati, A. Radi, T. Wilson, G. Wright, K. M. Shen, J. Geck, H. Zhang, V. Novák, and G. A. Sawatzky, "An in-vacuum diffractometer for resonant elastic soft x-ray scattering," Review of Scientific Instruments **82**, 073104 (2011).

[274] P. Park, Y.-G. Kang, J. Kim, K. H. Lee, H.-J. Noh, M. J. Han, and J.-G. Park, "Field-tunable toroidal moment and anomalous hall effect in noncollinear antiferromagnetic weyl semimetal $Co_{1/3}TaS_2$," npj Quantum Materials **7**, 1–7 (2022).

[275] G. Wang, R. Carter, and D. Douglass, "High-temperature sulfidation of fe-nb alloys," Oxidation of metals **32**, 273–294 (1989).

[276] M. Drábek, J. Hybler, M. Rieder, and V. B$\acute{}$ohmová, "The system Fe-Nb-S and its geological implications," The Canadian Mineralogist **48**, 1059–1068 (2010).

[277] J. Mahy, G. A. Wiegers, F. van Bolhuis, A. Diedering, and R. J. Haange, "X-ray and electron diffraction study of intercalates Ag_xTaS_2," physica status solidi (a) **107**, 873–887 (1988).

[278] J. K. Krause, T. C. Long, T. Egami, and D. G. Onn, "Low-temperature specific heat of the metallic glasses $Fe_xNi_{80-x}P_{14}B_6$ and $(Fe_yNi_{100-y})_{79}P_{13}B_8$ for the spin-glass and spin-cluster-glass regimes," Phys. Rev. B **21**, 2886–2896 (1980).

[279] H. Park, O. Heinonen, and I. Martin, "First-principles study of magnetic states and the anomalous hall conductivity of $M Nb_3S_6$ (M = Co, Fe, Mn, andNi)," Phys. Rev. Materials **6**, 024201 (2022).

[280] T. Tsuji, Y. Yamamura, H. Watanabe, K. Saito, and M. Sorai, "Heat capacity of intercalated layered materials Fe_xNbS_2 at low temperature," Journal of Thermal Analysis and Calorimetry **57**, 839 – 846 (1999).

[281] T. Tsuji, Y. Yamamura, M. Koyano, S. Katayama, and M. Ito, "Thermodynamic and magnetic properties of intercalated layered compounds Fe_xNbS_2," Journal of Alloys

and Compounds **317-318**, 213–216 (2001), the 13th International Conference on Solid Compounds of Transition Elements.

[282] N. Barišić, I. Smiljanić, P. Popčević, A. Bilušić, E. Tutiš, A. Smontara, H. Berger, J. Jaćimović, O. Yuli, and L. Forró, "High-pressure study of transport properties in $Co_{0.33}NbS_2$," Phys. Rev. B **84**, 075157 (2011).

[283] S. Magalhaes, A. Schmidt, F. Zimmer, and B. Coqblin, "Spin glass and antiferromagnetism in Kondo-lattice disordered system," The European Physical Journal B-Condensed Matter and Complex Systems **34**, 447–453 (2003).

[284] Z. Wang and C. D. Batista, "Resistivity minimum in diluted metallic magnets," Phys. Rev. B **101**, 184432 (2020).

[285] Z. Wang, K. Barros, G.-W. Chern, D. L. Maslov, and C. D. Batista, "Resistivity minimum in highly frustrated itinerant magnets," Phys. Rev. Lett. **117**, 206601 (2016).

[286] A. D. LaForge, S. H. Pulido, R. J. Cava, B. C. Chan, and A. P. Ramirez, "Quasispin glass in a geometrically frustrated magnet," Phys. Rev. Lett. **110**, 017203 (2013).

[287] Z. Fu, Y. Zheng, Y. Xiao, S. Bedanta, A. Senyshyn, G. G. Simeoni, Y. Su, U. Rücker, P. Kögerler, and T. Brückel, "Coexistence of magnetic order and spin-glass-like phase in the pyrochlore antiferromagnet $Na_3Co(CO_3)_2Cl$," Phys. Rev. B **87**, 214406 (2013).

[288] C. V. Topping and S. J. Blundell, "A.C. susceptibility as a probe of low-frequency magnetic dynamics," Journal of Physics: Condensed Matter **31**, 013001 (2018).

[289] N. J. Ghimire, M. A. McGuire, D. S. Parker, B. Sipos, S. Tang, J.-Q. Yan, B. C. Sales, and D. Mandrus, "Magnetic phase transition in single crystals of the chiral helimagnet $Cr_{1/3}NbS_2$," Phys. Rev. B **87**, 104403 (2013).

[290] S. Polesya, S. Mankovsky, H. Ebert, P. G. Naumov, M. A. ElGhazali, W. Schnelle, S. Medvedev, S. Mangelsen, and W. Bensch, "$Mn_{1/4}NbS_2$: Magnetic and magnetotrans-

port properties at ambient pressure and ferro- to antiferromagnetic transition under pressure," Phys. Rev. B **102**, 174423 (2020).

[291] M. F. Collins, *Magnetic critical scattering*, Vol. 4 (Oxford university press, 1989).

[292] M. Cooper and W. Stirling, "Magnetic x-ray scattering," Radiation Physics and Chemistry **56**, 85–99 (1999).

[293] M. Stekiel, P. Čermák, C. Franz, W. Simeth, S. Weber, E. Ressouche, W. Schmidt, K. Nemkovski, H. Deng, A. Bauer, C. Pfleiderer, and A. Schneidewind, "Incommensurate antiferromagnetic order in ceptal$_3$," Phys. Rev. Res. **5**, 013058 (2023).

[294] S. Nakatsuji, Y. Nambu, and S. Onoda, "Novel geometrical frustration effects in the two-dimensional triangular-lattice antiferromagnet $NiGa_2S_4$ and related compounds," J. Phys. Soc. Jpn. **79**, 011003 (2010).

[295] H. Takeya, K. Ishida, K. Kitagawa, Y. Ihara, K. Onuma, Y. Maeno, Y. Nambu, S. Nakatsuji, D. E. MacLaughlin, A. Koda, and R. Kadono, "Spin dynamics and spin freezing behavior in the two-dimensional antiferromagnet $NiGa_2S_4$ revealed by Ga-NMR, NQR and μSR measurements," Phys. Rev. B **77**, 054429 (2008).

[296] H. Yamaguchi, S. Kimura, M. Hagiwara, Y. Nambu, S. Nakatsuji, Y. Maeno, and K. Kindo, "High-field electron spin resonance in the two-dimensional triangular-lattice antiferromagnet $NiGa_2S_4$," Phys. Rev. B **78**, 180404 (2008).

[297] H. Yamaguchi, S. Kimura, M. Hagiwara, Y. Nambu, S. Nakatsuji, Y. Maeno, A. Matsuo, and K. Kindo, "High-field esr and magnetization of the triangular lattice antiferromagnet $NiGa_2S_4$," J. Phys. Soc. Jpn. **79**, 054710 (2010).

[298] D. E. MacLaughlin, Y. Nambu, S. Nakatsuji, R. H. Heffner, L. Shu, O. O. Bernal, and K. Ishida, "Unconventional spin freezing and fluctuations in the frustrated antiferromagnet $NiGa_2S_4$," Phys. Rev. B **78**, 220403 (2008).

[299] A. Yaouanc, P. Dalmas de Réotier, Y. Chapuis, C. Marin, G. Lapertot, A. Cervellino, and A. Amato, "Short-range magnetic ordering process for the triangular-lattice compound $NiGa_2S_4$: A positive muon spin rotation and relaxation study," Phys. Rev. B **77**, 092403 (2008).

[300] Y. Nambu, J. S. Gardner, D. E. MacLaughlin, C. Stock, H. Endo, S. Jonas, T. J. Sato, S. Nakatsuji, and C. Broholm, "Spin fluctuations from hertz to terahertz on a triangular lattice," Phys. Rev. Lett. **115**, 127202 (2015).

[301] S. Nakatsuji, Y. Nambu, H. Tonomura, O. Sakai, S. Jonas, C. Broholm, H. Tsunetsugu, Y. Qiu, and Y. Maeno, "Spin disorder on a triangular lattice," Science **309**, 1697–1700 (2005).

[302] C. Stock, S. Jonas, C. Broholm, S. Nakatsuji, Y. Nambu, K. Onuma, Y. Maeno, and J.-H. Chung, "Neutron-scattering measurement of incommensurate short-range order in single crystals of the $S = 1$ triangular antiferromagnet $NiGa_2S_4$," Phys. Rev. Lett. **105**, 037402 (2010).

[303] H. Kawamura and A. Yamamoto, "Vortex-induced topological transition of the bilinear–biquadratic heisenberg antiferromagnet on the triangular lattice," J. Phys. Soc. Jpn. **76**, 073704 (2007).

[304] H. Kawamura, A. Yamamoto, and T. Okubo, "Z_2-vortex ordering of the triangular-lattice heisenberg antiferromagnet," Journal of the Physical Society of Japan **79**, 023701 (2010).

[305] T. Okubo and H. Kawamura, "Signature of a Z_2 vortex in the dynamical correlations of the triangular-lattice heisenberg antiferromagnet," Journal of the Physical Society of Japan **79**, 084706 (2010).

[306] Y. Nambu, K. Aoyama, H. Kawamura, T. Gentile, W. Chen, S. Watson, Q. Ye, and

Y. Qiu, "Observation of a spin chirality driven topological transition in a van der waals magnet," preprint (2022), rs.3.rs-1535863/v1.

[307] R. Tamura and N. Kawashima, "First-order transition to incommensurate phase with broken lattice rotation symmetry in frustrated heisenberg model," J. Phys. Soc. Jpn. **77**, 103002 (2008).

[308] K. Takubo, T. Mizokawa, J.-Y. Son, Y. Nambu, S. Nakatsuji, and Y. Maeno, "Unusual superexchange pathways in an NiS_2 triangular lattice with negative charge-transfer energy," Phys. Rev. Lett. **99**, 037203 (2007).

[309] K. Takubo, T. Mizokawa, Y. Nambu, and S. Nakatsuji, "Electronic structure study of triangular lattices in $FeGa_2S_4$, $Fe_2Ga_2S_5$, and $NiGa_2S_4$: Photoemission spectroscopy and hartree-fock calculations," Phys. Rev. B **79**, 134422 (2009).

[310] Y. Nambu, S. Nakatsuji, and Y. Maeno, "Coherent behavior and nonmagnetic impurity effects of spin disordered state in $NiGa_2S_4$," Journal of the Physical Society of Japan **75**, 043711 (2006).

[311] Y. Nambu, S. Nakatsuji, Y. Maeno, E. K. Okudzeto, and J. Y. Chan, "Spin dependent impurity effects on the 2d frustrated magnetism of $NiGa_2S_4$," Phys. Rev. Lett. **101**, 207204 (2008).

[312] Y. Nambu and S. Nakatsuji, "Two-dimensional magnetism and spin-size effect in the $S = 1$ triangular antiferromagnet $NiGa_2S_4$," Journal of Physics: Condensed Matter **23**, 164202 (2011).

[313] Y. Nambu, R. T. Macaluso, T. Higo, K. Ishida, and S. Nakatsuji, "Structural properties of the two-dimensional triangular antiferromagnet $NiGa_2S_4$," Phys. Rev. B **79**, 214108 (2009).

[314] J. Takano and H. Tsunetsugu, "Theory of impurity effects on the spin nematic state," Journal of the Physical Society of Japan **80**, 094707 (2011).

[315] R. Huang, M. Zhang, C. An, Y. Zhou, Y. Zhou, X. Chen, and Z. Yang, "Pressure-induced mott insulator-metal transition and structural phase transitions in the triangular antiferromagnet $NiGa_2S_4$," Phys. Rev. B **107**, 144106 (2023).

[316] E. Weschke and E. Schierle, "The UE46 PGM-1 beamline at Bessy II," Journal of large-scale research facilities JLSRF **4**, A127–A127 (2018).

[317] K.-J. Zhou, A. Walters, M. Garcia-Fernandez, T. Rice, M. Hand, A. Nag, J. Li, S. Agrestini, P. Garland, H. Wang, S. Alcock, I. Nistea, B. Nutter, N. Rubies, G. Knap, M. Gaughran, F. Yuan, P. Chang, J. Emmins, and G. Howell, "I21: An advanced high-resolution resonant inelastic x-ray scattering beamline at Diamond Light Source," Journal of Synchrotron Radiation **29**, 563–580 (2022).

[318] A. Singh, H. Y. Huang, Y. Y. Chu, C. Y. Hua, S. W. Lin, H. S. Fung, H. W. Shiu, J. Chang, J. H. Li, J. Okamoto, C. C. Chiu, C. H. Chang, W. B. Wu, S. Y. Perng, S. C. Chung, K. Y. Kao, S. C. Yeh, H. Y. Chao, J. H. Chen, D. J. Huang, and C. T. Chen, "Development of the soft x-ray agm–ags rixs beamline at the Taiwan Photon Source," Journal of Synchrotron Radiation **28**, 977–986 (2021).

[319] A. Stunault, F. de Bergevin, D. Wermeille, C. Vettier, T. Brückel, N. Bernhoeft, G. J. McIntyre, and J. Y. Henry, "k-edge resonant x-ray magnetic scattering from $RbMnF_3$," Phys. Rev. B **60**, 10170–10179 (1999).

[320] S. Kang, K. Kim, B. H. Kim, J. Kim, K. I. Sim, J.-U. Lee, S. Lee, K. Park, S. Yun, T. Kim, *et al.*, "Coherent many-body exciton in van der waals antiferromagnet $NiPS_3$," Nature **583**, 785–789 (2020).

[321] M. F. DiScala, D. Staros, A. de la Torre, A. Lopez, D. Wong, C. Schulz, M. Barkowiak, V. Bisogni, J. Pelliciari, B. Rubenstein, and K. W. Plumb, "Elucidating the role of dimensionality on the electronic structure of the van der waals antiferromagnet $NiPS_3$," Advanced Physics Research **3**, 2300096 (2024).

[322] W. He, Y. Shen, K. Wohlfeld, J. Sears, J. Li, J. Pelliciari, M. Walicki, S. Johnston, E. Baldini, V. Bisogni, M. Mitrano, and M. P. M. Dean, "Magnetically propagating Hund's exciton in van der Waals antiferromagnet $NiPS_3$," Nature Communications **15** (2024), 10.1038/s41467-024-47852-x.

[323] S. Son, Y. Lee, J. H. Kim, B. H. Kim, C. Kim, W. Na, H. Ju, S. Park, A. Nag, K.-J. Zhou, Y.-W. Son, H. Kim, W.-S. Noh, J.-H. Park, J. S. Lee, H. Cheong, J. H. Kim, and J.-G. Park, "Multiferroic-enabled magnetic-excitons in 2D quantum-entangled van der waals antiferromagnet NiI_2," Advanced Materials **34**, 2109144 (2022).

[324] C. A. Occhialini, Y. Tseng, H. Elnaggar, Q. Song, M. Blei, S. A. Tongay, V. Bisogni, F. M. de Groot, J. Pelliciari, and R. Comin, "Nature of excitons and their ligand-mediated delocalization in nickel dihalide charge-transfer insulators," arXiv preprint arXiv:2404.10818 (2024), 10.48550/arXiv.2404.10818.

[325] A. Nag, H. C. Robarts, F. Wenzel, J. Li, H. Elnaggar, R.-P. Wang, A. C. Walters, M. García-Fernández, F. M. F. de Groot, M. W. Haverkort, and K.-J. Zhou, "Many-body physics of single and double spin-flip excitations in NiO," Phys. Rev. Lett. **124**, 067202 (2020).

[326] N. Bernhoeft, "Geometrical effects in diffraction analysis," Acta Crystallographica Section A: Foundations of Crystallography **55**, 274–288 (1999).

[327] T. Tomita, Y. Nambu, S. Nakatsuji, S. Koeda, M. Hedo, and Y. Uwatoko, "Pressure dependence of electrical transport in the triangular antiferromagnetic insulators $FeGa_2S_4$ and $Fe_2Ga_2S_5$," Journal of the Physical Society of Japan **78**, 094603 (2009).

[328] S. Y. Kim, T. Y. Kim, L. J. Sandilands, S. Sinn, M.-C. Lee, J. Son, S. Lee, K.-Y. Choi, W. Kim, B.-G. Park, C. Jeon, H.-D. Kim, C.-H. Park, J.-G. Park, S. J. Moon, and T. W. Noh, "Charge-spin correlation in van der waals antiferromagnet $NiPS_3$," Phys. Rev. Lett. **120**, 136402 (2018).

[329] X. Wang, J. Cao, H. Li, Z. Lu, A. Cohen, A. Haldar, H. Kitadai, Q. Tan, K. S. Burch, D. Smirnov, W. Xu, S. Sharifzadeh, L. Liang, and X. Ling, "Electronic raman scattering in the 2D antiferromagnet $NiPS_3$," Science Advances **8**, eabl7707 (2022).

[330] K. Huang and E. Manousakis, "Antiferromagnetic order and high-temperature superconductivity," Phys. Rev. B **36**, 8302–8308 (1987).